

NASA Contractor Report 3530

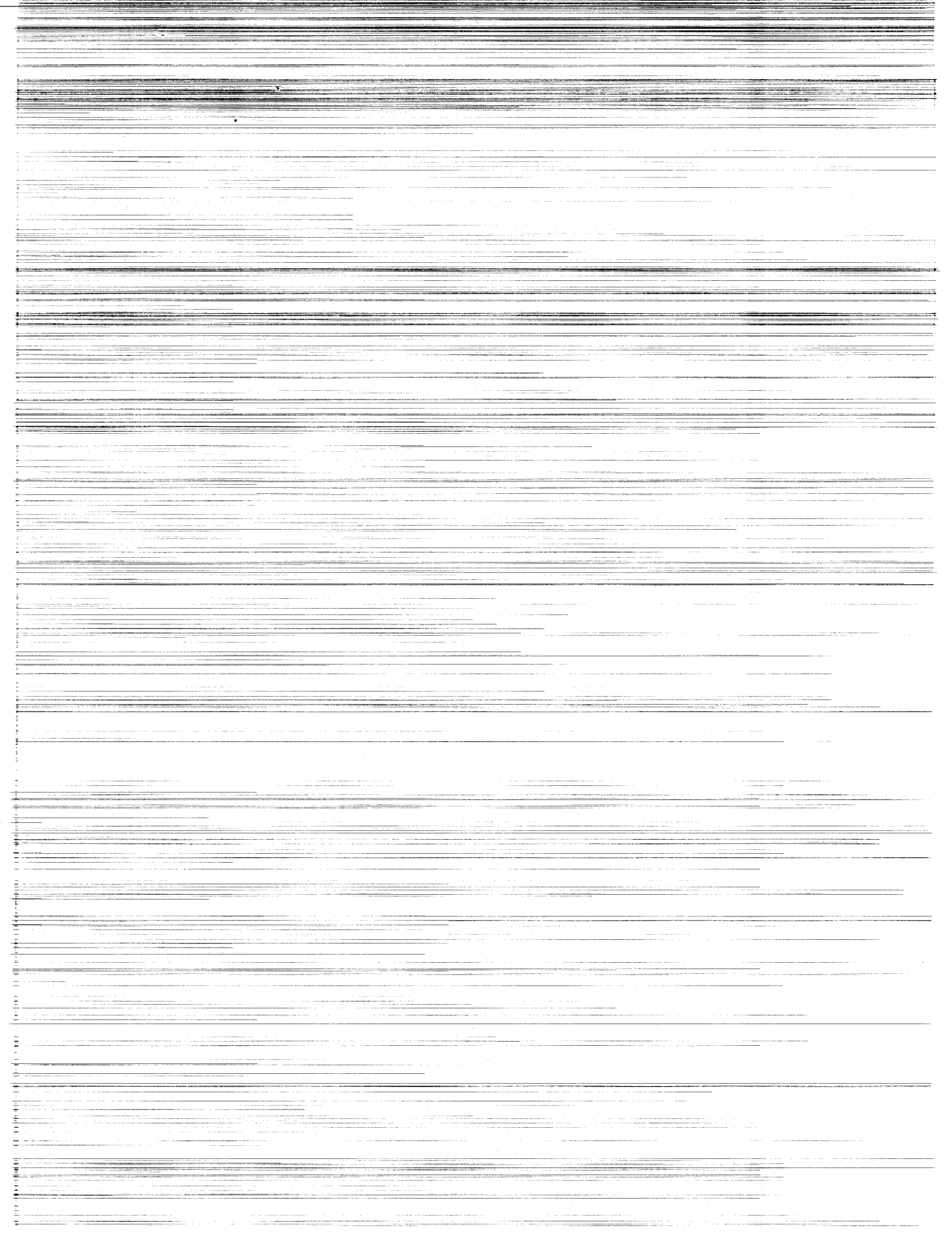
**Experimental Studies of
Flow Separation of Three
Airfoils at Low Speeds**

**E. J. Rodgers, H. C. Seetharam,
and W. H. Wentz, Jr.**

**GRANT NGR 17-003-021
MARCH 1982**

NASA





NASA Contractor Report 3530

Experimental Studies of Flow Separation of Three Airfoils at Low Speeds

E. J. Rodgers, H. C. Seetharam,
and W. H. Wentz, Jr.

*Wichita State University
Wichita, Kansas*

Prepared for
Langley Research Center
under Grant NGR 17-003-021

NASA

National Aeronautics
and Space Administration

**Scientific and Technical
Information Branch**

1982

Use of trade names or names of manufacturers in this report does not constitute an official endorsement of such products or manufacturers, either expressed or implied, by the National Aeronautics and Space Administration.

SUMMARY

Wind tunnel tests have been conducted on the NASA LS(1)-0421 Mod, NACA 2412 and NASA GA(W)-2 airfoil sections at a Reynolds number of 2.2×10^6 and a Mach number of 0.13. Detailed measurements of flow fields associated with turbulent boundary layers of these airfoils have been obtained at pre-stall, near-stall, and post-stall angles of attack. Velocity and pressure survey results over the airfoil and in the associated wake are presented for fully attached flow conditions through the stalled flow condition. Extensive force, pressure, tuft survey, hot-film survey, local skin friction and boundary layer data are also included.

Pressure distributions and separation point locations of the NACA 2412 and the NASA GA(W)-2 airfoils show good agreement with theory at the pre-stall and near-stall angles of attack. The pressure distributions of the NASA LS(1)-0421 Mod airfoil show good agreement with theory for angles of attack up to 8.5° (pre-stall) but the separation point locations of this airfoil do not agree well with theory at angles of attack of 8.5° and higher. Boundary layer displacement thickness and momentum thickness agree well with theory up to the point of separation for each airfoil when the separated flow region extends over no more than $0.2c$. There is disparity between the extent of flow reversal in the wake as measured by pressure and hot-film probes for each of the airfoils. The difference is attributed to the intermittent nature of the flow reversal.

1

2
3
4
5
6
7
8
9
10
11
12
13
14
15
16
17
18
19
20
21
22
23
24
25
26
27
28
29
30
31
32
33
34
35
36
37
38
39
40
41
42
43
44
45
46
47
48
49
50
51
52
53
54
55
56
57
58
59
60
61
62
63
64
65
66
67
68
69
70
71
72
73
74
75
76
77
78
79
80
81
82
83
84
85
86
87
88
89
90
91
92
93
94
95
96
97
98
99
100

101
102
103
104
105
106
107
108
109
110
111
112
113
114
115
116
117
118
119
120
121
122
123
124
125
126
127
128
129
130
131
132
133
134
135
136
137
138
139
140
141
142
143
144
145
146
147
148
149
150
151
152
153
154
155
156
157
158
159
160
161
162
163
164
165
166
167
168
169
170
171
172
173
174
175
176
177
178
179
180
181
182
183
184
185
186
187
188
189
190
191
192
193
194
195
196
197
198
199
200

201
202
203
204
205
206
207
208
209
210
211
212
213
214
215
216
217
218
219
220
221
222
223
224
225
226
227
228
229
230
231
232
233
234
235
236
237
238
239
240
241
242
243
244
245
246
247
248
249
250

INTRODUCTION

NASA Langley has sponsored experimental research work on separated flow fields on airfoils at Wichita State University since 1974. Detailed flow field data for the GA(W)-1 with flap nested (Ref. 1) and with a Fowler flap deployed (Ref. 2) have been reported earlier. The data of Reference 1 has provided Naik and Zumwalt new directions in formulating mathematical models for separated flows (Ref. 3).

In order to broaden the base of experimental data it was considered important to obtain additional experimental data for an older NACA airfoil section and two newer NASA sections, each having different thickness and camber distributions than the GA(W)-1. With this objective in mind the NASA LS(1)-0421 Mod (hereafter referred to as 0421), NACA 2412, and NASA GA(W)-2 airfoils were selected for additional separated flow research. The results are presented in this report.

It is anticipated that the results of the research of this report will provide an additional data base for formulating a universal mathematical model of separated flow fields associated with airfoils at low speeds.

SYMBOLS

To the maximum extent possible, physical measurements are presented in non-dimensional form. Dimensional quantities are given in both International (SI) Units and U.S. Customary Units. All measurements were made in U.S. Customary Units. Conversion factors between SI Units and U.S. Customary Units are given in Reference 4. The following symbols are used in the present report:

c	Wing chord
c_d	Airfoil section drag coefficient, $\frac{\text{section drag}}{q_\infty c}$
c_f	Local skin friction coefficient, $\frac{\tau}{q_\infty}$
c_l	Airfoil section lift coefficient, $\frac{\text{section lift}}{q_\infty c}$
c_m	Airfoil section pitching moment coefficient with respect to .25c location, $\frac{\text{section moment}}{q_\infty c^2}$
c_{ps}	Static pressure coefficient, $\frac{p_s - p_\infty}{q_\infty}$
c_{pt}	Total pressure coefficient, $\frac{p_t - p_\infty}{q_\infty}$
H	Shape factor (δ^*/δ^{**})
h	Razor blade thickness/2
p_s	Local static pressure
p_t	Local total pressure
p_∞	Free stream static pressure
q_∞	Free stream dynamic pressure
RN	Reynolds number based on wing chord and free stream conditions
T	Turbulence intensity
U	Velocity at the edge of the boundary layer, non-dimensionalized with respect to free stream velocity
u	Local velocity non-dimensionalized with respect to free stream velocity, $\sqrt{\frac{p_t - p_s}{q_\infty}}$
u_x	Non-dimensionalized component of local velocity in the free stream direction
x	Streamwise coordinate
z	Vertical coordinate

α	Angle of attack, degrees
Δp	Pressure difference between the pressure reading with razor blade in position and the true undisturbed static pressure
δ	Boundary layer thickness
δ^*	Boundary layer displacement thickness, $\int_0^{\delta} (1 - \frac{u}{U}) dz$
δ^{**}	Boundary layer momentum thickness, $\int_0^{\delta} \frac{u}{U} (1 - \frac{u}{U}) dz$
τ	Shear stress

APPARATUS AND PROCEDURE

Tests

The experimental investigations were carried out in the WSU 213 cm x 305 cm (7' x 10') low speed wind tunnel fitted with a 213 cm x 91.4 cm (7' x 3') two-dimensional insert (Ref. 5). Each airfoil section 61 cm (24") in chord and 91.4 cm (36") in span, was mounted in turn in the 2-D insert. Figure 1 shows airfoil profile shapes and coordinates. Surface static pressure taps constructed of 1.07 mm (0.042") I.D. stainless steel tubing were distributed along the mid-span section of each airfoil. Flow field surveys were conducted at pre-stall, near-stall and post-stall angles of attack. Table 1 shows the angles of attack associated with these conditions for each of the airfoils.

The Reynolds number of all the tests was 2.2×10^6 based on the airfoil chord and the Mach number was 0.13. Transition was insured by employing 2.5 mm (0.1") wide strips of #80 carborundum grit at 0.05c on both upper and lower surfaces. In

Table 1
Test Angles of Attack

Airfoil	Pre-Stall	Near-Stall	Post-Stall
0421 Mod	8.5°	10.6°	12.7°
2412	12.4°	14.4°	16.4°
GA(W)-2	10.3°	14.4°	18.3°

this test series details of the flow field were investigated only on the upper surface of the model, and in the wake. At each angle of attack, fourteen chordwise survey stations were selected covering the airfoil upper surface and the wake.

Basic force measurements, surface pressure and local skin friction distributions, flow visualization and hot-film surveys were also obtained to supplement the flow field data.

Instrumentation

Velocities at heights more than 2.5 mm (.10") above the local surface of each airfoil were obtained using a five-tube pressure sensing pitch-yaw probe of 3.175 mm (0.125") diameter (Fig. 2). Velocities very close to the airfoil surface and in regions of flow reversal of the NASA 0421 and NACA 2412 airfoil were obtained by a four-tube probe having a pair of pitot and static tubes positioned 180° apart along the tube axis (Fig. 3). The axis of the static tube was located at a height of 0.25 mm (0.01") above the pitot-tube axis. Velocities very close to the surface of the GA(W)-2 airfoil were obtained by a 2-tube probe (Fig. 4) consisting of two 0.610 mm outside diameter hypodermic tubes soft soldered together and sealed at the ends. A hole 0.343 mm in diameter was drilled in each of the tubes as shown.

These two tubes were then inserted and soldered into two more progressively larger hypodermic tubes and into a steel cylindrical stem. The velocities in the wake of the GA(W)-2 airfoil in the regions where flow reversal existed were obtained by the four-tube probe. The four- and five-tube probes were mounted in tandem, straddling the model centerline, spaced 7.62 cm (3") on either side of the centerline.

Hot-film surveys were conducted to scan the regions of moderate and heavy turbulence employing a 0.05 mm (.002") diameter single-film probe with linearizer, and a 0.15 mm (.006") diameter split-film probe (Fig. 5).

Local skin friction was measured by the technique outlined by East (Ref. 6) employing commercially available razor blades of 0.1 mm (0.0041") thickness. Each blade was trimmed to a 6.4 mm x 6.4 mm (0.25" x 0.25") square and positioned at the surface static port location where the local skin friction was to be evaluated. Details of the razor blade dimensions are given in Figure 6.

Unbonded strain gage pressure transducers with a range of ± 17.2 kilo-newtons/m² (± 2.5 psi) were used for all pressure measurements.

Methods

Lift and moment data for each airfoil were obtained from the tunnel main balance system. Drag was calculated from wake surveys measured at the 0.5c station downstream from the trailing edge. Flow velocity data were acquired by initially tilting the two- (or four-) and five-tube probes to align with the local slope of the surface. Near-wall velocity data were obtained by aligning the two-(or four-)tube probe axis perpendicular to the direction of the local surface, with the tip aligned for zero yaw. For distances more than 2.5 mm above the surface, the five-tube pressure readings were used to obtain total and static pressure, as well as local upwash angle through appropriate calibration curves.

Flow reversal was indicated by observing the higher reading from the forward- and aft-facing total tubes on the four-tube probe. The data reduction program selected flow direction based upon these readings, and utilized the appropriate static pressure tube reading to calculate velocity. As stated previously, the four-tube probe readings were utilized for regions of reversed flow. Attempts to obtain readings by rotating the five-tube probe 180° in yaw for regions of flow reversal were unsatisfactory. The data usually indicated flow direction opposite to probe direction for both forward and reversed positions. The four-tube probe gave reasonably consistent results. The discrepancies between the two instruments are attributed to the unsteady nature of the reversed flow, and the high damping characteristics of the five-tube probe. Measurements in the wake were made with the probes aligned in the free-stream direction (zero tilt).

Tuft surveys and oil flow methods were employed for observation of the surface flow patterns and determination of the separation point.

Hot-film surveys were made with the traversing mechanism employed for the four- and five-tube surveys. Photos of the velocity fluctuations displayed on the oscilloscope were also recorded.

Local skin friction was measured by positioning the razor blade as shown in Figure 6. This method involves relating the skin friction (τ) to the difference between the pressure recorded at the static hole with the blade in position, and the true undisturbed local surface static pressure (blade removed). Details of geometrical limitations and calibration are given in Reference 6. Important dimensions are tabulated in Figure 6 for the present experimental set-up.

During the course of the present experiments, it was found that under certain conditions the velocity probe and probe mechanism created an aerodynamic interference which

affected the separation point location, and consequently had a large effect on surface pressures and other parameters. As a result of special calibration studies, a new test section ceiling and a new probe mount system were designed and installed. The new design permitted placing most of the mechanism outside the test section.

Special calibrations and studies of all test data revealed that the troublesome adverse interference of the unmodified probe mechanism was a significant problem only at the post-stall angles of attack on the NACA 2412 and GA(W)-2 airfoils. Review of data from earlier research revealed that the probe mount interference did not significantly affect the extensive flow measurements made on the 17% thick GA(W)-1 airfoil (Refs. 1,2).

Therefore, the post-stall flow measurement run series were repeated only for the NACA 2412 and GA(W)-2 airfoils at the post-stall angles, and the original data for these conditions were discarded. The runs with the original probe mount for the NACA 2412 and GA(W)-2 airfoils at the pre-stall and near-stall angles were not repeated, on the basis that discrepancies noted did not warrant complete re-measurement.

The flow surveys of the LS(1)-0421 Mod airfoil were all accomplished after the probe mount modification described above. Table 2 summarizes the experimental setup information for the data presented in this report. Details of the special calibrations and hardware are given in Appendix A.

Table 2 - Probe Mount Set-Up

<u>Airfoil</u>	<u>Angle of Attack</u>		
	<u>Pre-Stall</u>	<u>Near-Stall</u>	<u>Post-Stall</u>
0421 Mod	modified	modified	modified
2412	unmodified	unmodified	modified
GA(W)-2	unmodified	unmodified	modified

In order to inform the reader as to the experimental setup for all measurements presented in this report, flow survey graphs have been labelled "Unmodified Probe Mount" or "Modified Probe Mount," as appropriate. Types of data affected by this interference were: 2-tube, 4-tube, 5-tube and hot-film anemometer measurements. Other measurements made without use of the probe mount system were unaffected.

Data Reduction

Force data, with usual wind tunnel boundary corrections, surface pressures, local velocities and flow inclinations were calculated from the measured wind tunnel raw data by computer routines developed for the IBM 1130 and 360 computers and HP 2112 mini-computer at WSU. Angles of attack tabulated on the various figures have been corrected for tunnel wall effects, based upon measured lift and linear aerodynamic theory. The local velocity is expressed in a non-dimensional form as the ratio of local to free stream velocity. Experimental velocity profiles were plotted by computer routines written for the IBM 1130 computer and HP 2112 mini-computer.

Calibration of the five-tube probe is discussed in detail in Reference 7. All the pressure instrumentation employed in the present tests is heavily damped and therefore records time-averaged values.

The two-tube probe was calibrated against the five-tube probe with the dynamic pressure as a variable. At all times both the five- and two-tube probes were aligned in the vertical plane of the free stream velocity (zero yaw). A linear curve was fitted to the calibration data and used in the data reduction program to calculate the true dynamic pressure and hence velocity as indicated by difference in pressure between forward and aft holes on the two-tube probe. Fore and aft symmetry was assumed so that a single calibration curve could be used in regions of reversed or non-reversed flow.

Typical oscilloscope traces from the hot-film probe were photographically recorded. Digital volt meter readings of the hot-film probe data were recorded manually. The hot-film was calibrated from time to time during the course of the tests to compensate for wind tunnel temperature variations. Maximum calibration shifts amounted to 6% of free stream velocity.

The pressure difference Δp , between the surface pressure recorded by the static port with the blade in position and the undisturbed static pressure, is related to the skin friction τ by a calibration equation given in Reference 6. The data reduction program utilizes this equation to calculate the local skin friction coefficient.

RESULTS

Presentation of Results

The results of the present investigation are presented in figures as listed in Table 3.

Table 3
List of Figures

Type data	Airfoil	Instrument	α	Figures
Airfoil geometry	0421	---	---	1A
	2412	---	---	1B
	GA(W)-2	---	---	1C
Instrument details		5-tube probe	---	2
		4-tube probe	---	3
		2-tube probe	---	4
		Hot-film probe	---	5
		Razor-blade technique	---	6
Lift, drag and pitching moment	0421	Force balance and wake probe	-8° to $+24.4^\circ$	7A
	2412	Force balance and wake probe	-4° to $+18.0^\circ$	7B
	GA(W)-2	Force balance and wake probe	-8° to $+20.0^\circ$	7C
Surface pressures	0421	Surface tubes	-8° to $+21.4^\circ$	8A
	2412	Surface tubes	-4° to $+16.4^\circ$	8B
	GA(W)-2	Surface tubes	$10.3^\circ, 14.4^\circ, 18.3^\circ$	8C
Surface flow	0421	Tufts	0.2° to 16.9°	9A
	2412	Tufts	0.2° to 20.3°	9B
	GA(W)-2	Tufts	4.3° to 20.3°	9C
Velocity profiles	0421	5-tube and 4-tube probes	$8.5^\circ, 10.6^\circ, 12.7^\circ$	10A
	2412	5-tube and 4-tube probes	$12.4^\circ, 14.4^\circ, 16.4^\circ$	10B
	GA(W)-2	5-tube and 2-tube probes	$10.3^\circ, 14.4^\circ, 18.3^\circ$	10C

Table 3 (continued)

Type data	Airfoil	Instrument	α	Figures
Near-wall velocity profiles	0421	5-tube and 4-tube probes	$8.5^\circ, 10.6^\circ, 12.7^\circ$	11A
	2412	5-tube and 4-tube probes	$12.4^\circ, 14.4^\circ, 16.4^\circ$	11B
	GA(W)-2	5-tube and 2-tube probes	$10.3^\circ, 14.4^\circ, 18.3^\circ$	11C
Static pressure profiles	0421	5-tube probe	$8.5^\circ, 10.6^\circ, 12.7^\circ$	12A
	2412	5-tube probe	$12.4^\circ, 14.4^\circ, 16.4^\circ$	12B
	GA(W)-2	5-tube probe	$10.3^\circ, 14.4^\circ, 18.3^\circ$	12C
Static pressure field contours	0421	5-tube probe	$8.5^\circ, 10.6^\circ, 12.7^\circ$	13A
	2412	5-tube probe	$12.4^\circ, 14.4^\circ, 16.4^\circ$	13B
	GA(W)-2	5-tube probe	$10.3^\circ, 14.4^\circ, 18.3^\circ$	13C
Boundary layer displacement thickness	0421	5-tube probe	$8.5^\circ, 10.6^\circ, 12.7^\circ$	14A
	2412	5-tube probe	$12.4^\circ, 14.4^\circ, 16.4^\circ$	14B
	GA(W)-2	5-tube probe	$10.3^\circ, 14.4^\circ, 18.3^\circ$	14C
Boundary layer momentum thickness	0421	5-tube probe	$8.5^\circ, 10.6^\circ, 12.7^\circ$	15A
	2412	5-tube probe	$12.4^\circ, 14.4^\circ, 16.4^\circ$	15B
	GA(W)-2	5-tube probe	$10.3^\circ, 14.4^\circ, 18.3^\circ$	15C
Boundary layer shape factor	0421	5-tube probe	$8.5^\circ, 10.6^\circ, 12.7^\circ$	16A
	2412	5-tube probe	$12.4^\circ, 14.4^\circ, 16.4^\circ$	16B
	GA(W)-2	5-tube probe	$10.3^\circ, 14.4^\circ, 18.3^\circ$	16C

Table 3 (continued)

Type data	Airfoil	Instrument	α	Figures
Displacement thickness distribution	0421	5-tube probe	8.5°, 10.6°, 12.7°	17A
	2412	5-tube probe	12.4°, 14.4°, 16.4°	17B
	GA(W)-2	5-tube probe	10.3°, 14.4°, 18.3°	17C
Separation streamline	0421	5-tube probe	10.6°, 12.7°	18A
	2412	5-tube probe	16.4°	18B
	GA(W)-2	5-tube probe	18.3°	18C
Velocity and pressures in wake	0421	5-tube probe	8.5°, 10.6°, 12.7°	19A
	2412	5-tube probe	12.4°, 14.4°, 16.4°	19B
	GA(W)-2	5-tube probe	10.3°, 14.4°, 18.3°	19C
Total pressure contours in wake	0421	5-tube probe	8.5°, 10.6°, 12.7°	20A
	2412	5-tube probe	12.4°, 14.4°, 16.4°	20B
	GA(W)-2	5-tube probe	10.3°, 14.4°, 18.3°	20C
Hot-film field surveys	0421	Hot-film anemometer	8.5°, 10.6°, 12.7°	21A
	2412	Hot-film anemometer	12.4°, 14.4°, 16.4°	21B
	GA(W)-2	Hot-film anemometer	10.3°, 14.4°, 18.3°	21C
Skin friction	0421	Razor blade	0.2°, 8.5°, 10.6°, 12.7°	22A
	2412	Razor blade	0.2°, 12.4°, 14.4°, 16.4°	22B
	GA(W)-2	Razor blade	0.2°, 8.3°, 10.3°, 14.4°, 18.3°	22C
Flow separation points	GA(W)-1 GA(W)-2 0421 2412	} Oil and tuft studies	8.5° to 18.4°	23
Flow reattachment points	GA(W)-1 GA(W)-1 0421 2412	} 5-tube probe	8.5° to 18.4°	24

Discussion

Forces: (Figure 7). These tests were conducted primarily to supplement the flow field data and to provide additional data at low Reynolds number with NASA standard roughness.

Results of the lift, drag and pitching moment measurements for the NASA 0421 airfoil are shown along with the experimental data at Reynolds numbers of 2.0×10^6 from Reference 8. The agreement between the two sets of data as seen in Figure 7 is good over most of the test range. The greatest deviation appears in the drag coefficient data at the moderate to high lift coefficients.

Results of lift, drag and pitching moment measurements for the NACA 2412 airfoil from the present tests at a Reynolds number of 2.2×10^6 are shown, along with data from earlier WSU tests at $RN = 2.9 \times 10^6$, and from NACA tests (Ref. 9) at $RN = 3.1 \times 10^6$ clean, and at $RN = 5.7 \times 10^6$ with NACA standard roughness. The data show consistent increase of $C_{l_{max}}$ with Reynolds number, and corresponding reductions in C_d . The differences between data with NACA grit and WSU grit are expected, since the NACA grit was larger and was applied over a much larger region, causing severe losses in $C_{l_{max}}$ and corresponding increases in drag at high lift coefficients. The WSU drag and pitching moment data agree reasonably well with the results of Reference 9.

Results of the lift, drag and pitching moment measurements for the GA(W)-2 airfoil are also shown along with the experimental data at a Reynolds number of 2.2×10^6 from Reference 10. The agreement between the two sets of data is good over most of the test range. The greatest deviations appear at the maximum measured post-stall angle of 18.3° and at the negative 10° angle of attack.

Pressure Distributions: (Figure 8). Surface pressure distributions measured at a number of different angles of attack are shown. These include the angles of attack at which detailed

flow studies were conducted. Theoretical pressure distributions obtained using the method of Reference 11 are also given.

The boundary layer separation points of these airfoils determined from flow visualization studies at each angle of attack are marked on the figures by the vertical line and symbols. It is seen that these separation points are consistent with the beginning of a region of constant pressure for each angle. Constancy of pressure is characteristic of separated flow regions.

Flow Visualization Studies: (Figure 9). Flow visualization studies were carried out by attaching tufts to the upper surface of the model every 0.10c. In order to study the influence of the side wall boundary layers on separation patterns, tufts were also applied to the side walls. No evidence of premature side wall separation was observed.

Tuft photographs of the NASA 0421 airfoil show that at a near-stall angle of attack of 8.5° separation appears to occur at about 0.8c. At higher angles of attack the separation point moves forward and is consistent with the stall behavior pattern shown in Figure 7.

Tuft photos for the NACA 2412 airfoil show the flow is very steady up to 8.3° . At 12.4° the last two rows of tufts are disturbed with a few tufts exhibiting reversal near the mid-span section. At 14.4° angle of attack ($C_{l_{max}}$) separation progresses upstream with the last two rows of tufts (aft of 0.80 chord) showing reversal. Tufts at the 0.70 chord station are disturbed, with some tufts indicating possible intermittent reversal at near mid-span. The flow is reasonably two-dimensional. At post-stall angles of attack ($\alpha = 16.3^\circ, 18.3^\circ$ and 20.3°) the regions of separation grow progressively larger and the flow pattern appears to have a three-dimensional character. The tufts on the side wall appear to be undisturbed.

Tuft photos are shown for the NASA GA(W)-2 airfoil for an angle of attack range of 4.3° to 20.3° . The flow is very steady up to 8.3° . At 12.4° the last two rows of tufts are disturbed with a few tufts exhibiting reversal near the mid-span section.

At 14.4° angle of attack, separation progresses upstream with the last two rows of tufts (aft of 0.70 chord) showing reversal. Tufts at the 0.70 chord station are disturbed, with some tufts indicating possible intermittent reversal at near mid-span. The flow again appears to be reasonably two-dimensional. At post-stall angles of attack ($\alpha = 16.4^\circ$ to 20.3°) the regions of separation grow larger and larger and the flow pattern becomes asymmetric. Thus the extreme post-stall flow pattern appears to have a three-dimensional character. The tufts on the side walls again appear to be undisturbed.

Limited oil-flow studies were conducted at the pre-stall, near-stall and post-stall angles of attack, to obtain more detailed definition of separation locations than the tuft studies provide. Since the oil flow is heavily damped, the surface streak patterns tend to represent a mean separation location which is much more difficult to define from tuft patterns. Results of the analysis of combined oil flow and tuft studies are given in Table 4, along with theoretical values calculated by the methods of Reference 11.

Table 4
Separation

Airfoil	Angle of Attack	Experimental Separation Location from Oil and Tuft Studies	Theoretical Separation Location
0421	8.5°	.80c	.90c
	10.6°	.65c	.83c
	12.7°	.50c	.77c
2412	12.4°	.92c	.92c
	14.4°	.80c	.82c
	16.4°	.40c	.65c
GA(W)-2	10.3°	.95c	.96c
	14.4°	.80c	.81c
	18.3°	.45c	.67c

These observed separation points are consistent with surface pressure distributions. The experimental results from Table 4 are presented in Figure 23 along with similar data from GA(W)-1 airfoil tests. These results show that initial separation is delayed on the 2412 airfoil, but once initial separation occurs it progresses forward at a greater rate with angle of attack than the other three airfoils. The NASA 0421 airfoil separates at a lower angle of attack than the other three airfoils, but the progression of separation is not as rapid as that of the NACA 2412.

Velocity Plots: (Figures 10 and 11). Computer plots of the measured velocity profiles at the mid-span section are shown. The five-tube probe did not indicate stable reversed flow either over the airfoil surface or in the wake. In regions where reversed flow exists either the calibration limits of the probe were exceeded or the indicated dynamic pressure was negative for probe yaw directions of both 0° and 180° . The dotted velocity profile lines shown for the near- and post-stall angles of attack were obtained from flow measurements taken with the four-tube probe. Inclinations of the flow were not determinable with this probe and therefore are not shown.

Detailed near-wall velocity profiles obtained from four-tube probe measurements for the 0421 airfoil and 2412 airfoil, and from two-tube probe measurements for the GA(W)-2 airfoil are presented. Velocities from the five-tube probe measurements are presented for comparison for some cases (see Figure 11). The five-tube and two- or four-tube measurements in general agree within less than $\pm 5\%$ of free stream velocity. Discrepancies between the probe types do not follow any consistent pattern.

The flow over the aft portion of an airfoil at near-stall and post-stall angles of attack is unsteady with intermittent reversing. Appendix B compares velocity profile

measurements as obtained by two of the pressure probes used in the present tests and a high-response split-film anemometer used in subsequent separated flow research. These studies show that the turbulent fluctuations near reversal are large, but that the pressure probes indicate approximately the average velocity, and approximately the proper average reversal location.

Static Pressure Profiles: (Figure 12). Static pressure profiles at various chordwise stations on the airfoils were obtained using the five-tube probe. These data show changes in pressure with distance above the airfoil surface for locations near the leading edge, with the gradients becoming lower for more aft locations. These trends are consistent with high negative pressure peaks and thin boundary layers near the leading edge, and lower negative pressures and thicker boundary layers at more aft locations.

Static Pressure Contours: (Figure 13). Static pressure contours derived from the pressure distributions obtained at ten chordwise stations and four stations in the wake are shown. The characteristic high pressure plateau reported in Reference 1 can be seen for all three airfoils in the pre-stall or near-stall condition. At the post-stall angle of attack neither the NACA 2412 nor the GA(W)-2 airfoil exhibits the high pressure region. A vertical pressure gradient from lower surface region to upper surface is also observed in the wake of the three airfoils for pre-stall and near-stall angles of attack.

Boundary Layer Characteristics: (Figures 14 through 18). The displacement and momentum thicknesses show substantial increases between pre-stall and post-stall conditions for all three airfoils. The rapid growth of the shape factor prior to separation, typical of turbulent separated boundary layers, is clearly seen. A comparison between measured shape factors at separation and typical values of H (from Ref. 12) is shown in Table 5.

Table 5
Shape Factors at Separation

Airfoil	Angle of Attack	Separation Point from Tuft and Oil Flow Observations	Measured Shape Factor H	Normally Expected Value of H
0421	8.5°	.80c	2.07	1.8 to 2.2
	10.6°	.65c	1.67	1.8 to 2.2
	12.7°	.50c	1.62	1.8 to 2.2
2412	12.4°	.92c	2.12	1.8 to 2.2
	14.4°	.80c	1.97	1.8 to 2.2
	16.4°	.40c	1.53	1.8 to 2.2
GA(W)-2	10.3°	.95c	2.06	1.8 to 2.2
	14.4°	.80c	1.76	1.8 to 2.2
	18.3°	.45c	1.58	1.8 to 2.2

The measured shape factor at pre-stall for all three airfoils is within the normal range of expected values as is the measured shape factor at $C_{l_{max}}$ for the NACA 2412 airfoil. The measured shape factor of the other two airfoils at near-stall angles of attack as well as all three airfoils at post-stall angles of attack however are lower than expected. The difference at the post-stall angles of attack is believed to be due to the characteristic post-stall turbulent fluctuations which were observed. In addition the flow at the post-stall angles of attack appears to be somewhat three-dimensional in reality.

The boundary layer displacement thickness superimposed on the three airfoils is shown in Figure 17. It can be seen that the slope of the augmented surface for all three airfoils follows the slope of the airfoil surface very closely up to the point of separation and then diverges away depending on the depth of the separated layer. This trend is also exhibited by the separation streamlines which are shown in Figure 18 for the three airfoils.

Velocity and Pressure Distributions in the Wake: (Figures 19 and 20). Profiles of velocity, static and total pressure are shown for the three airfoils for a vertical traverse range of $\pm 0.2c$ at each chordwise station at the test angles of attack. The progressive growth of the wake width in the longitudinal direction on each airfoil is seen as expected. Static pressure profiles exhibit slightly lower pressures above the airfoil than below. Progressive reduction of both vertical and longitudinal pressure gradients is observed in the wake.

Total pressure profiles are generally smooth, except for the NASA 0421 airfoil at the post-stall angle of attack. Contour plots of total pressure (Figure 20) are similar at pre-stall, near-stall and post-stall conditions. Total pressure gradients become smaller at the post-stall angle of attack compared to the pre-stall angle of attack.

Reattachment Point in the Wake: (Figure 19). An examination of the wake velocity profiles indicates the termination of regions of reversal for all three airfoils to be within a relatively short distance downstream from the airfoil trailing edge. This point, which is characterized by a single zero velocity point in the velocity profile, is referred to as the "reattachment point." The reattachment points obtained by inspection of the velocity profiles are tabulated in Table 6.

Table 6
Reattachment Point Location

Airfoil	Angle of Attack	Reattachment Point
0421	8.5°	$1.00 < x/c < 1.05$
	10.6°	$1.00 < x/c < 1.05$
	12.7°	$1.05 < x/c < 1.10$
2412	12.4°	$1.00 < x/c < 1.05$
	14.4°	$x/c \approx 1.05$
	16.4°	$x/c \approx 1.20$
GA(W)-2	10.3°	$1.00 < x/c < 1.05$
	14.4°	$x/c \approx 1.05$
	18.3°	$1.20 < x/c < 1.40$

These results are in general consistent with the observations of Reference 1, which showed that reattachment points for the GA(W)-1 airfoil were relatively close to the trailing edge.

Hot Film Survey: (Figure 21). Maps of the regions with varying degrees of turbulence are shown for the three airfoils tested. Tests conducted early in the experimental program utilized a single hot-film anemometer, which is insensitive to flow reversal. Interpretation of the single hot-film data for regions of reversal was done in the following manner. The flow was considered to be reversing whenever the trace indicated zero on the scope. At the outer edge of reversal zones, the flow may be intermittently reversing (less than 50% of the time), in view of the heavy turbulent mixing.

Tests conducted later in the experimental program utilized a split-film anemometer, which gives flow reversal information as well as velocity magnitude. The split-film data thus allow an

unambiguous determination of flow reversal. For runs with this instrument, it is possible to determine the percentage of time the flow is reversed, and the labeling on the figures indicates this information.

Table 7 shows which instrument was used for each test condition, and the figures are also labelled to identify the instrument used.

Table 7
Hot-Film Anemometry Instrumentation

Airfoil	Angle of Attack	Instrument
0421	8.5°	Split-film
	10.6°	Split-film
	12.7°	Split-film
2412	12.4°	Single-film
	14.4°	Single-film
	16.4°	Single-film
GA(W)-2	10.3°	Single-film
	14.4°	Single-film
	18.3°	Split-film

It is interesting to note that regions of reversal measured with the hot-films extend further downstream than the results obtained from the pressure probes. Regions of heavy turbulence extend more than 0.50c downstream from the trailing edge for all the cases of angle of attack considered. The differences between the hot-film observations and pressure probe results are attributed to the heavy damping of the pressure instrumentation used.

Skin Friction Distribution: (Figure 22). Local skin friction measurements for all three airfoils are compared with theoretical results calculated by the theoretical methods of Reference 11. At low to moderate angles of attack the upper surface experimental data generally show a higher level of skin friction than theory, while the lower surface data tends to straddle the theory. At near-stall to maximum lift angles of attack both the upper surface and lower surface data generally show good agreement with theory. At post-stall angles of attack the agreement between theory and experiment is good for stations ahead of separation. At 18.3° for the GA(W)-2 airfoil, valid skin friction measurements on the upper surface were obtained at only the .10 and .40 x/c stations. At all other upper surface stations the pressure readings with razor blade installed were lower than without razor blade. This was true for the razor blade in the normal position and reversed, indicating "negative" skin friction in both directions. From these measurements it is concluded that the upper surface flow on this airfoil was too unsteady to provide skin friction measurement by the razor blade method. Both the limited upper surface measurements and the lower surface data show considerable variance from the theory. This is not surprising since the surface pressure distribution and entire boundary layer development are quite different than predicted by attached flow theories.

Comparison of Airfoil Performance Data. Some of the data obtained for the airfoils of this test are compared with each other as well as with that of the GA(W)-1 airfoil of Reference 1. In particular, data discussed are those relating to separation point, and reattachment point in the wake.

Figure 23 is a plot of the separation point of each airfoil, measured from the nose of the airfoil, versus angle of attack. The separation points of the 0421 and GA(W)-1 airfoils move forward at approximately a constant rate as the angle of attack is increased. The separation points for the GA(W)-2 and 2412 airfoils however move at an increasing rate with increasing angle of attack.

The reattachment point variation with angle of attack is shown in Figure 24. The data shows that the reattachment points are located close to the trailing edge of all the airfoils. The most aft location observed was for the GA(W)-2 airfoil, at about 0.30c aft of the airfoil trailing edge at 18.3° angle of attack.

CONCLUSIONS

1. Experimental velocity profiles, flow inclinations, and static and total pressure distributions have been obtained for the NASA 0421, NACA 2412, and NASA GA(W)-2 airfoils at pre-stall, near-stall, and post-stall angle of attack conditions.

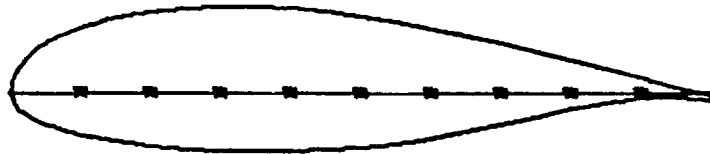
2. Extensive mapping of the flow regions about the airfoil with varying degrees of turbulence was done employing hot-film survey probes.

3. Surface pressure distributions, displacement thickness, and momentum thickness show good agreement with theory up to the measured separation point when the separated flow region extends over no more than 0.2c. The trend of the shape factor and skin friction coefficient with chordwise position agrees well with theory but the quantitative values can differ substantially. The separation point locations of the 12-percent-thick and 13-percent-thick airfoils (NACA 2412 and NASA GA(W)-2) compare well with theory at the pre-stall and near-stall angles of attack but those of the 21-percent-thick airfoil (NASA 0421) compare poorly with the theory.

4. Velocity measurements from the pressure-type probes indicate that the regions of reversed flow terminate at a reattachment point which is located a relatively short distance (about 0.05c) downstream from the airfoil trailing edge for the pre-stall and near-stall angles of attack. At post-stall angles of attack the reattachment point moves to between 0.1c and 0.3c downstream from the trailing edge. The hot-film measurements reveal that intermittent reversal extends somewhat further downstream than pressure data indicate, but even these regions are less than 0.5c in length.

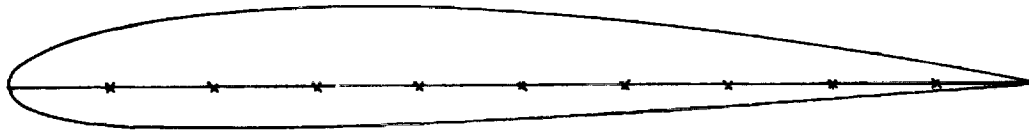
REFERENCES

1. Seetharam, H.C. and Wentz, W.H., Jr.: Experimental Studies of Flow Separation and Stalling on a Two-Dimensional Airfoil at Low Speeds. NASA CR-2560, July 1975.
2. Seetharam, H.C. and Wentz, W.H., Jr.: A Low Speed Two-Dimensional Study of Flow Separation on the GA(W)-1 Airfoil with 30-Percent Chord Fowler Flap. NASA CR-2844, May 1977.
3. Naik, S.N. and Zumwalt, G.W.: An Analytical Model for the Study of Highly Separated Flow on Low Speed Airfoils, Wichita State University, Aeronautical Engineering Dept., AR 77-2, 1977.
4. Mechtley, E.A.: The International System of Units--Physical Constants and Conversion Factors (Revised). NASA SP-7012, 1969.
5. Siew, R. J.: Calibration of a Two-Dimensional Insert for the WSU 7' x 10' Wind Tunnel. AR 73-2, Wichita State University, 1973.
6. East, L.F.: Measurement of Skin Friction at Low Subsonic Speeds by the Razor-Blade Technique. British R&M 3525, 1968.
7. Walker, J.K.: Calibration of a Five-Tube Probe, WSU AR 74-1, April 1974.
8. McGhee, R.J. and Beasley, W.D.: Wind-Tunnel Results for an Improved 21-Percent-Thick Low Speed Airfoil Section. NASA TM 78650, 1978.
9. Abbott, I.H. and Von Doenhoff, A.E.: Theory of Wing Sections. Dover Publications, 1959.
10. McGhee, R.J. and Beasley, W.D.: Effects of Thickness on the Aerodynamic Characteristics of an Initial Low-Speed Family of Airfoils for General Aviation Applications. NASA TMX-72843, 1976.
11. Smetana, F.O.; Summey, D.C.; Smith, N.S.; and Carden, R.K.: Light Aircraft Lift, Drag, and Moment Prediction - A Review and Analysis. NASA CR-2523, 1975.
12. Schlichting, H.: Boundary Layer Theory, McGraw-Hill Co., Fourth Edition, 1962.



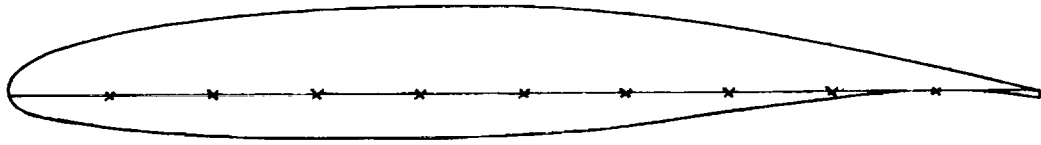
UPPER SURFACE		LOWER SURFACE	
x/c	z/c	x/c	z/c
0.0000	0.0000	0.0000	0.0000
.0020	.0156	.0020	-.0107
.0050	.0243	.0050	-.0177
.0125	.0383	.0125	-.0265
.0250	.0540	.0250	-.0352
.0375	.0651	.0375	-.0416
.0500	.0736	.0500	-.0468
.0750	.0865	.0750	-.0550
.1000	.0960	.1000	-.0614
.1250	.1034	.1250	-.0665
.1500	.1093	.1500	-.0707
.1750	.1141	.1750	-.0741
.2000	.1179	.2000	-.0770
.2250	.1208	.2250	-.0794
.2500	.1229	.2500	-.0813
.2750	.1243	.2750	-.0828
.3000	.1250	.3000	-.0839
.3250	.1250	.3250	-.0846
.3500	.1244	.3500	-.0849
.3750	.1233	.3750	-.0849
.4000	.1217	.4000	-.0846
.4250	.1196	.4250	-.0839
.4500	.1170	.4500	-.0828
.4750	.1140	.4750	-.0813
.5000	.1106	.5000	-.0794
.5250	.1068	.5250	-.0770
.5500	.1027	.5500	-.0740
.5750	.0983	.5750	-.0705
.6000	.0936	.6000	-.0666
.6250	.0886	.6250	-.0623
.6500	.0833	.6500	-.0576
.6750	.0778	.6750	-.0525
.7000	.0721	.7000	-.0472
.7250	.0662	.7250	-.0418
.7500	.0601	.7500	-.0364
.7750	.0539	.7750	-.0310
.8000	.0476	.8000	-.0256
.8250	.0412	.8250	-.0206
.8500	.0348	.8500	-.0159
.8750	.0284	.8750	-.0118
.9000	.0220	.9000	-.0086
.9250	.0156	.9250	-.0070
.9500	.0091	.9500	-.0069
.9750	.0025	.9750	-.0088
1.0000	-.0042	1.0000	-.0132

Figure 1A - Measured Coordinates of the LS(1)-0421 Mod Airfoil.



UPPER SURFACE		LOWER SURFACE	
x/c	z/c	x/c	z/c
0.000000	0.000000	0.000000	0.000000
.001000	.005657	.001000	-.005458
.005000	.012710	.005000	-.011716
.010000	.018025	.010000	-.016050
.015000	.022109	.015000	-.019165
.020000	.025548	.020000	-.021648
.025000	.028569	.025000	-.023725
.050000	.040234	.050000	-.030859
.075000	.048796	.075000	-.035202
.100000	.055578	.100000	-.038078
.125000	.061101	.125000	-.040007
.150000	.065639	.150000	-.041264
.175000	.069659	.175000	-.042016
.200000	.072375	.200000	-.042375
.225000	.074768	.225000	-.042424
.250000	.076600	.250000	-.042225
.275000	.077920	.275000	-.041826
.300000	.078767	.300000	-.041267
.325000	.079176	.325000	-.040582
.350000	.079174	.350000	-.039799
.375000	.078785	.375000	-.038941
.400000	.078030	.400000	-.038030
.425000	.076971	.425000	-.037041
.450000	.075668	.450000	-.035946
.475000	.074135	.475000	-.034760
.500000	.072385	.500000	-.033496
.525000	.070428	.525000	-.032164
.550000	.068274	.550000	-.030774
.575000	.065933	.575000	-.029336
.600000	.063411	.600000	-.027856
.625000	.060716	.625000	-.026341
.650000	.057853	.650000	-.024797
.675000	.054826	.675000	-.023229
.700000	.051639	.700000	-.021639
.725000	.048296	.725000	-.020032
.750000	.044798	.750000	-.018409
.775000	.041146	.775000	-.016771
.800000	.037342	.800000	-.015120
.825000	.033386	.825000	-.013455
.850000	.029276	.850000	-.011776
.875000	.025011	.875000	-.010080
.900000	.020588	.900000	-.008366
.925000	.016006	.925000	-.006631
.950000	.011260	.950000	-.004871
.975000	.006346	.975000	-.003083
1.000000	.001260	1.000000	-.001260

Figure 1B - Measured Coordinates of the NACA 2412 Airfoil.



UPPER SURFACE		LOWER SURFACE	
x/c	z/c	x/c	z/c
0.0000	0.0000	0.0000	0.0000
.0020	.0103	.0020	-.0066
.0050	.0163	.0050	-.0097
.0125	.0246	.0125	-.0144
.0250	.0336	.0250	-.0188
.0375	.0400	.0375	-.0223
.0500	.0451	.0500	-.0250
.0750	.0528	.0750	-.0294
.1000	.0588	.1000	-.0328
.1250	.0637	.1250	-.0357
.1500	.0677	.1500	-.0380
.1750	.0712	.1750	-.0398
.2000	.0742	.2000	-.0415
.2500	.0788	.2500	-.0438
.3000	.0820	.3000	-.0449
.3500	.0840	.3500	-.0452
.4000	.0849	.4000	-.0449
.4500	.0846	.4500	-.0437
.5000	.0833	.5000	-.0417
.5500	.0807	.5500	-.0386
.5750	.0789	.5750	-.0362
.6000	.0767	.6000	-.0337
.6250	.0739	.6250	-.0307
.6500	.0708	.6500	-.0276
.6750	.0672	.6750	-.0243
.7000	.0633	.7000	-.0210
.7250	.0591	.7250	-.0175
.7500	.0545	.7500	-.0143
.7750	.0497	.7750	-.0110
.8000	.0447	.8000	-.0078
.8250	.0395	.8250	-.0051
.8500	.0341	.8500	-.0028
.8750	.0285	.8750	-.0012
.9000	.0228	.9000	.0000
.9250	.0170	.9250	.0001
.9500	.0110	.9500	-.0007
.9750	.0049	.9750	-.0028
1.0000	-.0015	1.0000	-.0071

Figure 1C - Measured Coordinates of the GA(W)-2 Airfoil.

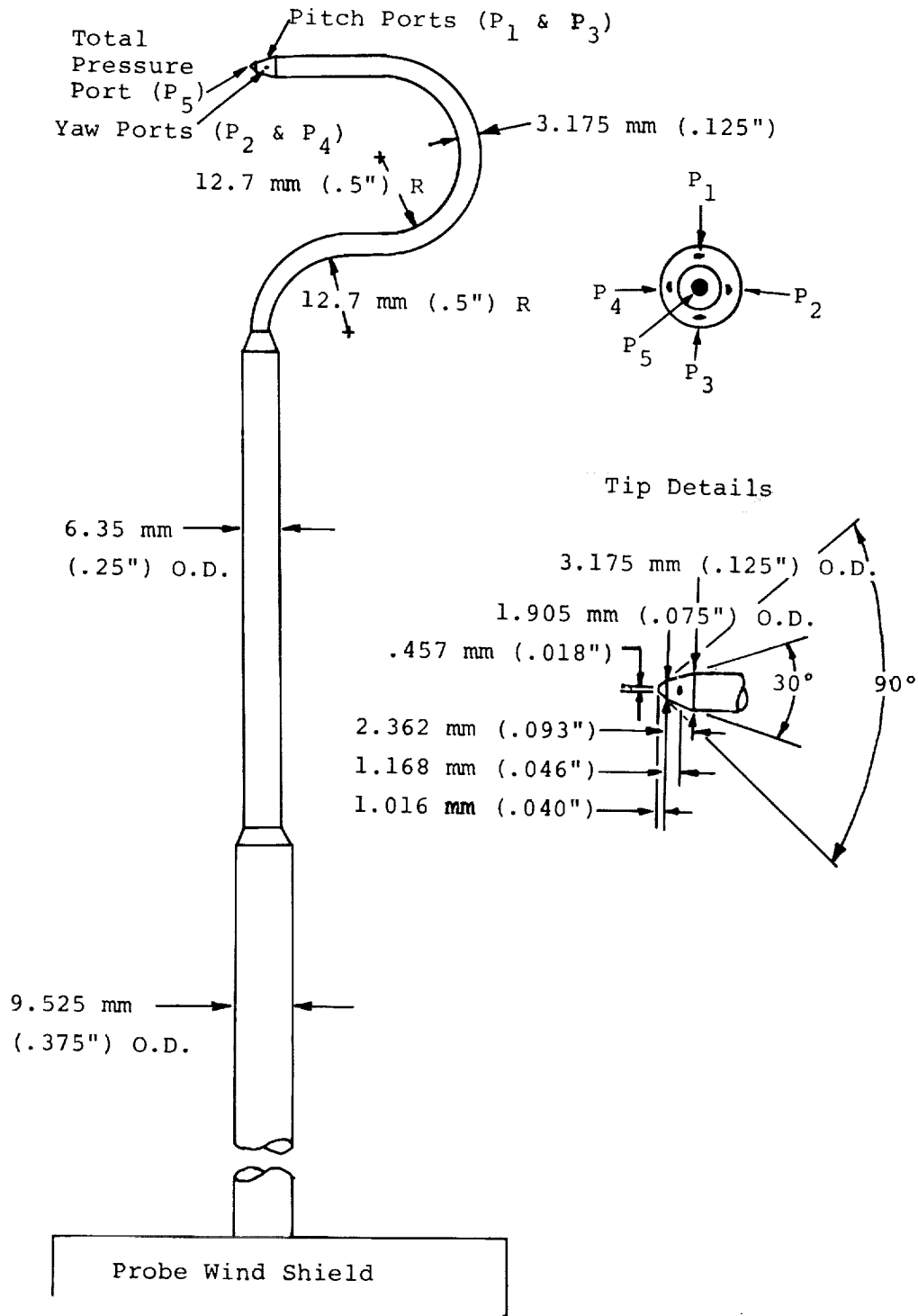


Figure 2 - Five Tube Probe.

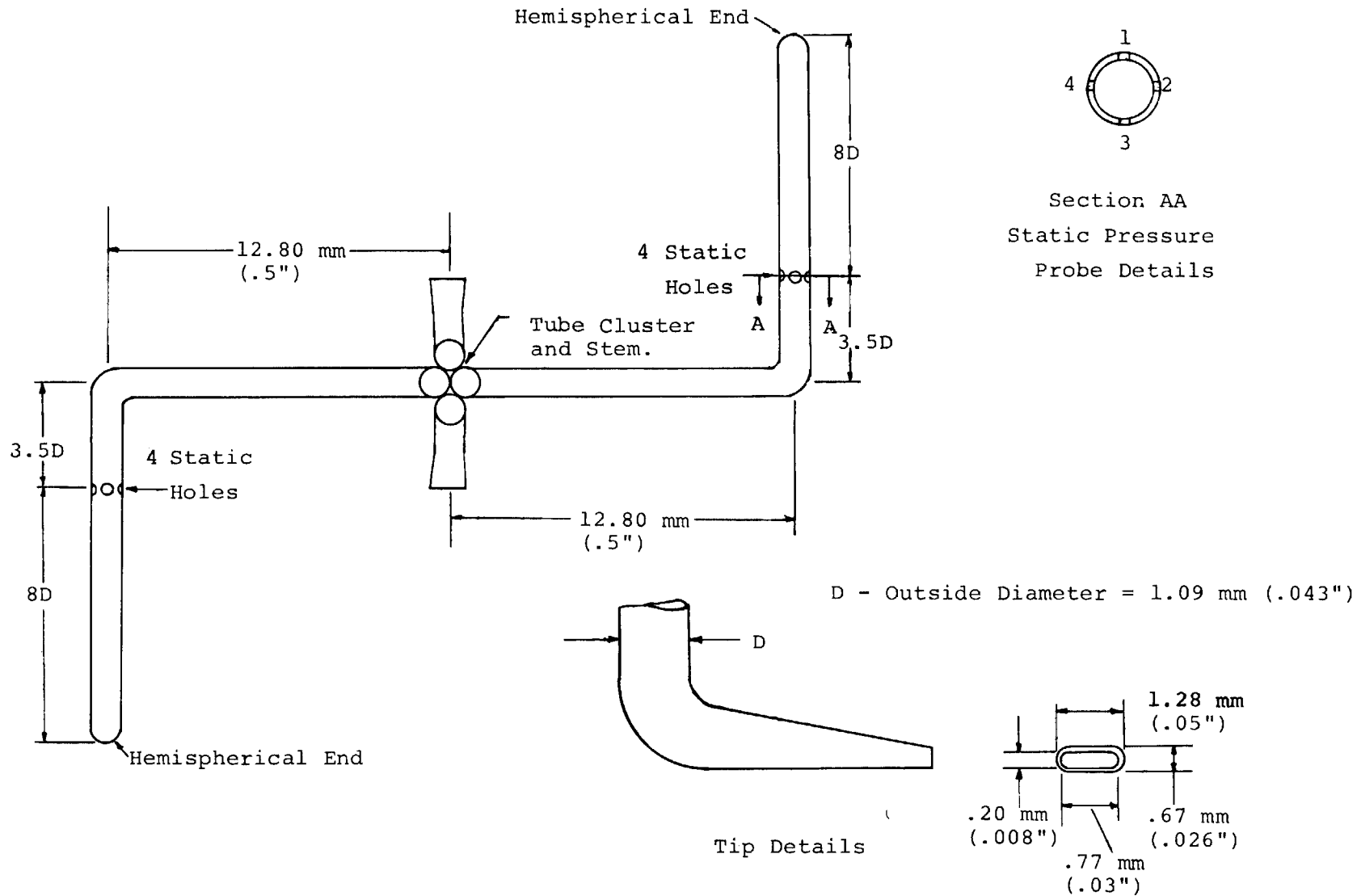


Figure 3 - Four Tube Probe.

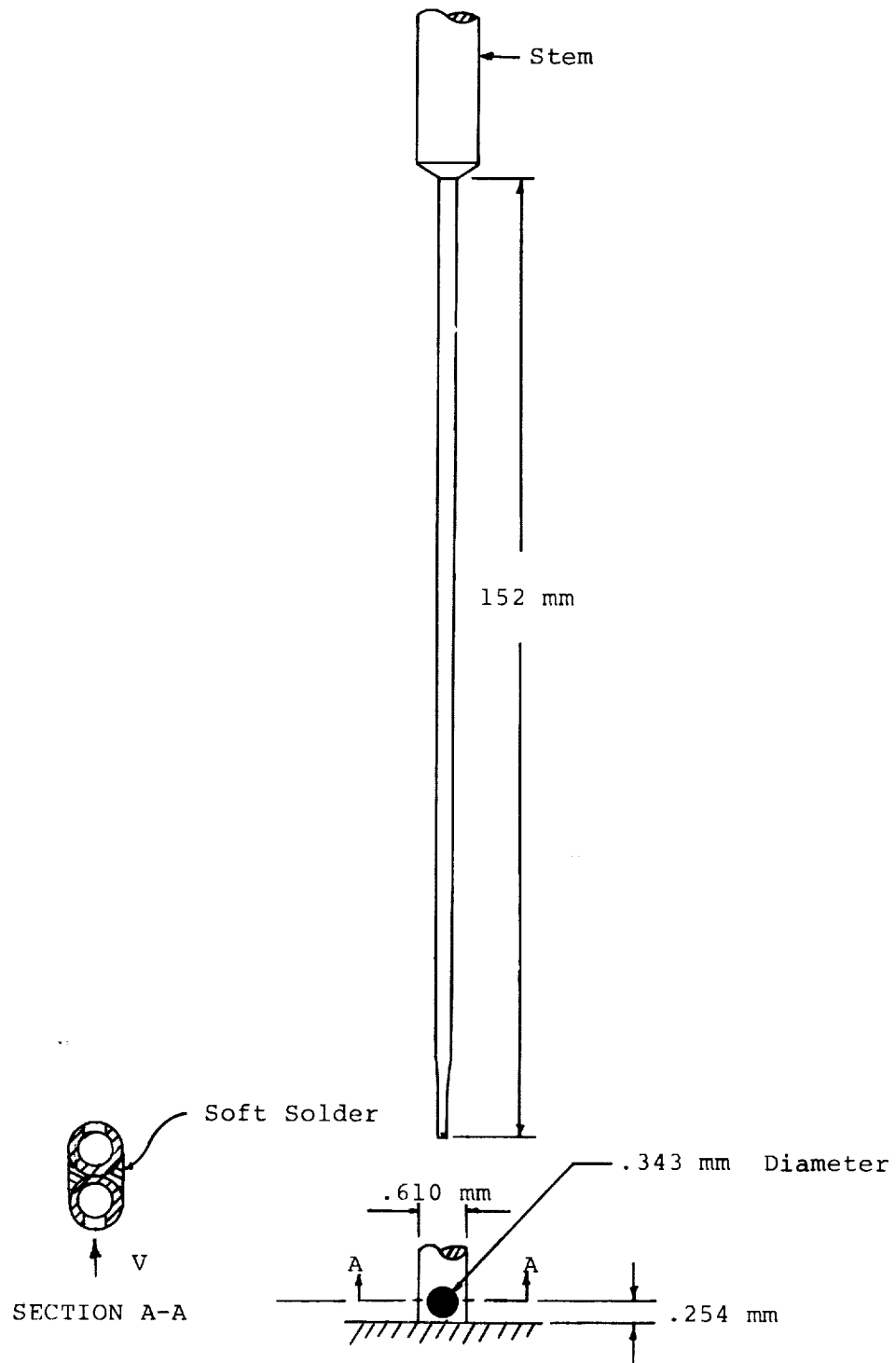


Figure 4 - Two-Tube Pressure Probe.

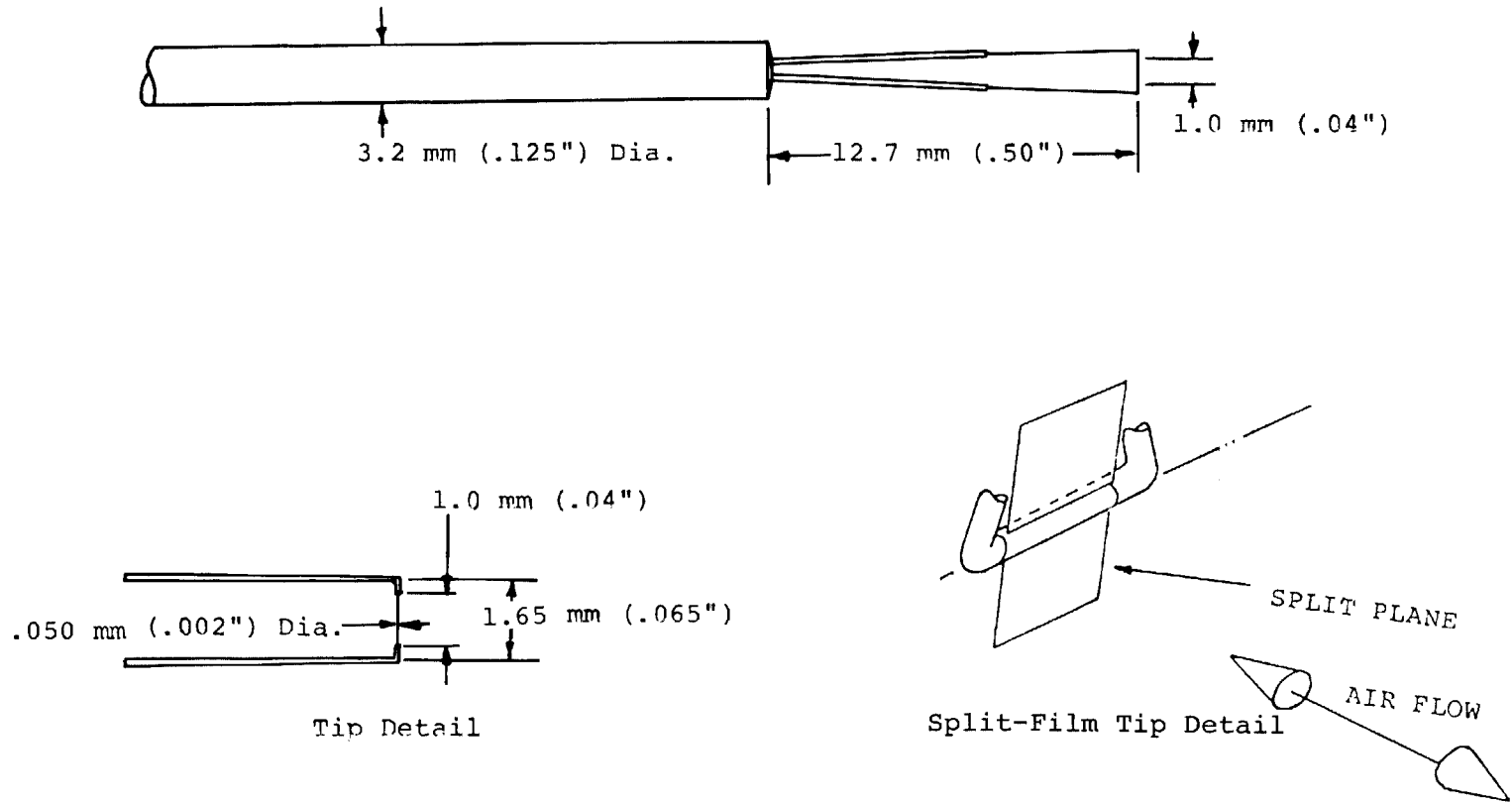
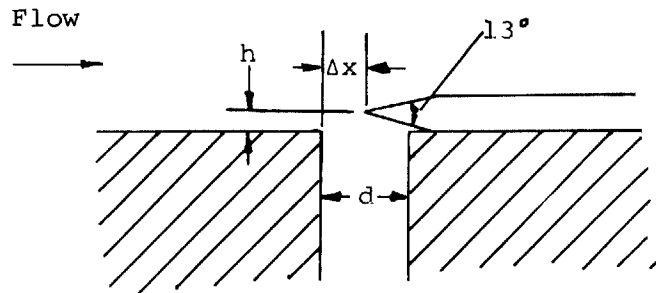
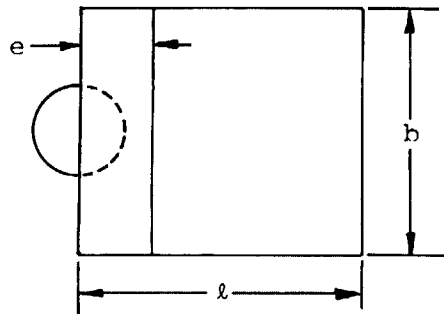


Figure 5 - Hot Film Probes.



Surface Static Pressure Tap



Dimensions

d	1.07 mm (.042")
e	.46 mm (.018")
h	.05 mm (.002")
l	6.35 mm (.25")
b	6.35 mm (.25")
d/h	21.4
b/h	127.
l/b	1.0
Δx	0.0

Criteria from Ref.6:

$$\frac{d}{h} > 6$$

$$\frac{b}{h} > 36$$

$$\frac{l}{b} = 1$$

$$\Delta x = 0$$

Figure 6 - Razor Blade Technique: Details of Dimensions and Positioning.

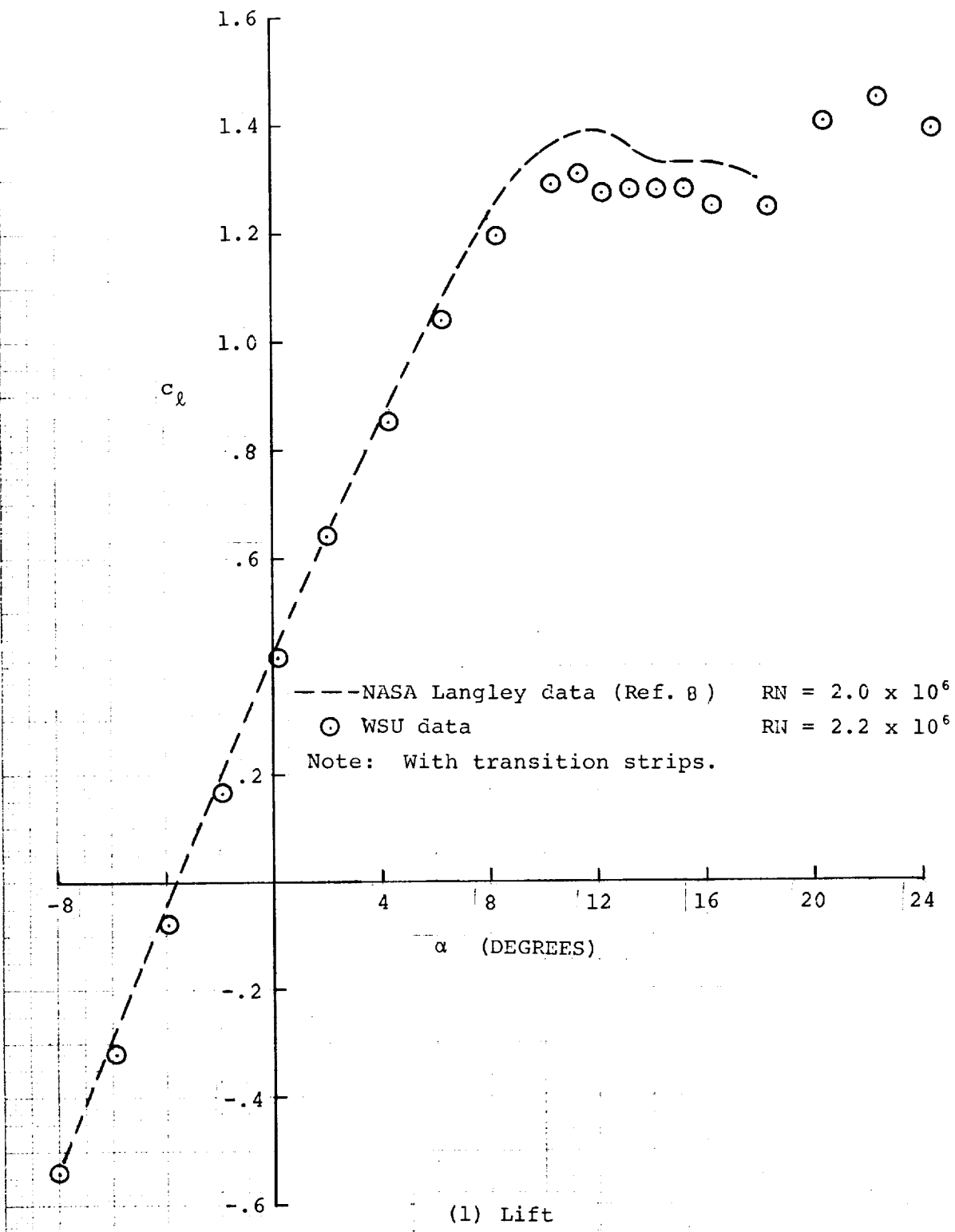
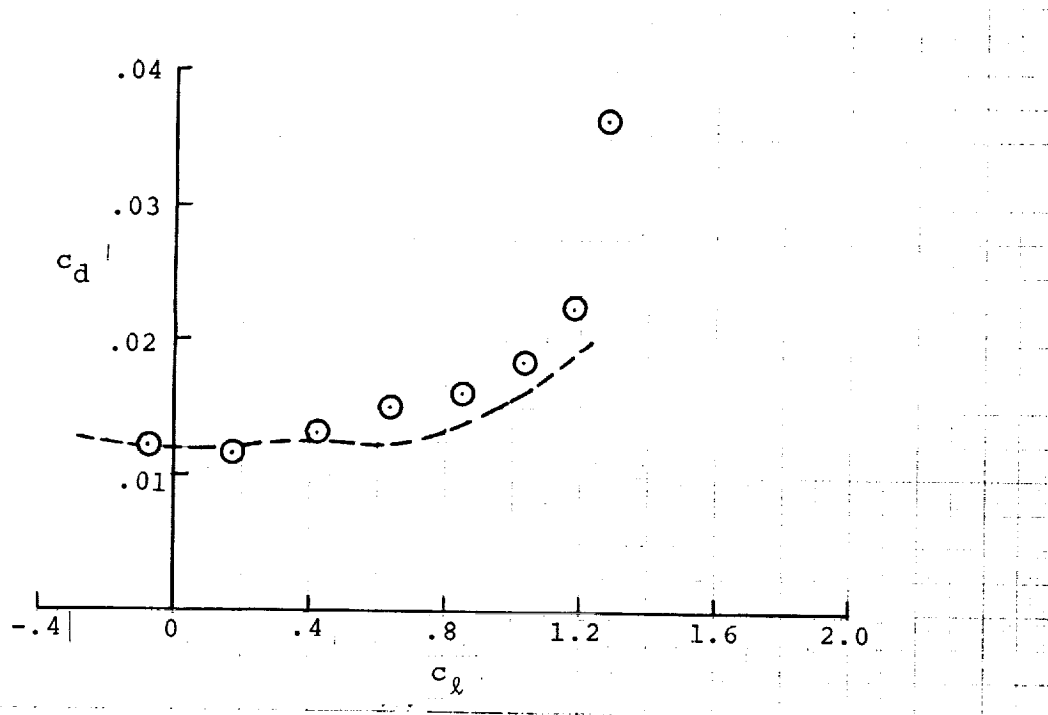
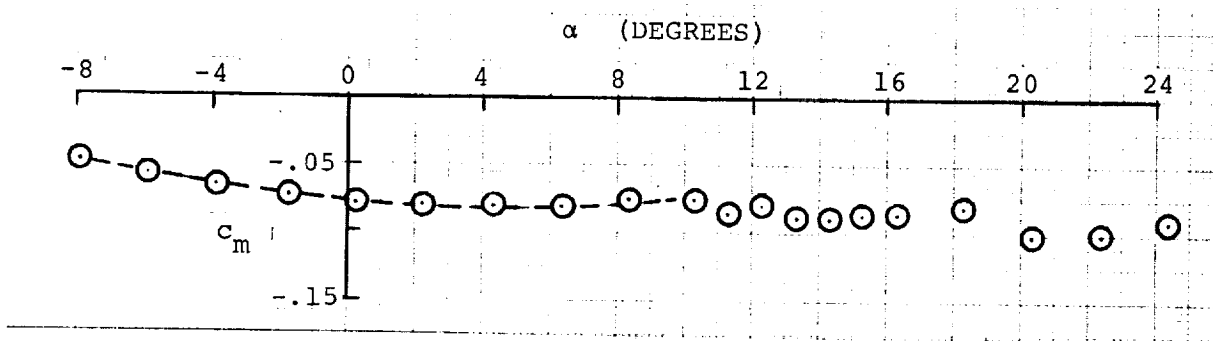


Figure 7A- Aerodynamic Coefficients of LS(1)-0421 Mod Airfoil.



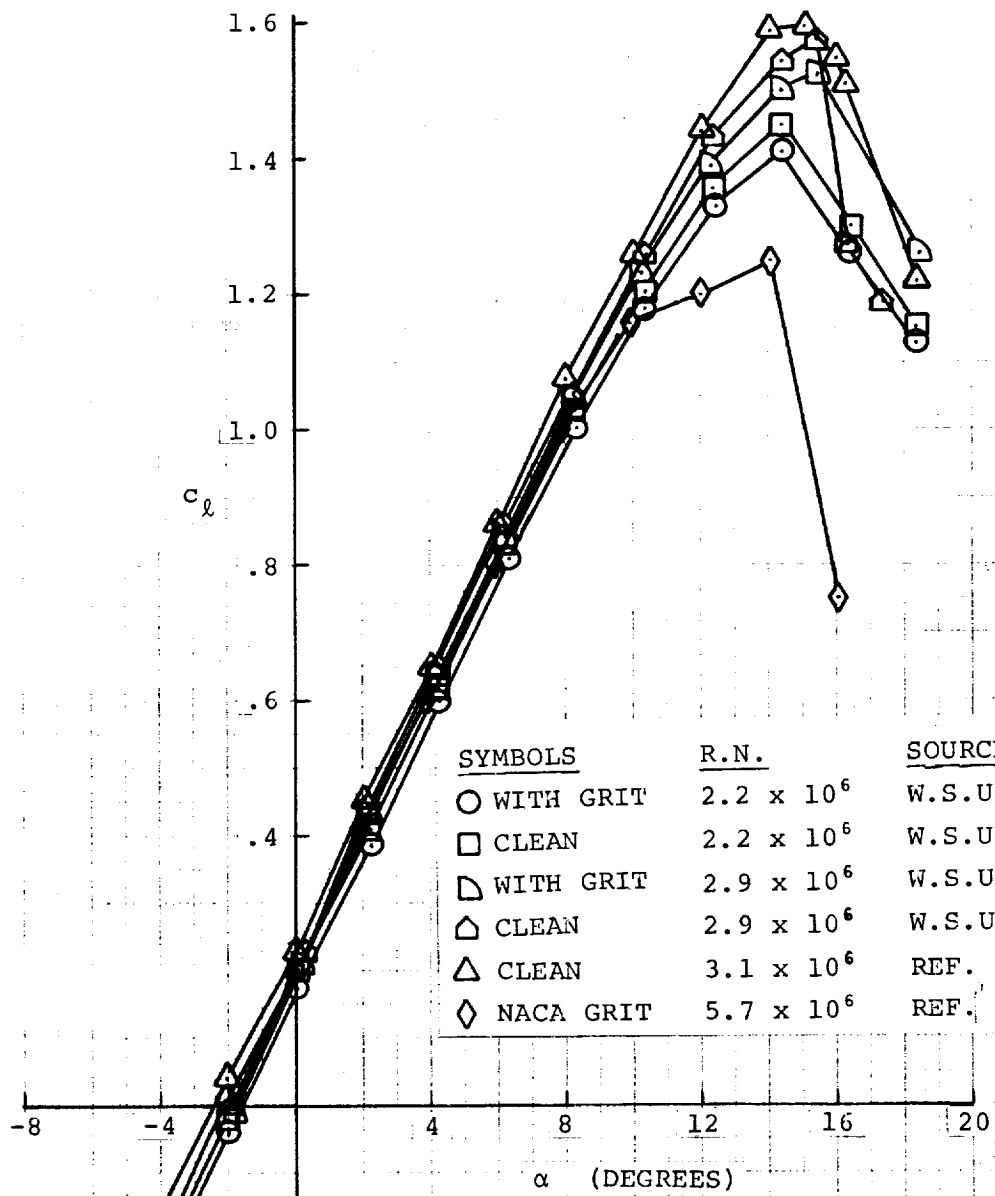
(2) Drag

--- NASA Langley data (Ref. 8) $RN = 2.0 \times 10^6$
 ⊙ WSU data $RN = 2.2 \times 10^6$
 Note: With transition strips.



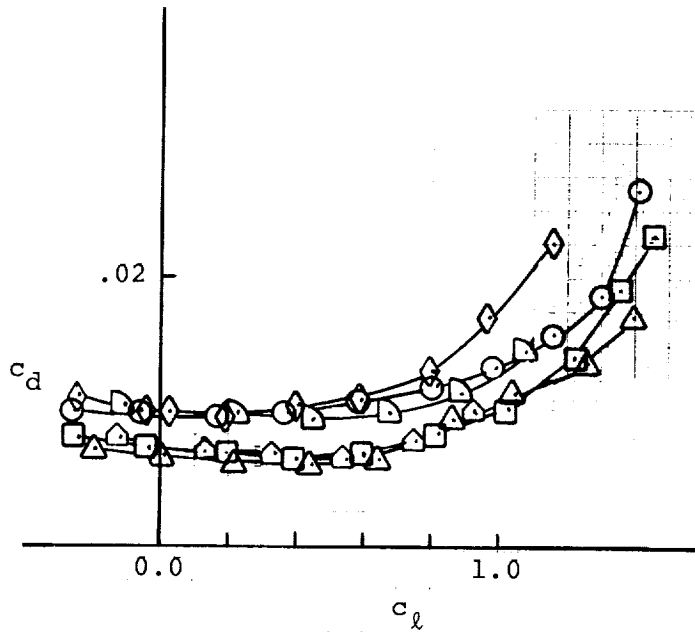
(3) Moment

Figure 7A- Concluded.



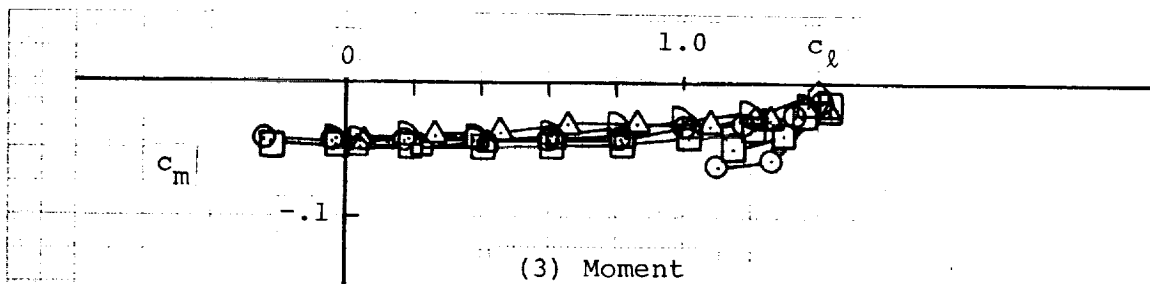
(1) Lift

Figure 7B- Aerodynamic Coefficients of NACA 2412 Airfoil.



(2) Drag

<u>SYMBOL</u>	<u>R.N.</u>	<u>SOURCE</u>
○ WITH GRIT	2.2×10^6	W.S.U.
□ CLEAN	2.2×10^6	W.S.U.
◻ WITH GRIT	2.9×10^6	W.S.U.
◻ CLEAN	2.9×10^6	W.S.U.
△ CLEAN	3.1×10^6	REF. 9
◊ NACA GRIT	5.7×10^6	REF. 9



(3) Moment

Figure 7B - Concluded.

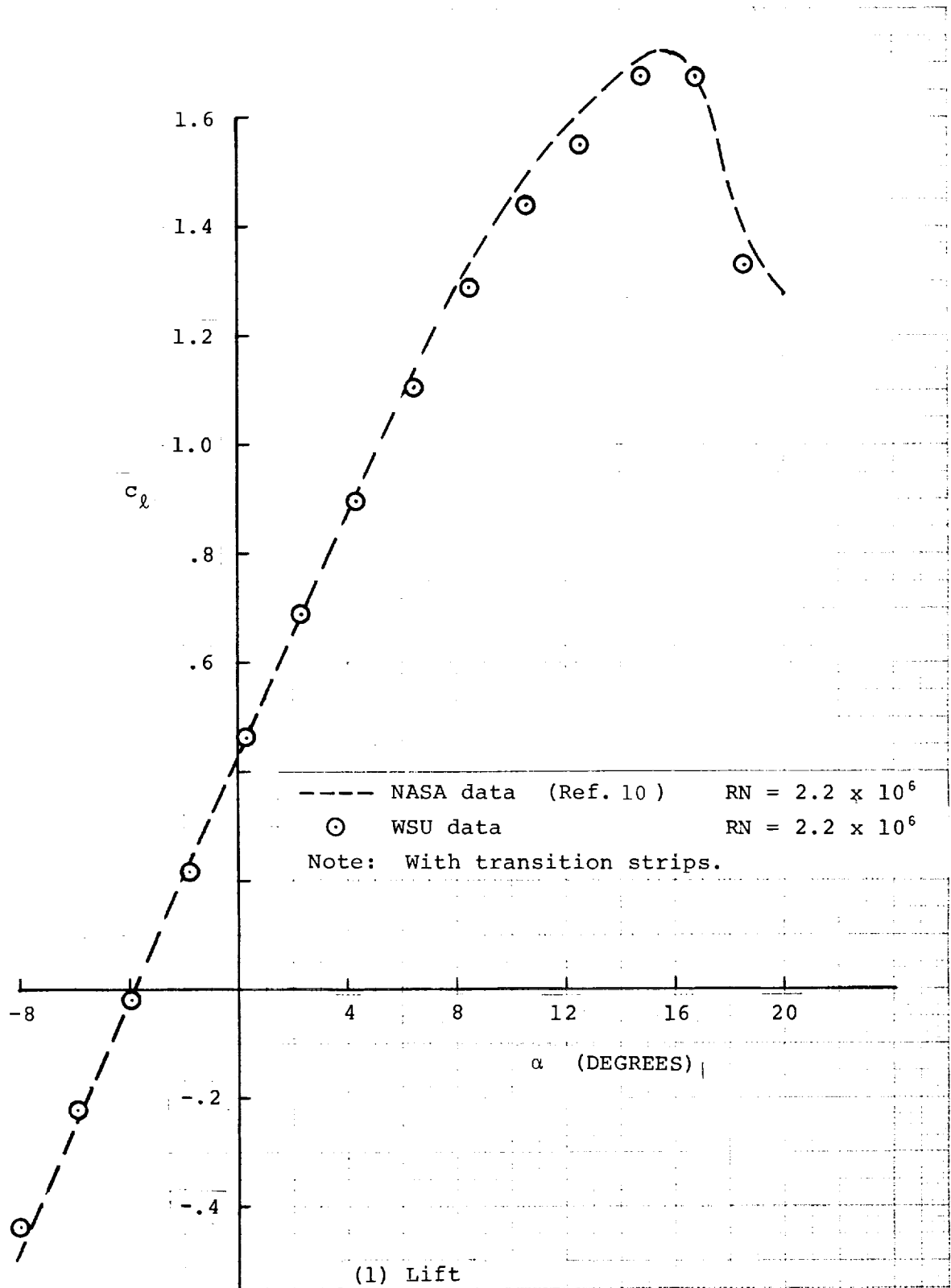
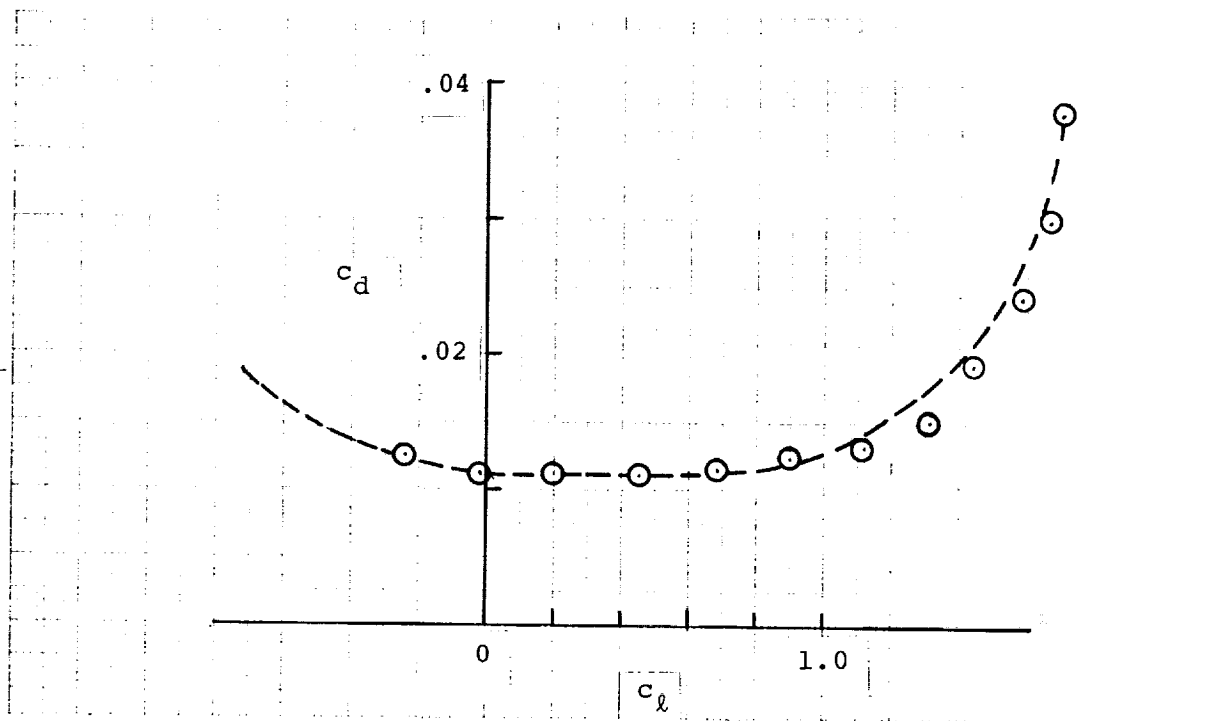


Figure 7C - Aerodynamic Coefficients of GA(W)-2 Airfoil.



(2) Drag

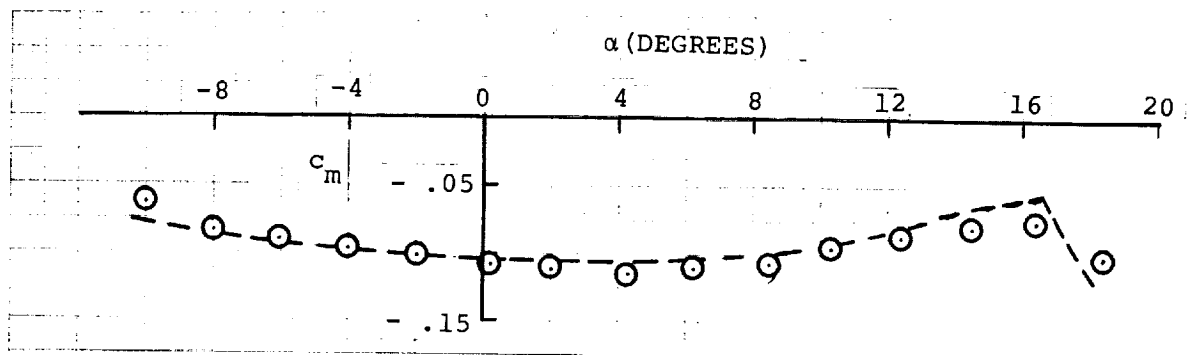
----- NASA data (Ref.10)

⊙ WSU data

$RN = 2.2 \times 10^6$

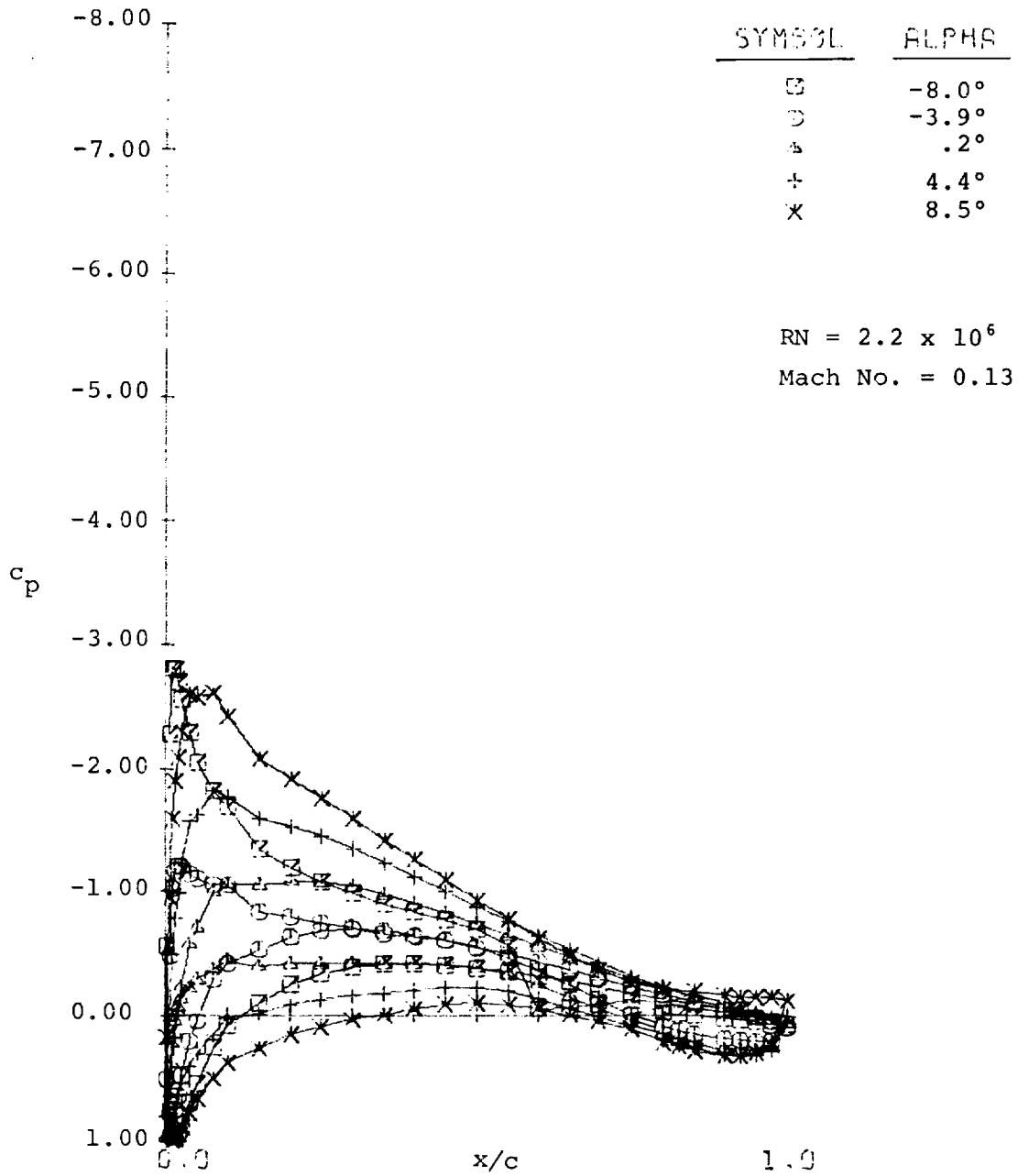
$RN = 2.2 \times 10^6$

Note: With transition strips.



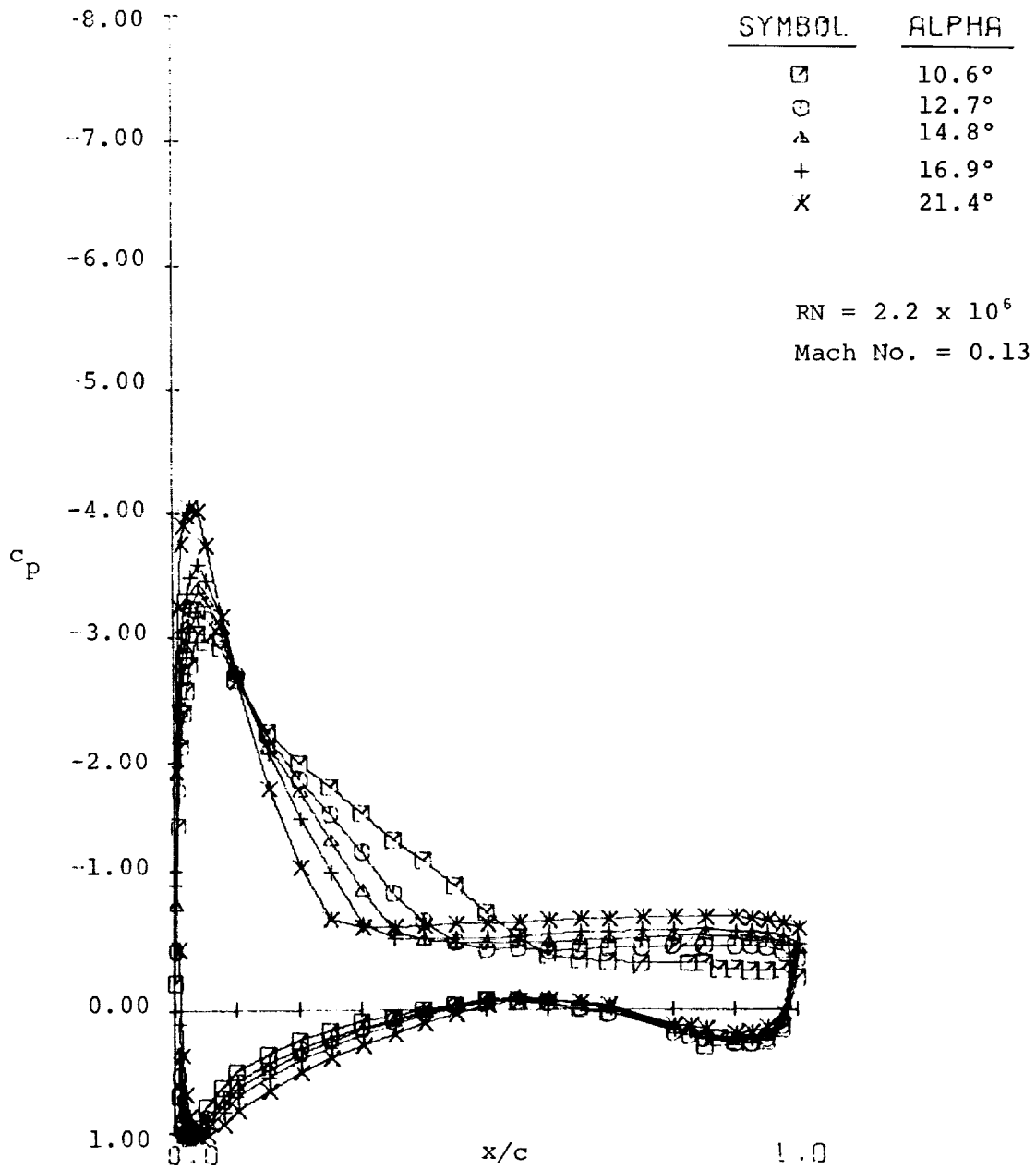
(3) Moment

Figure 7C - Concluded.



(1) Low angles of attack

Figure 8A- Pressure Distributions of LS(1)-0421 Mod Airfoil.



(2) High angles of attack

Figure 8A- Pressure Distributions of LS(1)-0421 Mod Airfoil.

○ Experiment

— Theory (Ref. 11)

Note: Theory predicts separation at $x/c = .91$ (lower surface).

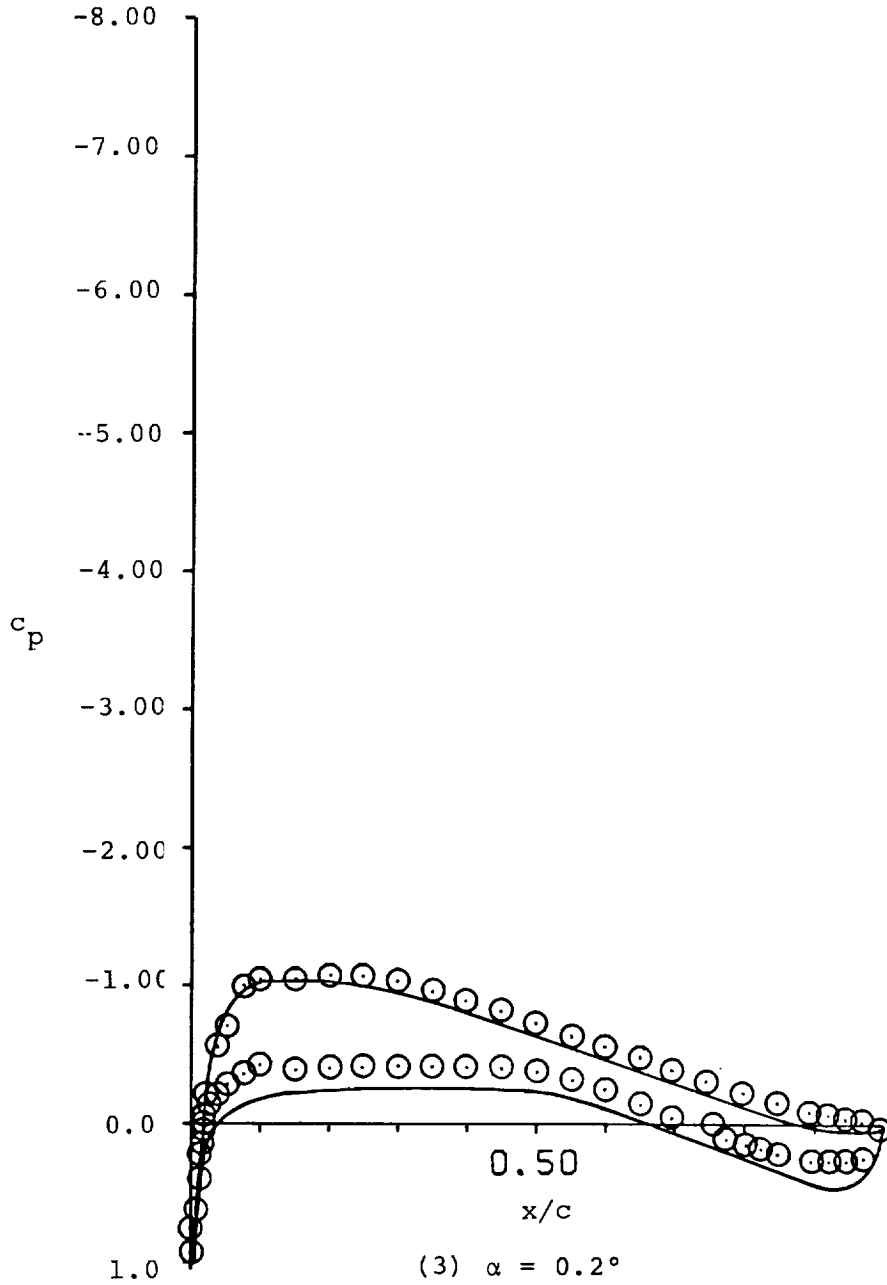


Figure 8A- Continued.

○ Experiment

— Theory (Ref.11)

Note: Theory predicts no separation.

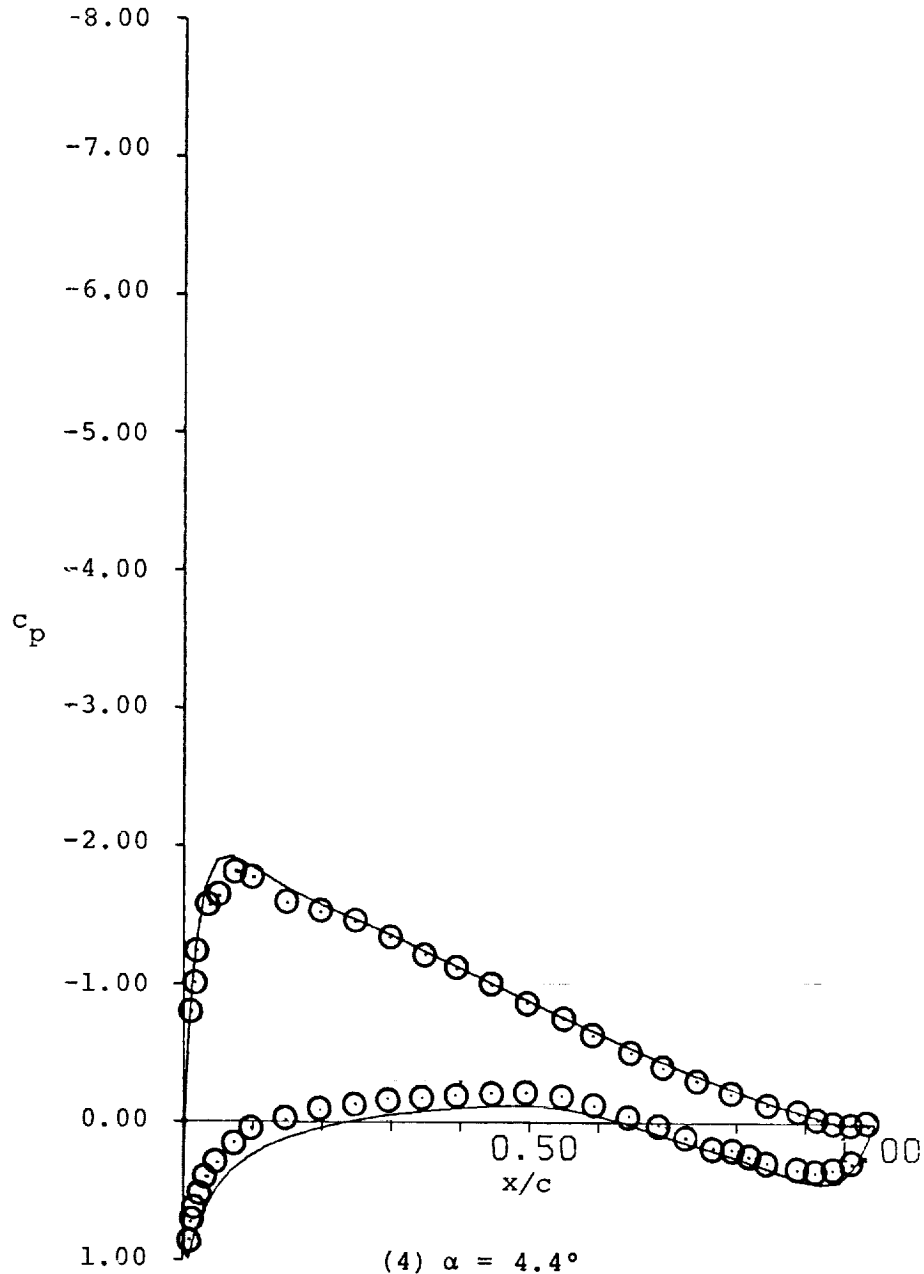


Figure 8A - Continued.

⊙ Experiment

— Theory (Ref.11)

Note: Theory predicts separation at $x/c = .9$ (upper surface).

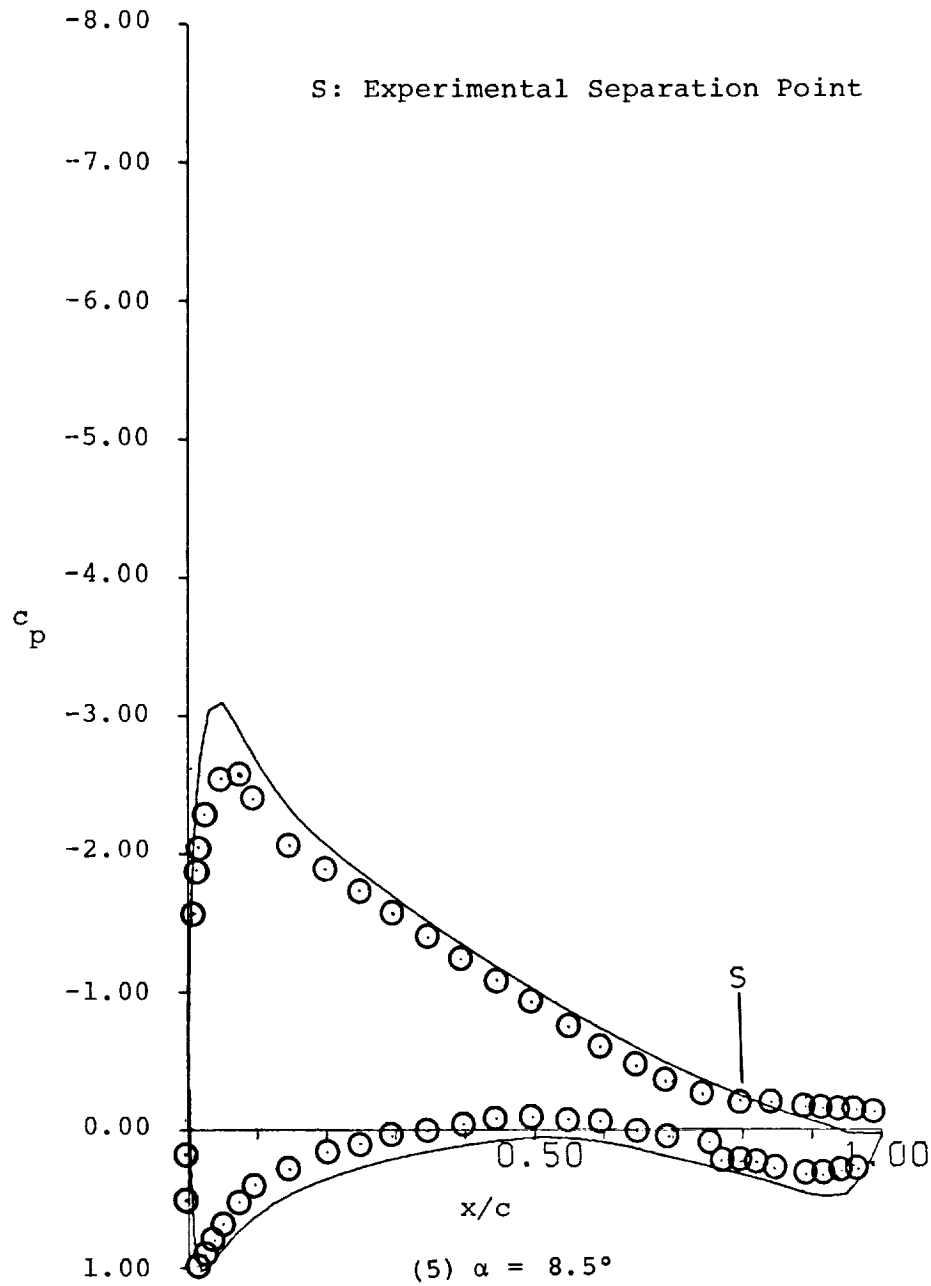
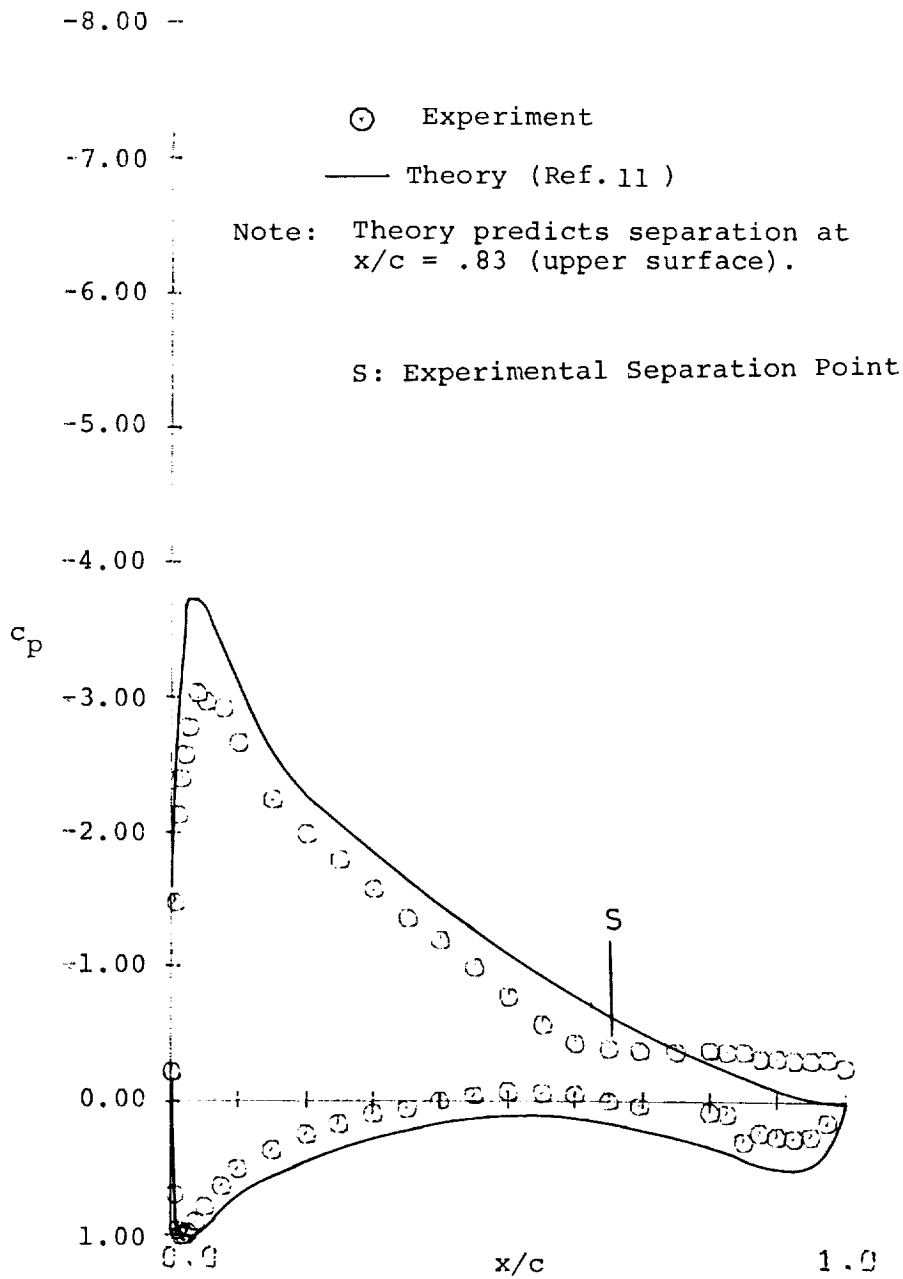


Figure 8A- Continued.



(6) $\alpha = 10.6^\circ$

Figure 8A - Continued.

○ Experiment

— Theory (Ref.11)

Note: Theory predicts separation at $x/c = .77$ (upper surface).

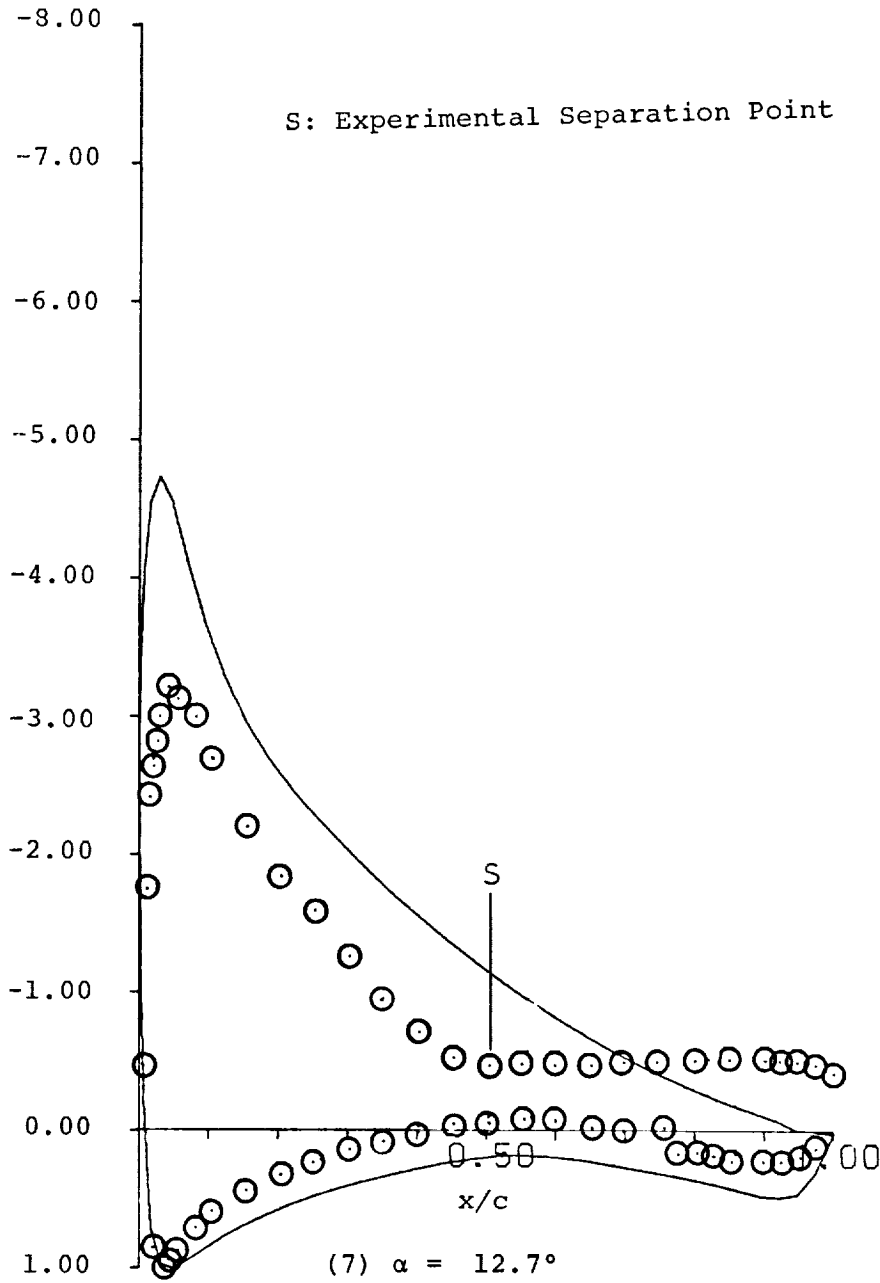


Figure 8A - Continued.

○ Experiment

— Theory (Ref.11)

Note: Theory predicts separation at $x/c = .66$ (upper surface).

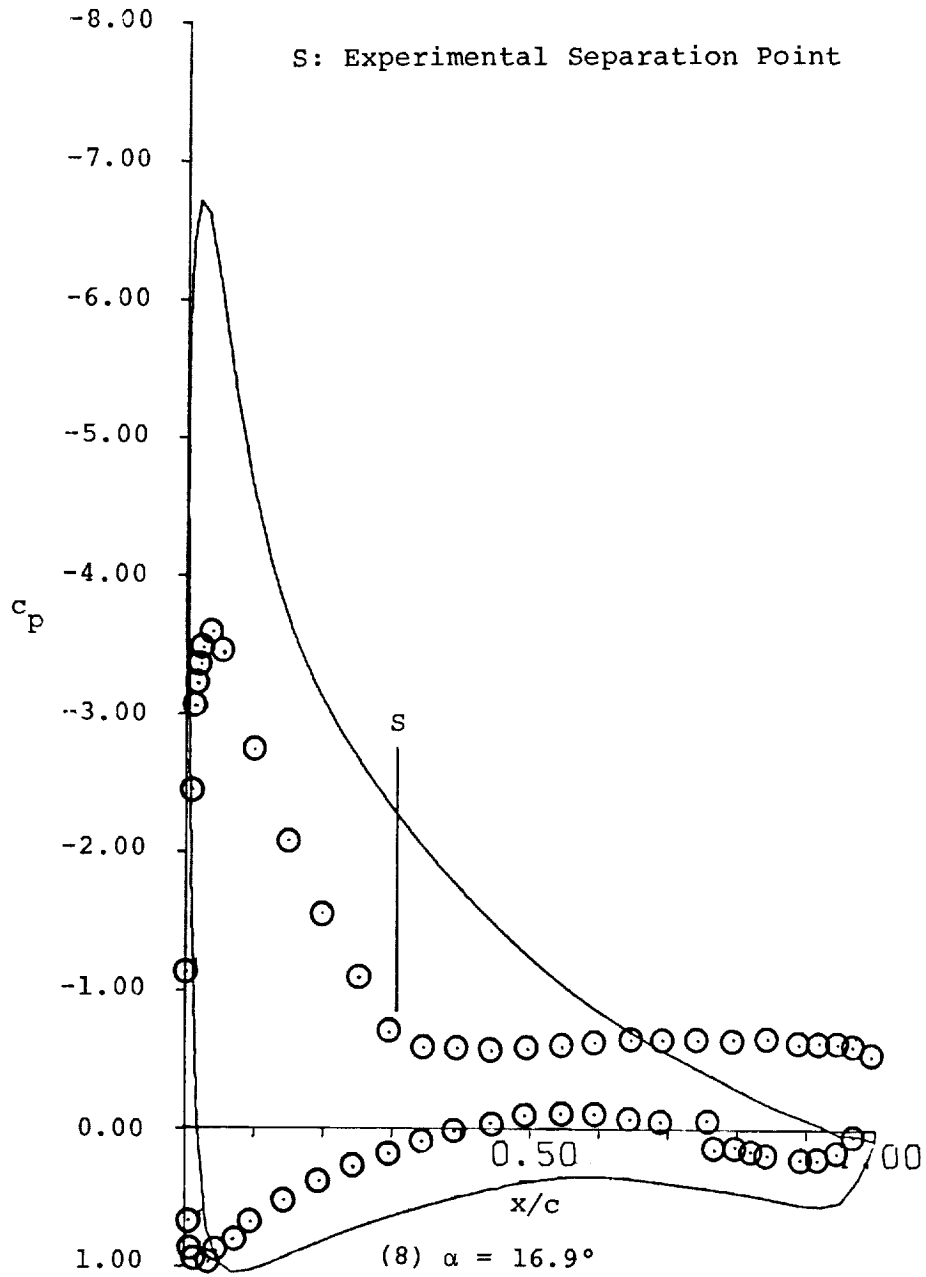
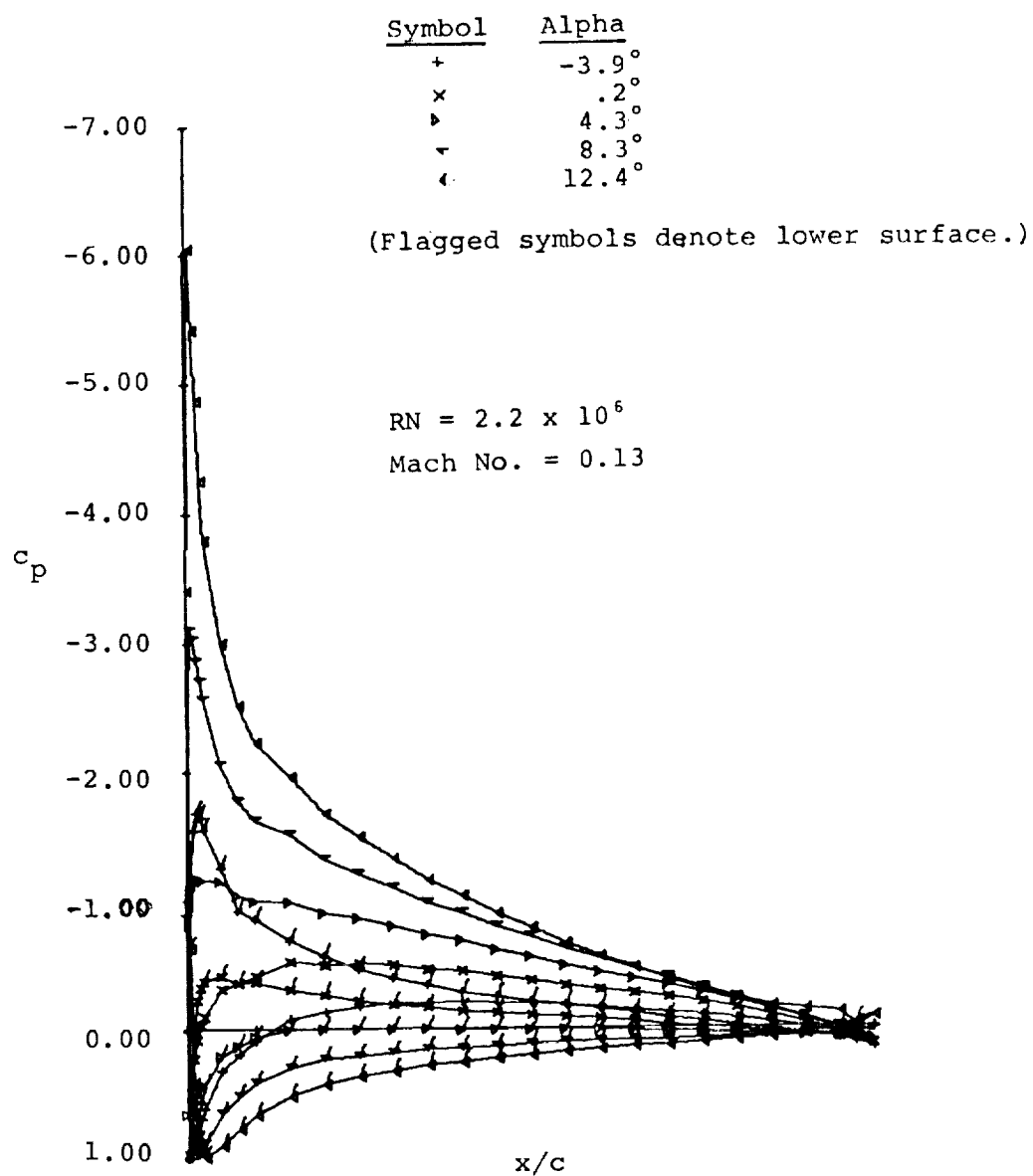
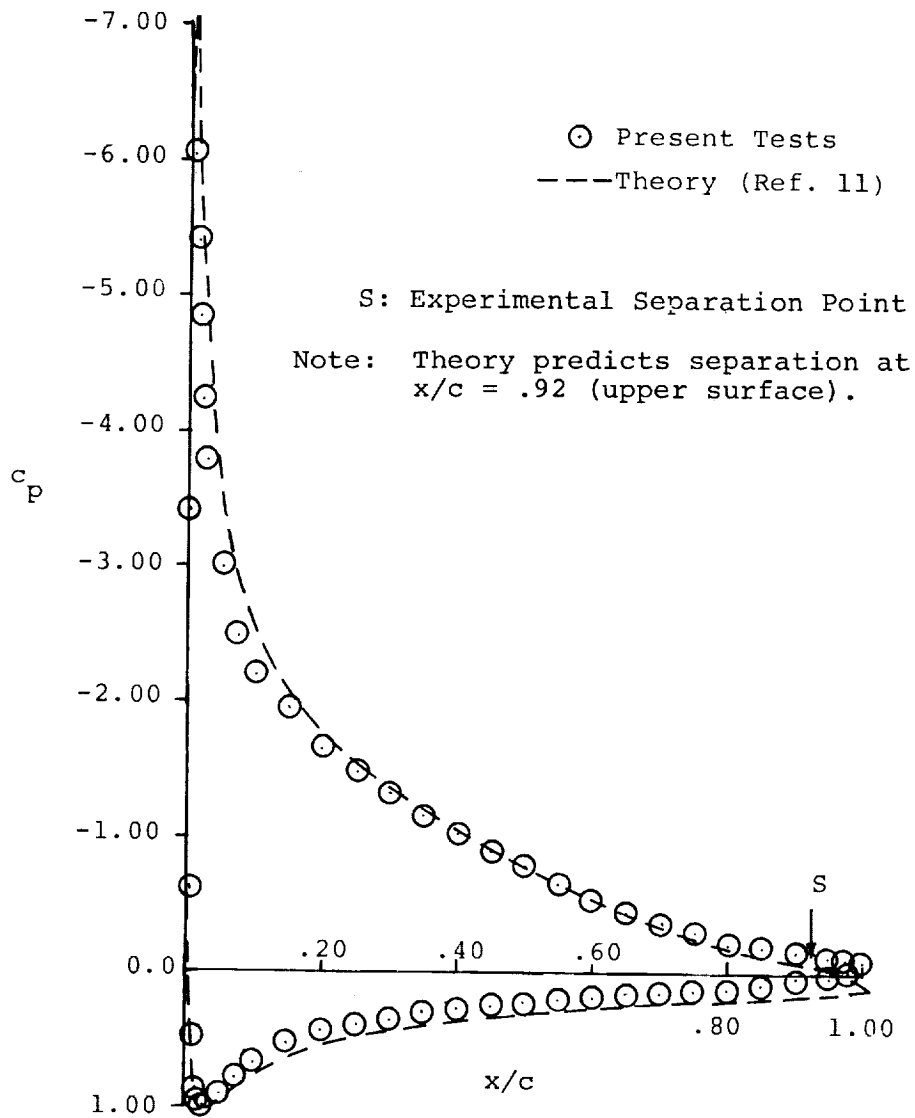


Figure 8A - Concluded.



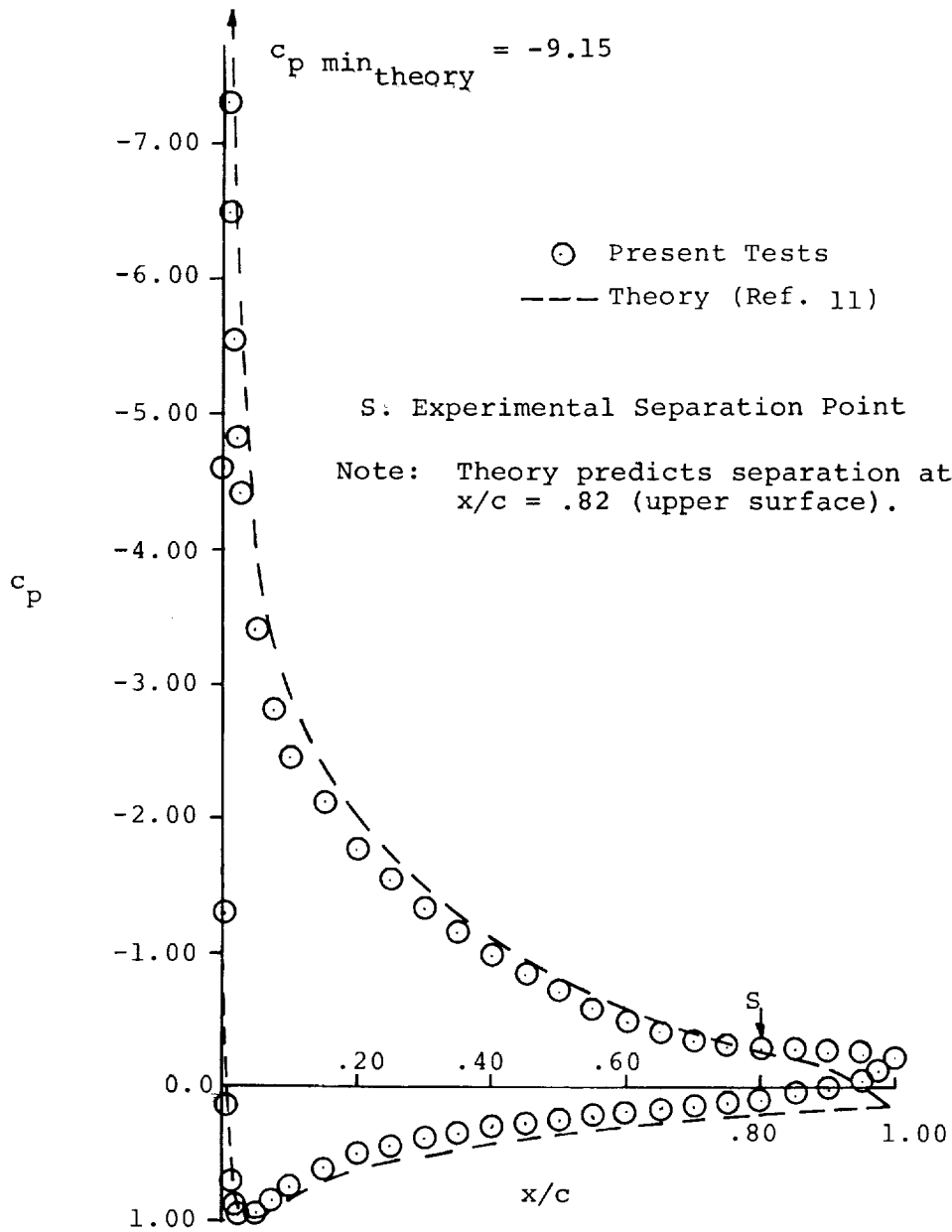
(1) Low angles of attack

Figure 8B - Pressure Distributions of NACA 2412 Airfoil.



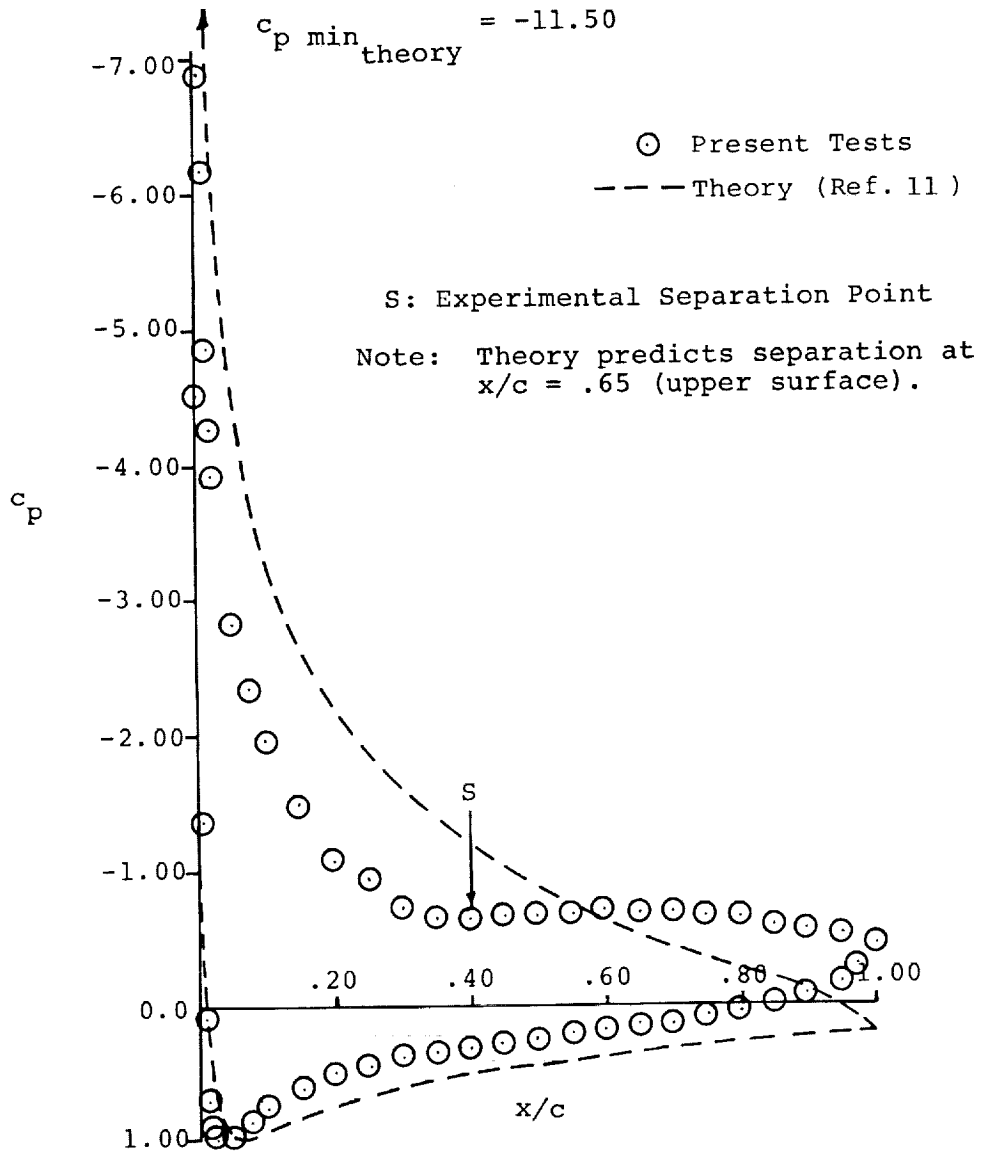
(2) Pre-stall angle of attack, $\alpha=12.4^\circ$

Figure 8B- Continued.



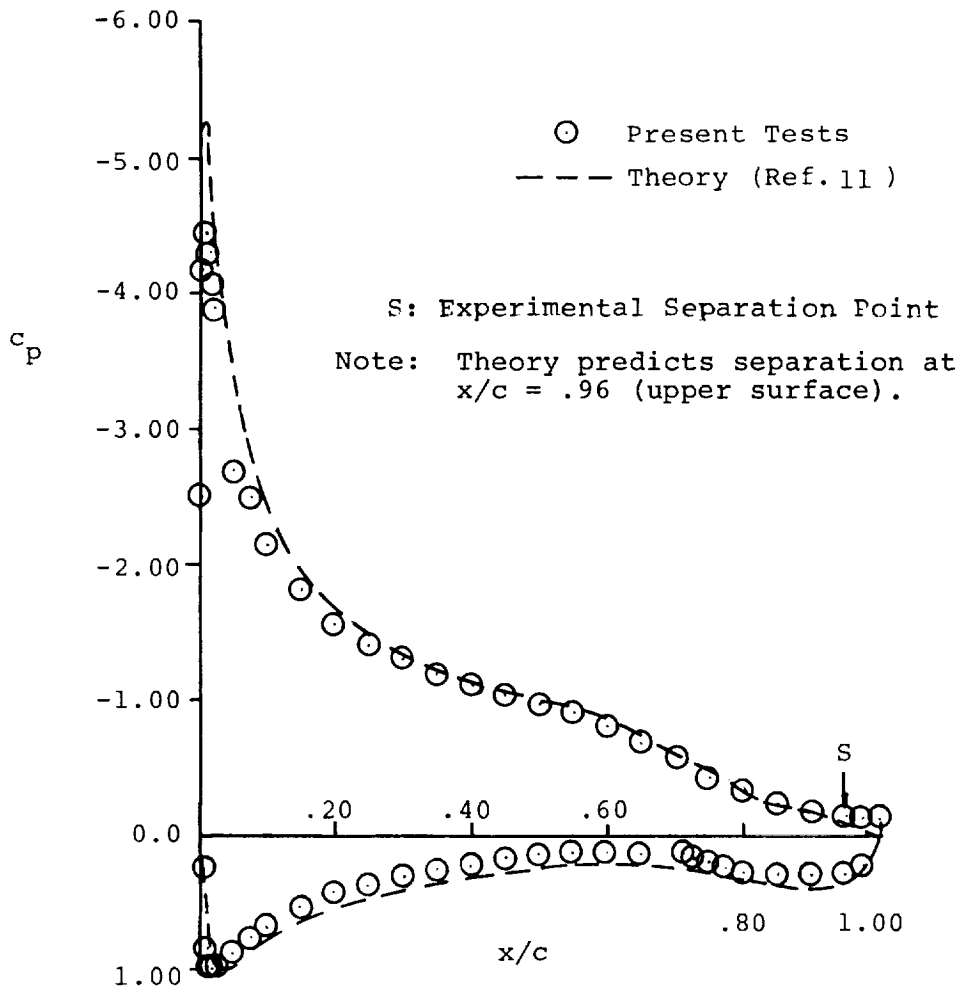
(3) Angle of attack for $c_{l_{\max}}$, $\alpha=14.4^\circ$

Figure 8B- Continued.



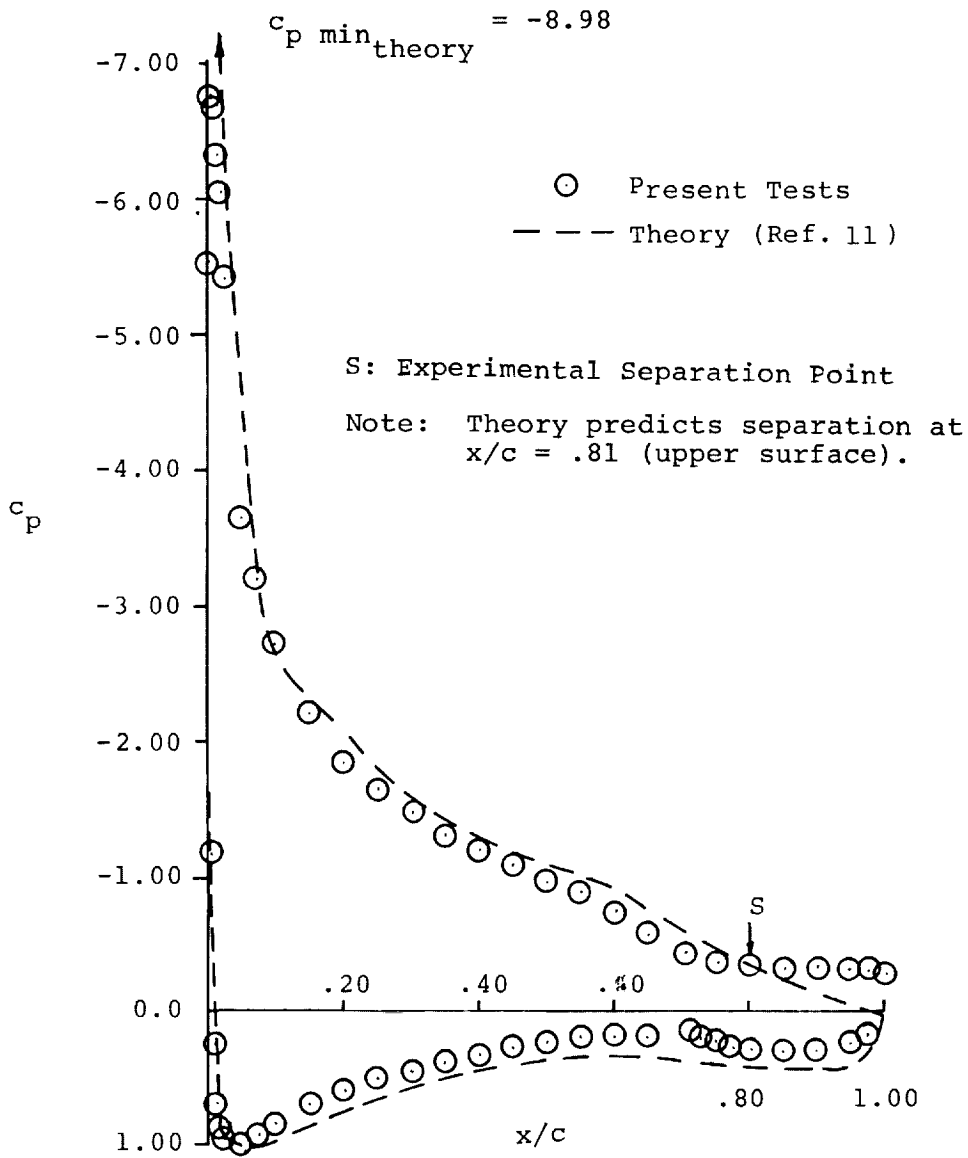
(4) Post-stall angle of attack, $\alpha=16.4^\circ$

Figure 8B- Concluded.



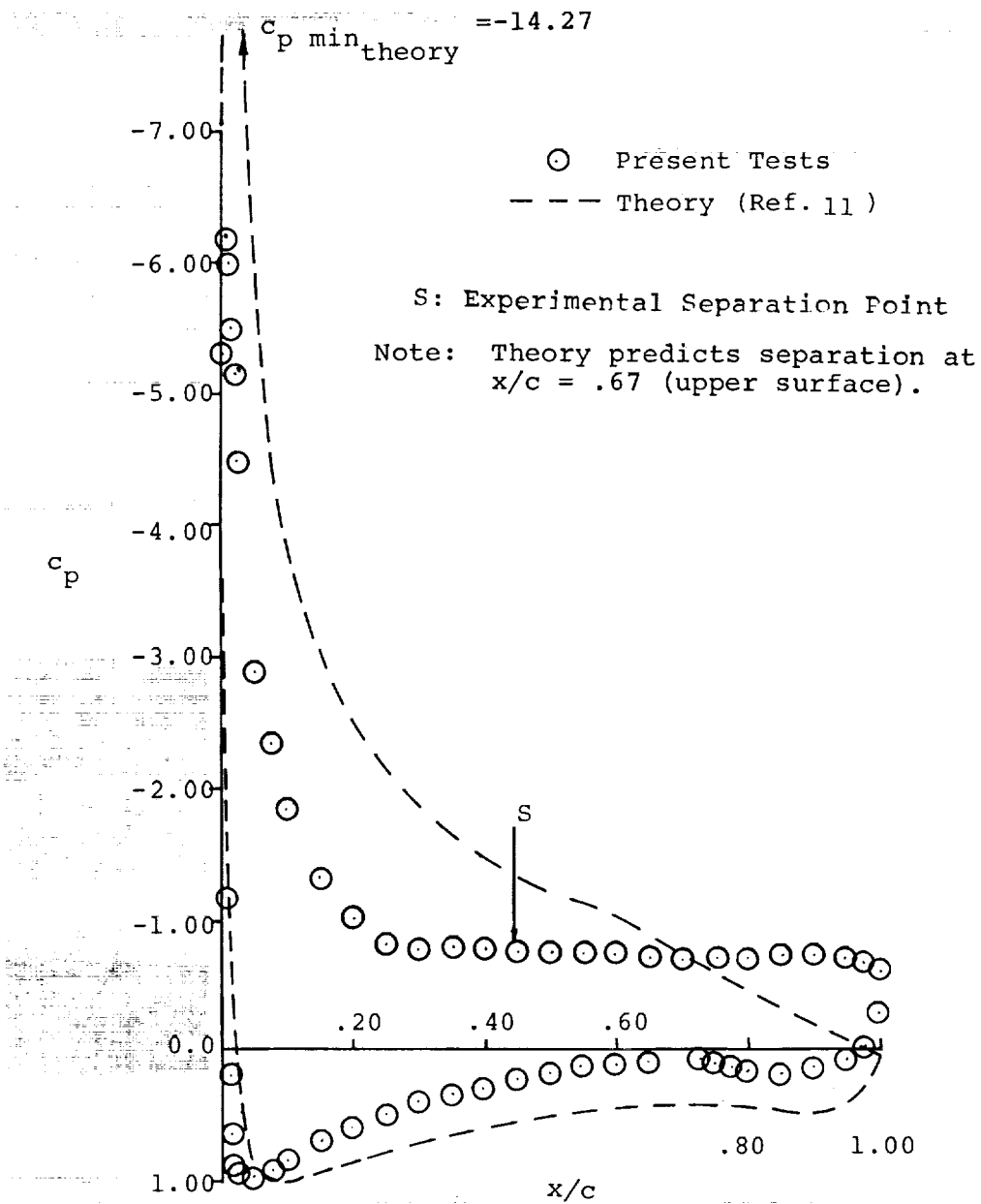
(1) Pre-Stall angle of attack, $\alpha = 10.3^\circ$

Figure 8C - Pressure Distributions of the GA(W)-2 Airfoil.



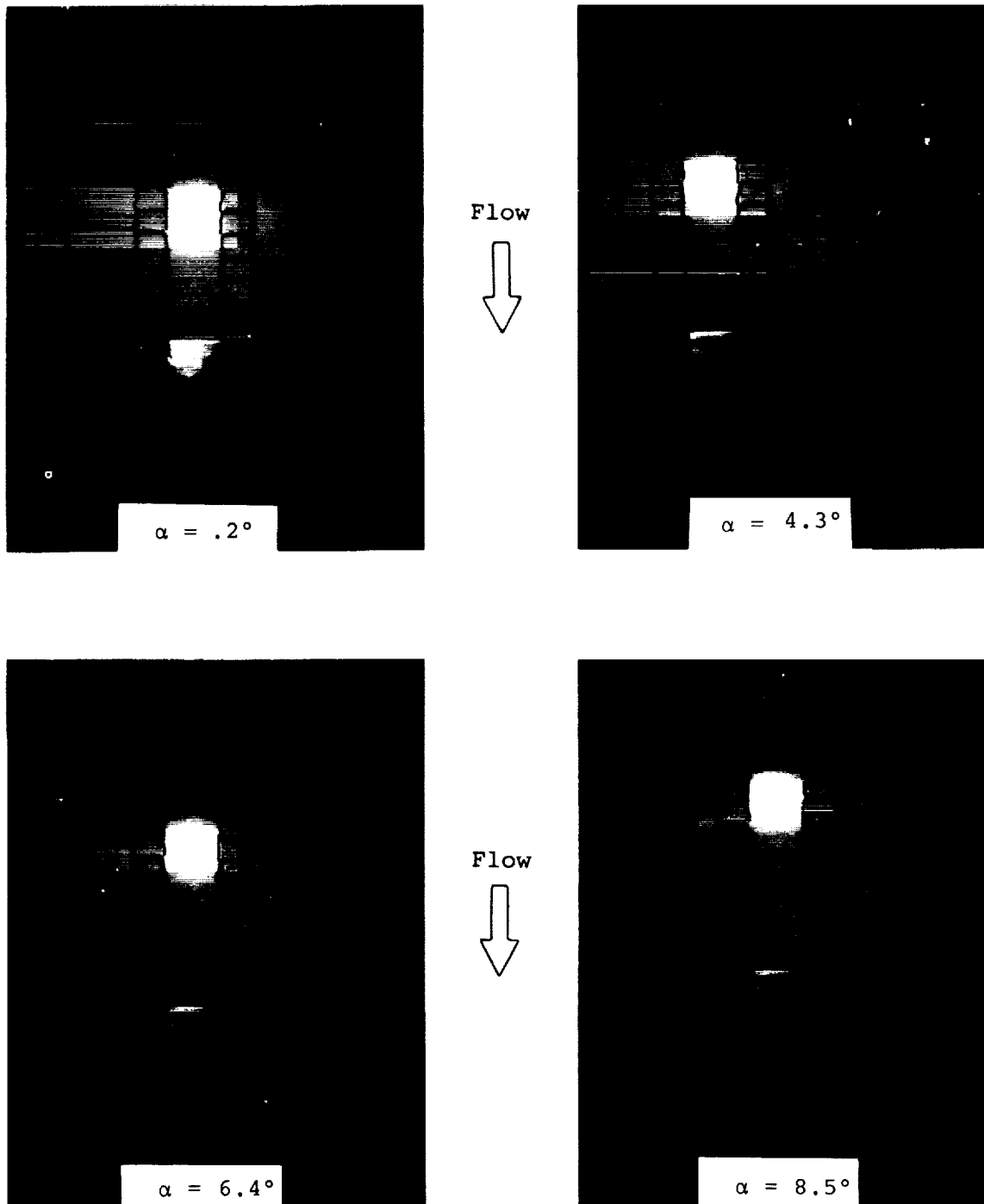
(2) Near-Stall angle of attack, $\alpha = 14.4^\circ$

Figure 8C- Continued.



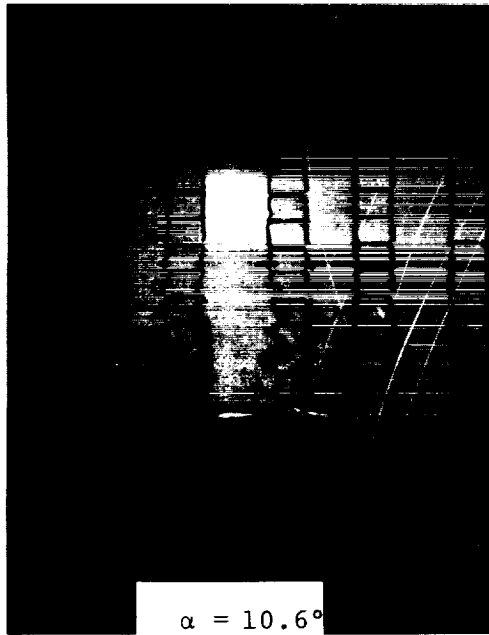
(3) Post-Stall angle of attack, $\alpha = 18.3^\circ$

Figure 8C- Concluded.

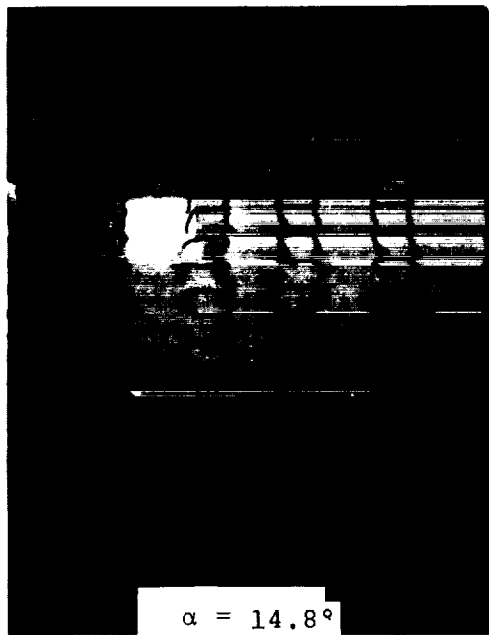


(1) Low to moderate angles of attack.

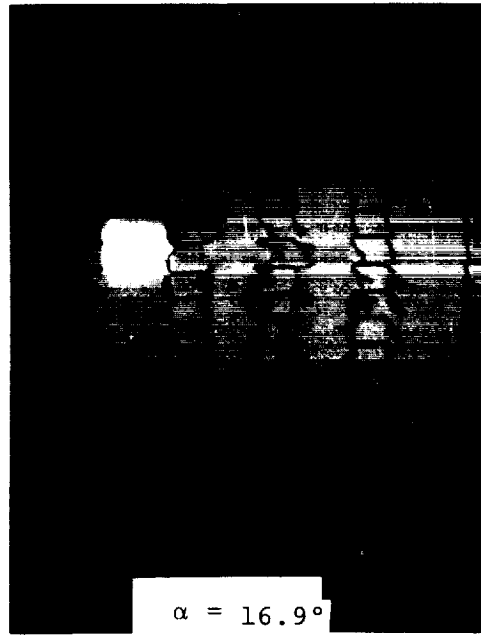
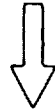
Figure 9A - Tuft Studies of LS(1)-0421 Mod Airfoil.



Flow

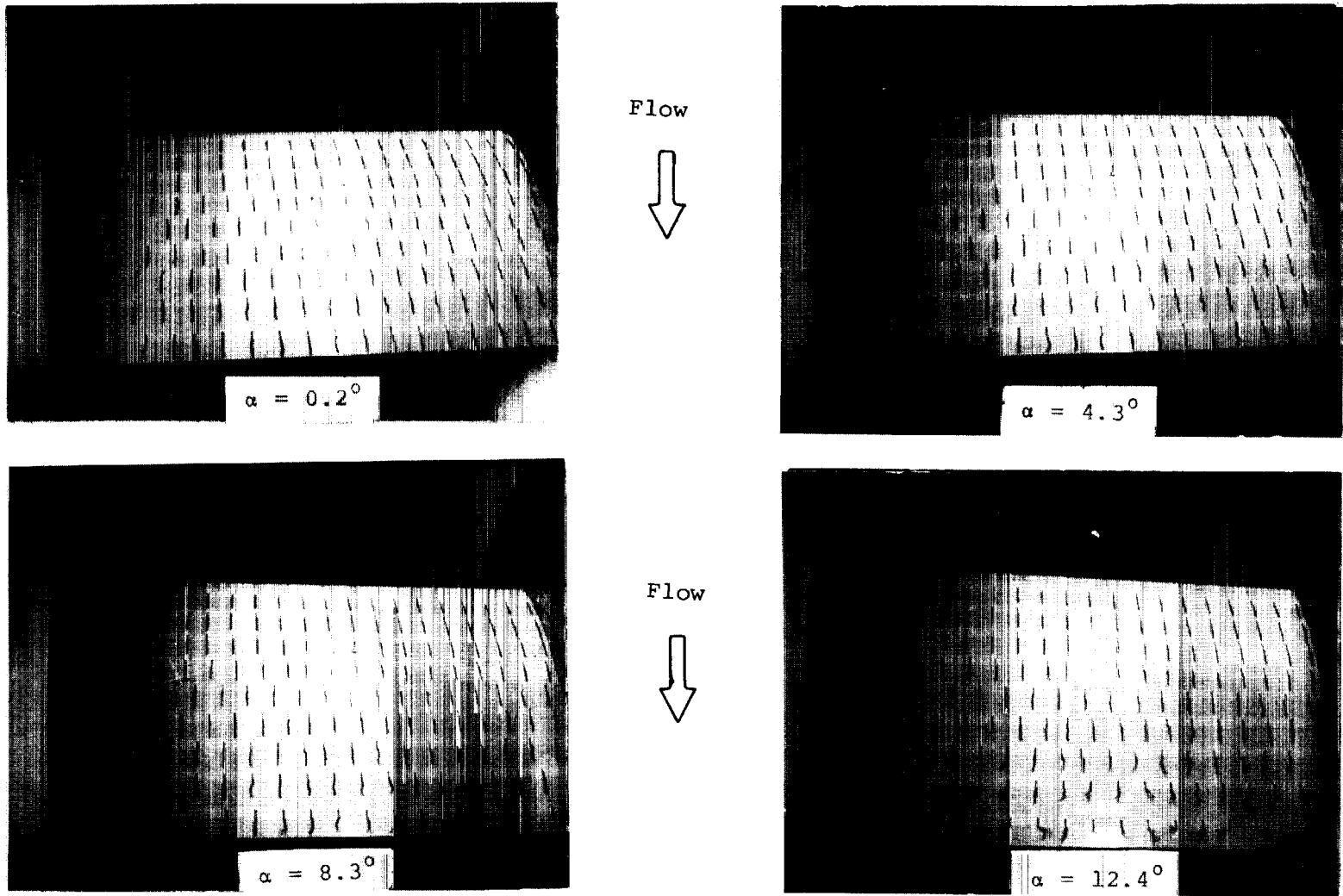


Flow



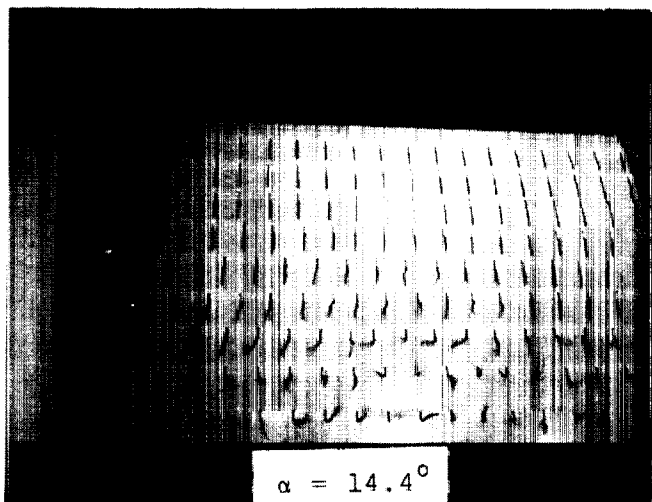
(2) High angles of attack.

Figure 9A - Concluded.

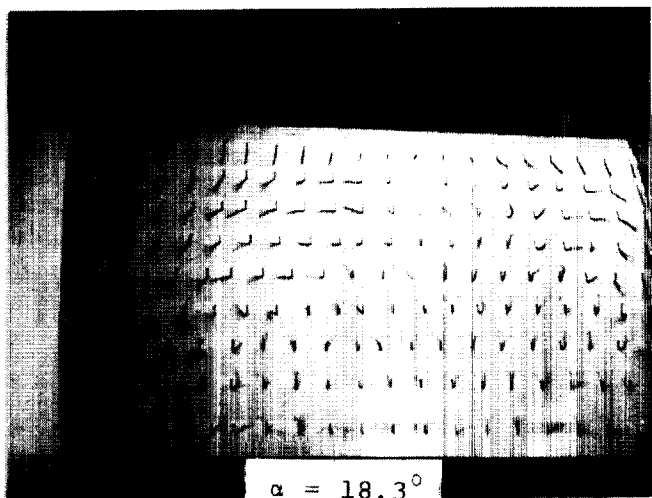
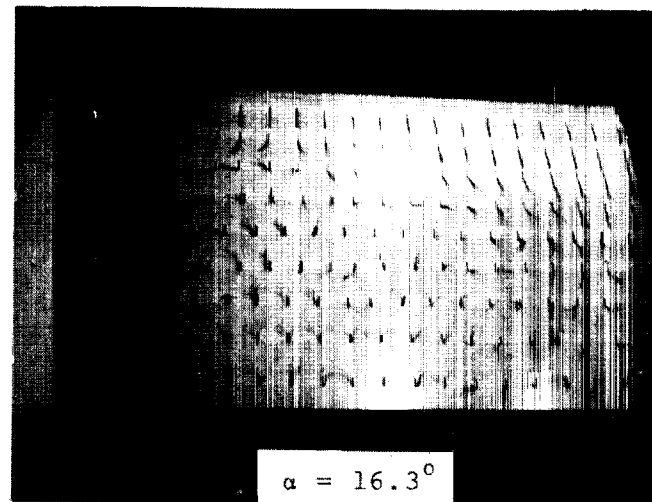
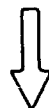


(1) Low to moderate angles of attack.

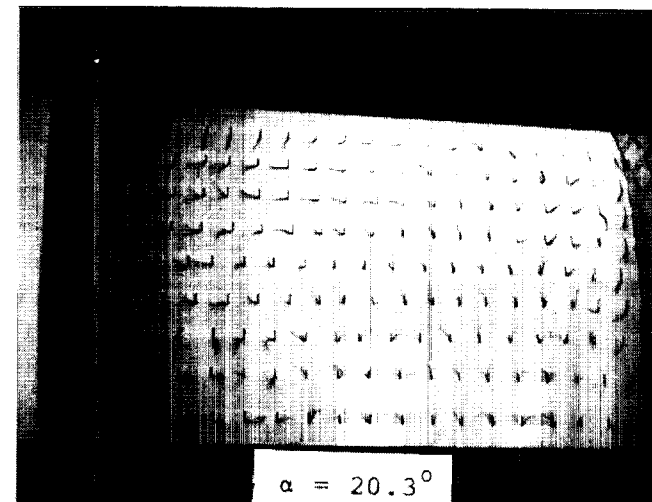
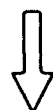
Figure 9B - Tuft Studies of NACA 2412 Airfoil.



Flow

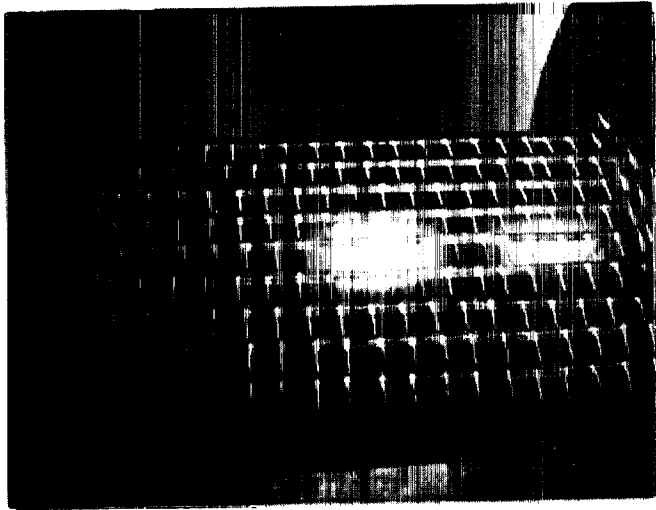


Flow

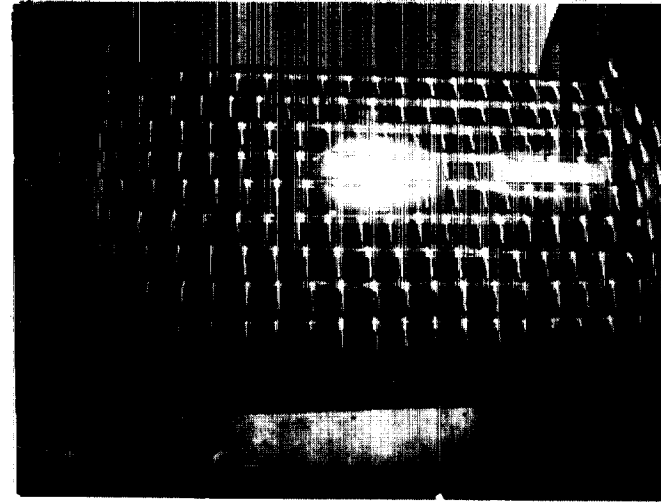


(2) High angles of attack

Figure 9B- Concluded.

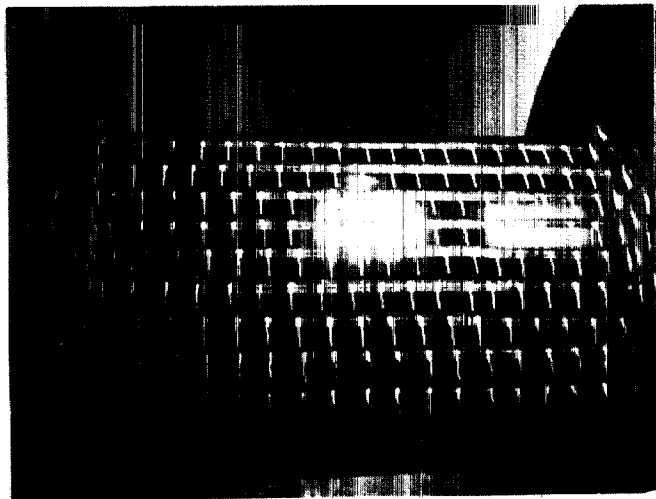
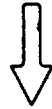


$\alpha = 4.3^\circ$

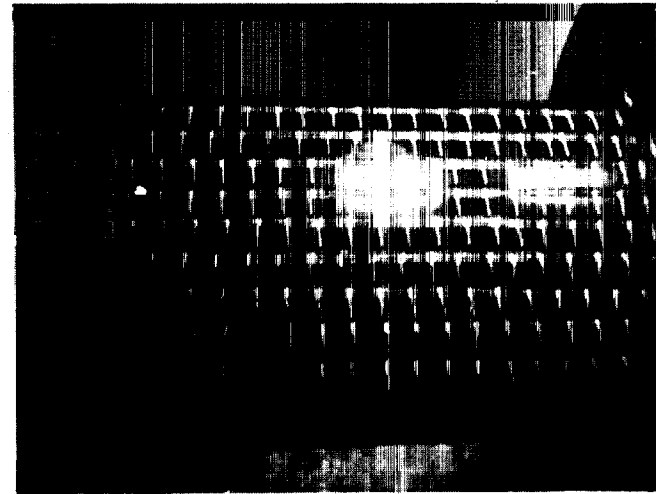


$\alpha = 8.3^\circ$

Flow

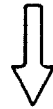


$\alpha = 10.3^\circ$



$\alpha = 12.4^\circ$

Flow



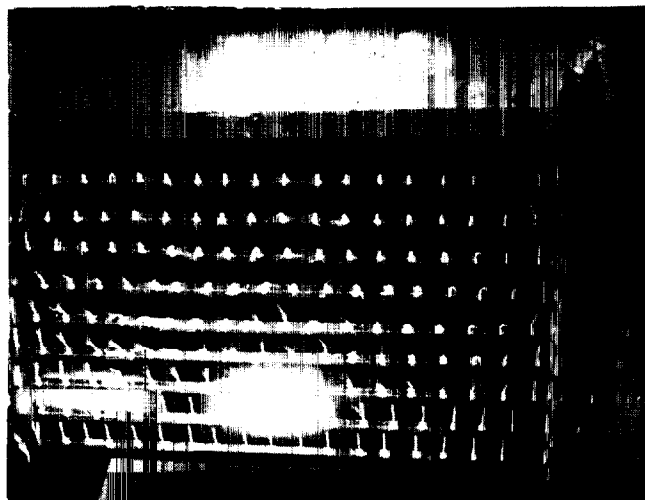
(1) Low to moderate angles of attack.

Figure 9C- Tuft Studies of GA(W)-2 Airfoil.

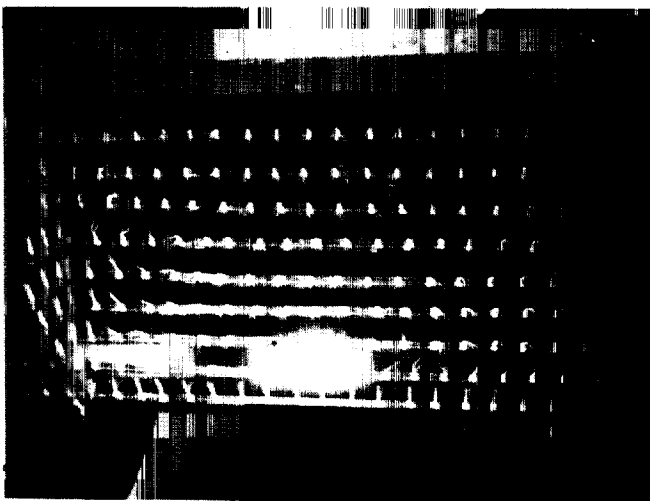
Figure 9C - Concluded.

(2) High angles of attack

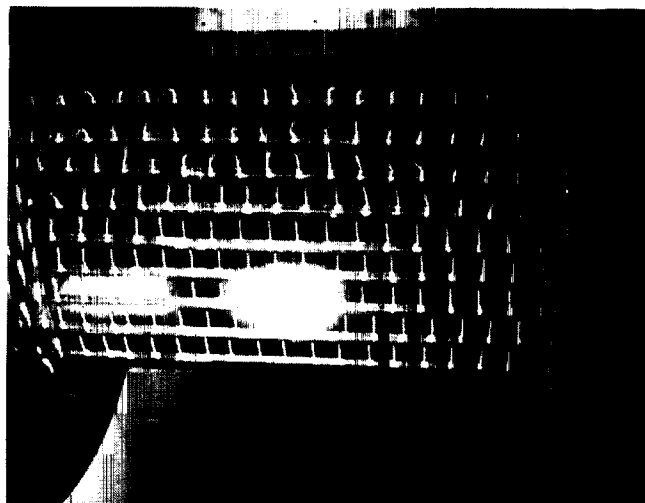
$\alpha = 18.3^\circ$



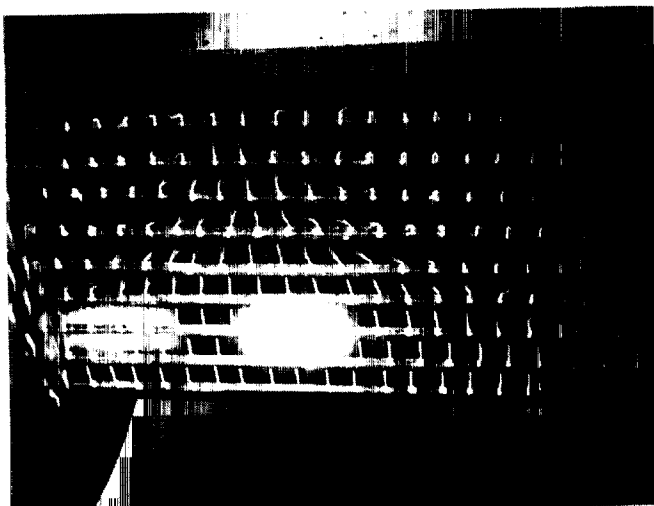
$\alpha = 20.3^\circ$

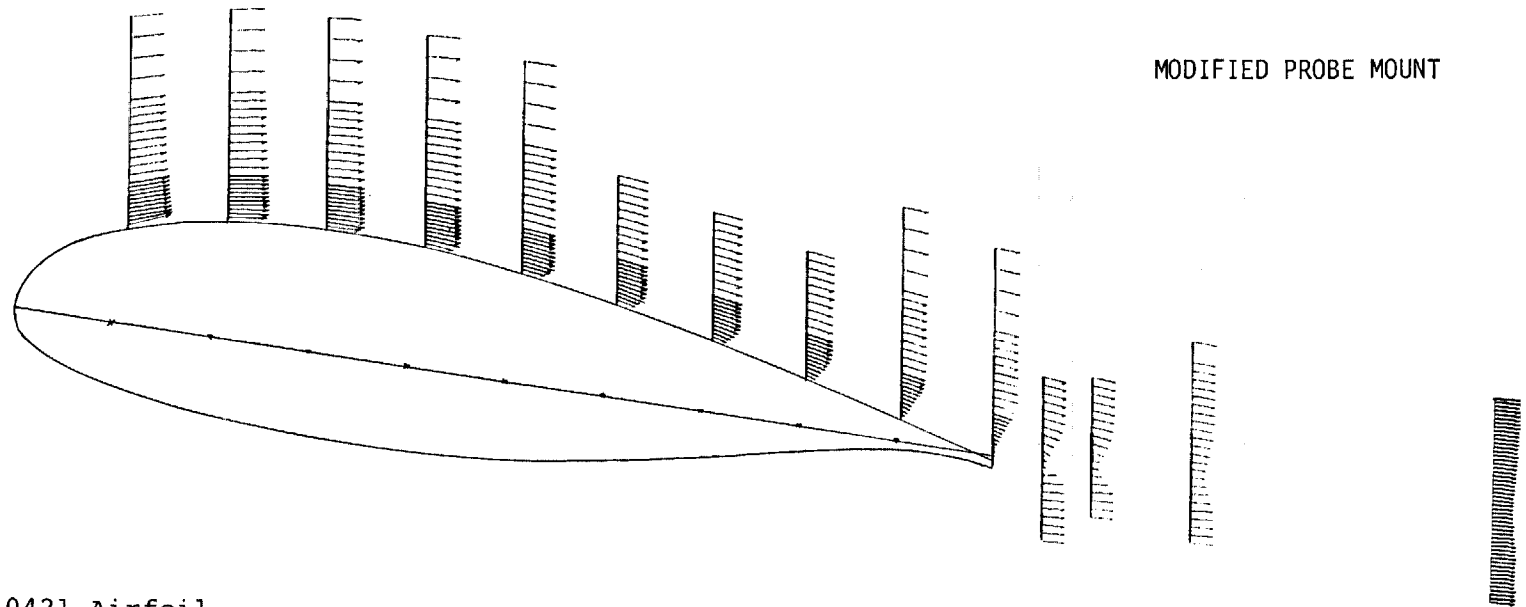


$\alpha = 14.4^\circ$



$\alpha = 16.4^\circ$

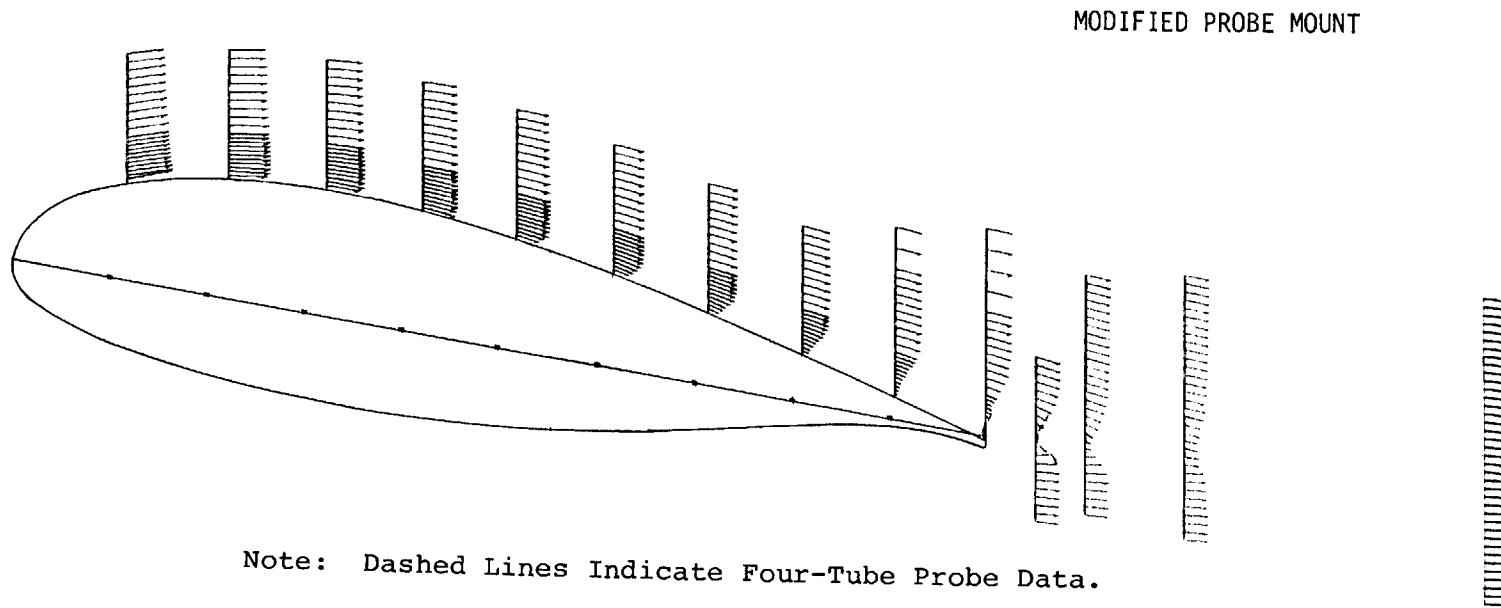




0421 Airfoil
Alpha = 8.5°
RN = 2.2×10^6
Mach No. = 0.13
 U_{inf} \rightarrow

(1) Pre-stall angle of attack, $\alpha = 8.5^\circ$

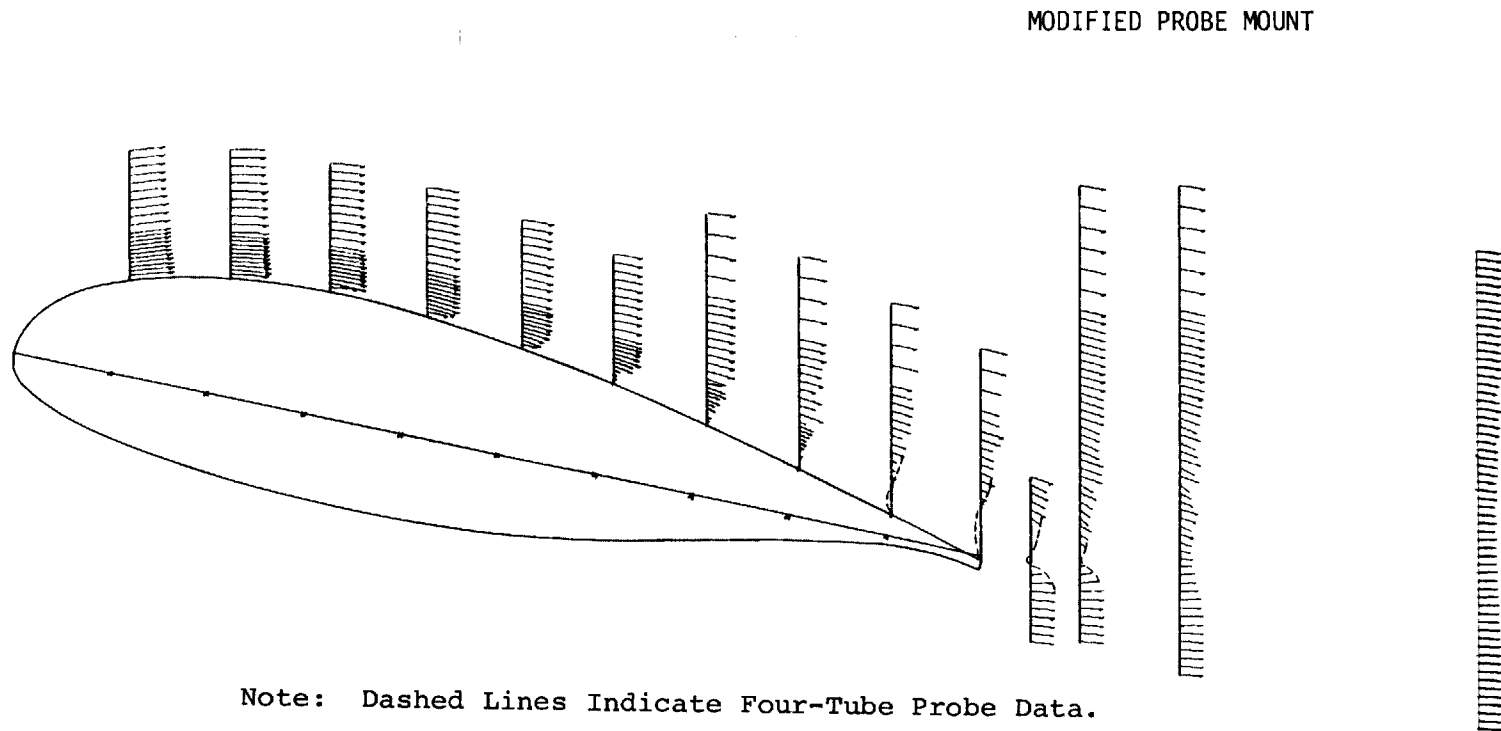
Figure 10A-Experimental Velocity Profiles of LS(1)-0421 Mod Airfoil.



0421 Airfoil
Alpha = 10.6°
RN = 2.2×10^6
Mach No. = 0.13
 U_{inf} →

(2) Near-stall angle of attack, $\alpha = 10.6^\circ$

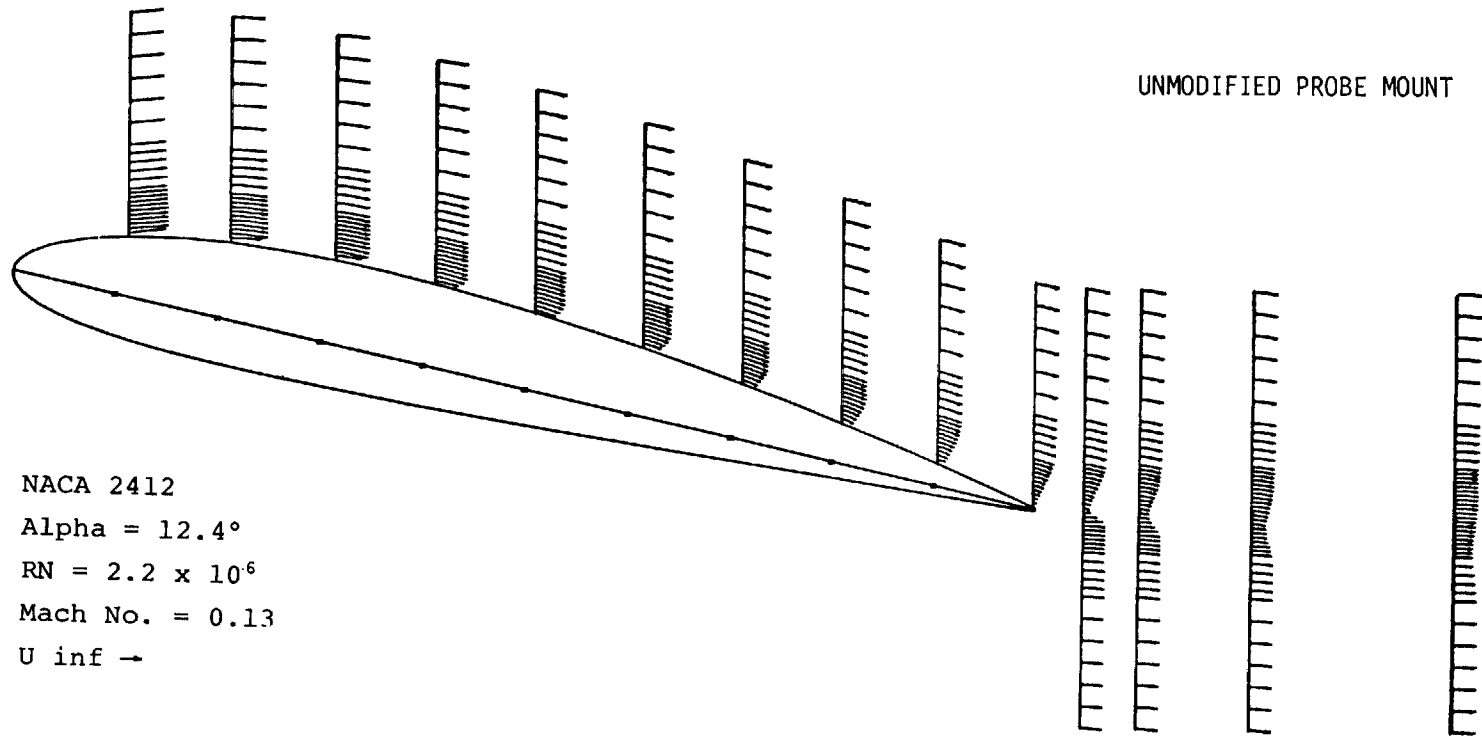
Figure 10A- Continued.



0421 Airfoil
 Alpha = 12.7°
 RN = 2.2×10^6
 Mach No. = 0.13
 U_{inf} —

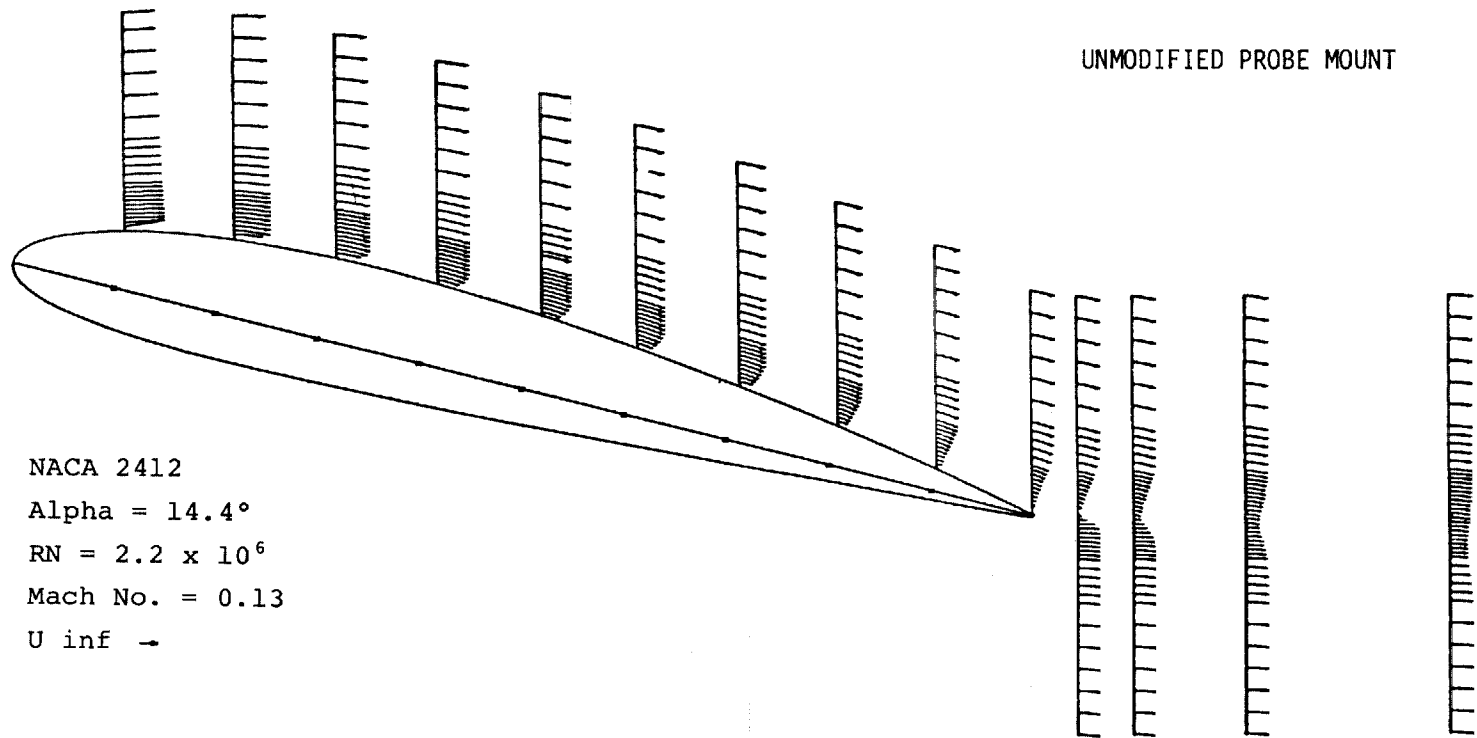
(3) Post-stall angle of attack, $\alpha = 12.7^\circ$

Figure 10A-Concluded.



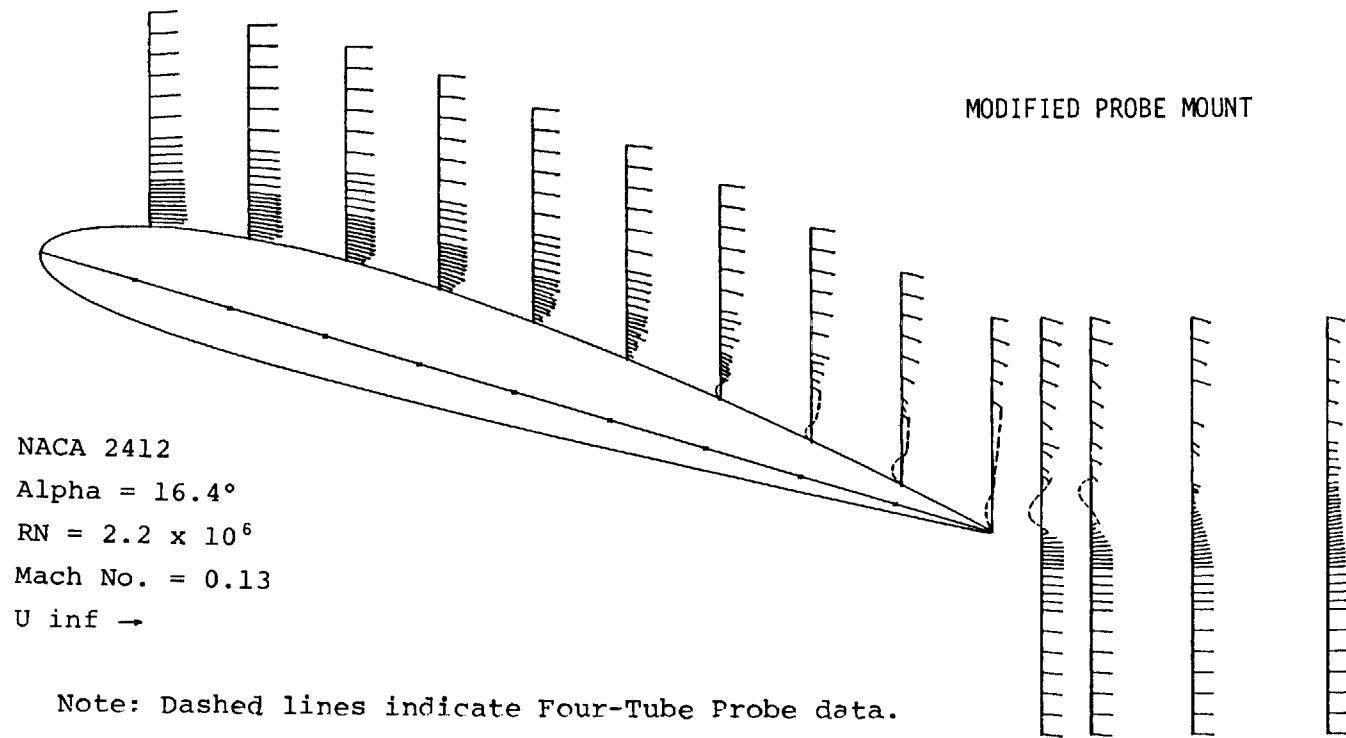
(1) Pre-stall angle of attack, $\alpha = 12.4^\circ$

Figure 10B - Experimental Velocity Profiles of NACA 2412 Airfoil.



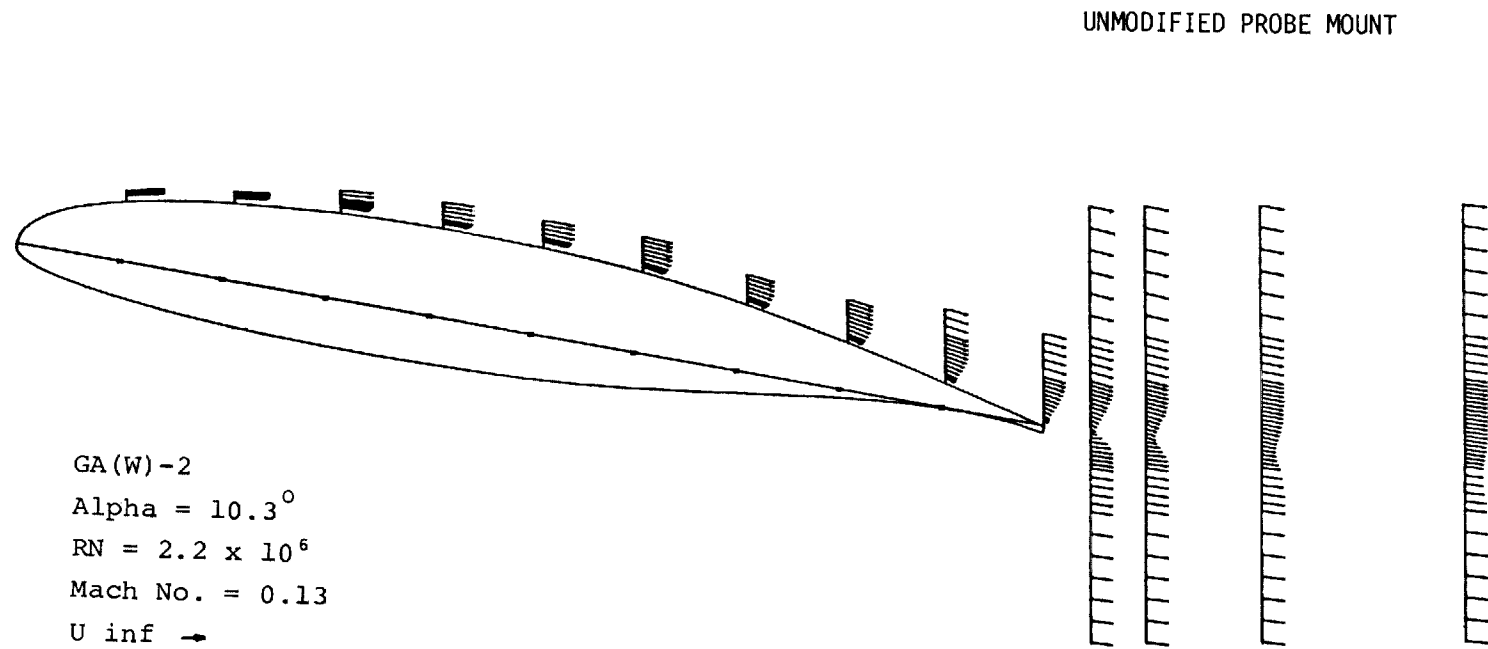
(2) Angle of attack for $c_{l_{\max}}$, $\alpha=14.4^\circ$

Figure 10B- Continued.



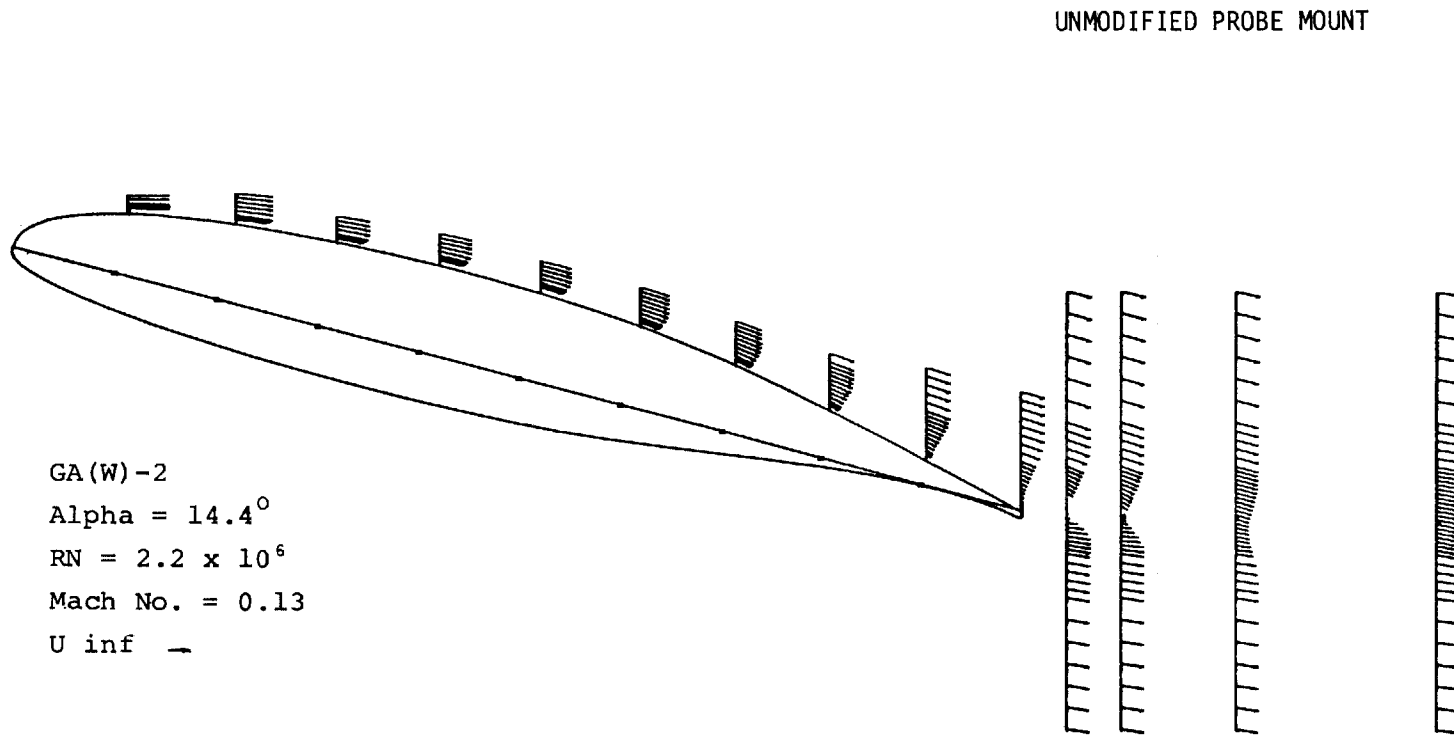
(3) Post-stall angle of attack, $\alpha=16.4^\circ$

Figure 10B-Concluded.



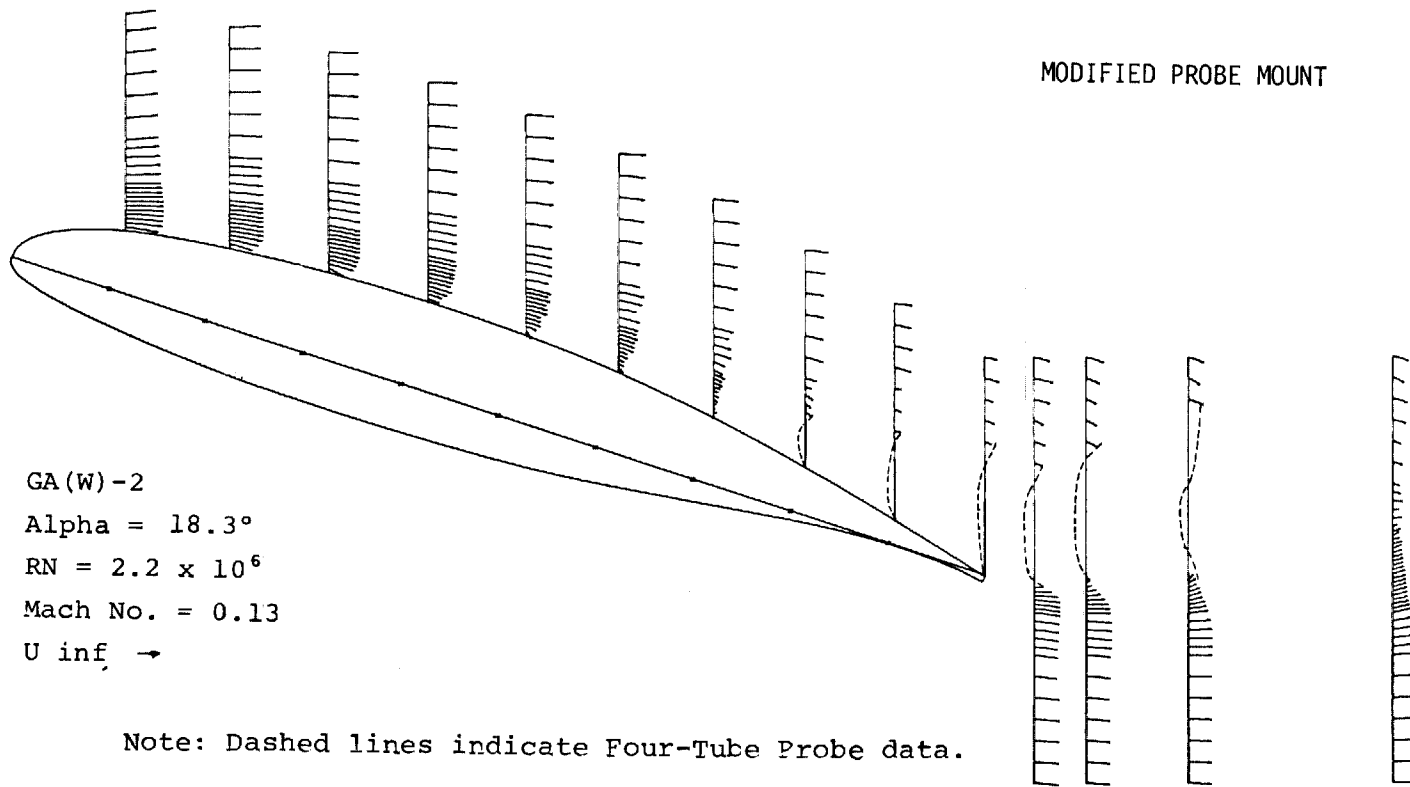
(1) Pre-Stall angle of attack, $\alpha = 10.3^\circ$

Figure 10C - Experimental Velocity Profiles Of GA(W)-2 Airfoil.



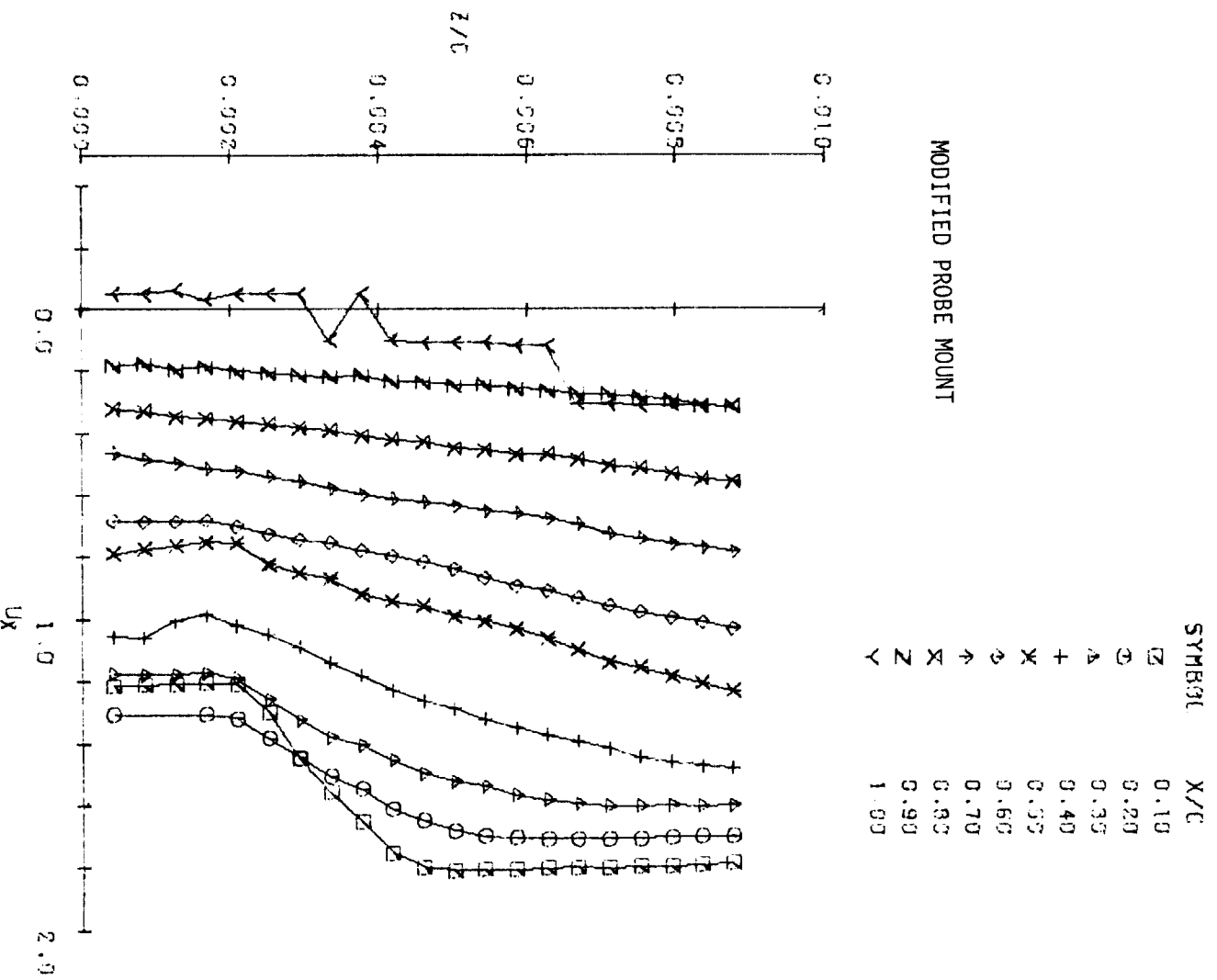
(2) Near- Stall angle of attack, $\alpha = 14.4^\circ$

Figure 10C- Continued.



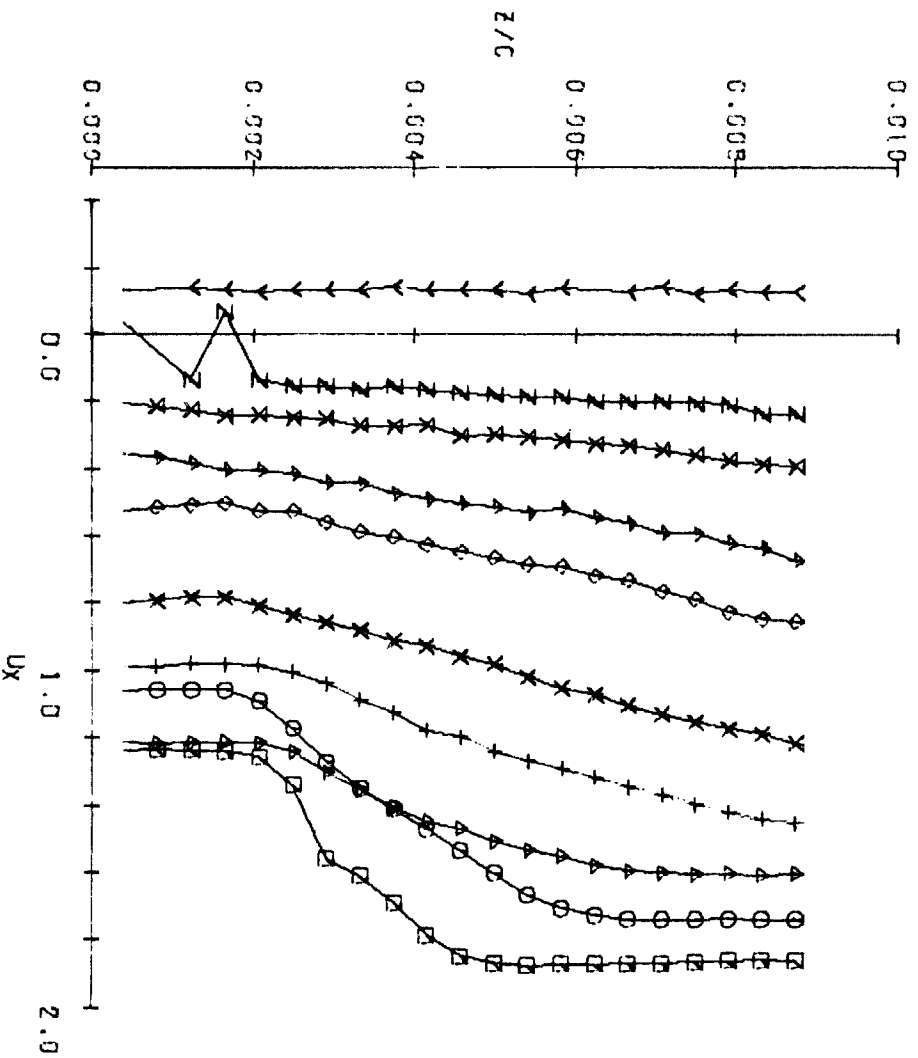
(3) Post-Stall angle of attack, $\alpha = 18.3^\circ$

Figure 10C - Concluded.



(1) Pre-stall angle of attack, $\alpha = 8.5^\circ$

Figure 11A - Near Wall Velocity Profiles, LS(1)-0421 Mod Airfoil.

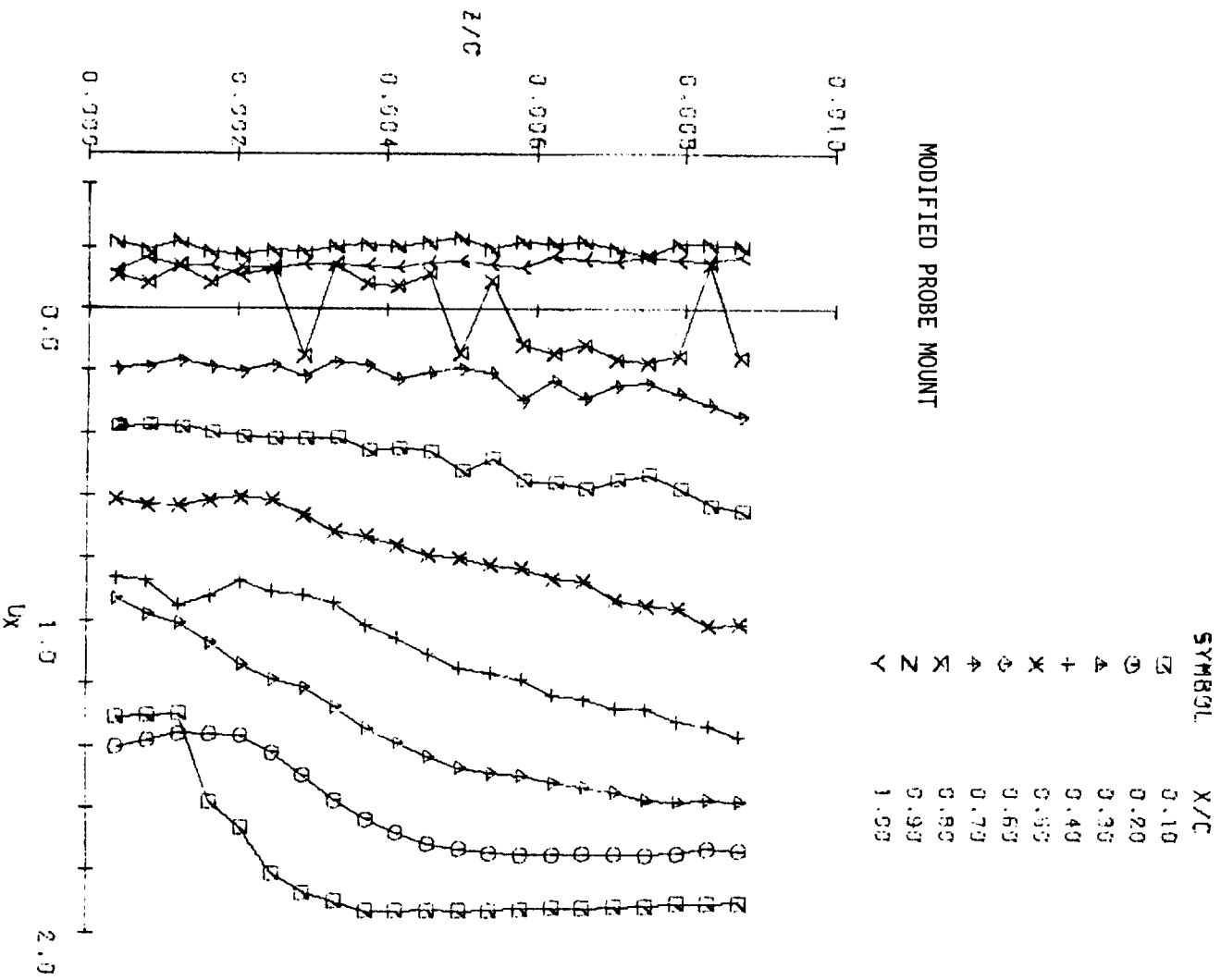


MODIFIED PROBE MOUNT

SYMBOL	X/C
□	0.10
⊙	0.20
△	0.30
+	0.40
×	0.50
◇	0.60
↖	0.70
×	0.80
z	0.90
γ	1.00

(2) Near-stall angle of attack, $\alpha = 10.6^\circ$

Figure 11A - Continued.

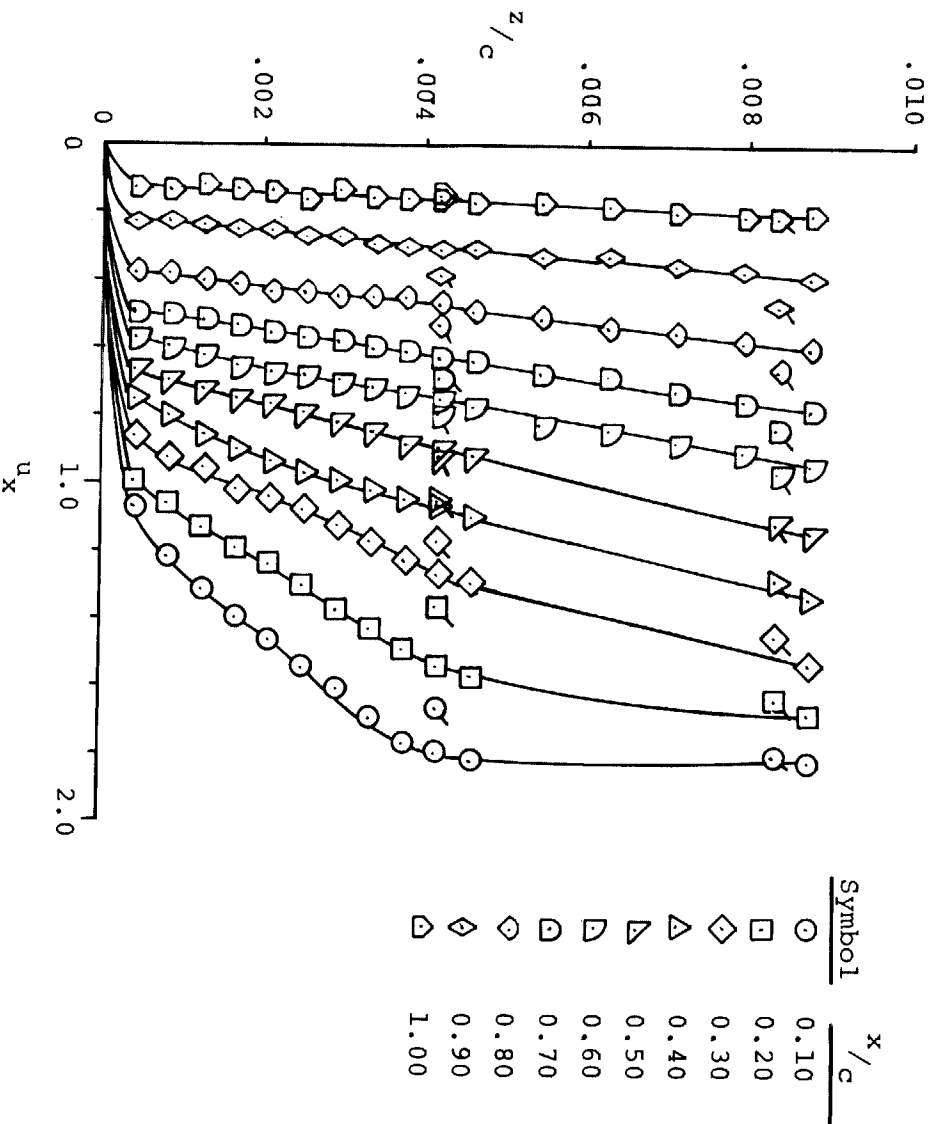


(3) Post-stall angle of attack, $\alpha = 12.7^\circ$

Figure 11A - Concluded.

UNMODIFIED PROBE MOUNT

Primed: Five Tube Probe
 Unprimed: Four Tube Probe

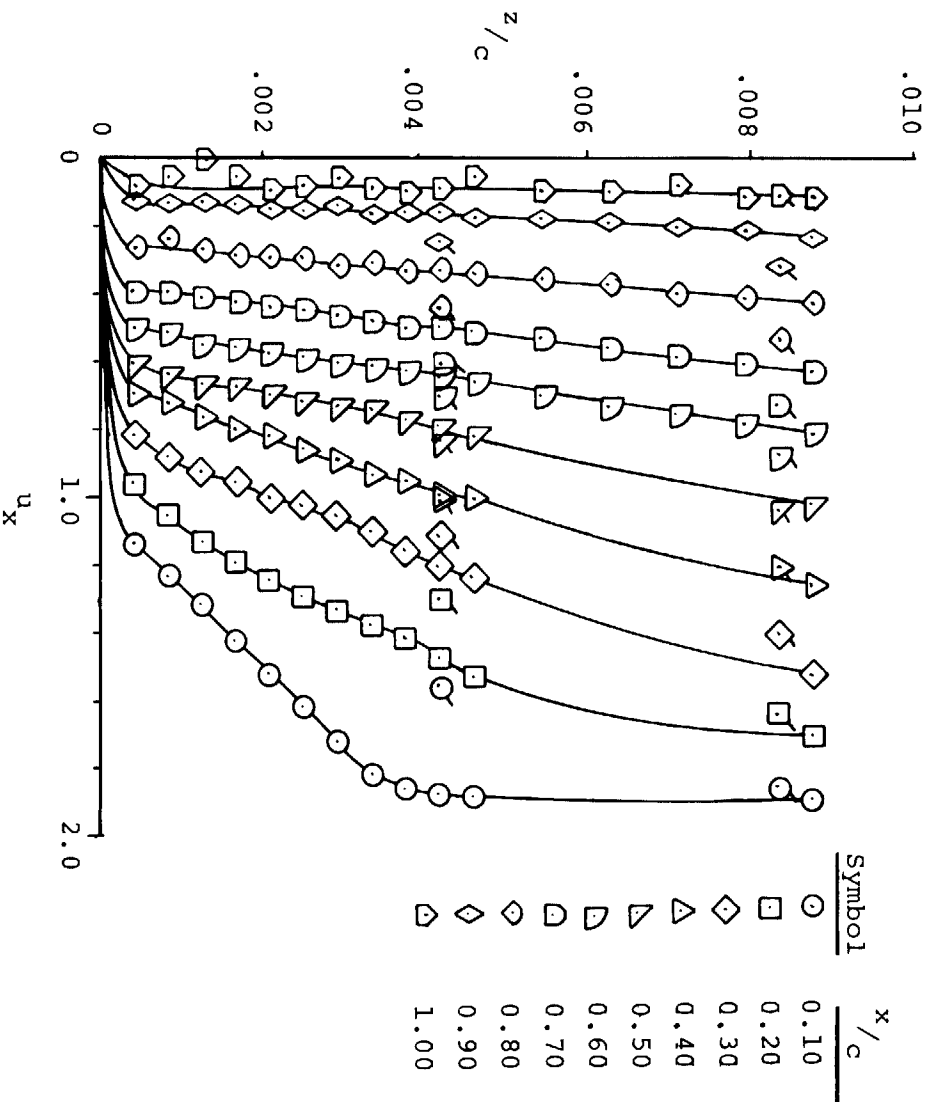


(1) Pre-stall angle of attack, $\alpha=12.4^\circ$

Figure 11B - Near Wall Velocity Profiles, MACA 2412 Airfoil.

UNMODIFIED PROBE MOUNT

Primed: Five Tube Probe
 Unprimed: Four Tube Probe

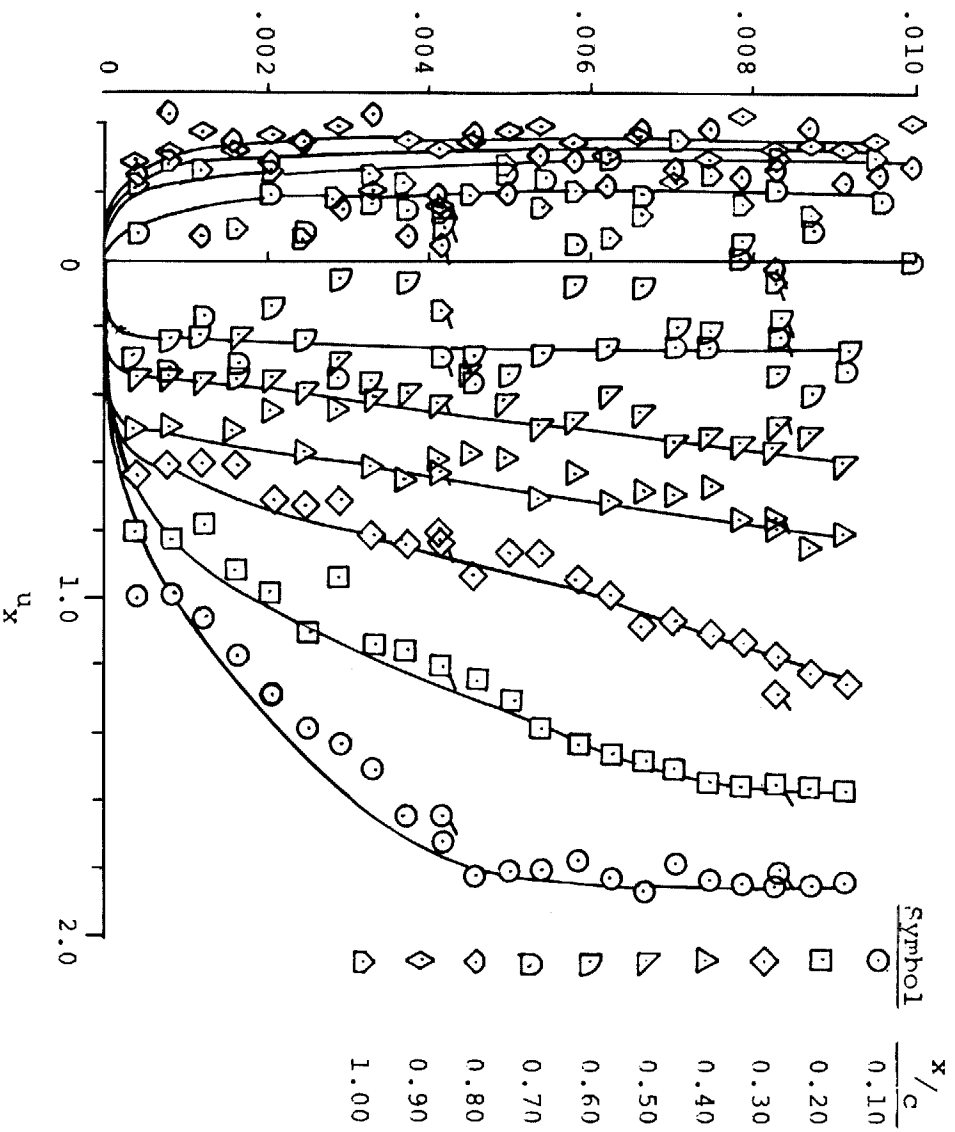


(2) Angle of attack for $c_{l, \max}$, $\alpha=14.4^\circ$

Figure 11B- Continued.

MODIFIED PROBE MOUNT

Primed: Five Tube Probe
 Unprimed: Four Tube Probe



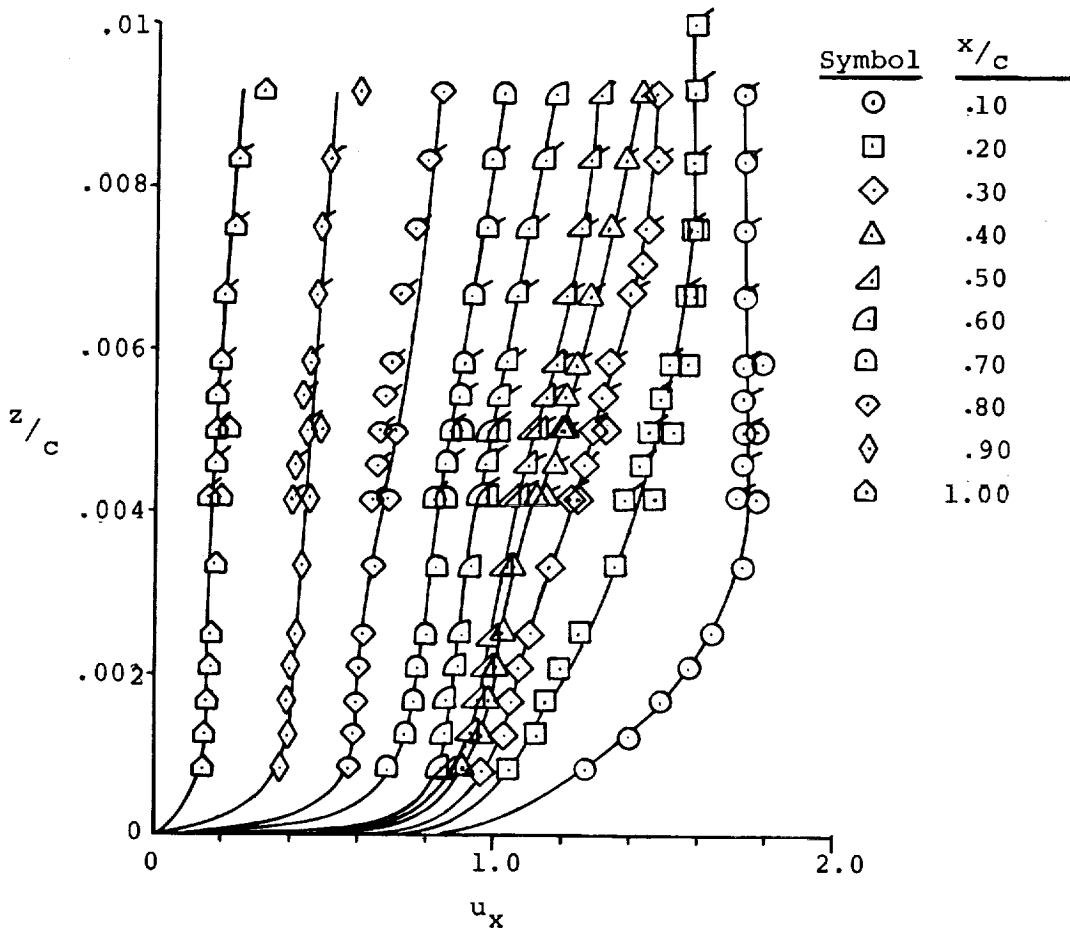
(3) Post-stall angle of attack, $\alpha=16.4^\circ$

Figure 11B - Concluded.

UNMODIFIED PROBE MOUNT

Primed: Five Tube Probe

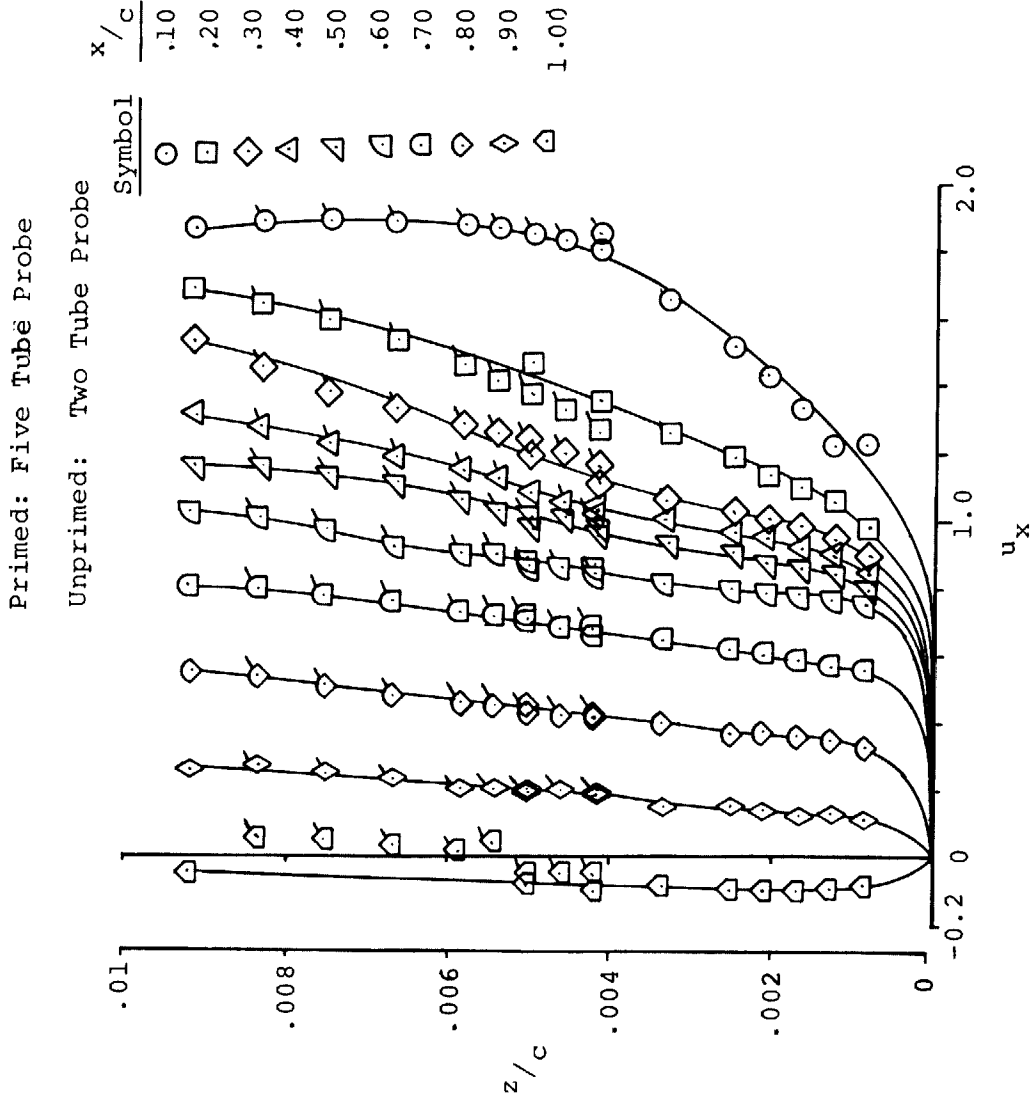
Unprimed: Two Tube Probe



(1) Pre-Stall angle of attack, $\alpha = 10.3^\circ$

Figure 11C - Near Wall Velocity Profiles., GA(W)-2 Airfoil.

UNMODIFIED PROBE MOUNT



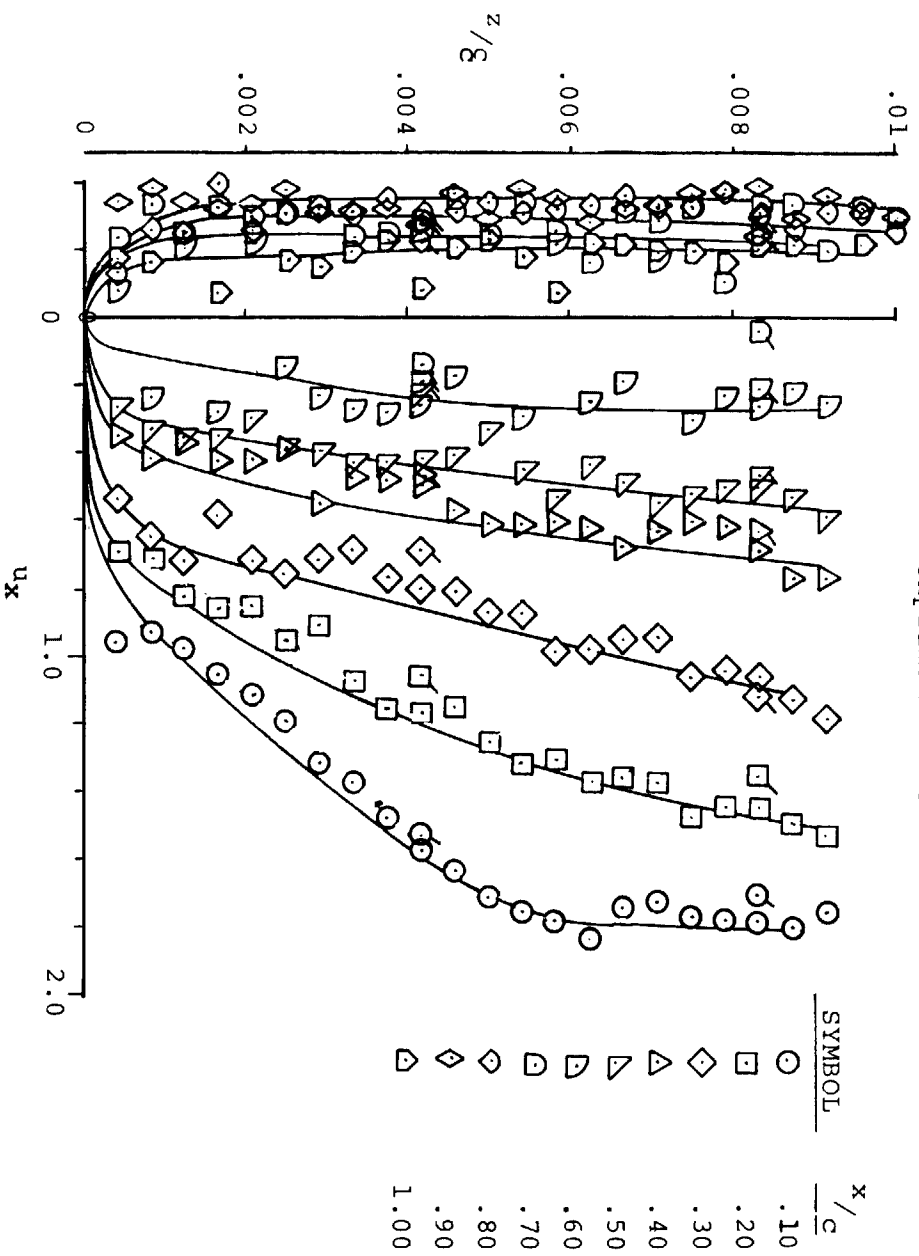
(2) Near-Stall angle of attack, $\alpha = 14.4^\circ$

Figure 11C- Continued.

MODIFIED PROBE MOUNT

Primed: Five Tube Probe

Unprimed: Two Tube Probe

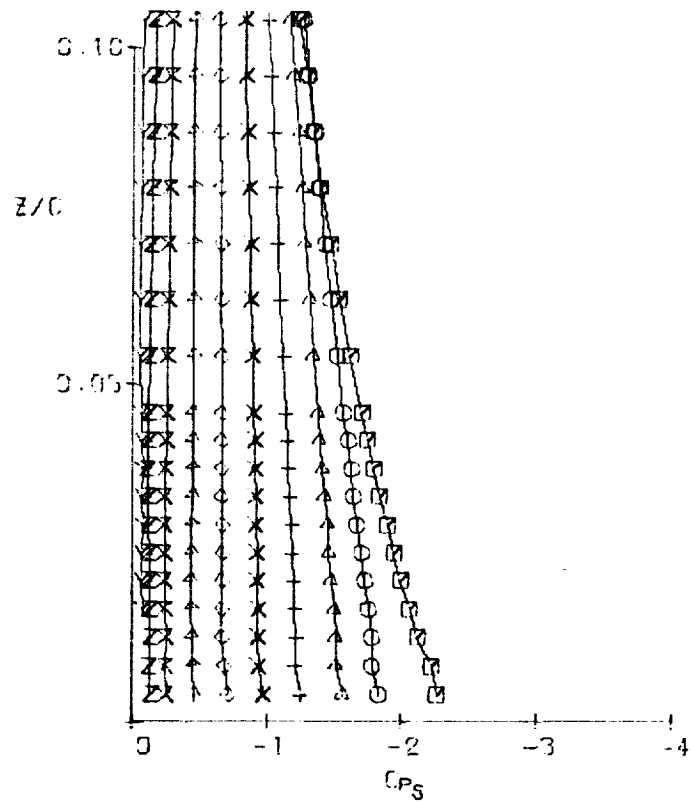


(3) Post-Stall angle of attack, $\alpha = 18.3^\circ$

Figure IIC - Concluded.

MODIFIED PROBE MOUNT

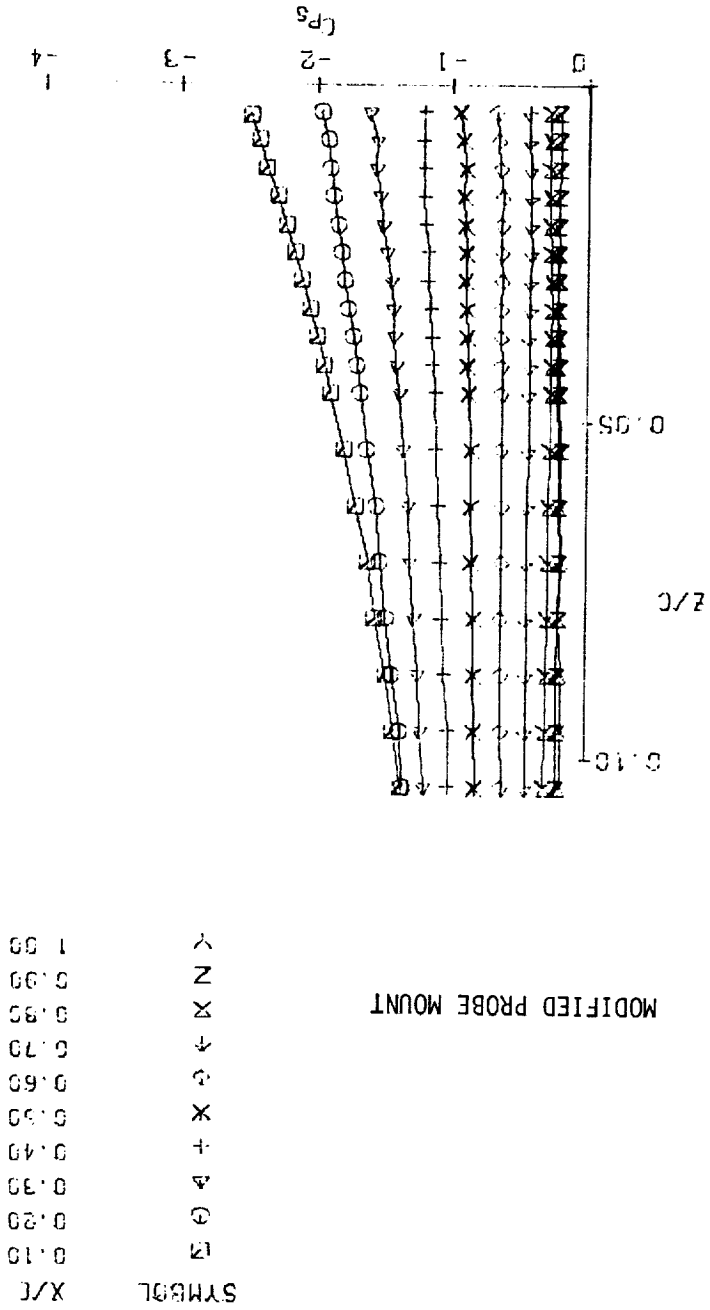
SYMBOL	X/C
◻	0.10
⊙	0.20
△	0.35
+	0.40
×	0.50
⊖	0.60
↑	0.70
↘	0.80
Z	0.90
Y	1.00



(1) Pre-stall angle of attack, $\alpha = 8.5^\circ$

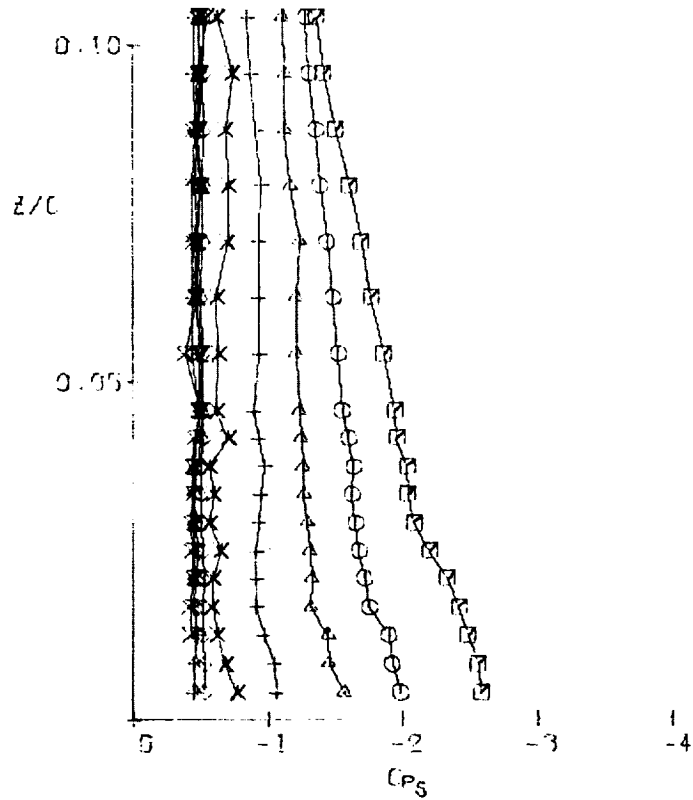
Figure 12A - Static Pressure Profiles, IS(1)-0421 Mod Airfoil.

(2) Near-stall angle of attack, $\alpha = 10.6^\circ$
 Figure 12A - Continued.



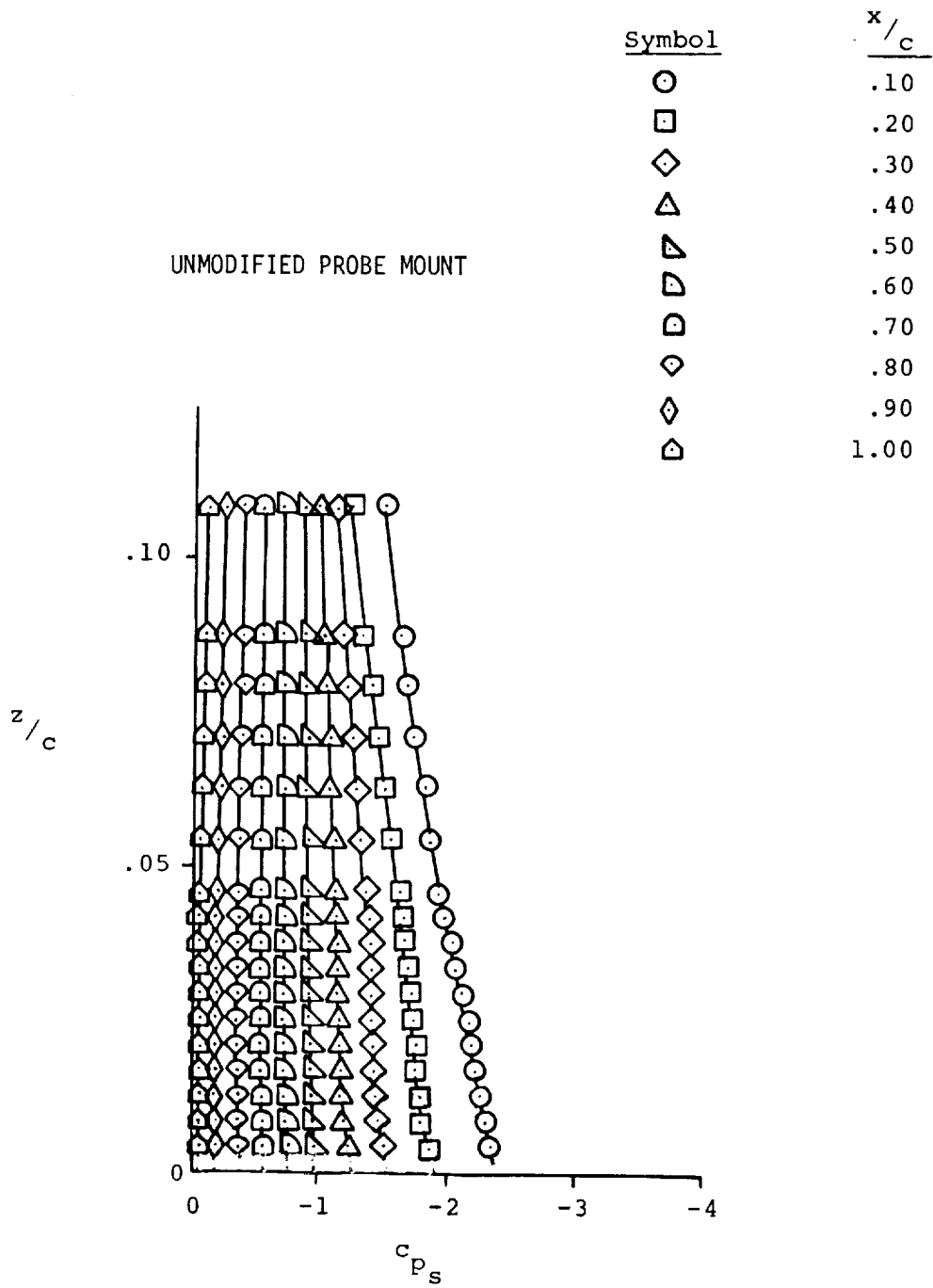
MODIFIED PROBE MOUNT

SYMBOL	X/C
□	0.10
○	0.20
△	0.30
+	0.40
×	0.50
◊	0.60
↑	0.70
×	0.80
Z	0.90
Y	1.00



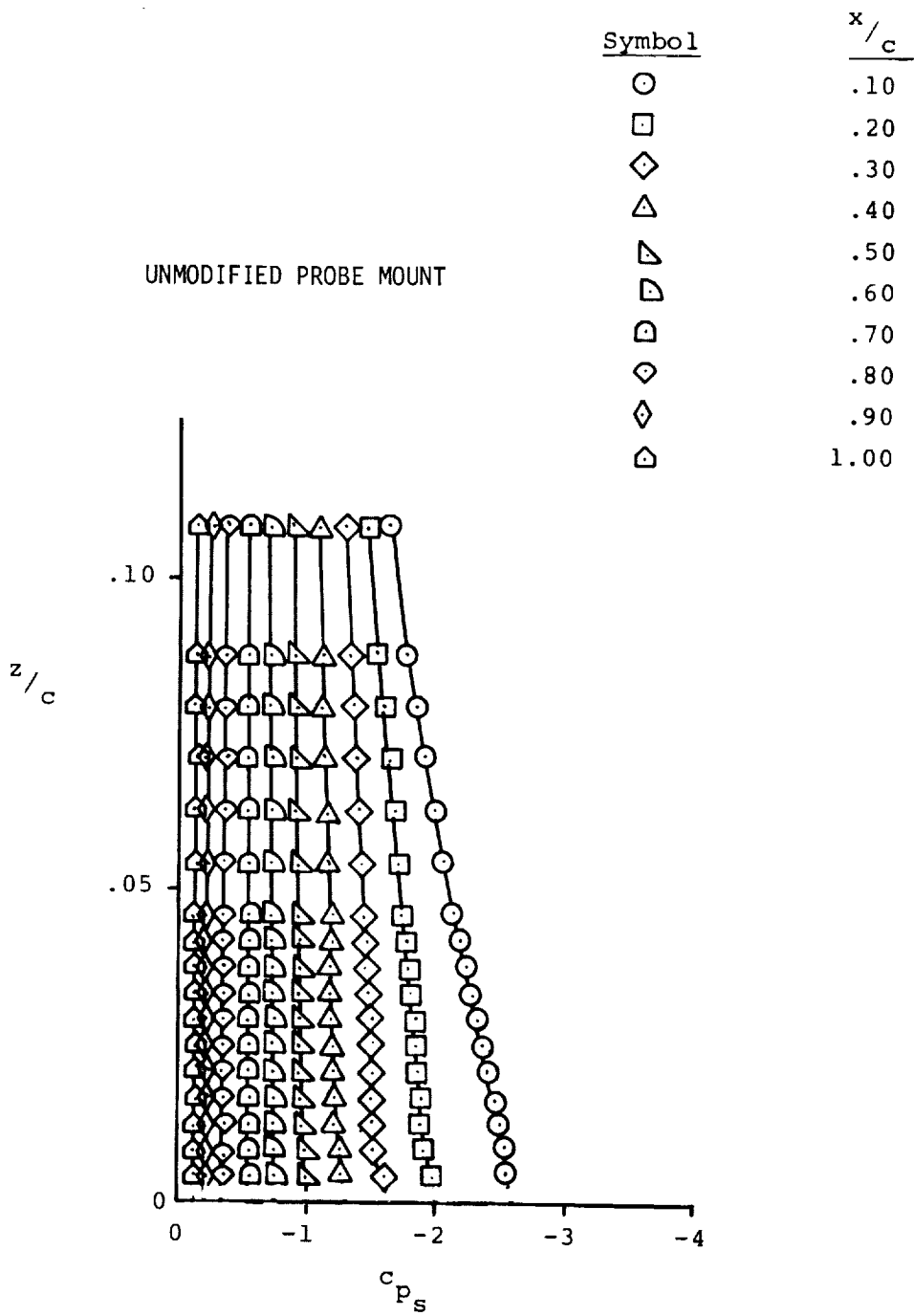
(3) Post-stall angle of attack, $\alpha = 12.7^\circ$

Figure 12A- Concluded.



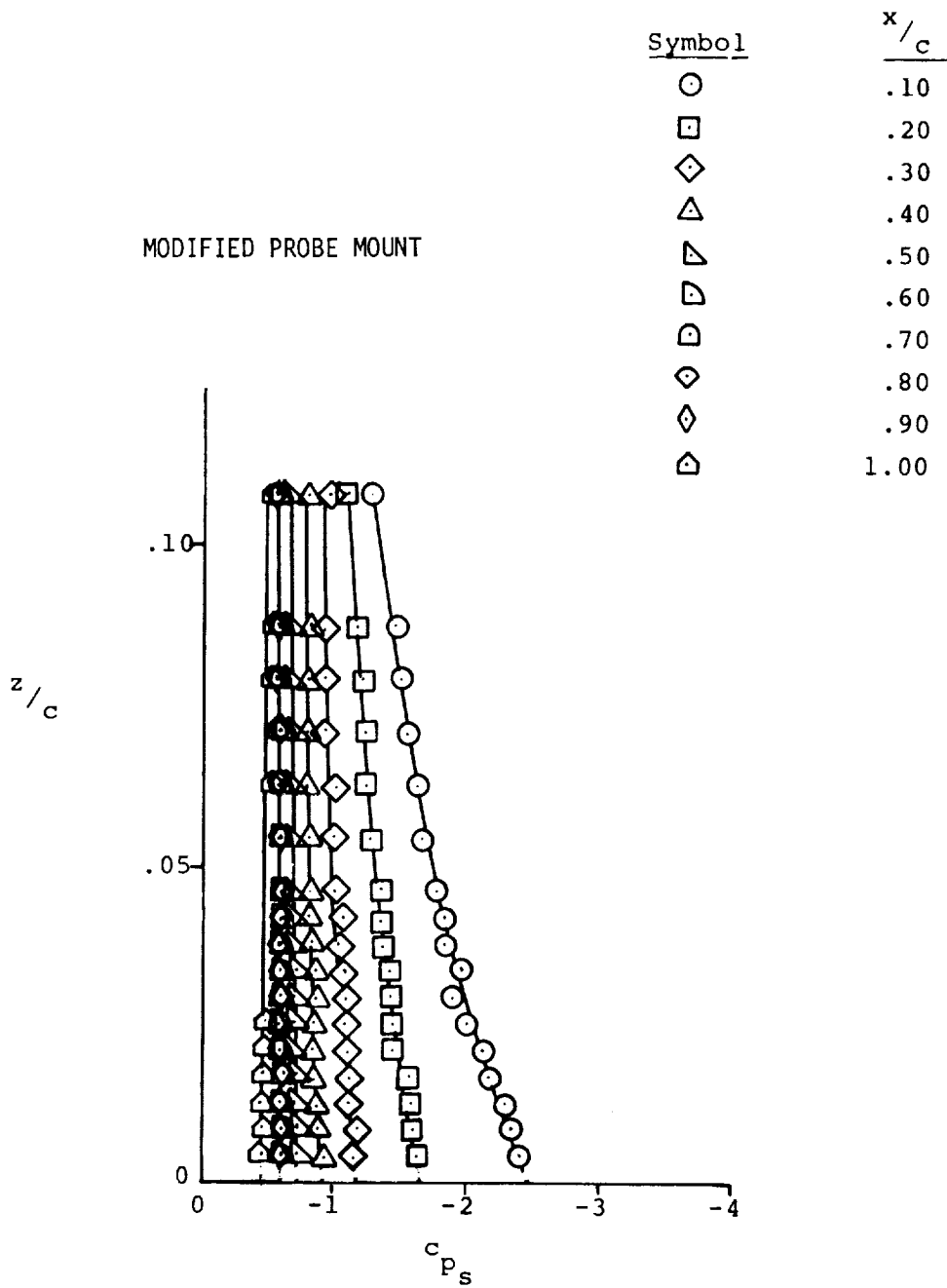
(1) Pre-stall angle of attack, $\alpha=12.4^\circ$

Figure 12B - Static Pressure Profiles, NACA 2412 Airfoil.



(2) Angle of attack for $c_{l_{max}}$, $\alpha=14.4^\circ$

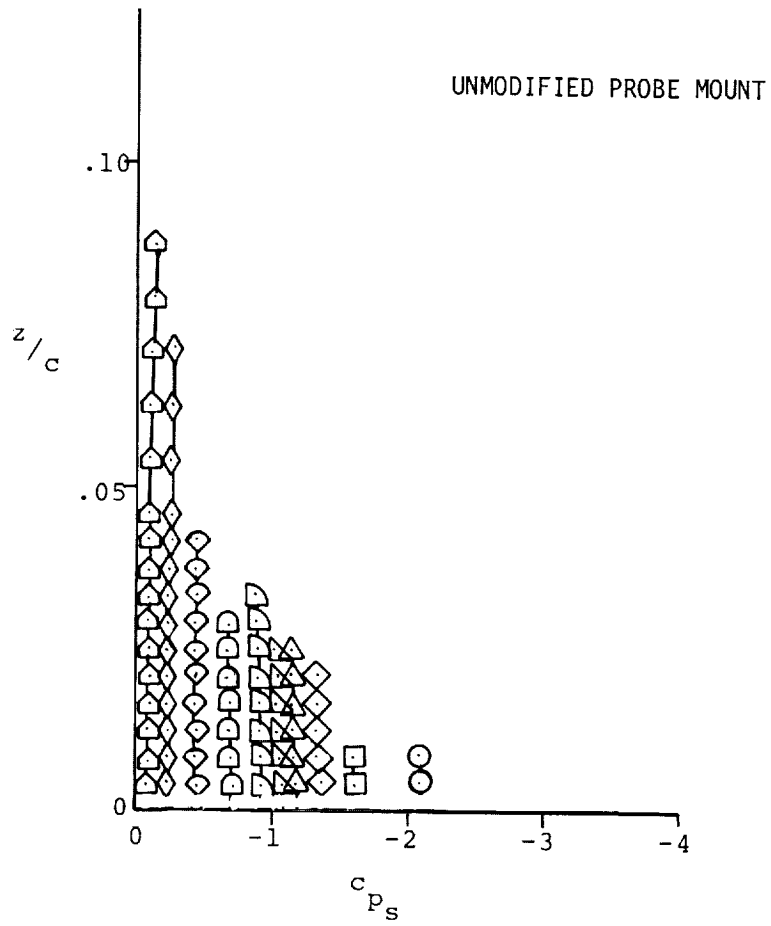
Figure 12B- Continued.



(3) Post-stall angle of attack, $\alpha=16.4^\circ$

Figure 12B - Concluded.

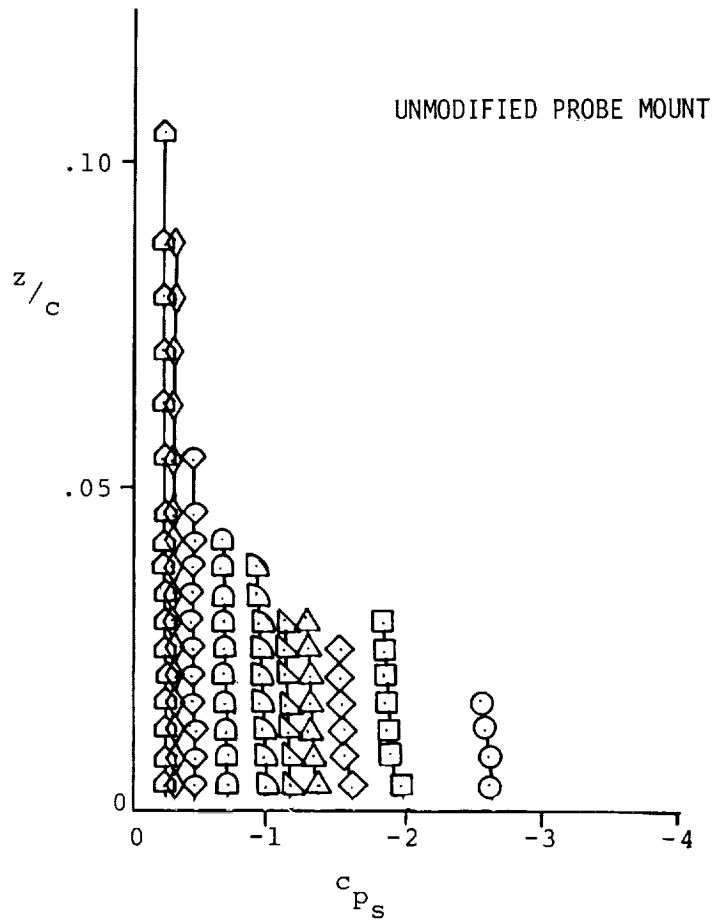
Symbol	x/c
○	.10
□	.20
◇	.30
△	.40
▴	.50
◐	.60
◑	.70
◒	.80
◓	.90
◔	1.00



(1) Pre-Stall angle of attack, $\alpha = 10.3^\circ$

Figure 12C - Static Pressure Profiles, GA(W)-2 Airfoil.

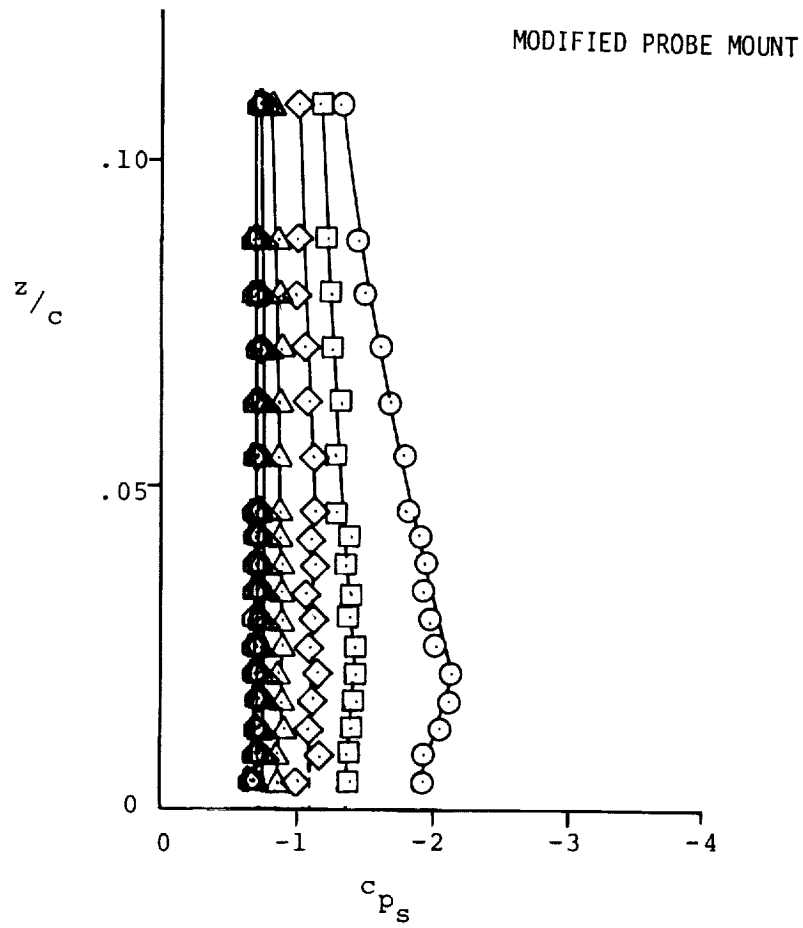
Symbol	x/c
○	.10
□	.20
◇	.30
△	.40
▴	.50
◐	.60
◑	.70
◒	.80
◅	.90
◆	1.00



(2) Near-Stall angle of attack, $\alpha = 14.4^\circ$

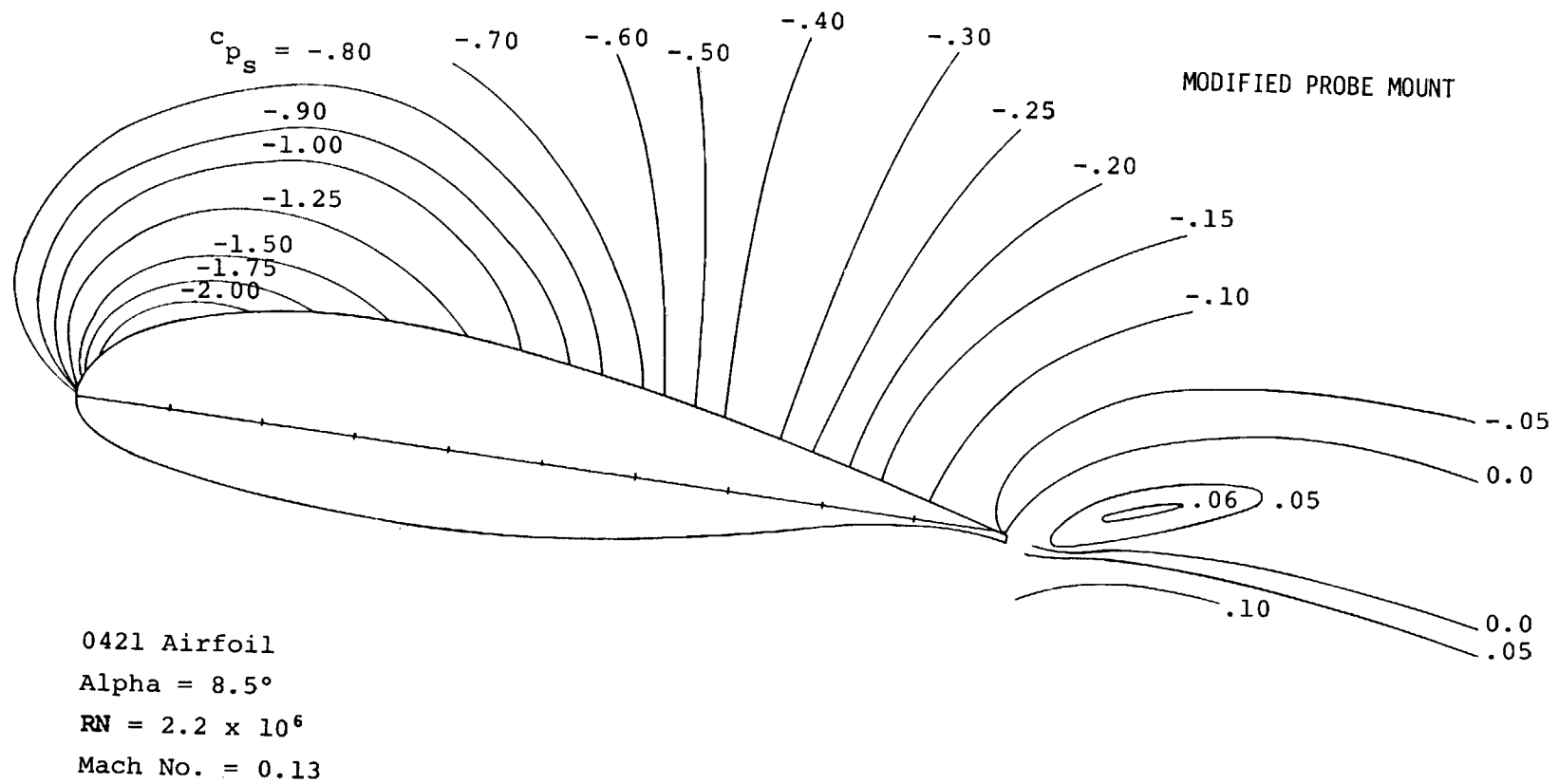
Figure 12C- Continued.

Symbol	x/c
○	.10
□	.20
◇	.30
△	.40
▴	.50
▾	.60
◐	.70
◑	.80
◒	.90
◓	1.00



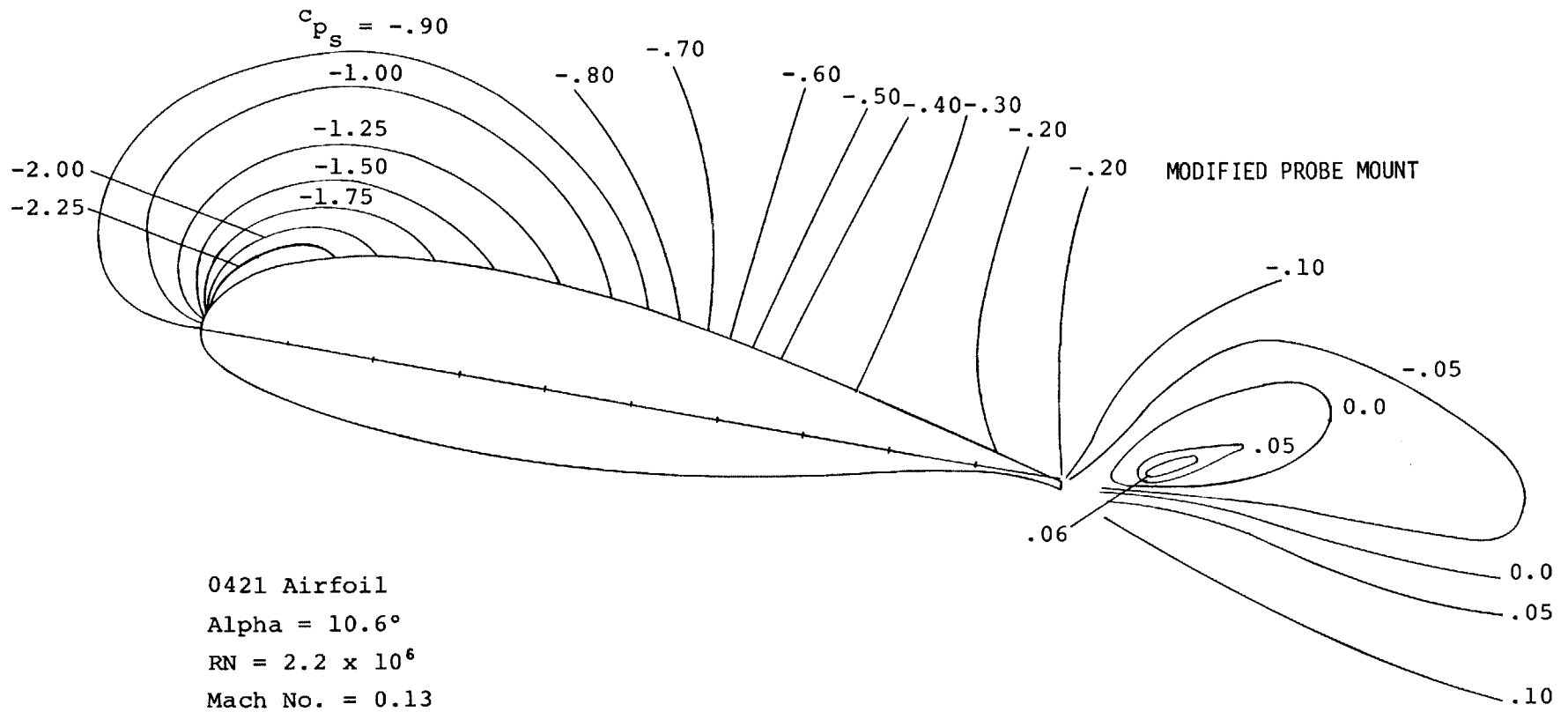
(3) Post-Stall angle of attack, $\alpha = 18.3^\circ$

Figure 12C- Concluded.



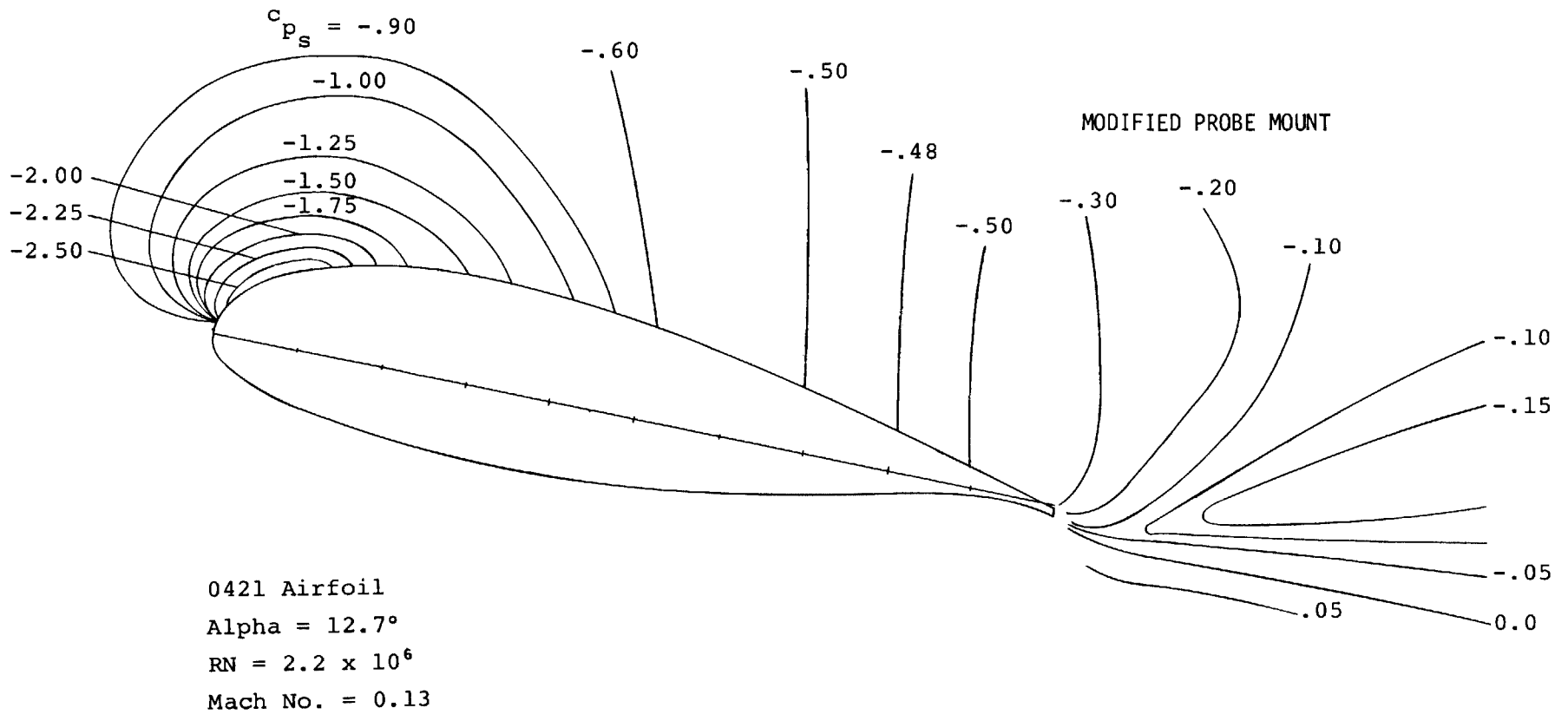
(1) Pre-stall angle of attack, $\alpha = 8.5^\circ$

Figure 13A - Static Pressure Field Contours, LS(1)-0421 Mod Airfoil.



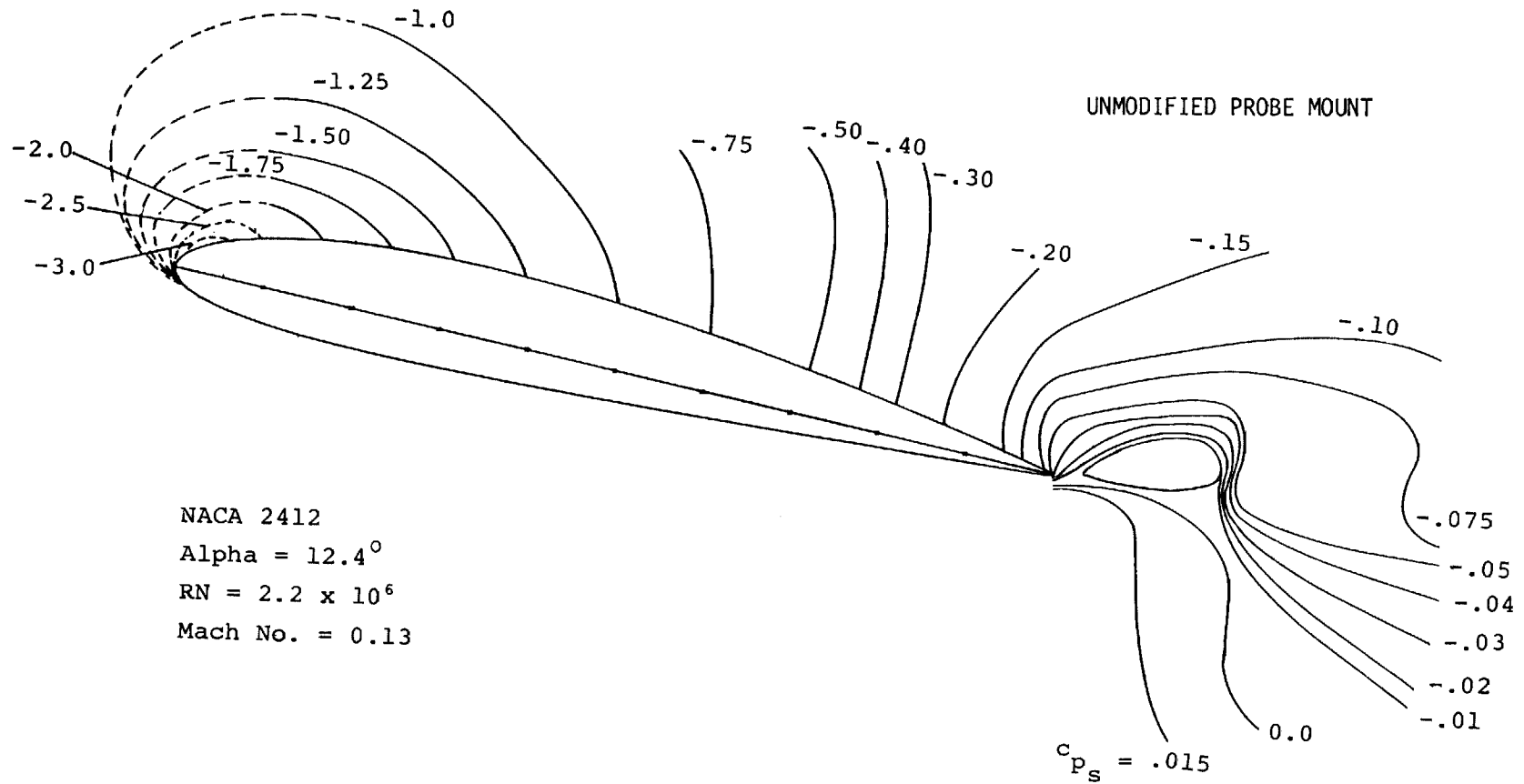
(2) Near-stall angle of attack, $\alpha = 10.6^\circ$

Figure 13A- Continued.



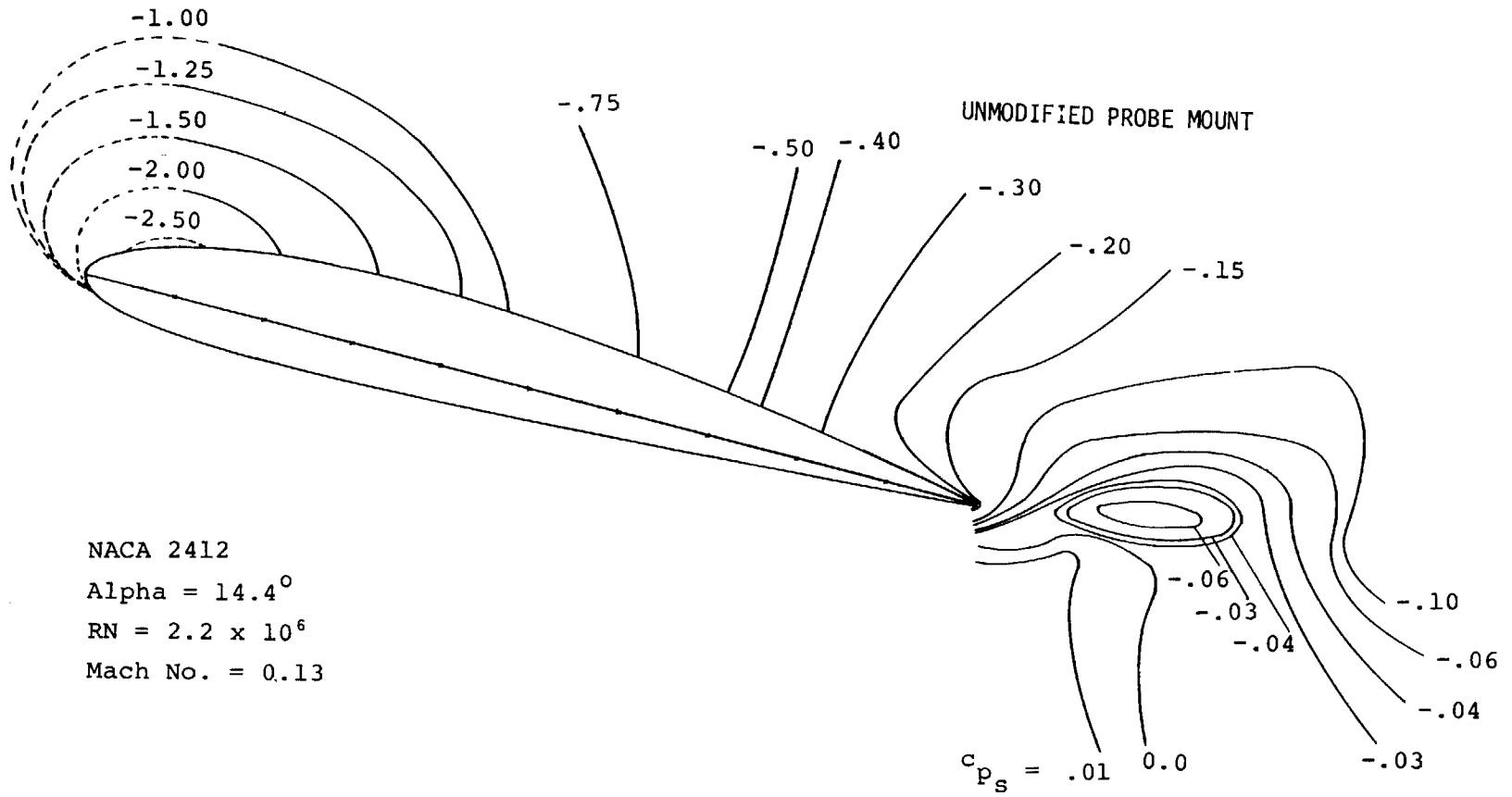
(3) Post-stall angle of attack, $\alpha = 12.7^\circ$

Figure 13A- Concluded.



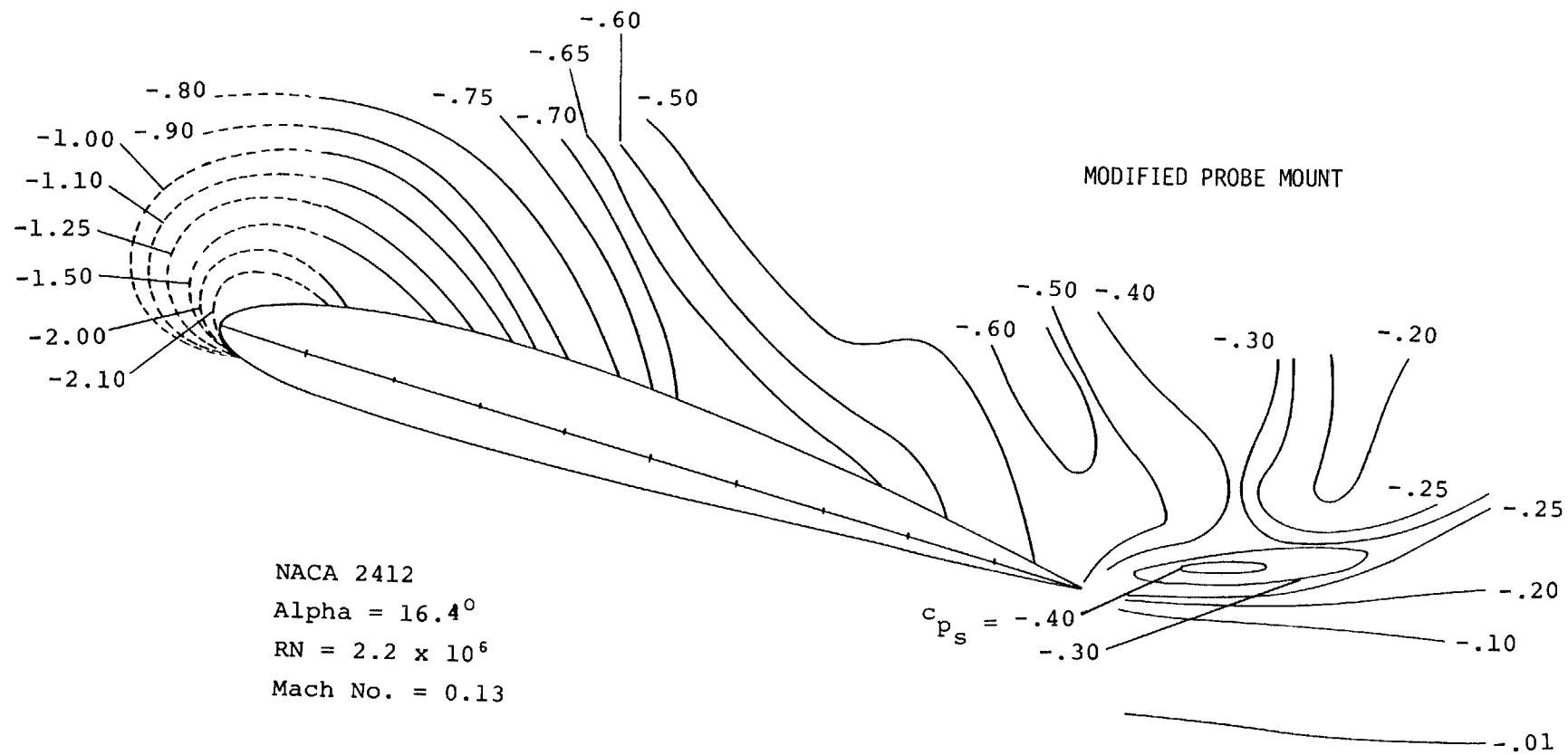
(1) Pre-stall angle of attack, $\alpha=12.4^\circ$

Figure 13B - Static Pressure Field Contours, NACA 2412 Airfoil.



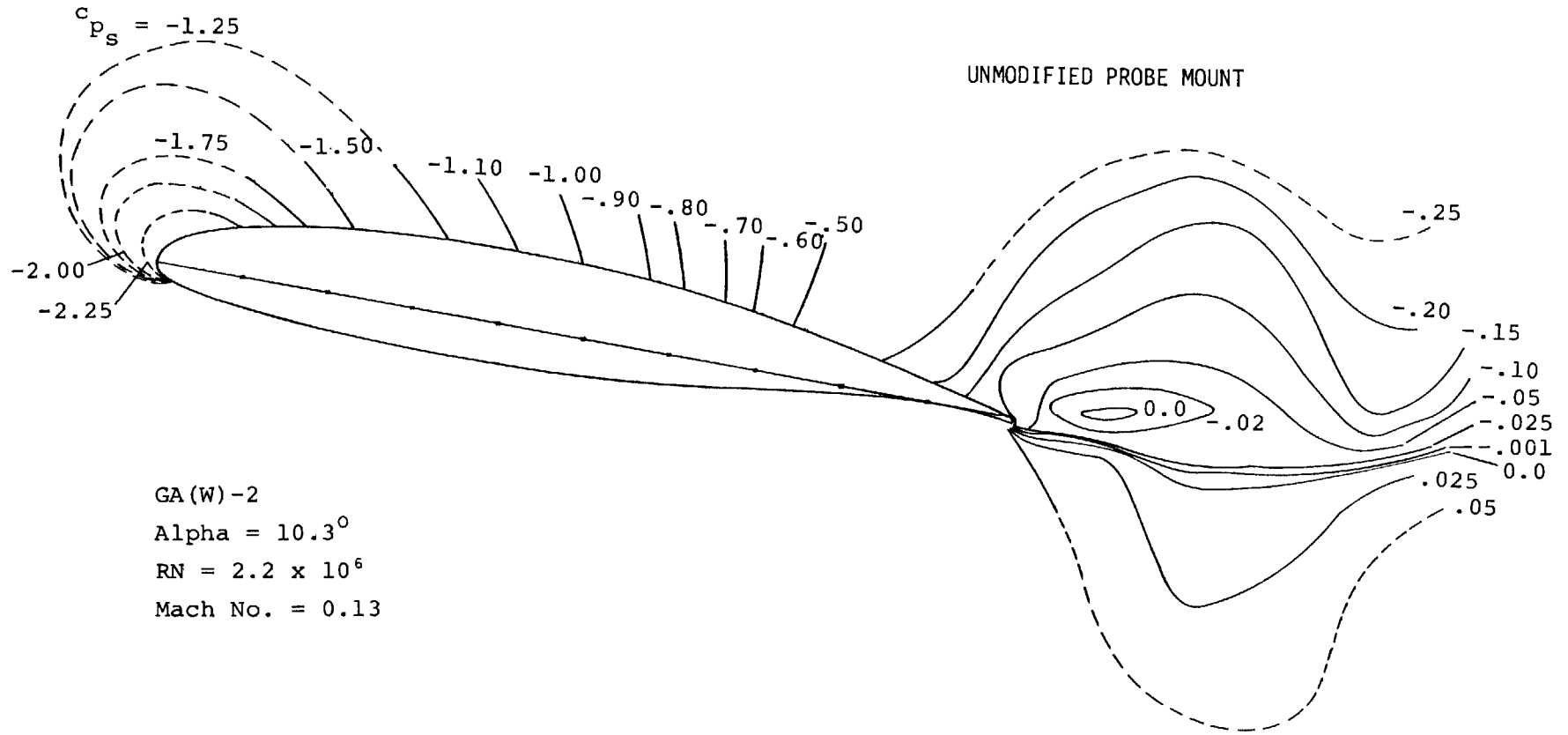
(2) Angle of attack for $c_{l_{max}}$, $\alpha=14.4^\circ$

Figure 13B- Continued.



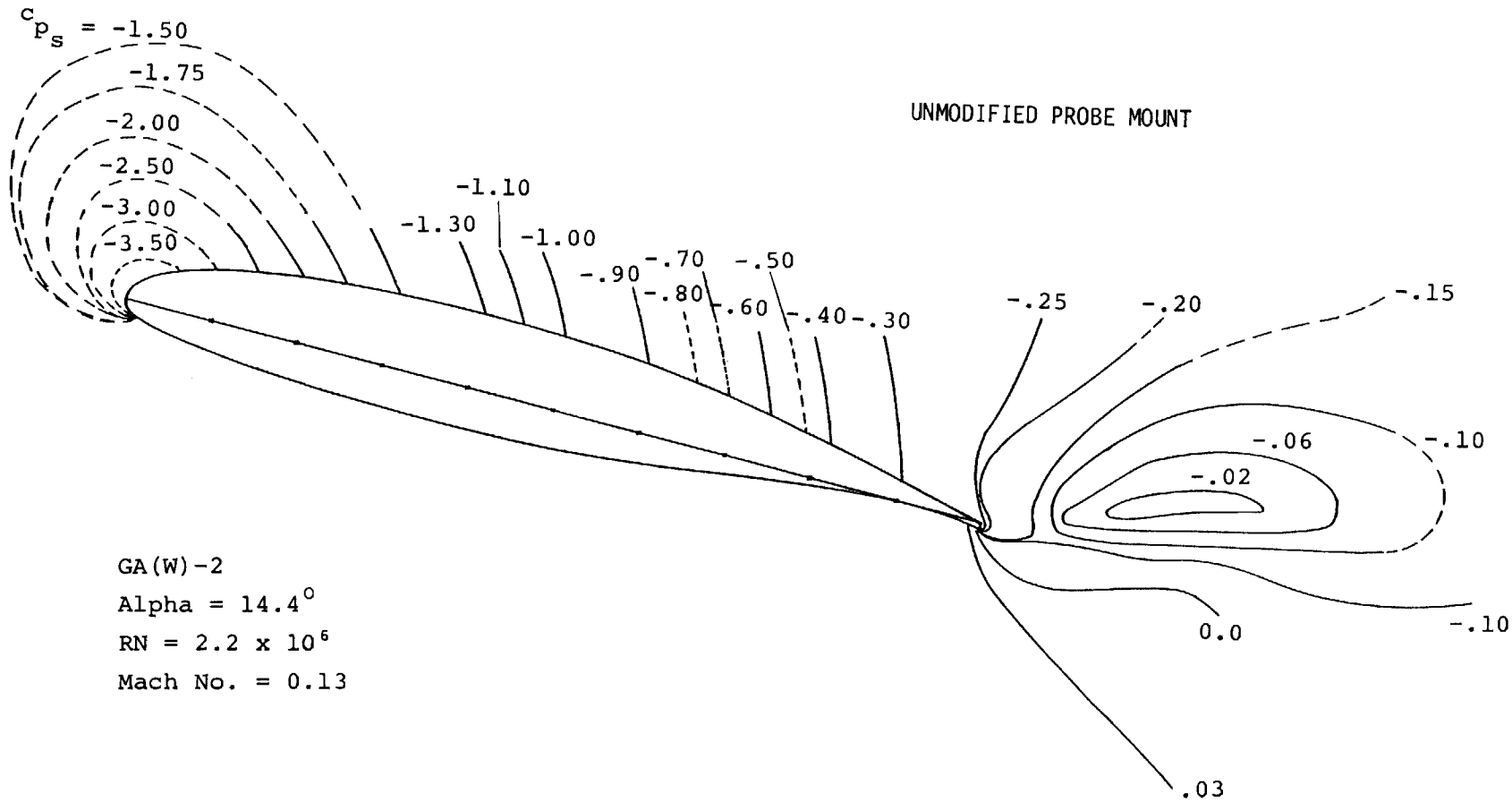
(3) Post-stall angle of attack, $\alpha = 16.4^\circ$

Figure 13B- Concluded.



(1) Pre-Stall angle of attack, $\alpha = 10.3^\circ$

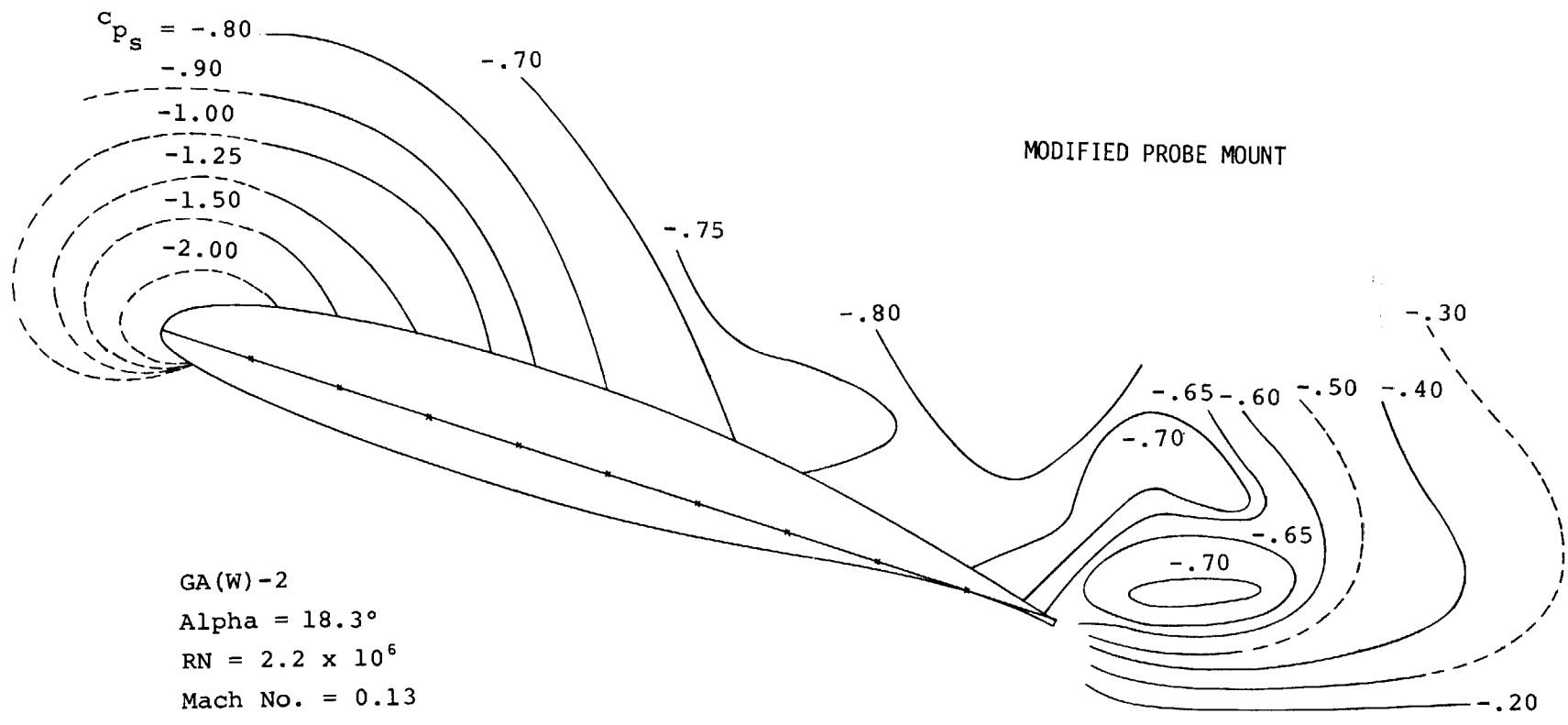
Figure 13C - Static Pressure Field Contours, GA(W)-2 Airfoil.



(2) Near-Stall angle of attack, $\alpha = 14.4^\circ$

Figure 13C- Continued.

96



GA(W)-2
Alpha = 18.3°
RN = 2.2 x 10⁶
Mach No. = 0.13

(3) Post-Stall angle of attack, $\alpha = 18.3^\circ$

Figure 13C- Concluded.

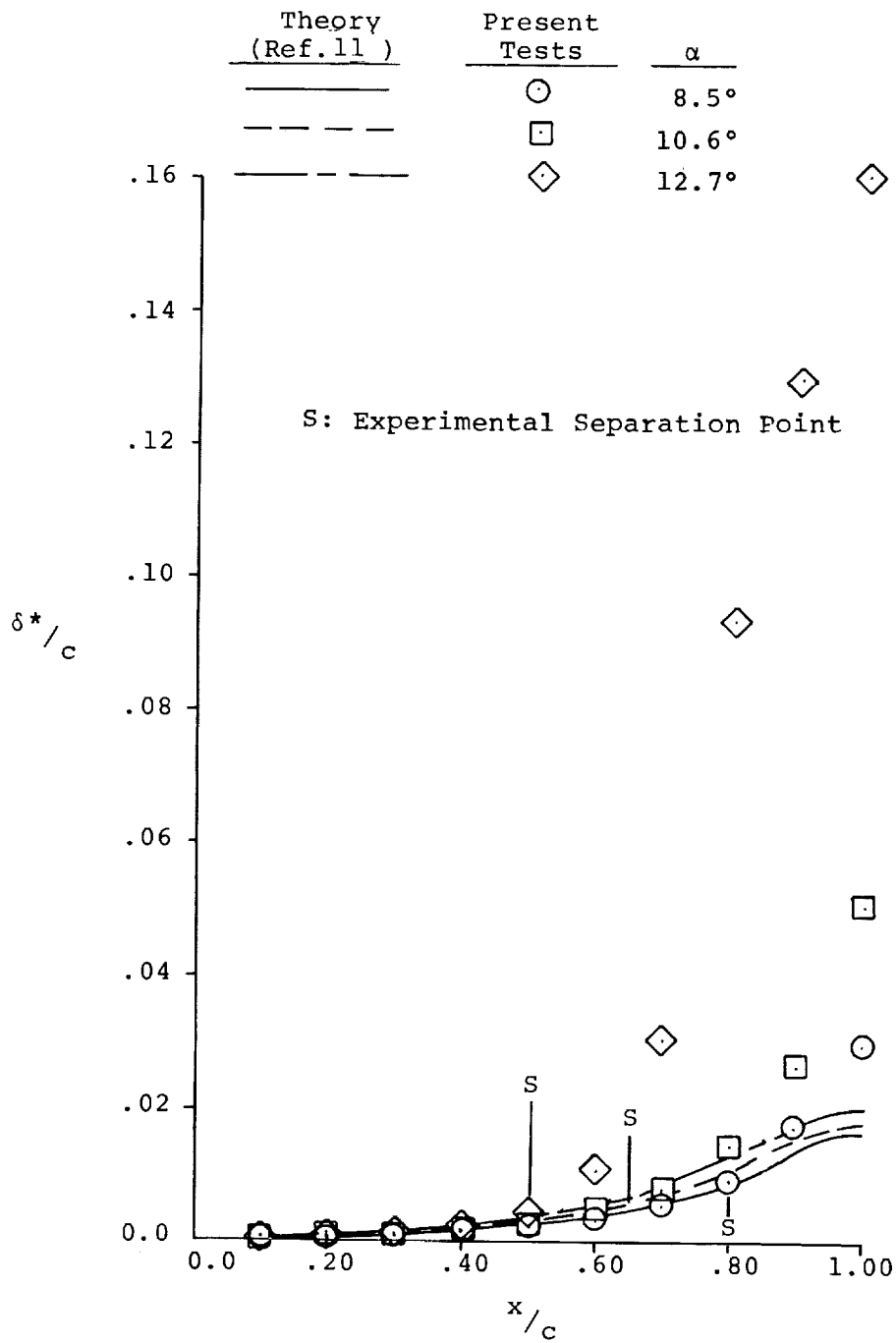


Figure 14A - Boundary Layer Displacement Thickness, LS(1)-0421 Mod Airfoil.

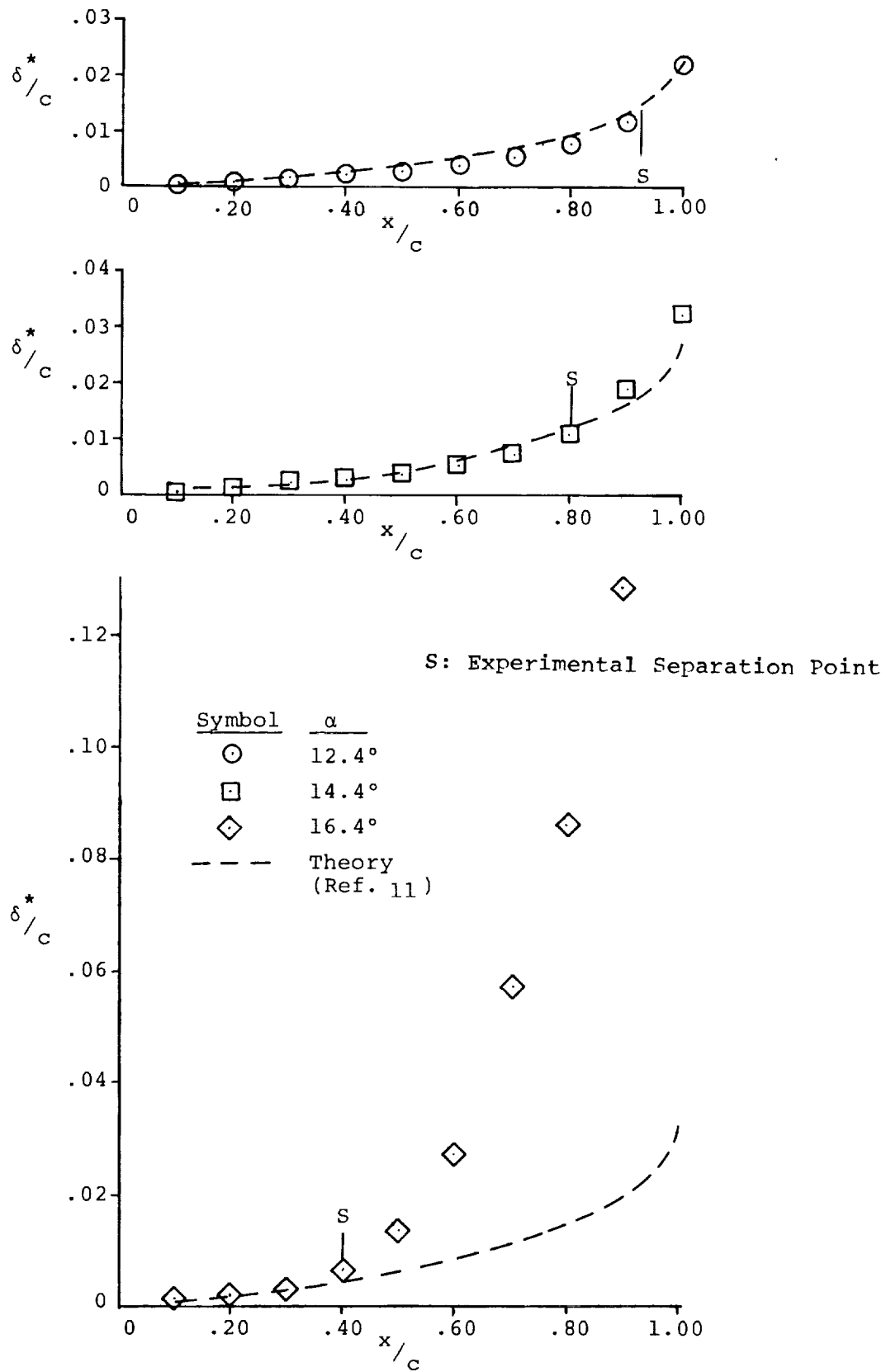


Figure 14B - Boundary Layer Displacement Thickness, NACA 2412 Airfoil.

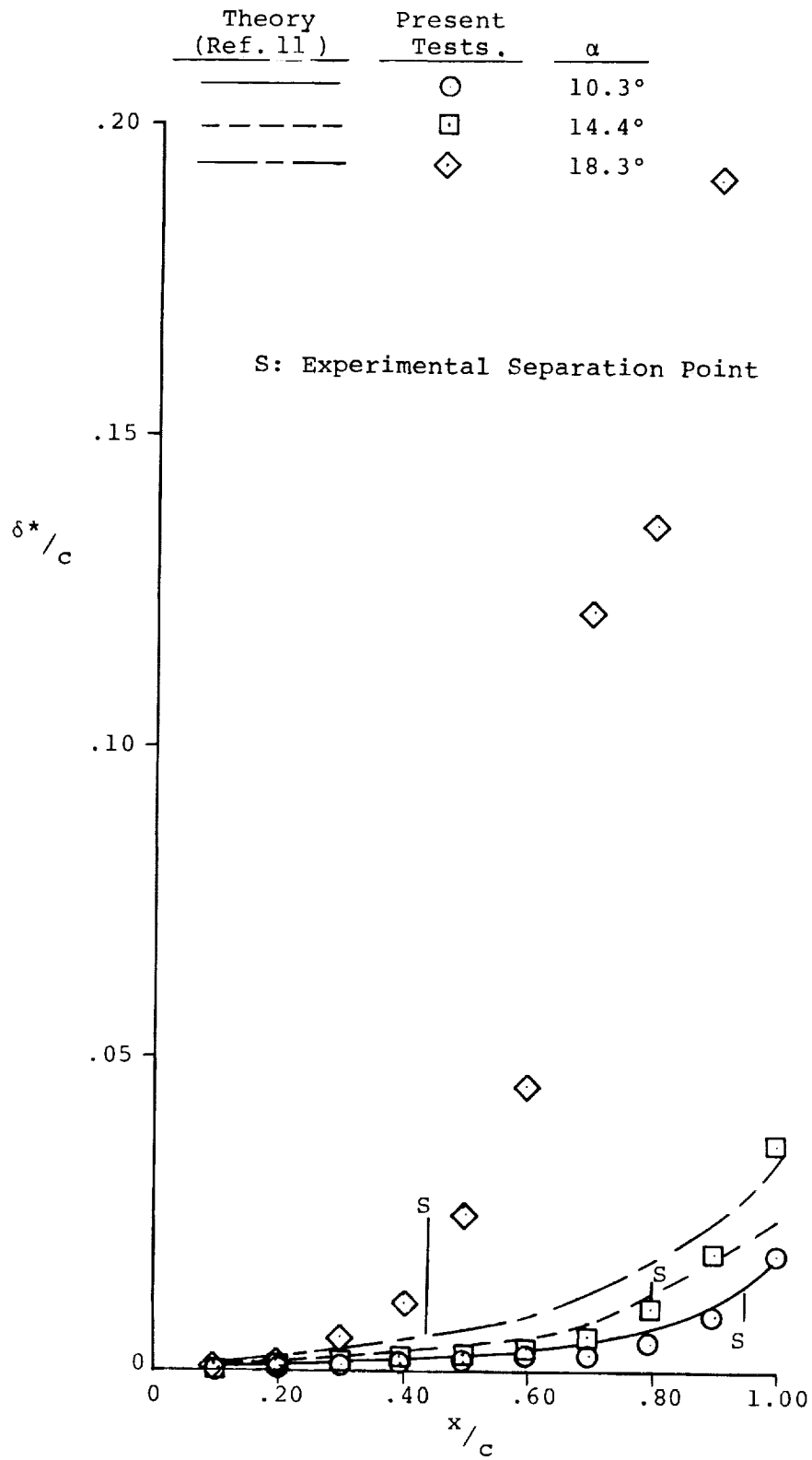


Figure 14C- Boundary Layer Displacement Thickness, GA(W)-2 Airfoil.

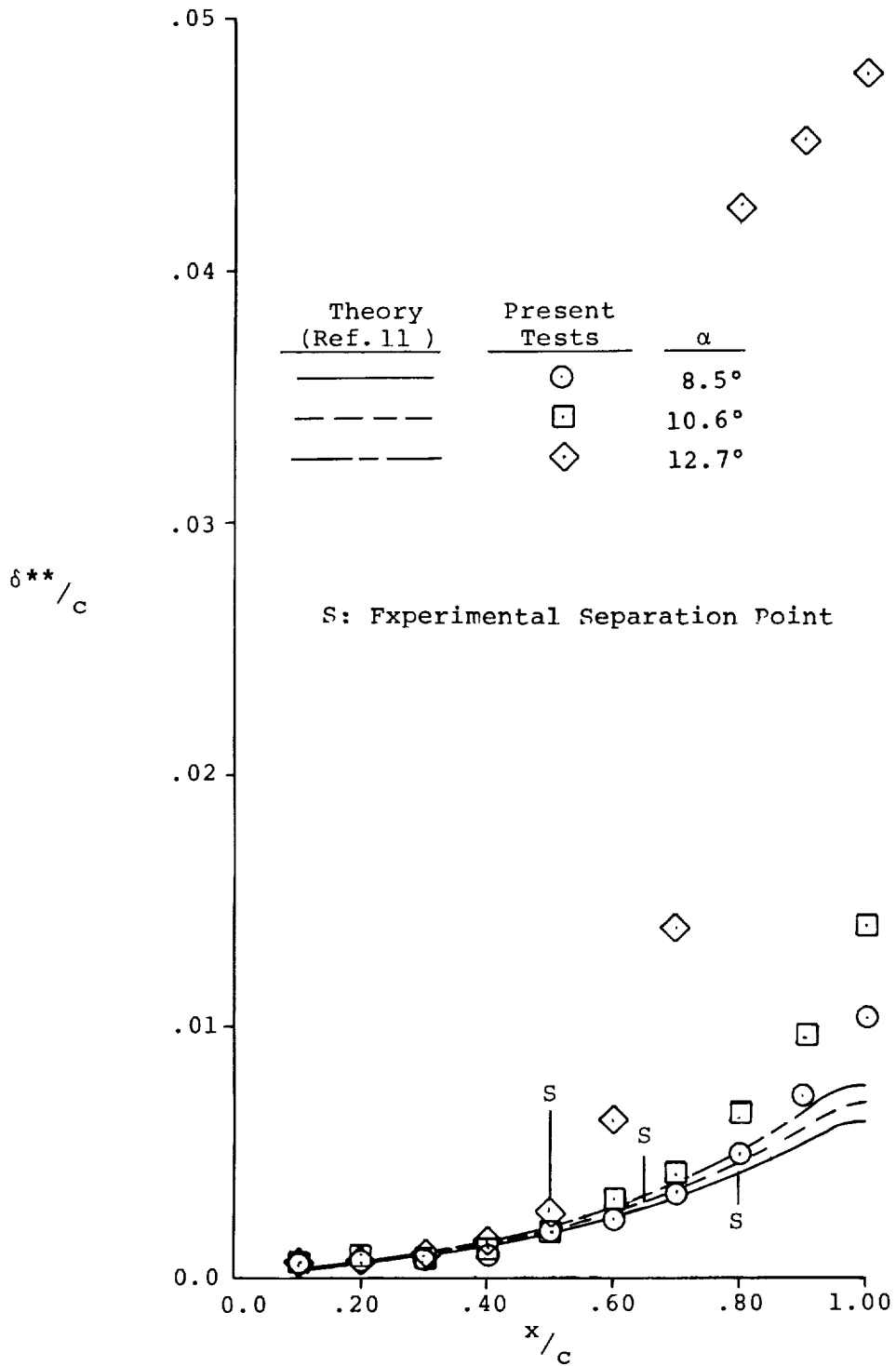


Figure 15A - Boundary Layer Momentum Thickness, LS(1)-0421 Mod Airfoil.

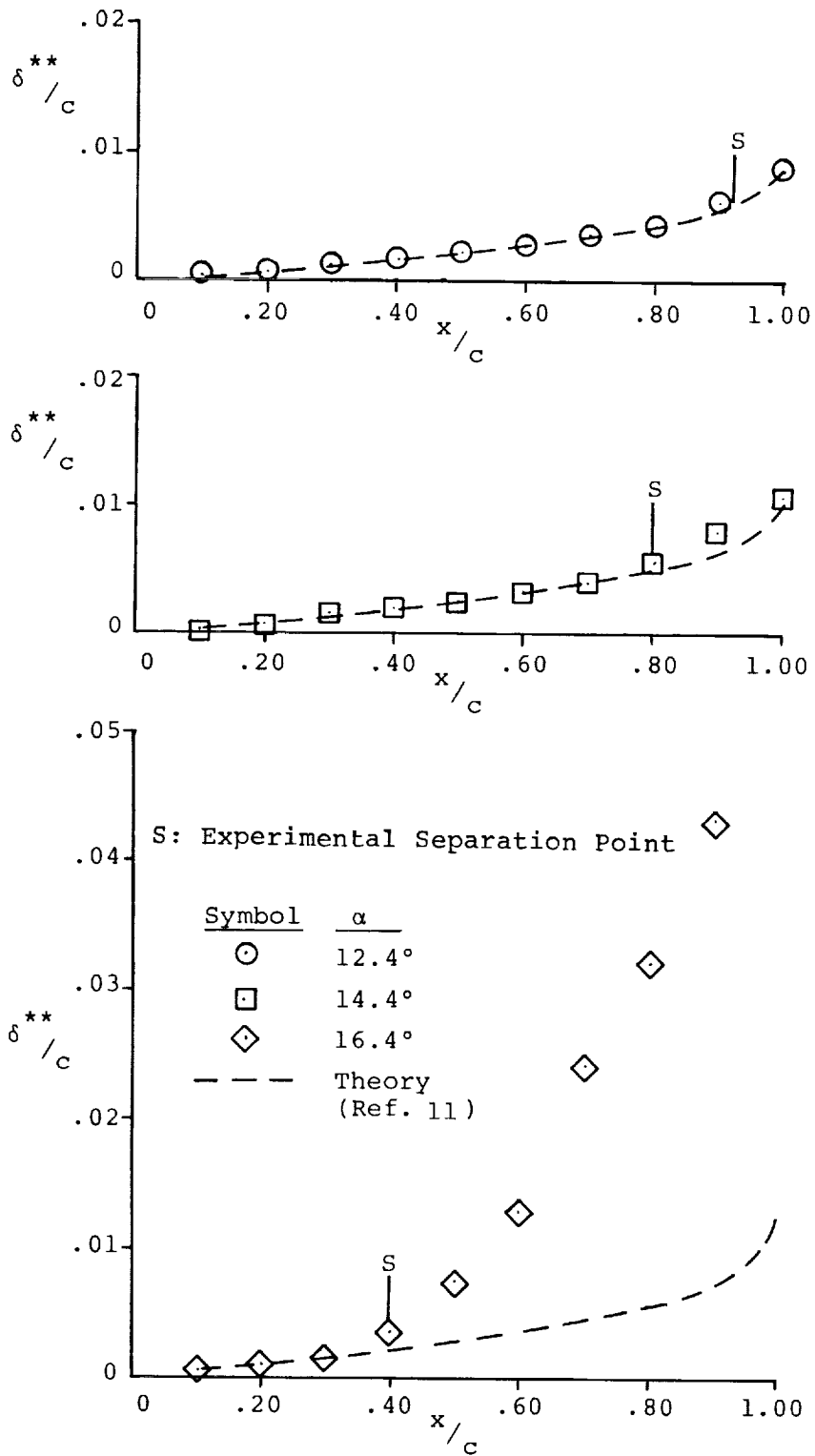


Figure 15B - Boundary Layer Momentum Thickness, NACA 2412 Airfoil.

Theory (Ref. 11)	Present Tests	α
—————	○	10.3°
- - - - -	□	14.4°
- - - - -	◇	18.3°

S: Experimental Separation Point

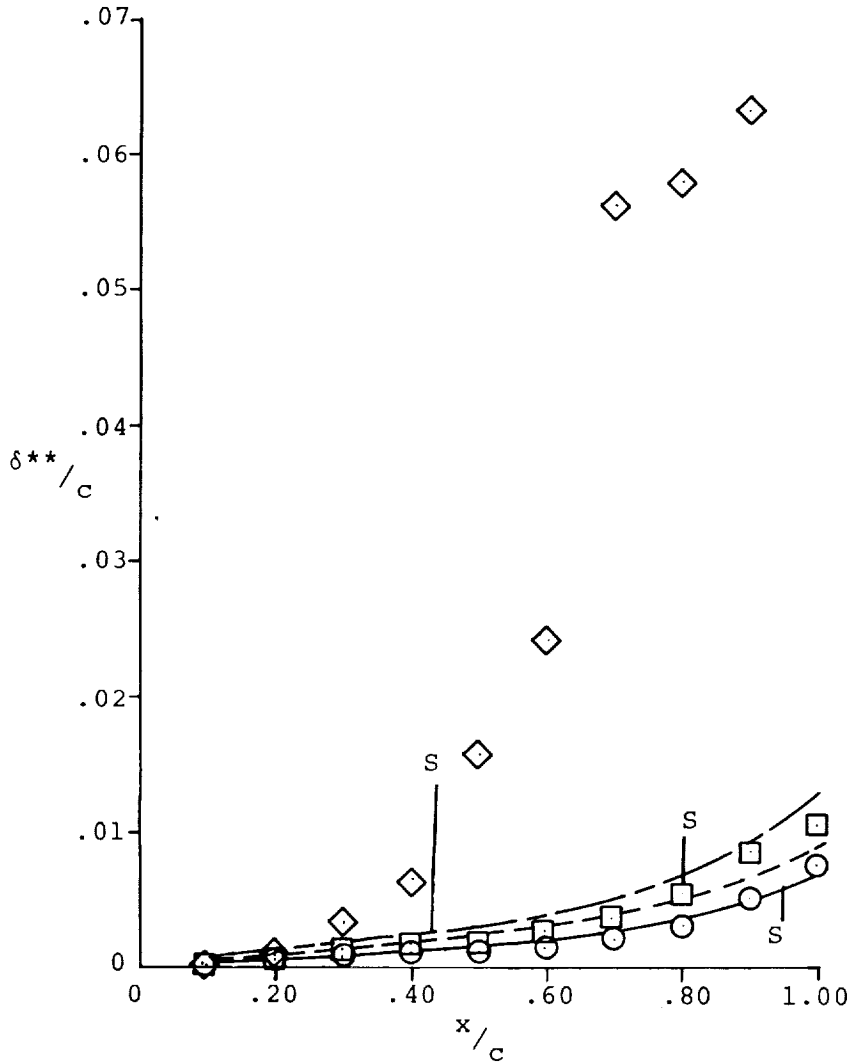


Figure 15C- Boundary Layer Momentum Thickness, GA(W)-2 Airfoil.

Theory (Ref. 11)	Present Tests	α
—————	○	8.5°
- - - - -	□	10.6°
- - - - -	◇	12.7°

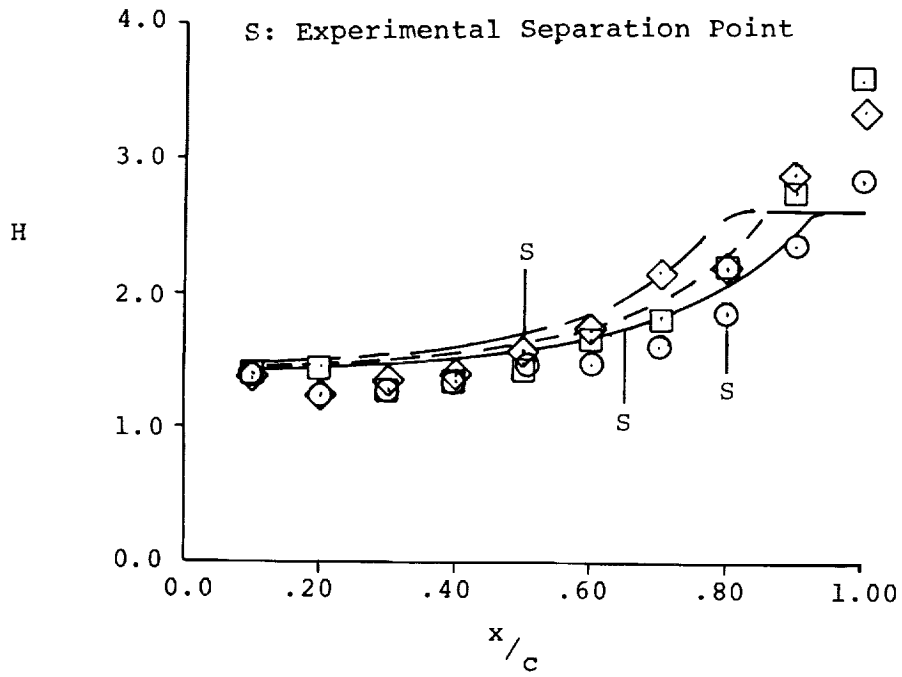


Figure 16A - Boundary Layer Shape Factor, LS(1)-0421 Mod Airfoil.

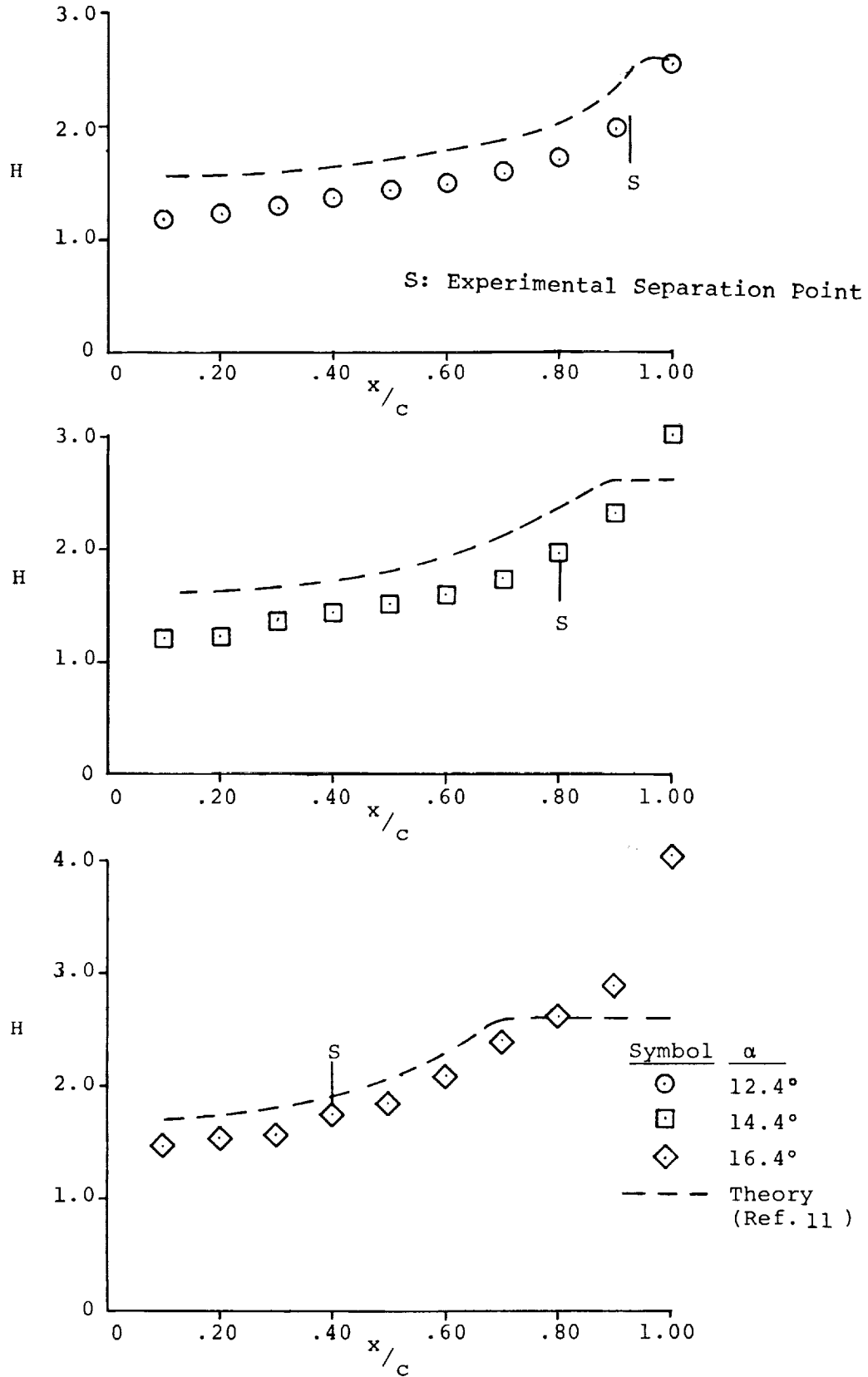


Figure 16B - Boundary Layer Shape Factor, NACA 2412 Airfoil.

Theory (Ref. 11)	Present Tests	α
—————	⊙	10.3°
- - - - -	⊠	14.4°
- · - · -	◇	18.3°

S: Experimental Separation Point

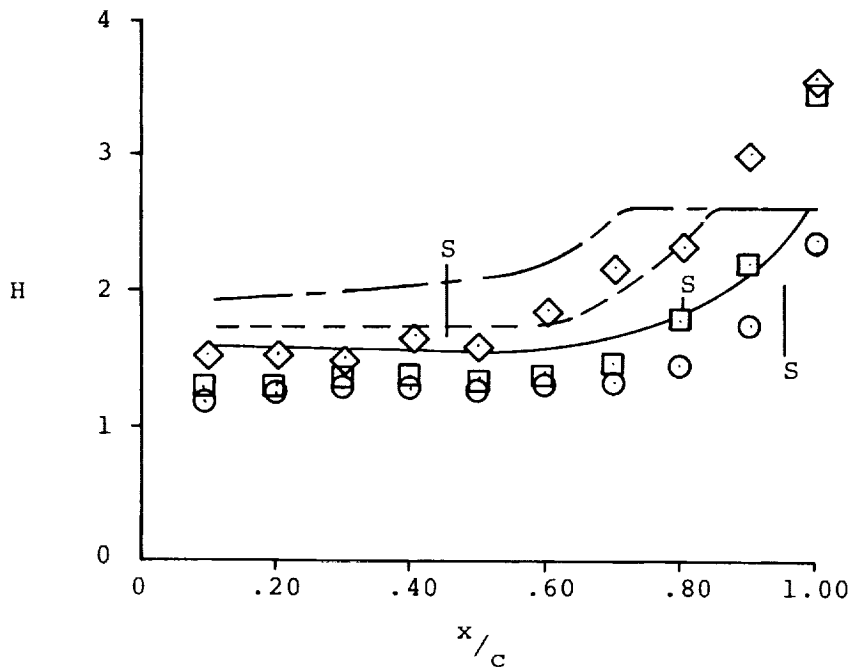


Figure 16C- Boundary Layer Shape Factor, GA(W)-2 Airfoil.

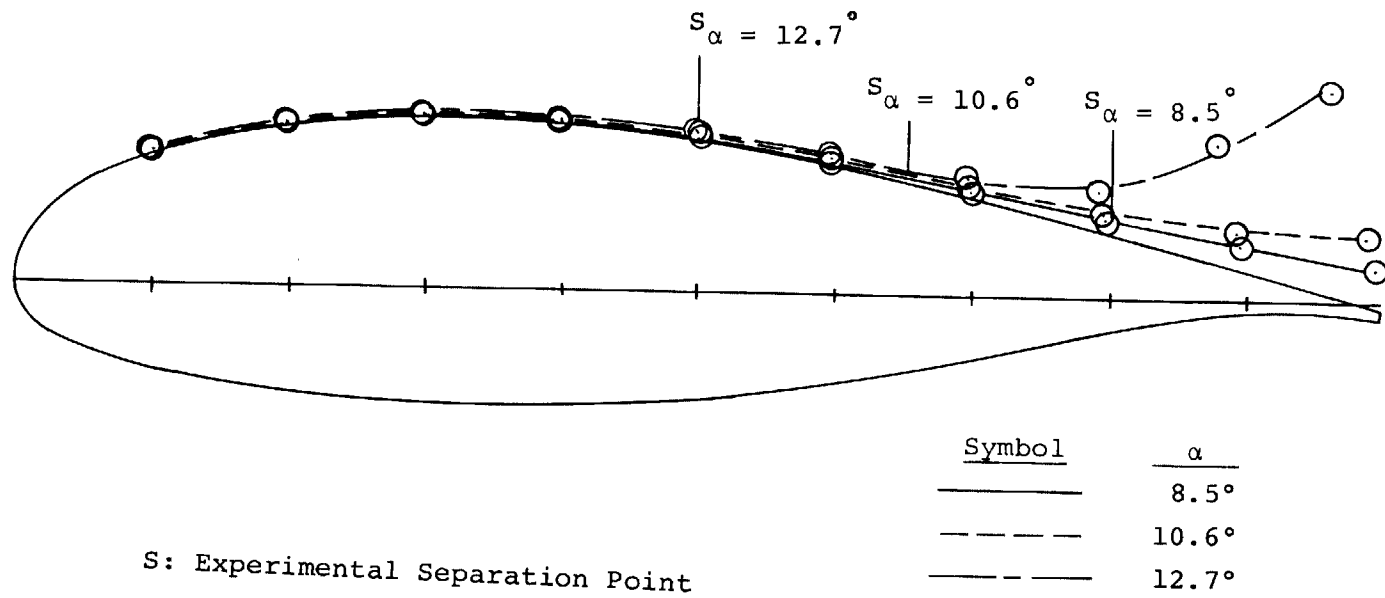


Figure 17A - Boundary Layer Displacement Thickness Distribution, LS(1)-0421 Mod Airfoil.

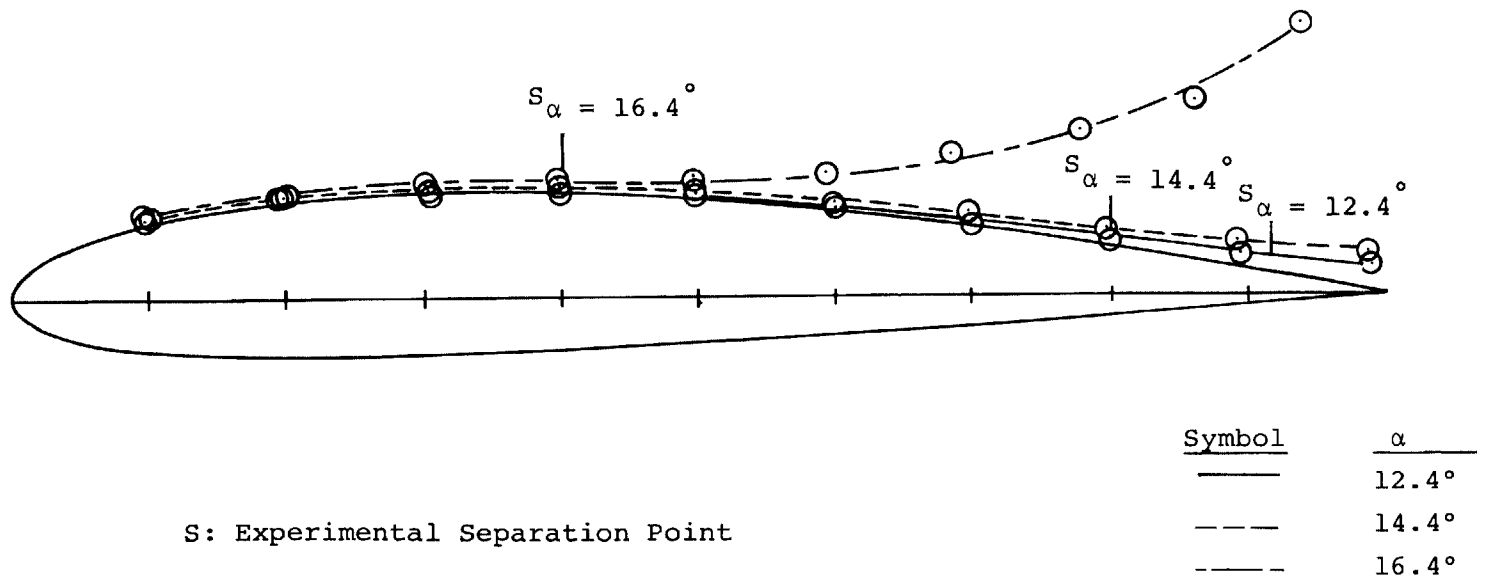


Figure 17B - Boundary Layer Displacement Thickness Distribution, NACA 2412 Airfoil.

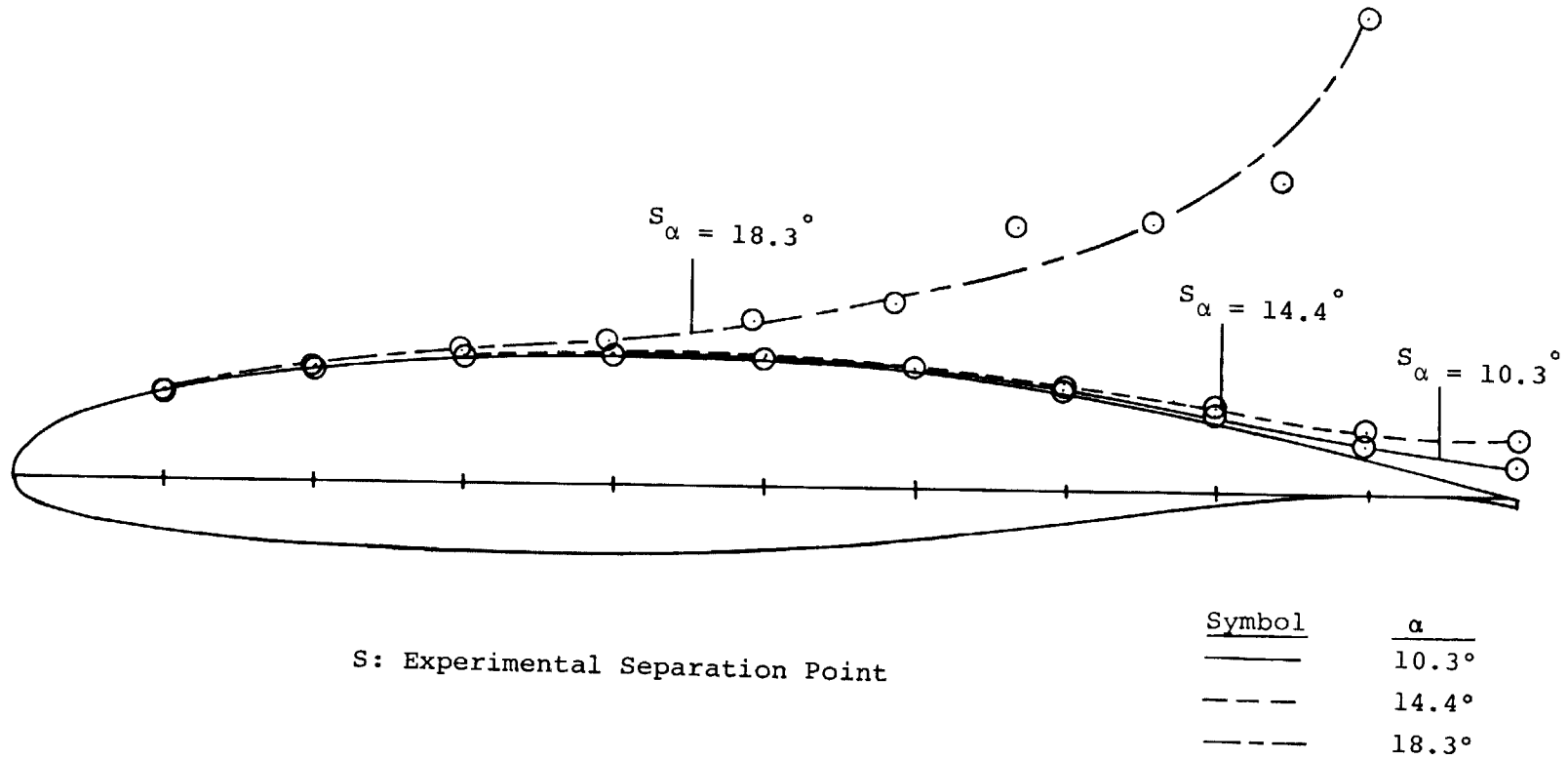


Figure 17C- Boundary Layer Displacement Thickness Distribution, GA(W)-2 Airfoil.

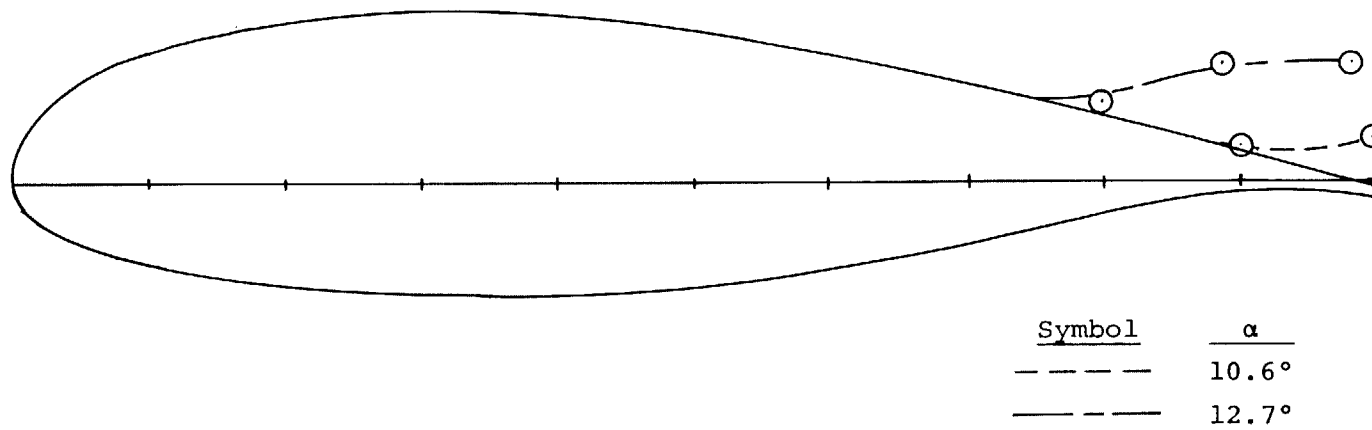


Figure 18A - Separation Streamlines, LS(1)-0421 Mod Airfoil.

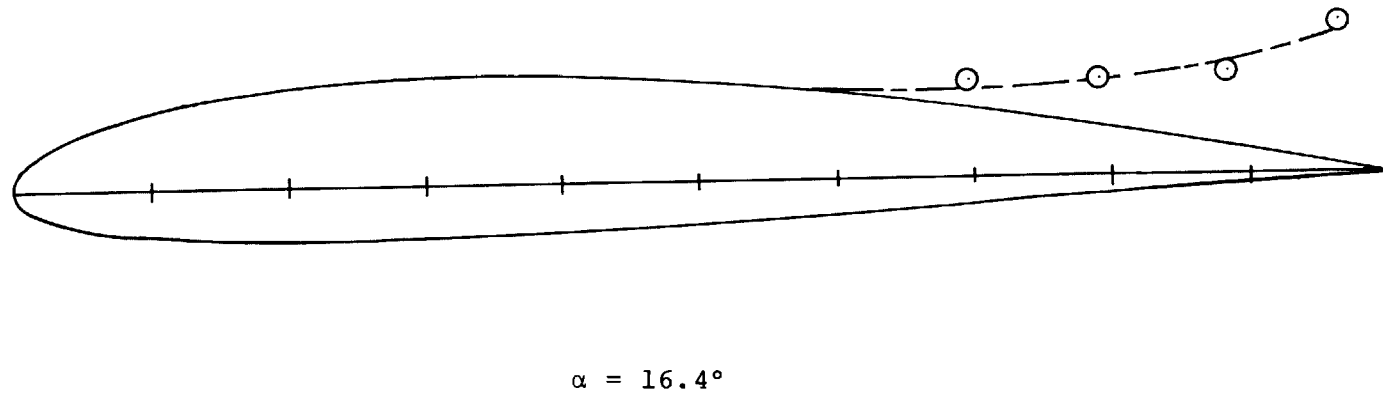


Figure 18B - Separation Streamline, NACA 2412 Airfoil.

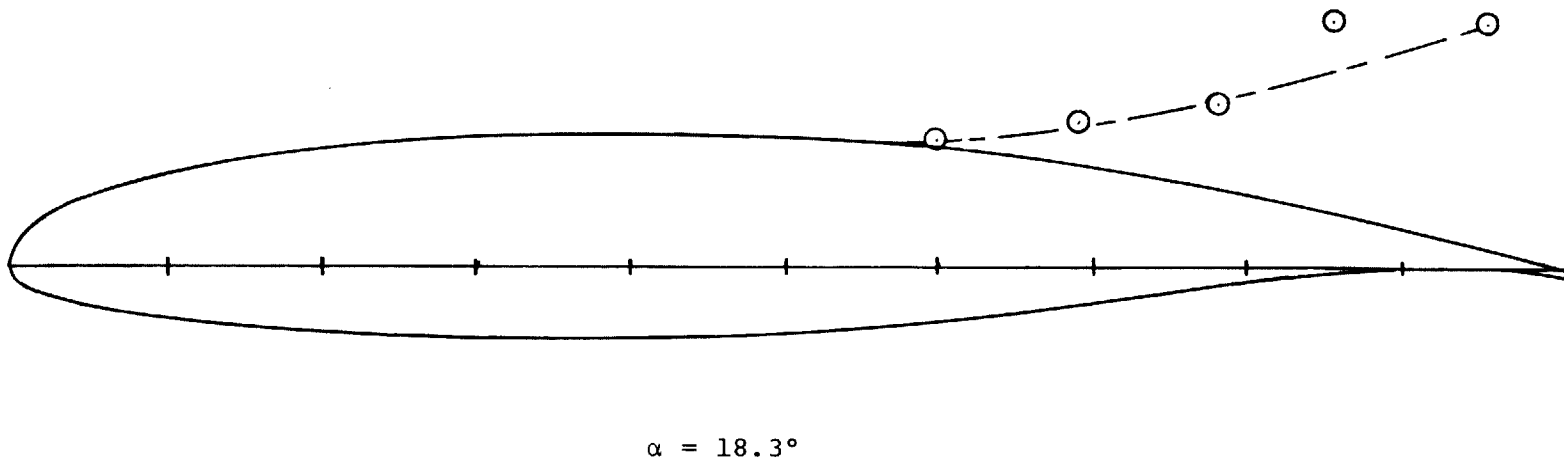
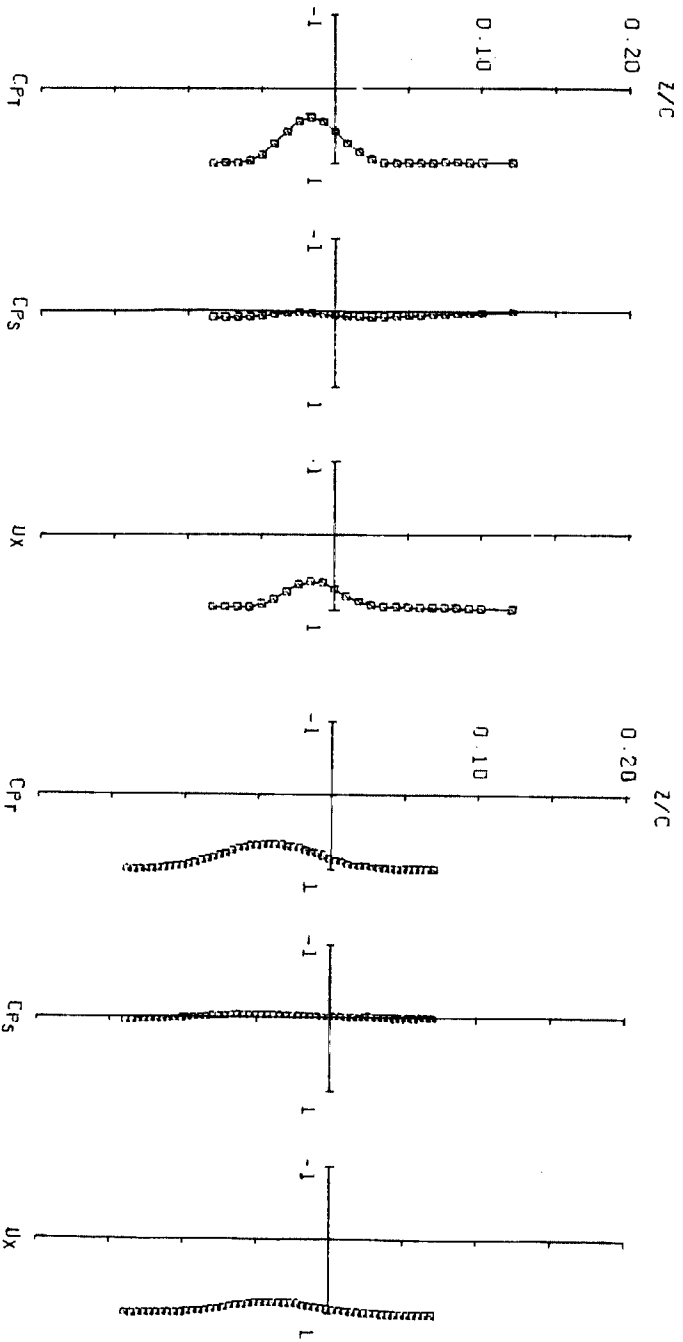
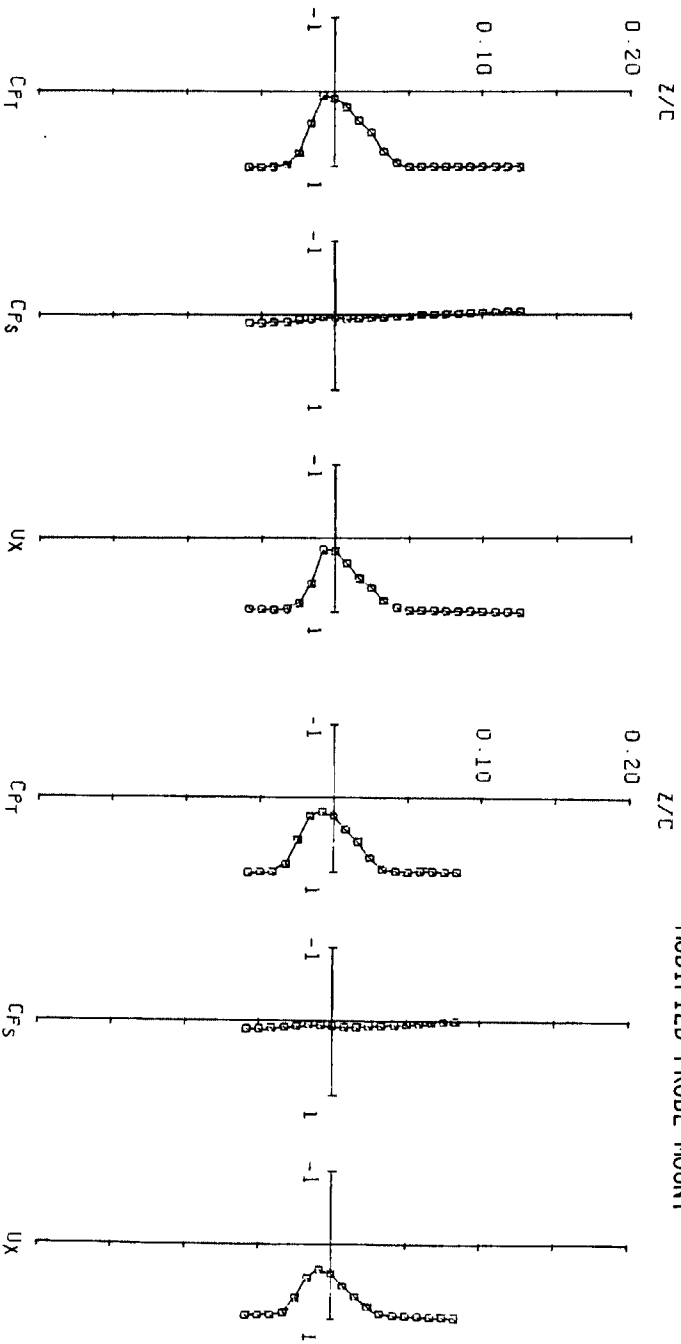


Figure 18C- Separation Streamline, GA(W) - 2 Airfoil.

MODIFIED PROBE MOUNT

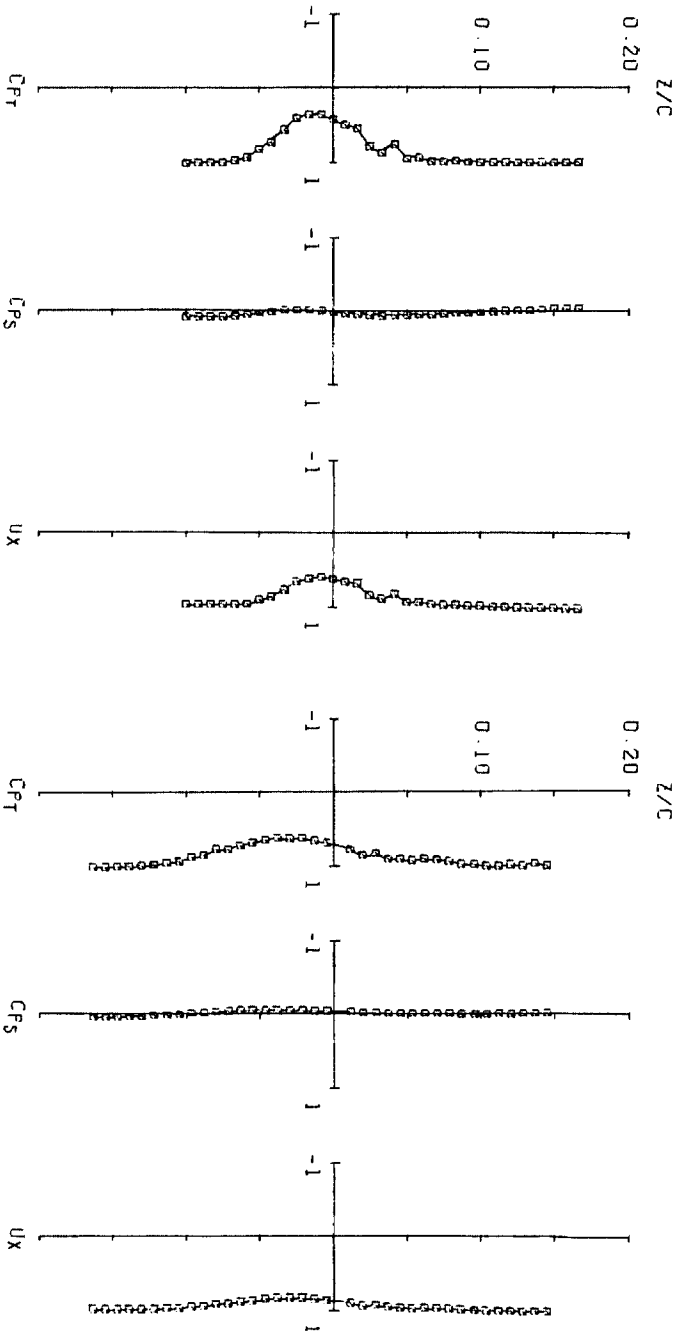
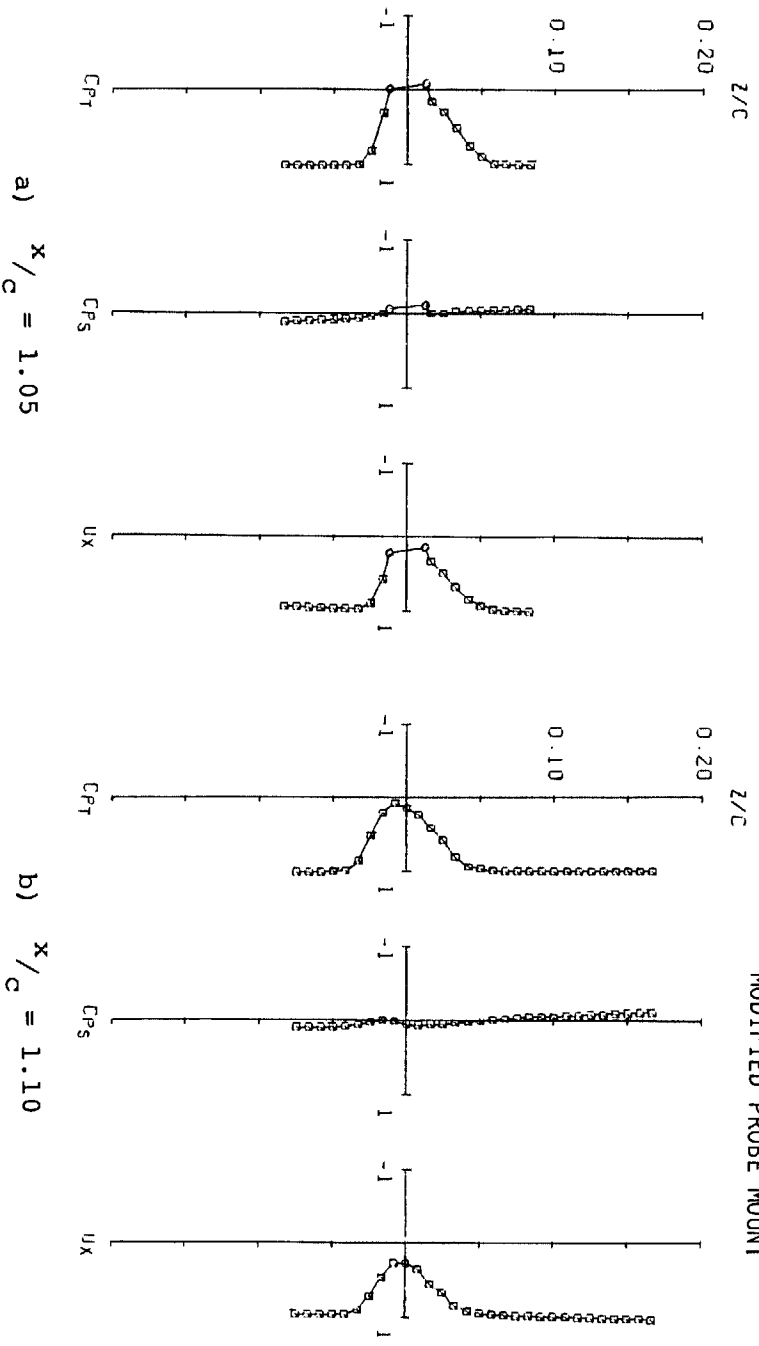


c) $x/c = 1.20$
 d) $x/c = 1.50$
 (1) Pre-stall angle of attack, $\alpha = 8.5^\circ$
 Figure 19A - Velocity and Pressure Distributions in the Wake,
 IS(1)-0421 Mod Airfoil

□ - Five Tube

○ - Four Tube

MODIFIED PROBE MOUNT

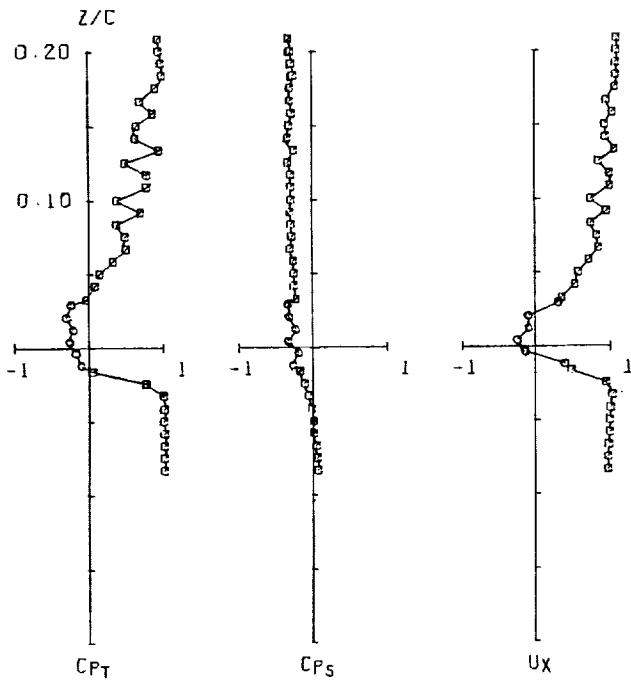


(2) Near-stall angle of attack, $\alpha = 10.6^\circ$
Figure 19A - Continued.

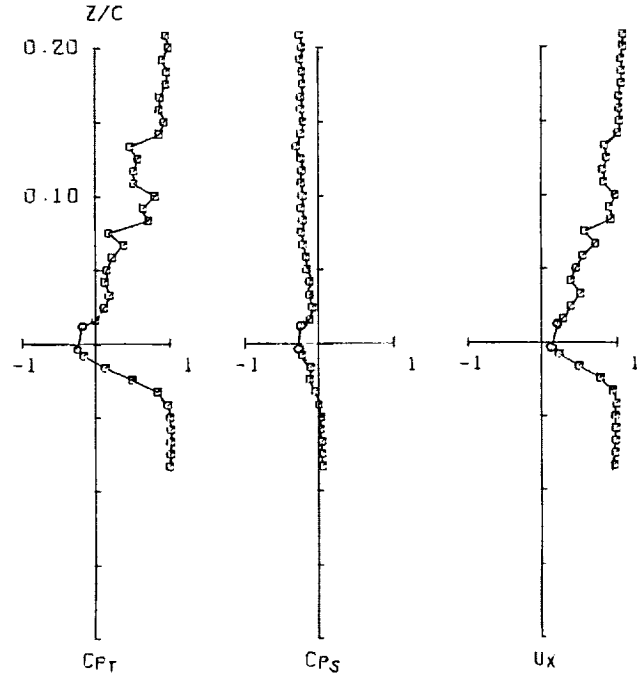
□ - Five Tube

○ - Four Tube

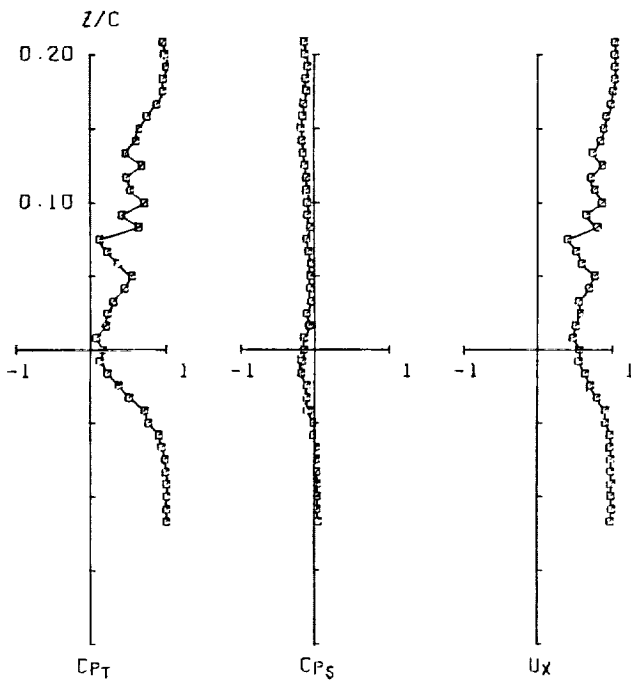
MODIFIED PROBE MOUNT



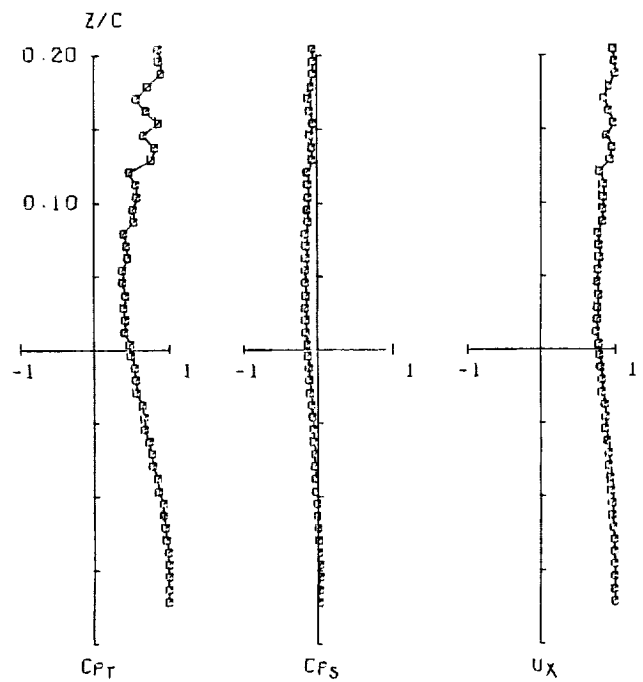
a) $x/c = 1.05$



b) $x/c = 1.10$



c) $x/c = 1.20$



d) $x/c = 1.50$

(3) Post-stall angle of attack, $\alpha = 12.7^\circ$

Figure 19A- Concluded.

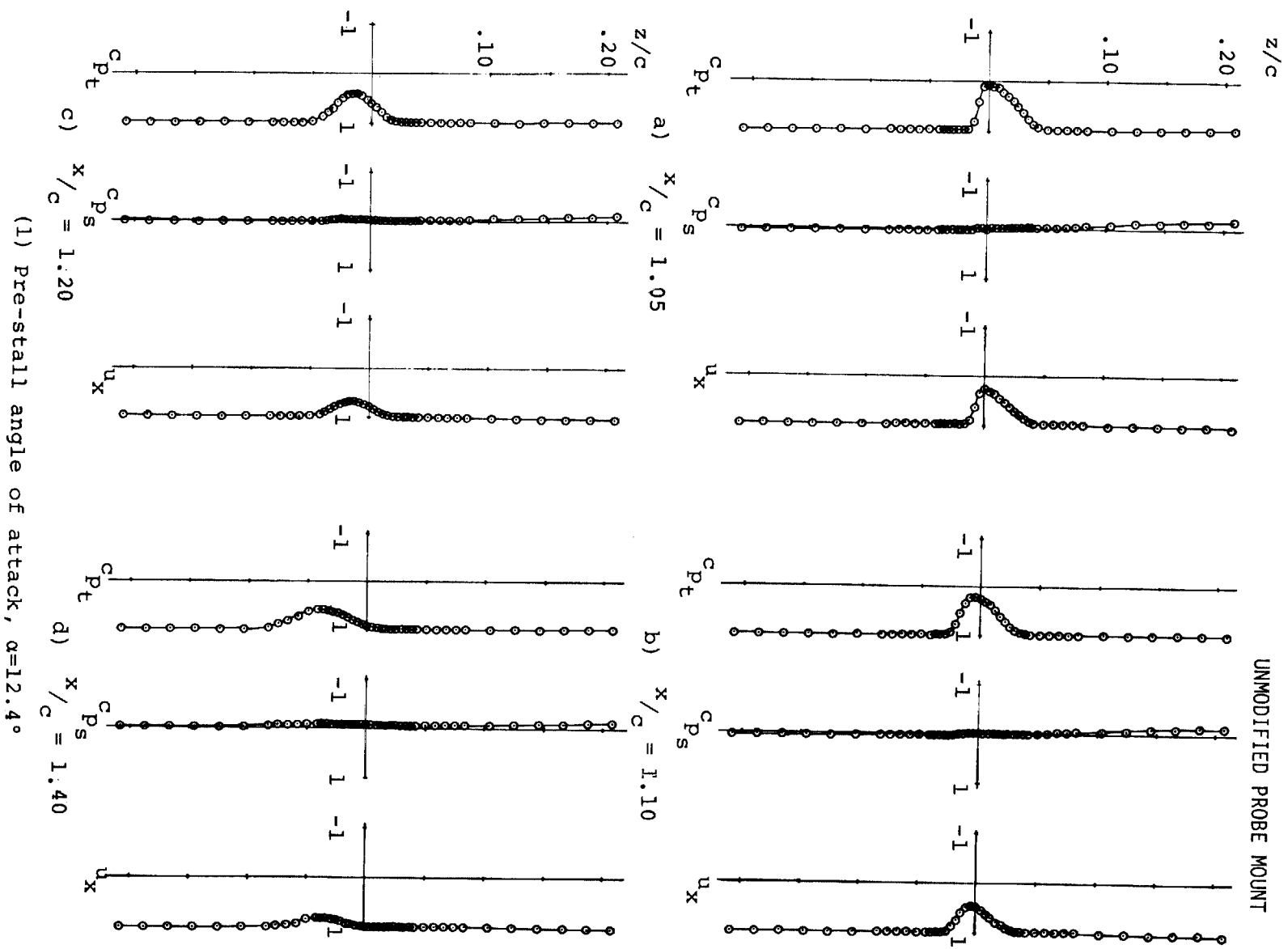
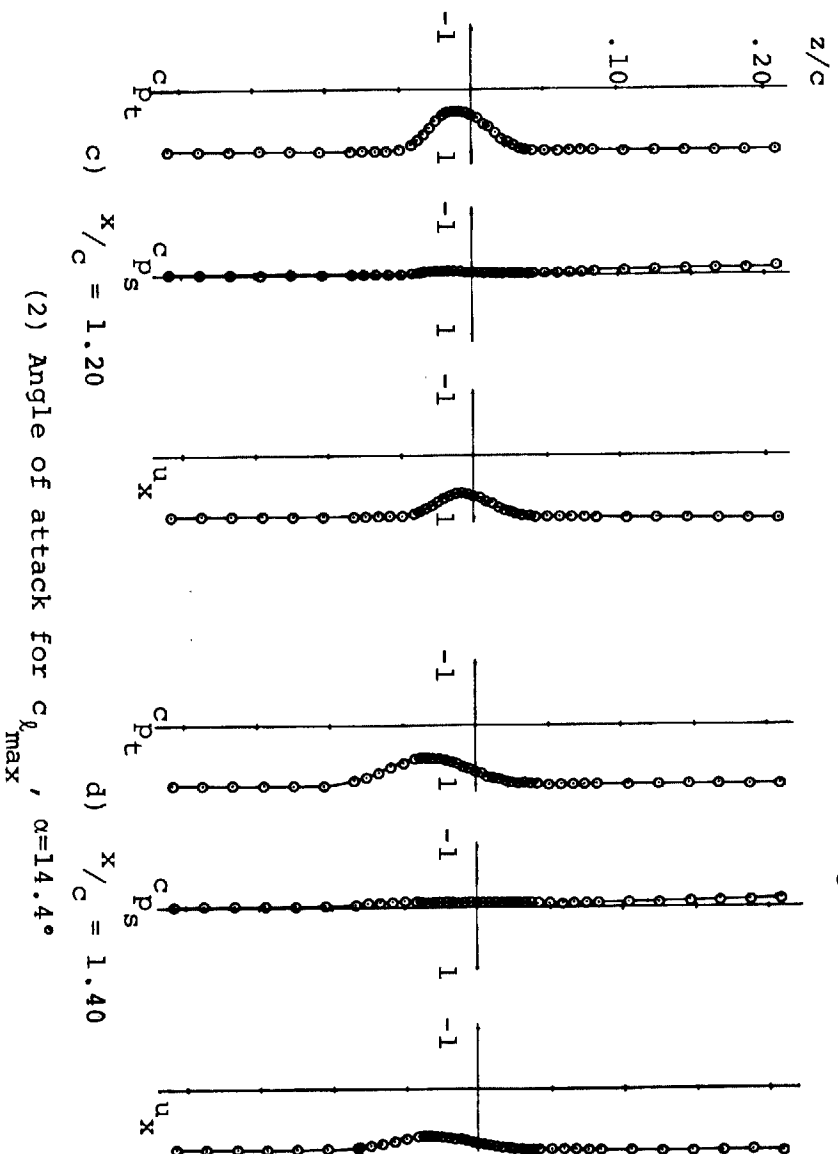
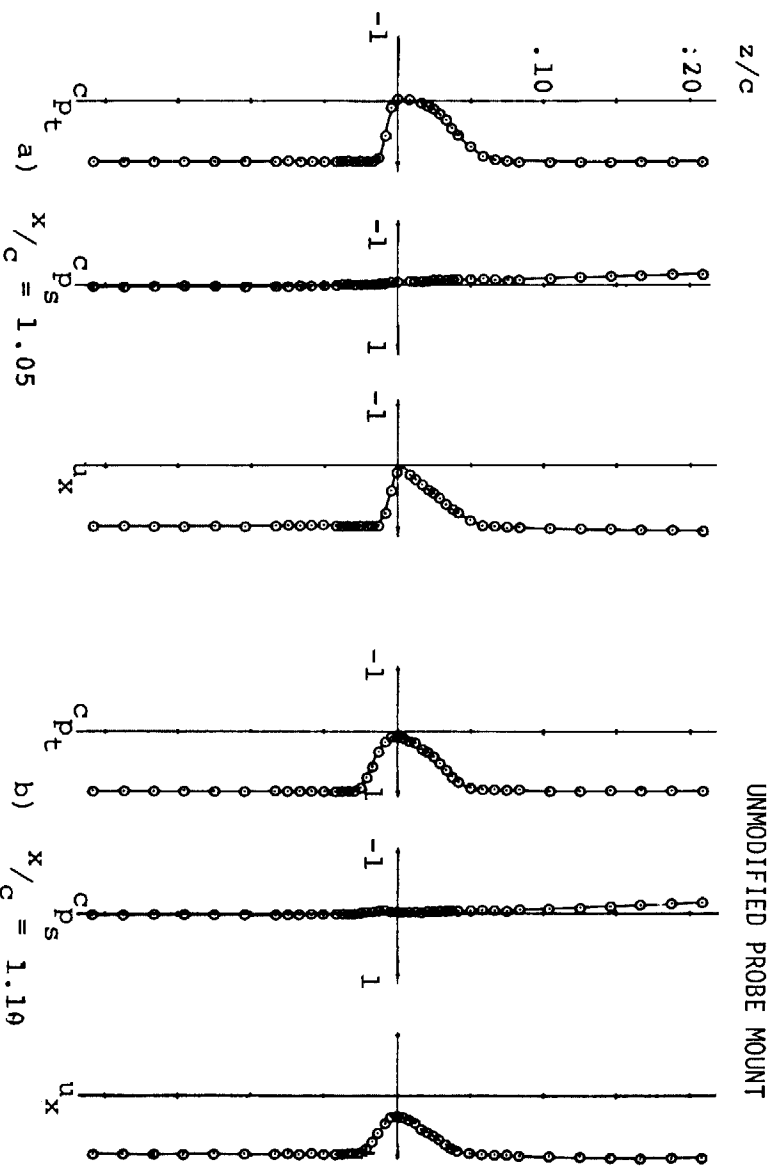


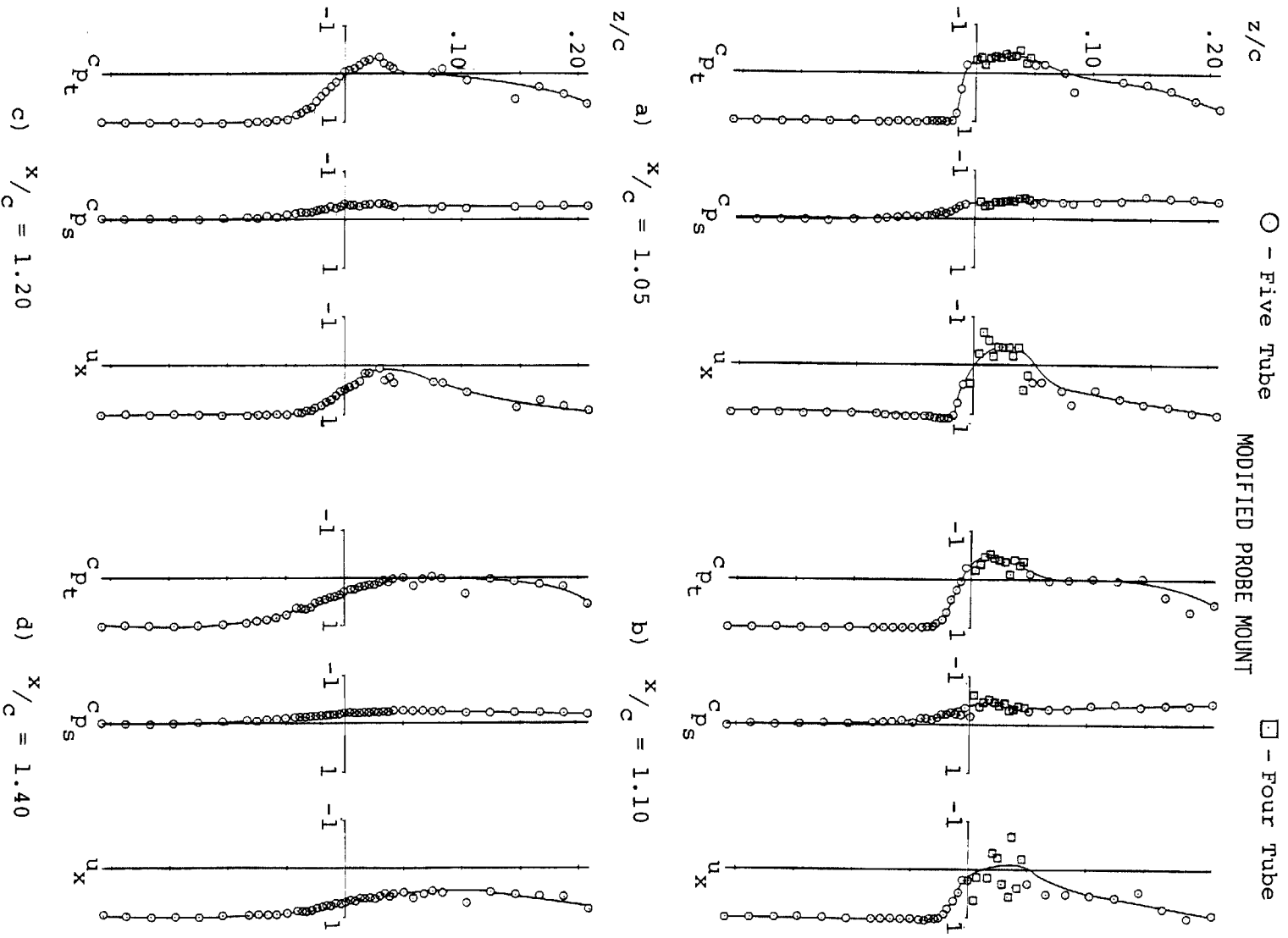
Figure 19B - Velocity and Pressure, Distributions in the Wake,
NACA 2412 Airfoil.

UNMODIFIED PROBE MOUNT



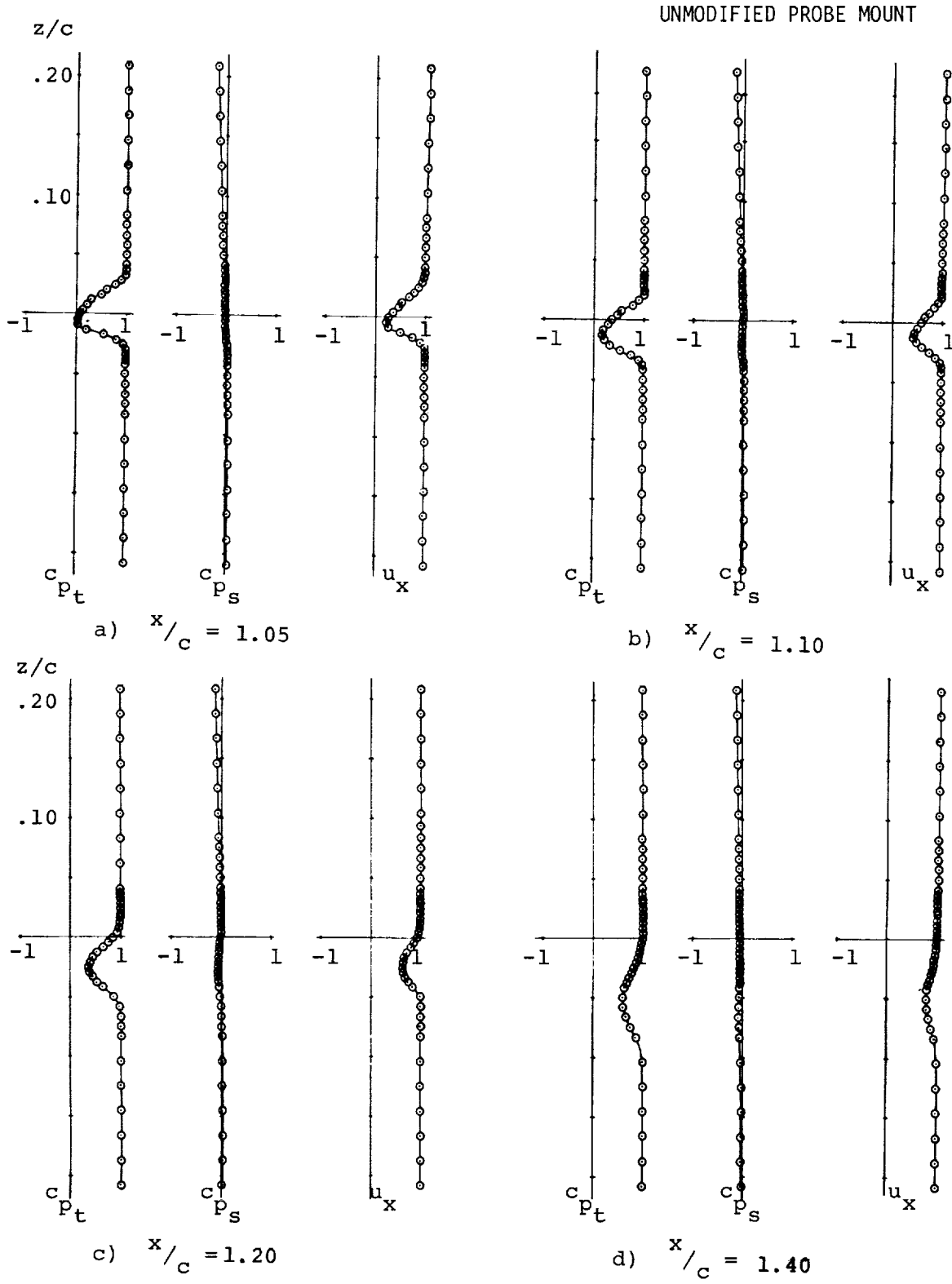
(2) Angle of attack for $C_{p_{max}}$, $\alpha=14.4^\circ$

Figure 19B - Continued.



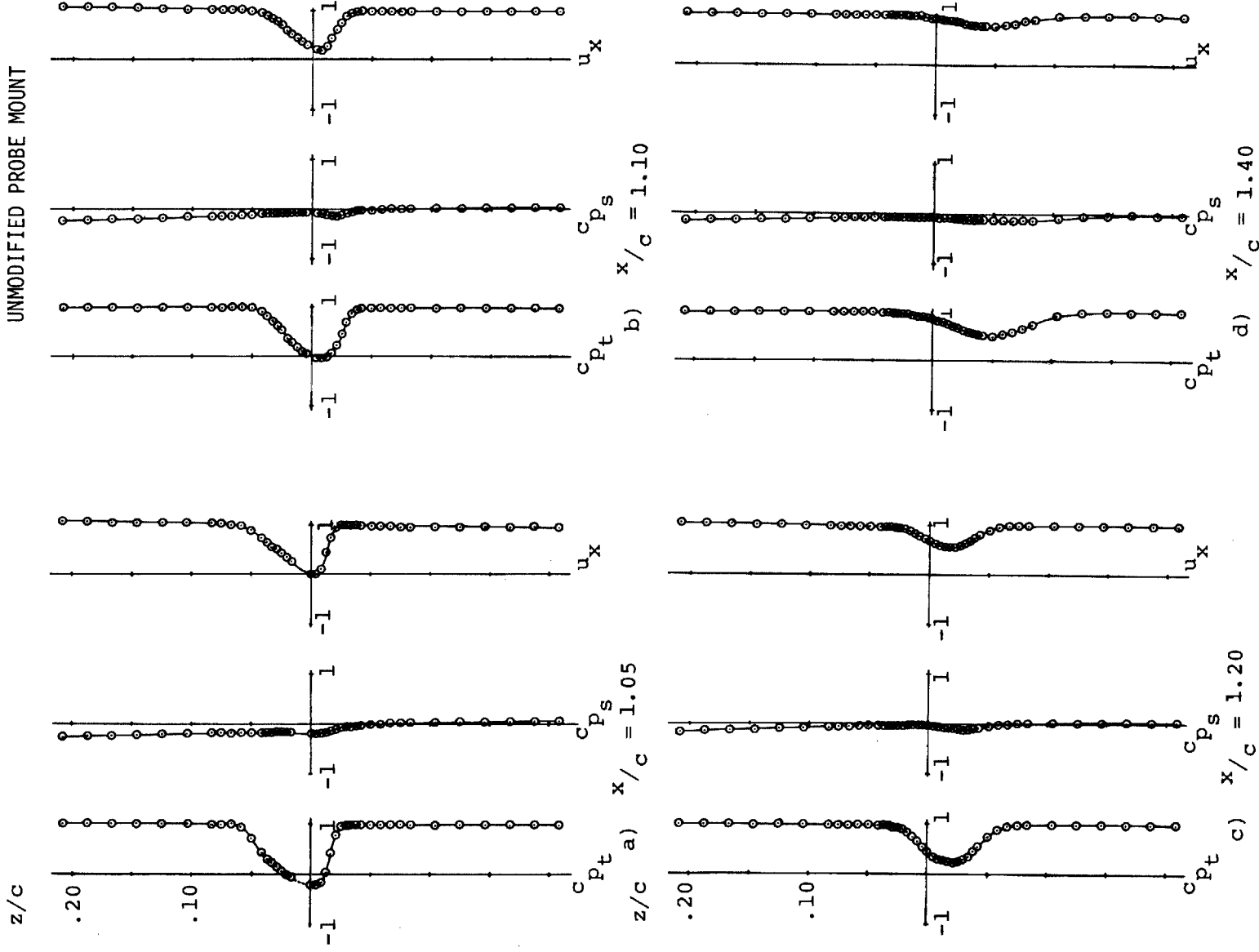
(3) Post-stall angle of attack, $\alpha=16.4^\circ$

Figure 19B- Concluded.



(1) Pre-Stall angle of attack, $\alpha = 10.3^\circ$
 Figure 19C- Velocity and Pressure Distributions in the Wake, GA(W)-2 Airfoil.

UNMODIFIED PROBE MOUNT



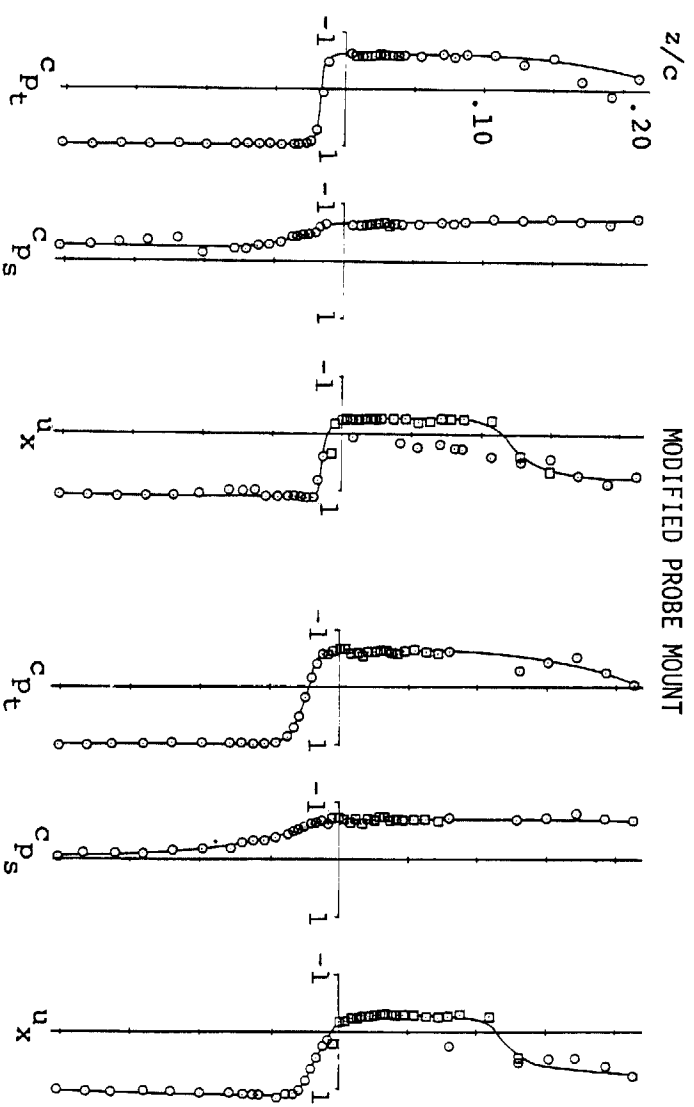
(2) Near-Stall angle of attack, $\alpha = 14.4^\circ$

Figure 19C- Continued.

○ Five-Tube Data

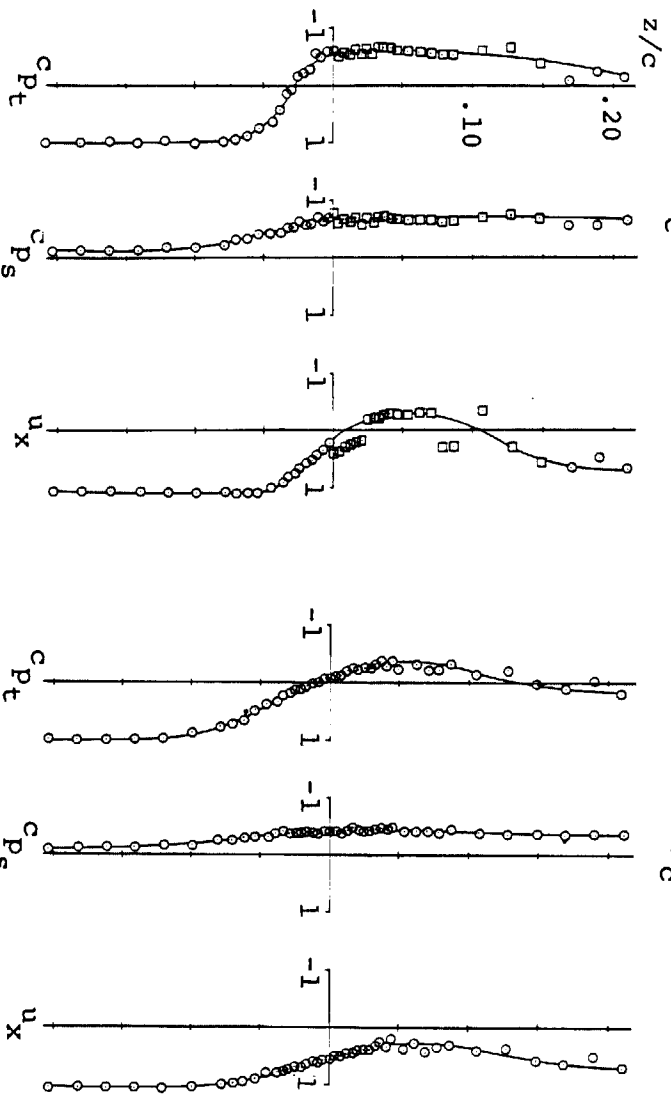
□ Four-Tube Data

MODIFIED PROBE MOUNT



a) $x/c = 1.05$

b) $x/c = 1.10$

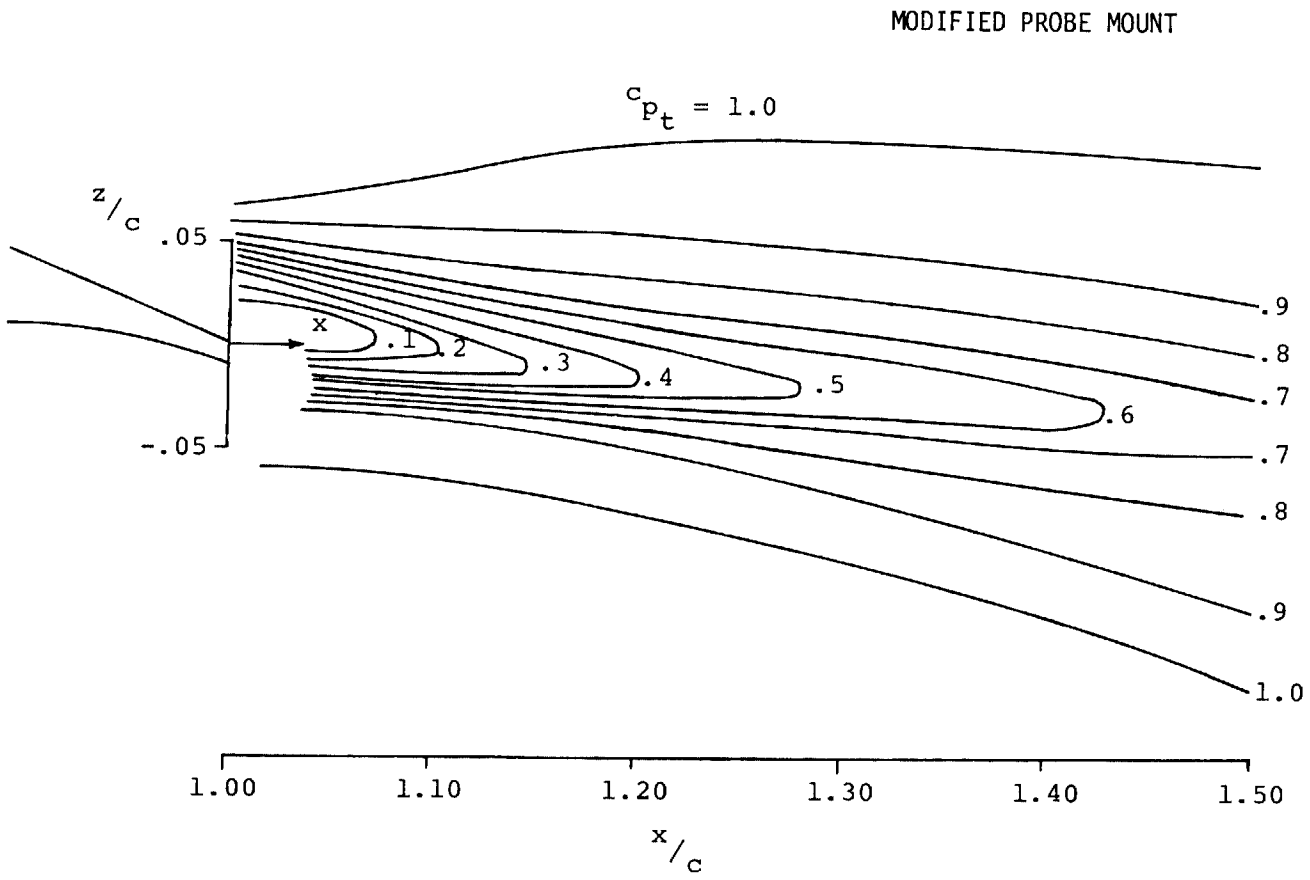


c) $x/c = 1.20$

d) $x/c = 1.40$

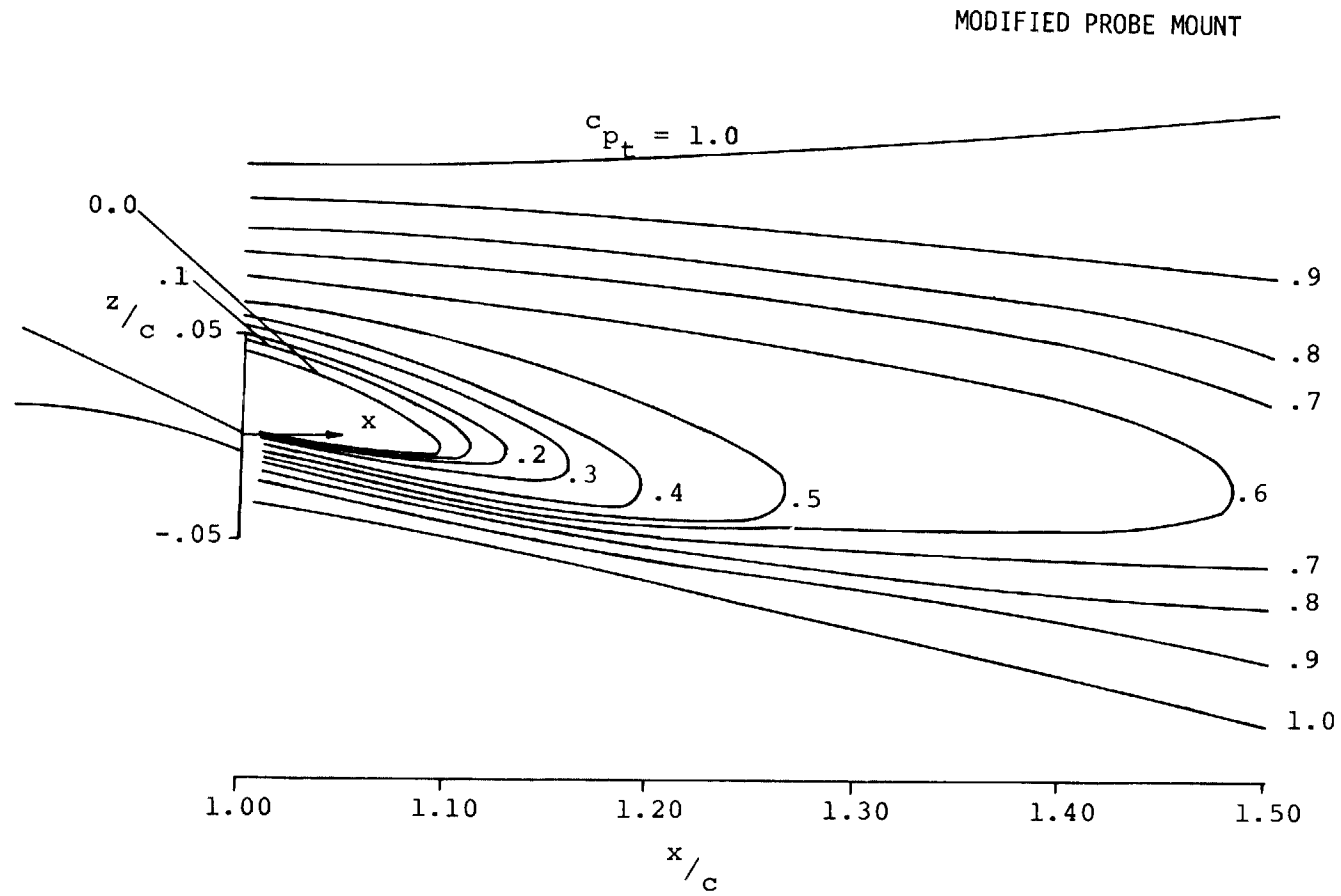
(3) Post-Stall angle of attack, $\alpha = 18.3^\circ$

Figure 19C - Concluded.



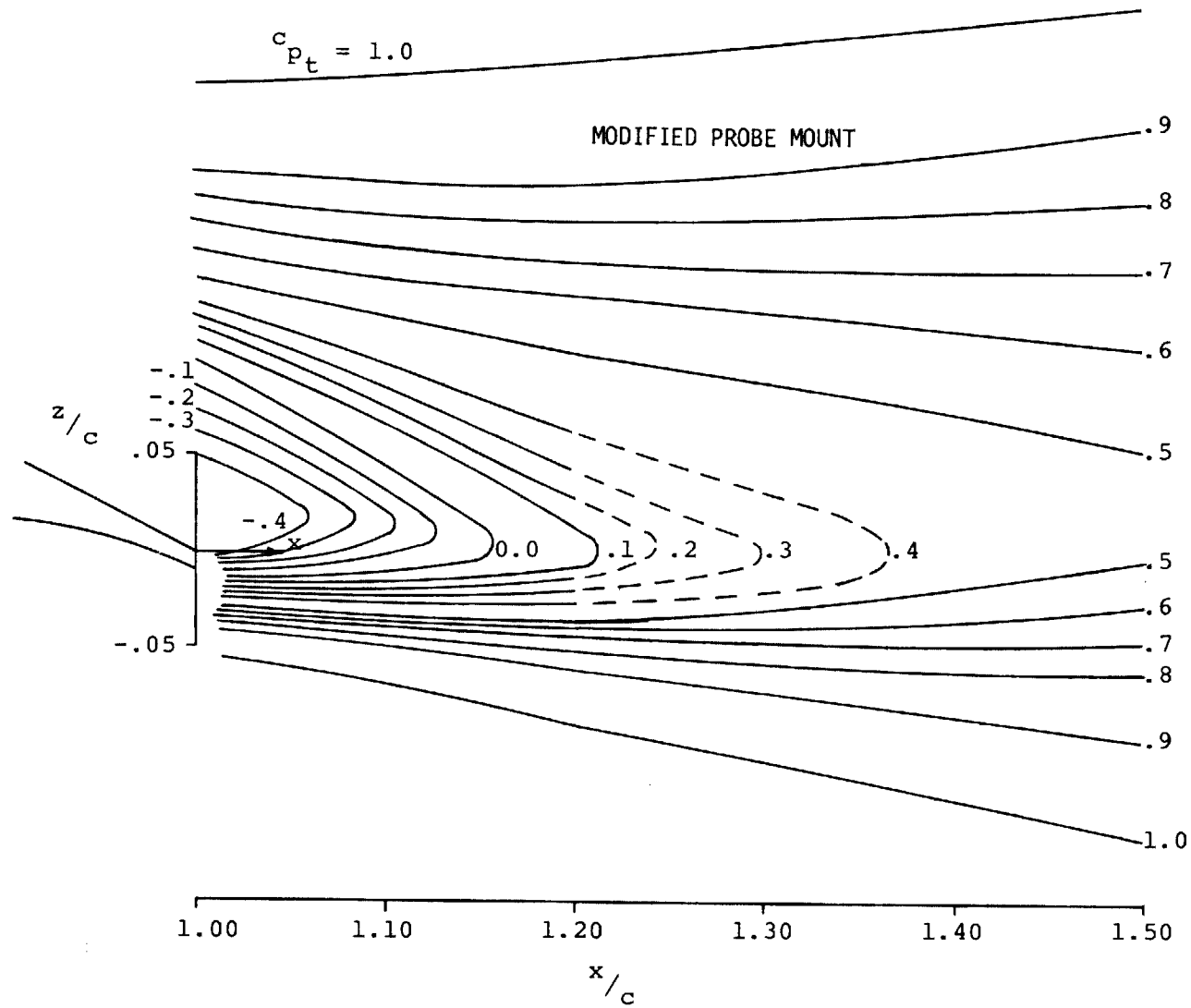
(1) Pre-stall angle of attack, $\alpha = 8.5^\circ$

Figure 20A - Wake Total Pressure Contours, LS(1)-0421 Mod Airfoil.



(2) Near-stall angle of attack, $\alpha = 10.6^\circ$

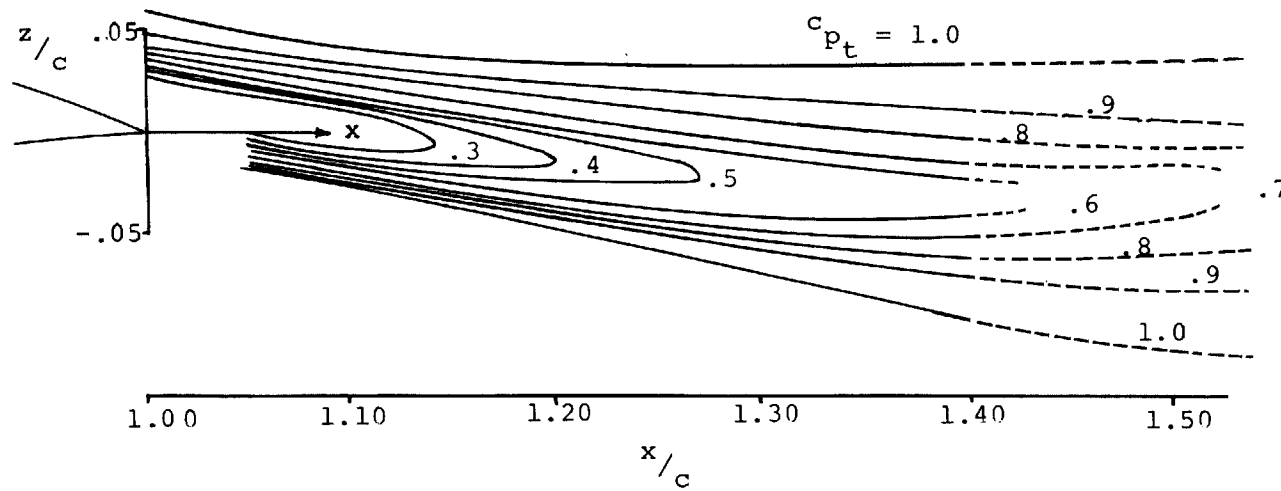
Figure 20A- Continued.



(3) Post-stall angle of attack, $\alpha = 12.7^\circ$

Figure 20A - Concluded.

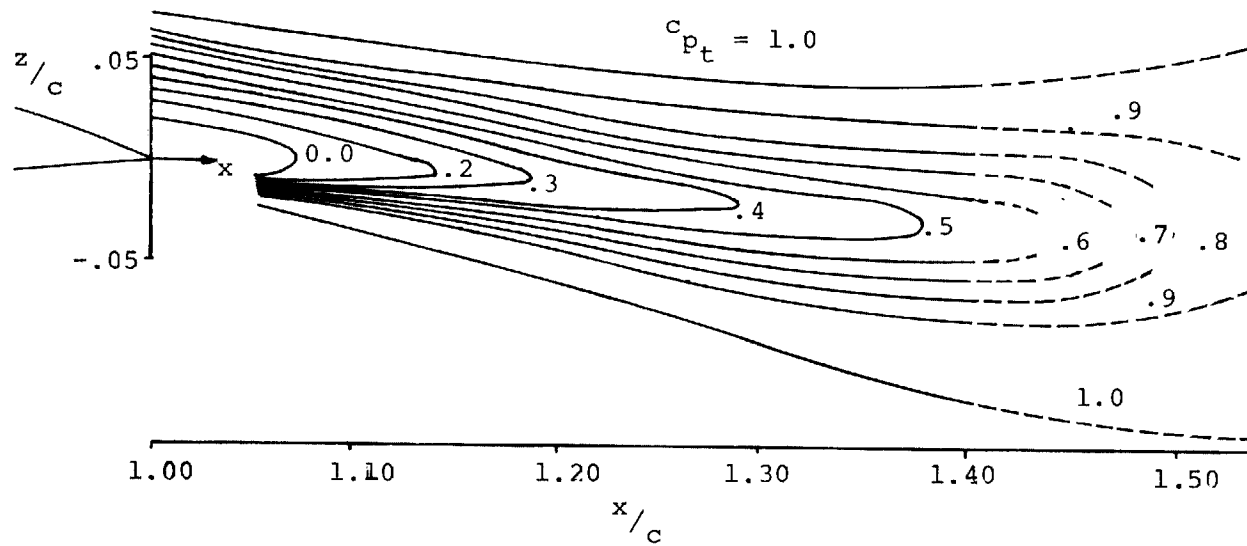
UNMODIFIED PROBE MOUNT



(1) Pre-stall angle of attack, $\alpha=12.4^\circ$

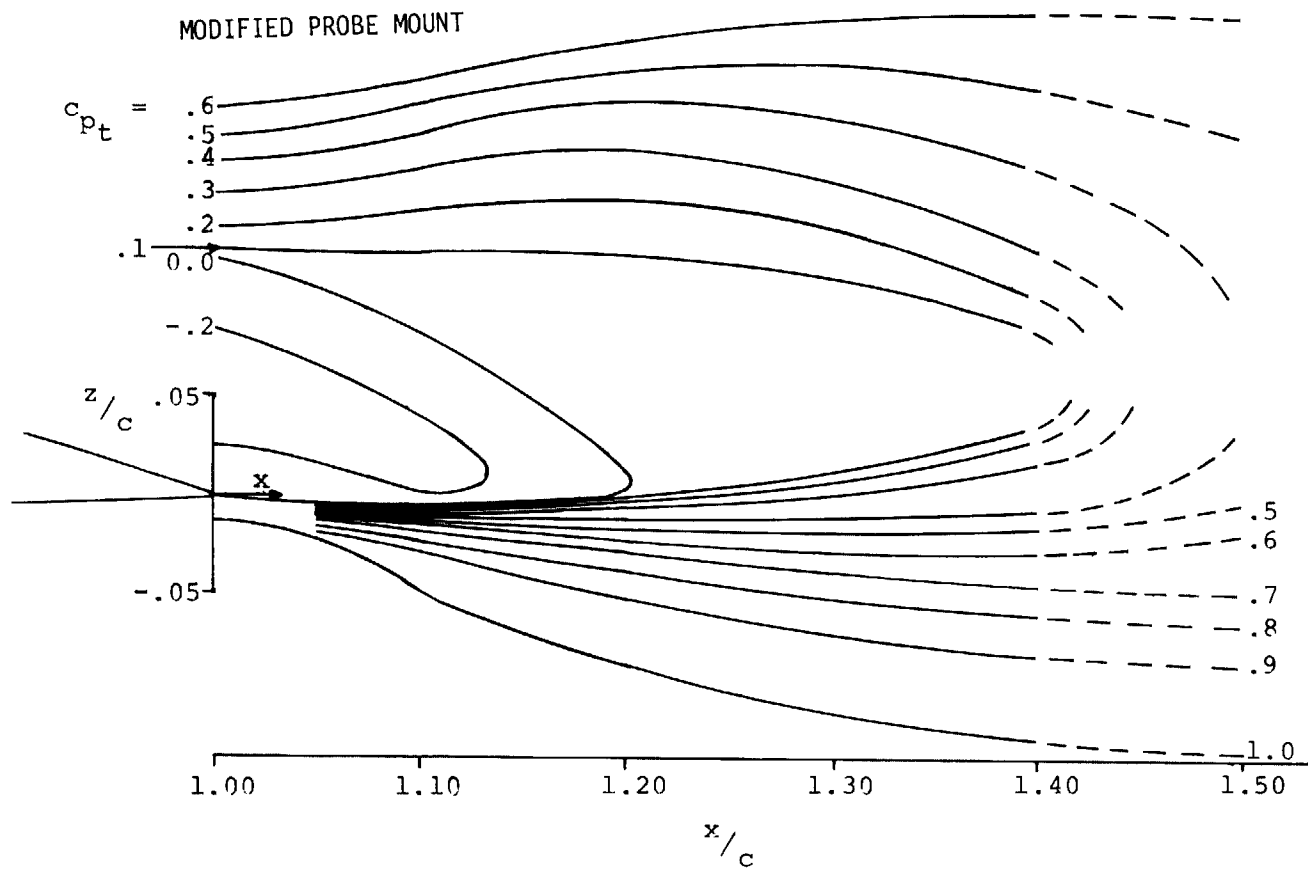
Figure 20B - Wake Total Pressure Contours, NACA 2412 Airfoil.

UNMODIFIED PROBE MOUNT



(2) Angle of attack for $c_{l_{\max}}$, $\alpha=14.4^\circ$

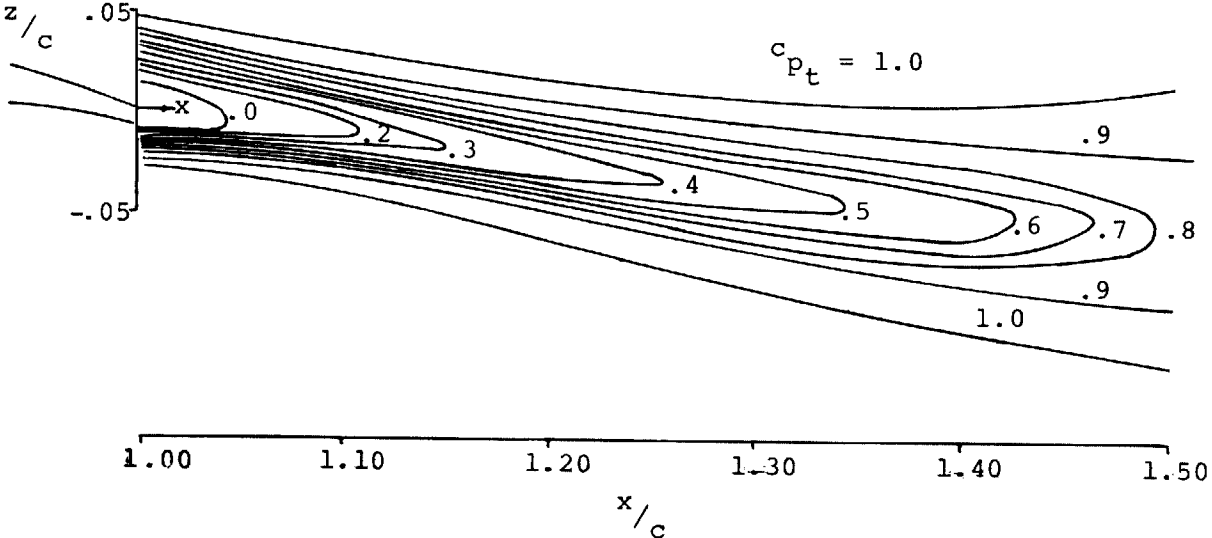
Figure 20B- Continued.



(3) Post-stall angle of attack, $\alpha=16.4^\circ$

Figure 20B- Concluded.

UNMODIFIED PROBE MOUNT

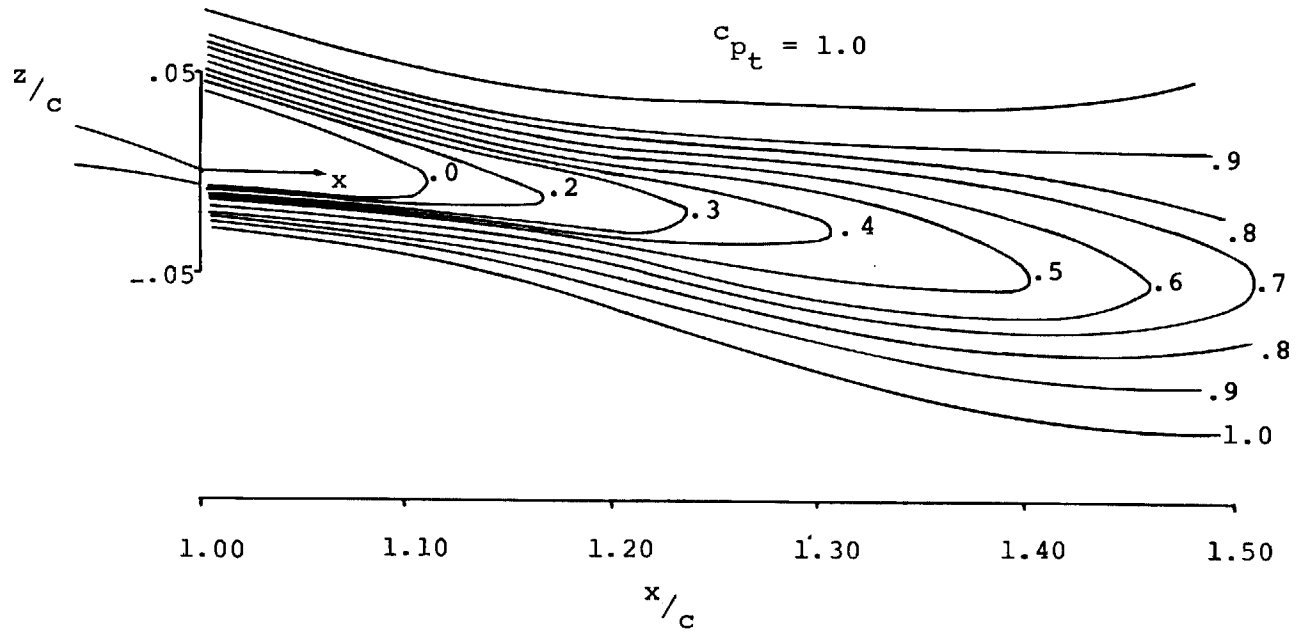


126

(1) Pre-Stall angle of attack, $\alpha = 10.3^\circ$

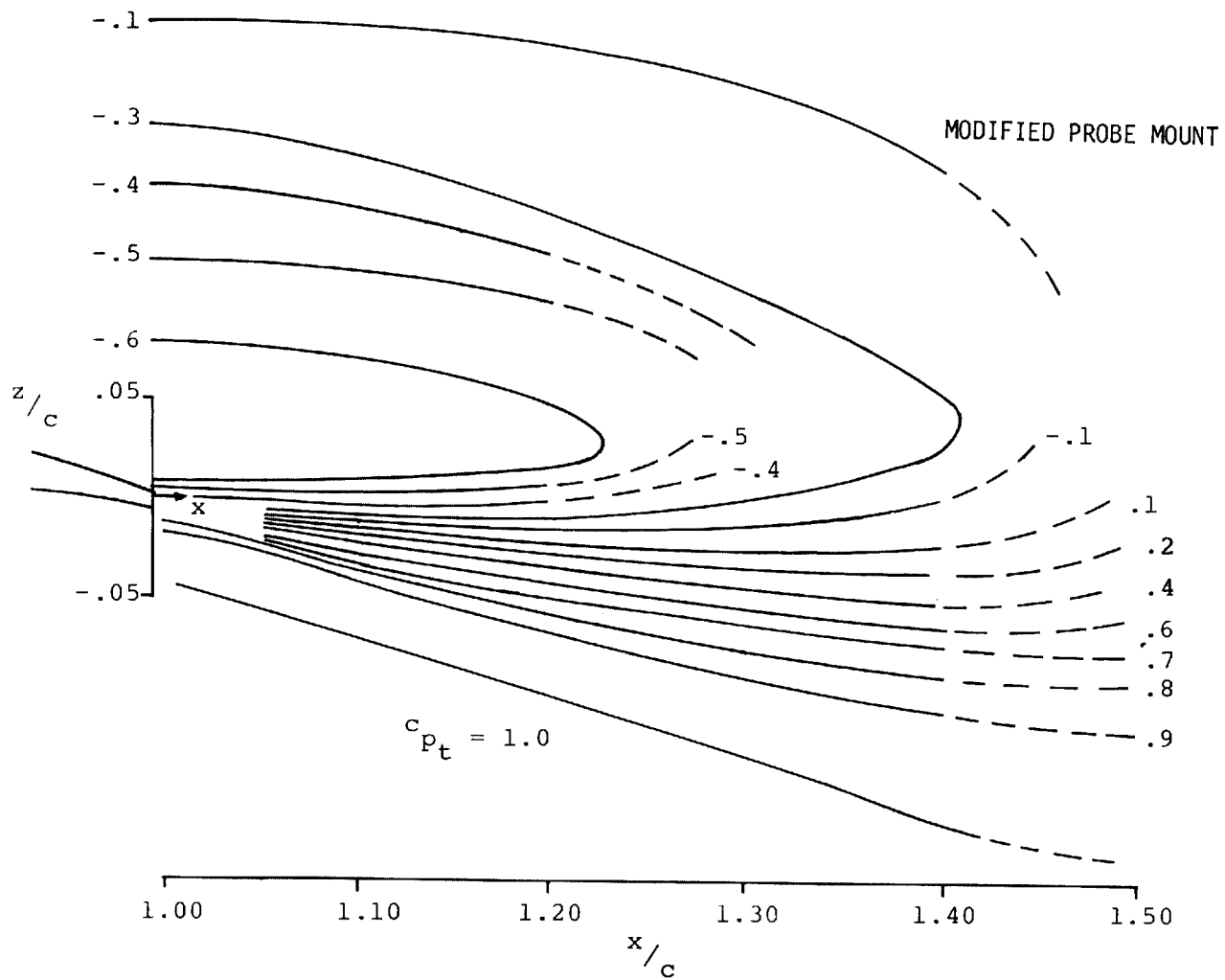
Figure 20C- Wake Total Pressure Contours, GA(W)-2 Airfoil.

UNMODIFIED PROBE MOUNT



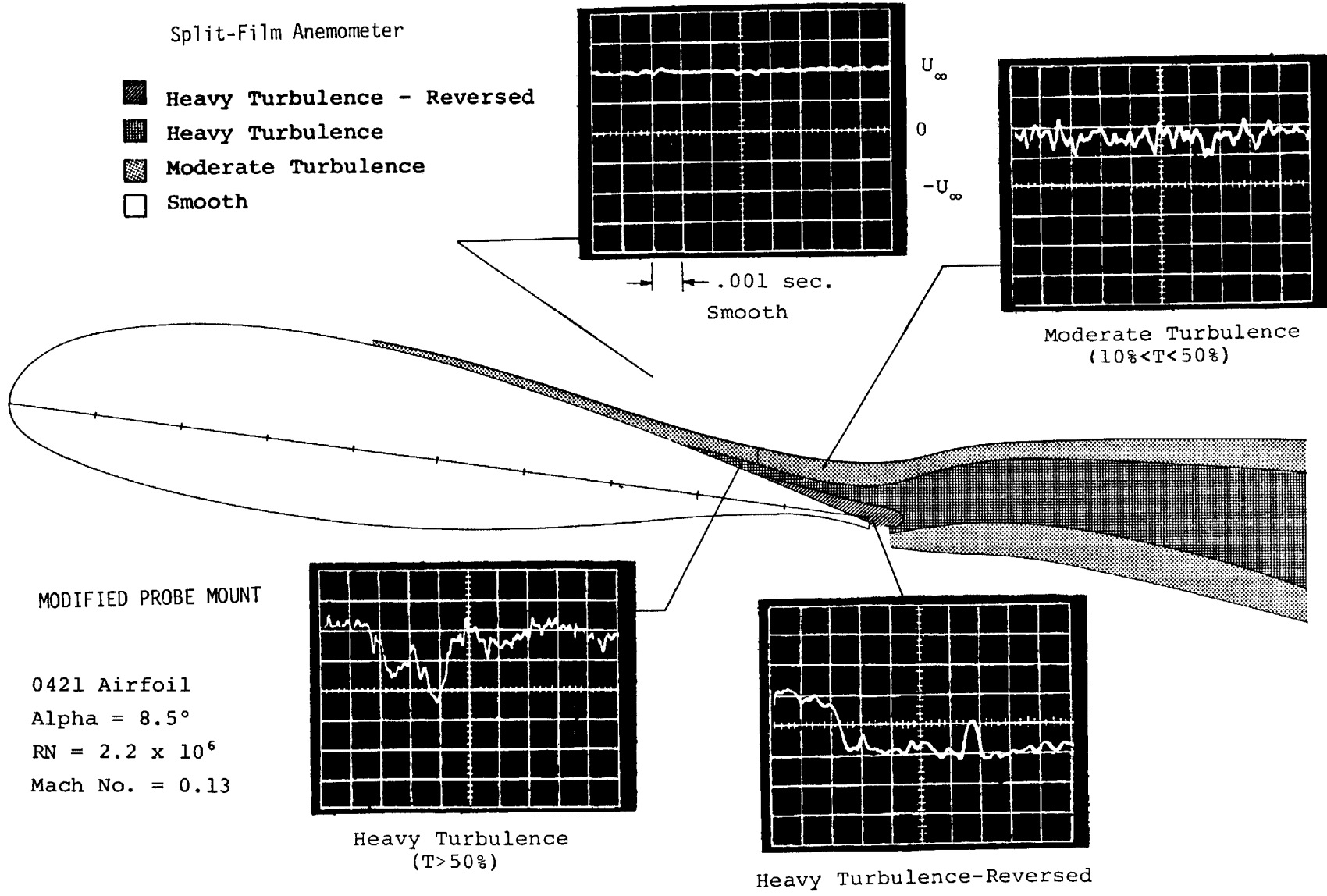
(2) Near- Stall angle of attack, $\alpha = 14.4^\circ$

Figure 20C- Continued.



(3) Post-Stall angle of attack, $\alpha = 18.3^\circ$

Figure 20C - Concluded.

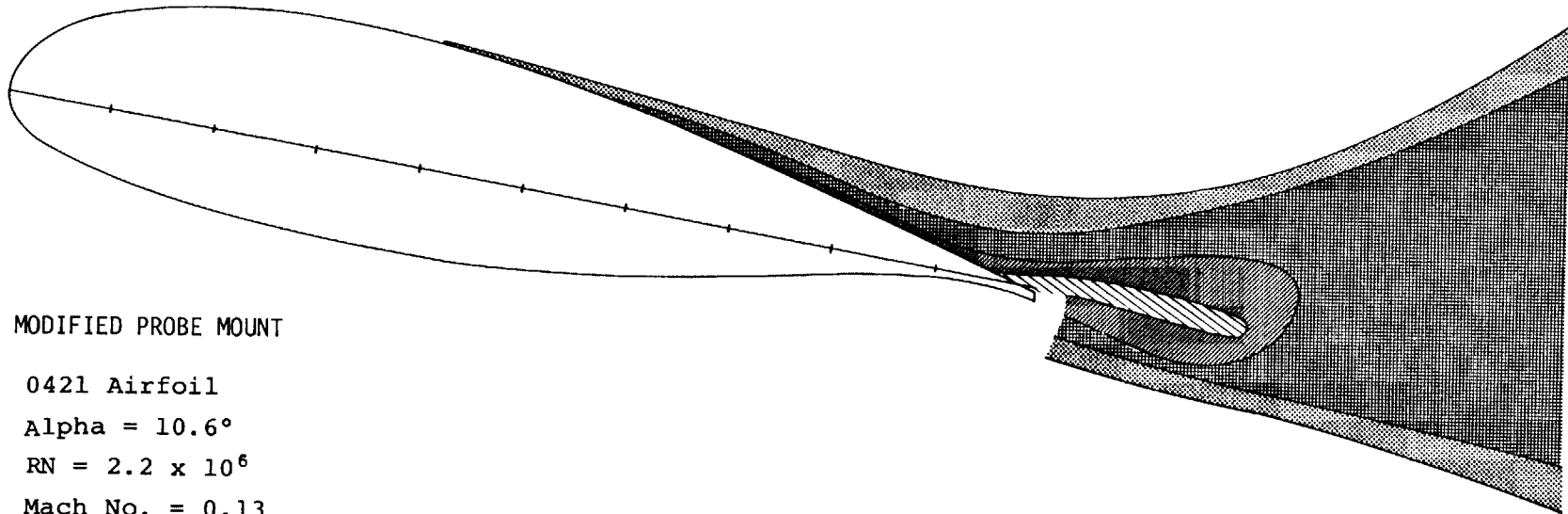


(1) Pre-stall angle of attack, $\alpha = 8.5^\circ$

Figure 21A--Hot Film Velocity Field Survey, LS(1)-0421 Mod Airfoil.

Split-Film Anemometer

- ▨ Heavy Turbulence - Reversed > 50% Time
- Heavy Turbulence - 1% Time < Reversed < 50% Time
- Heavy Turbulence
- ▤ Moderate Turbulence
- Smooth



MODIFIED PROBE MOUNT

0421 Airfoil

Alpha = 10.6°

RN = 2.2 x 10⁶

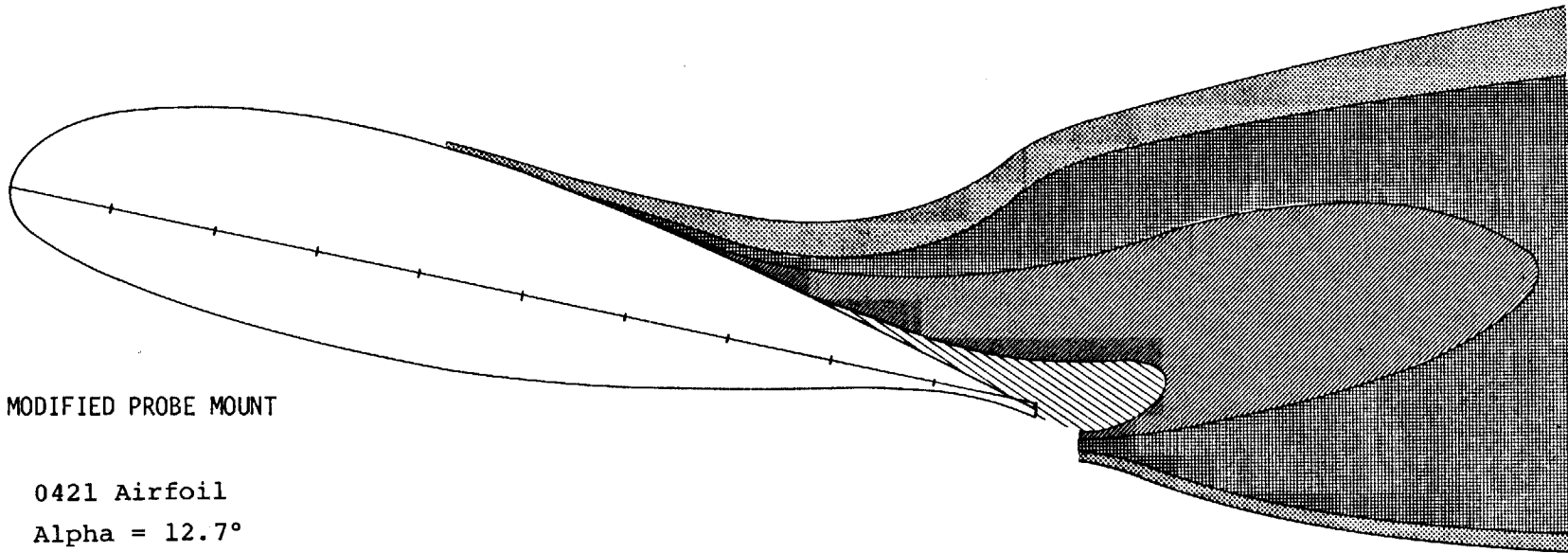
Mach No. = 0.13

(2) Near-stall angle of attack, $\alpha = 10.6^\circ$

Figure 21A- Continued.

Split-Film Anemometer

- ▨ Heavy Turbulence - Reversed > 50% Time
- Heavy Turbulence - 1% Time < Reversed < 50% Time
- Heavy Turbulence
- ▣ Moderate Turbulence
- Smooth



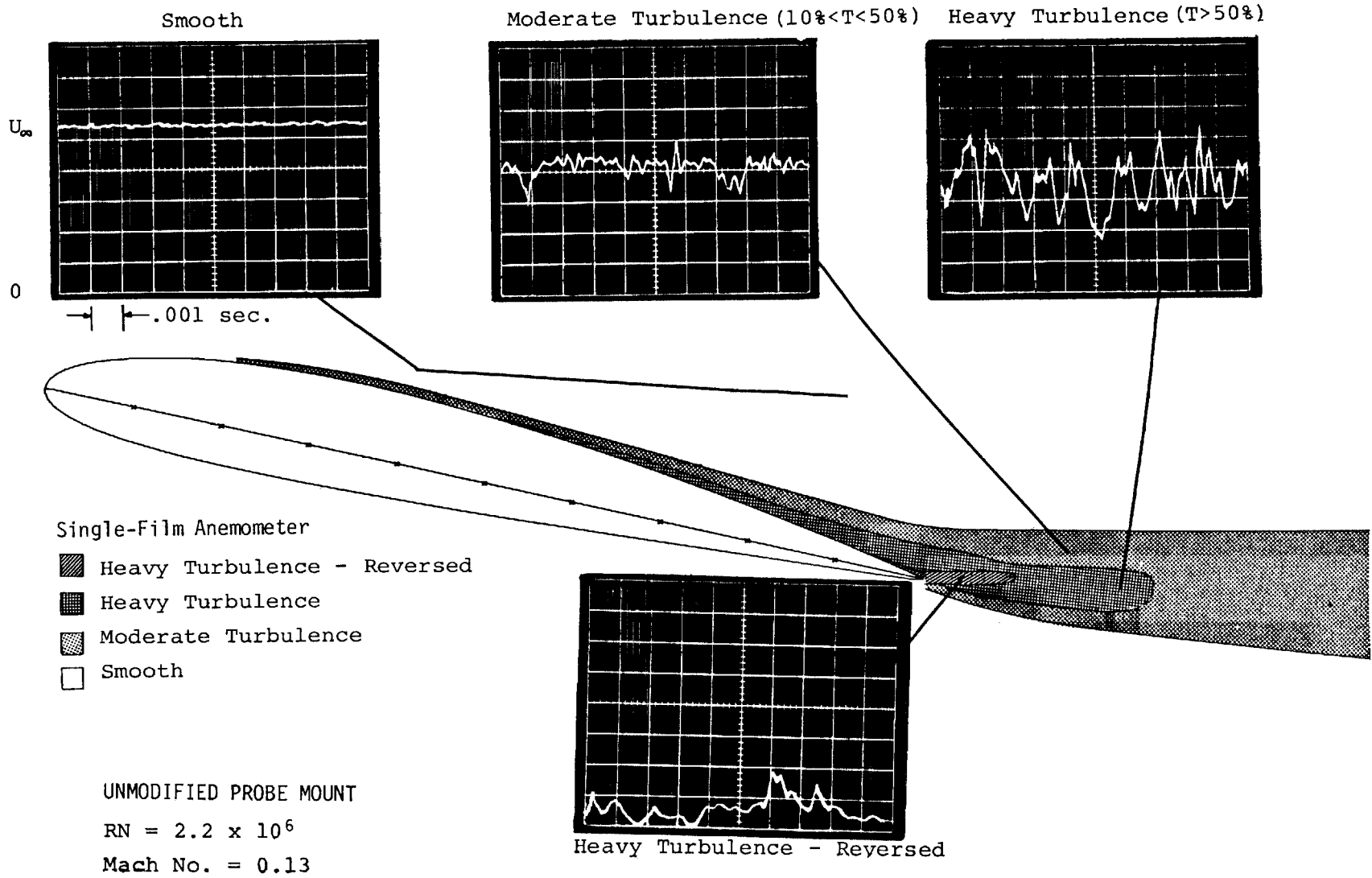
131

MODIFIED PROBE MOUNT

0421 Airfoil
Alpha = 12.7°
RN = 2.2 x 10⁶
Mach No. = 0.13

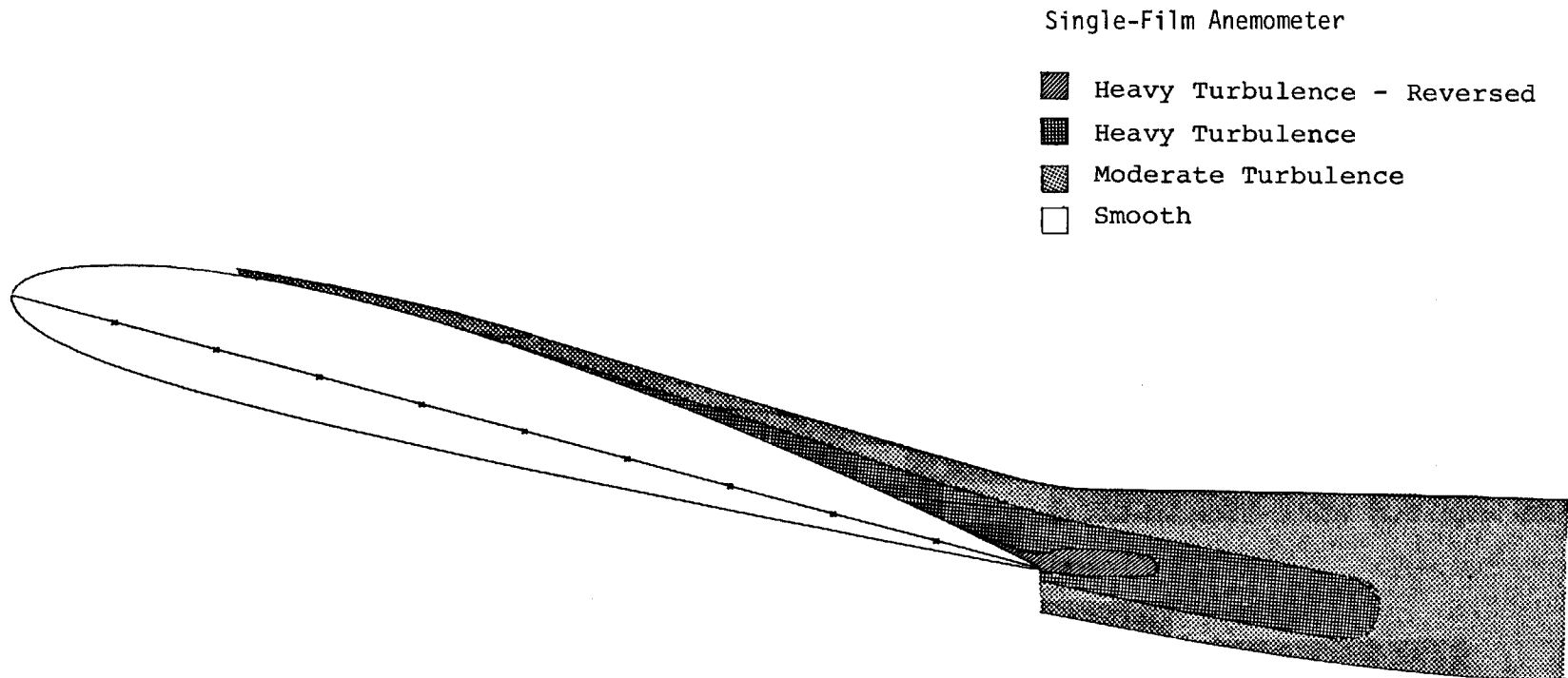
(3) Post-stall angle of attack, $\alpha = 12.7^\circ$

Figure 21A- Concluded.



(1) Pre-stall angle of attack, $\alpha = 12.4^\circ$

Figure 21B - Hot Film Velocity Field Survey, NACA 2412 Airfoil.



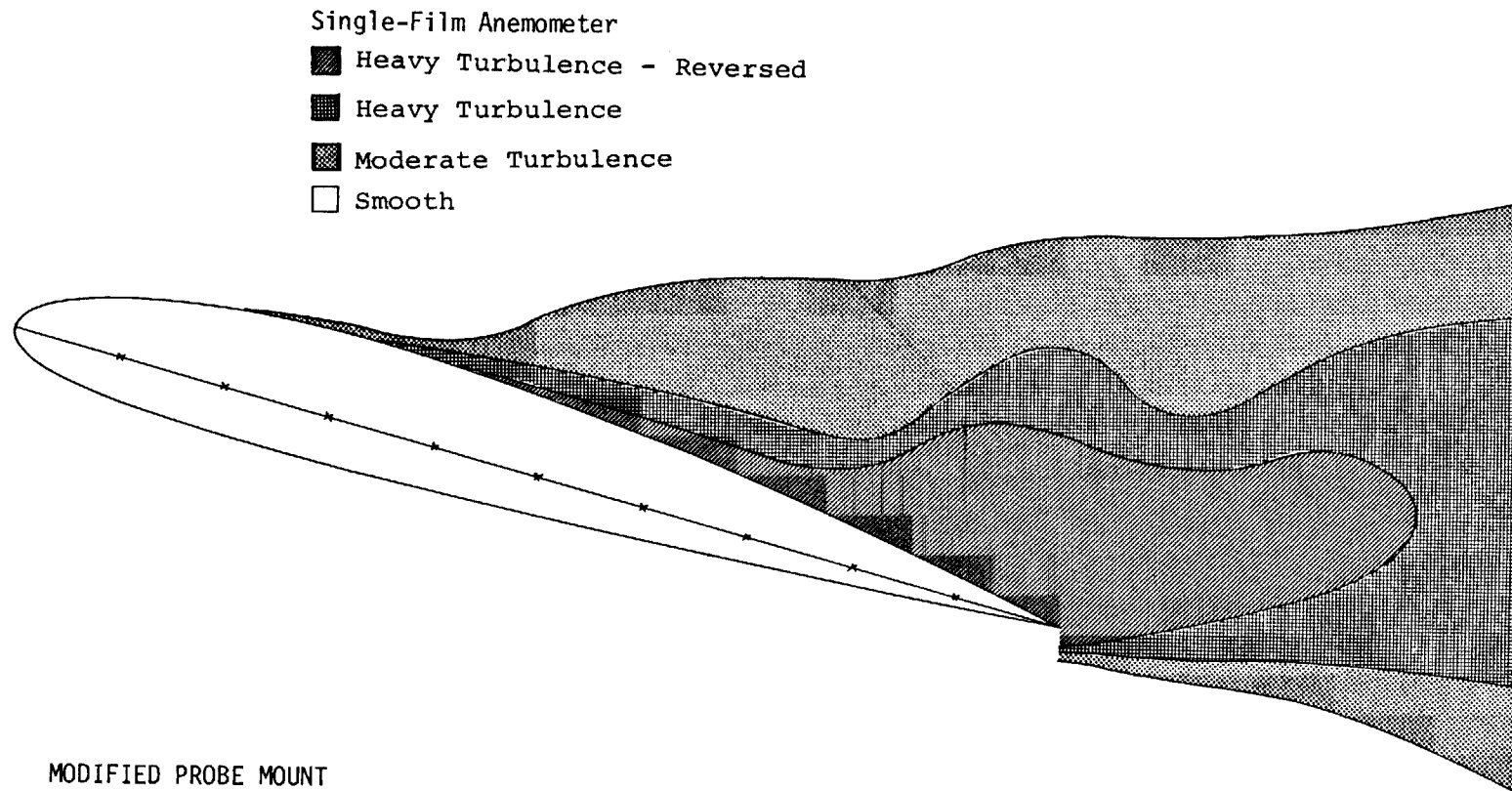
UNMODIFIED PROBE MOUNT

$RN = 2.2 \times 10^6$

Mach No. = 0.13

(2) Angle of attack for $c_{l_{max}}$, $\alpha=14.4^\circ$

Figure 21B- Continued.



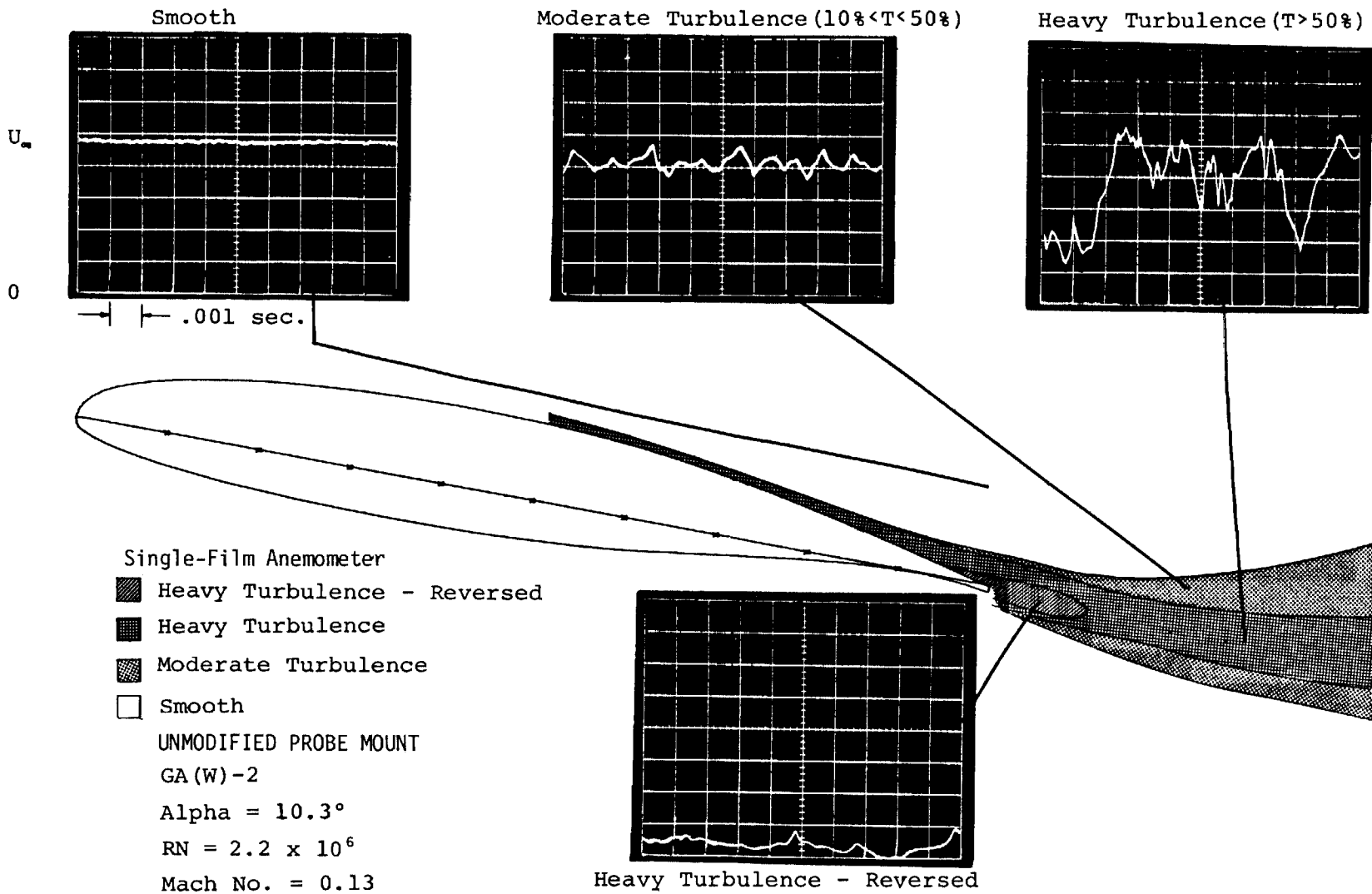
MODIFIED PROBE MOUNT

$Re = 2.2 \times 10^6$

Mach No. = 0.13

(3) Post-stall angle of attack, $\alpha = 16.4^\circ$

Figure 21B- Concluded.



(1) Pre-Stall angle of attack, $\alpha = 10.3^\circ$

Figure 21C--Hot Film Velocity Field Survey, GA(W)-2 Airfoil.

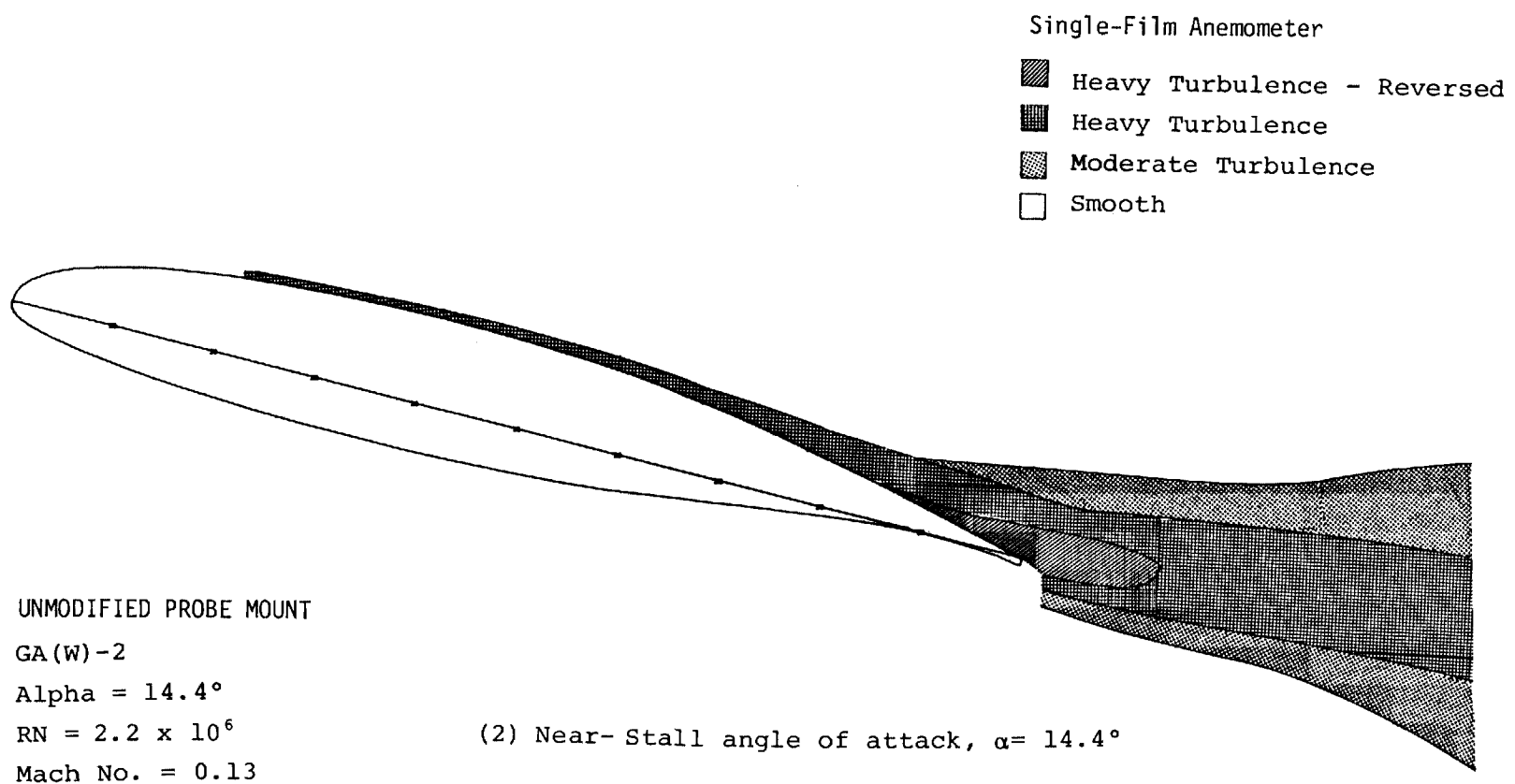


Figure 21C- Continued.

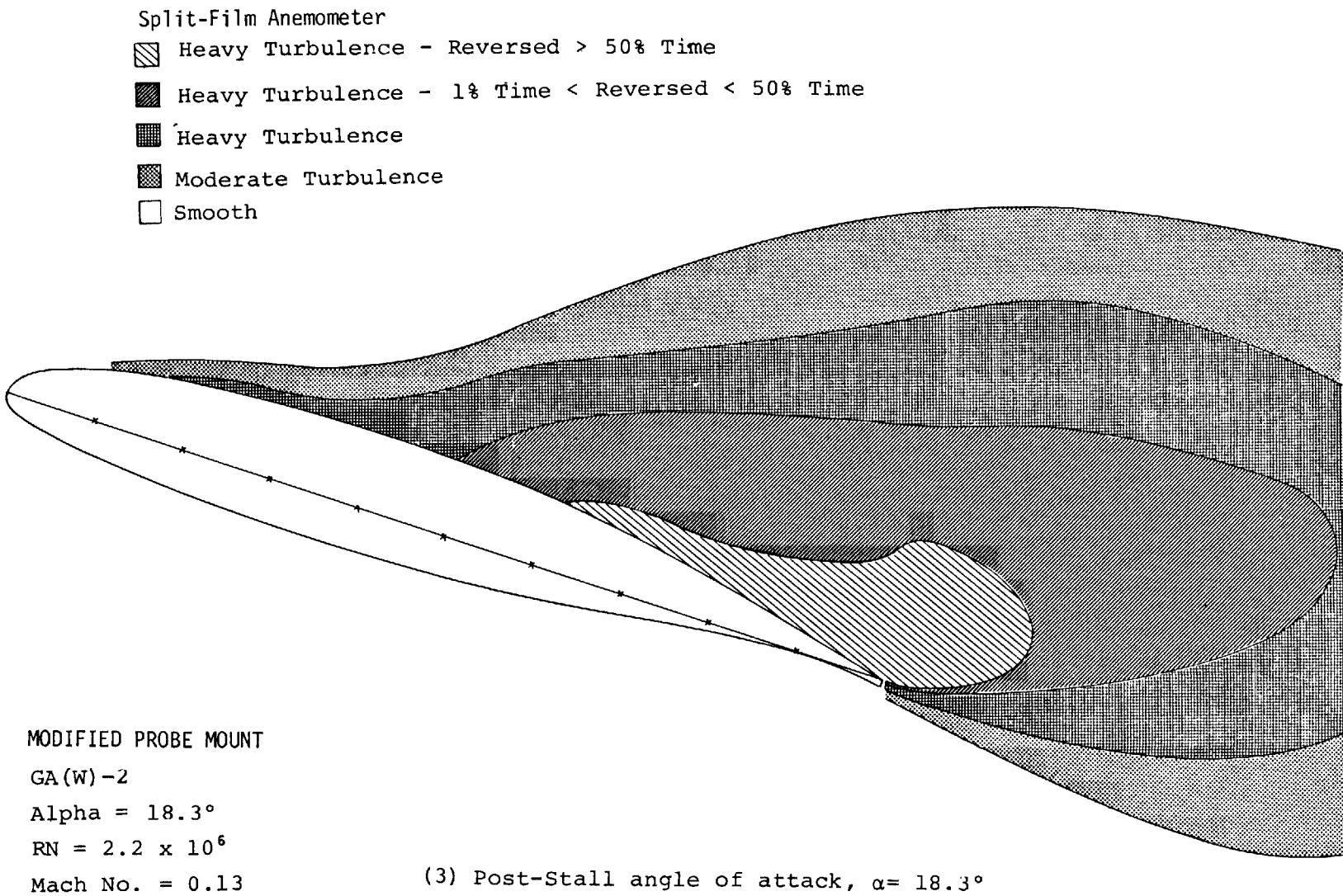
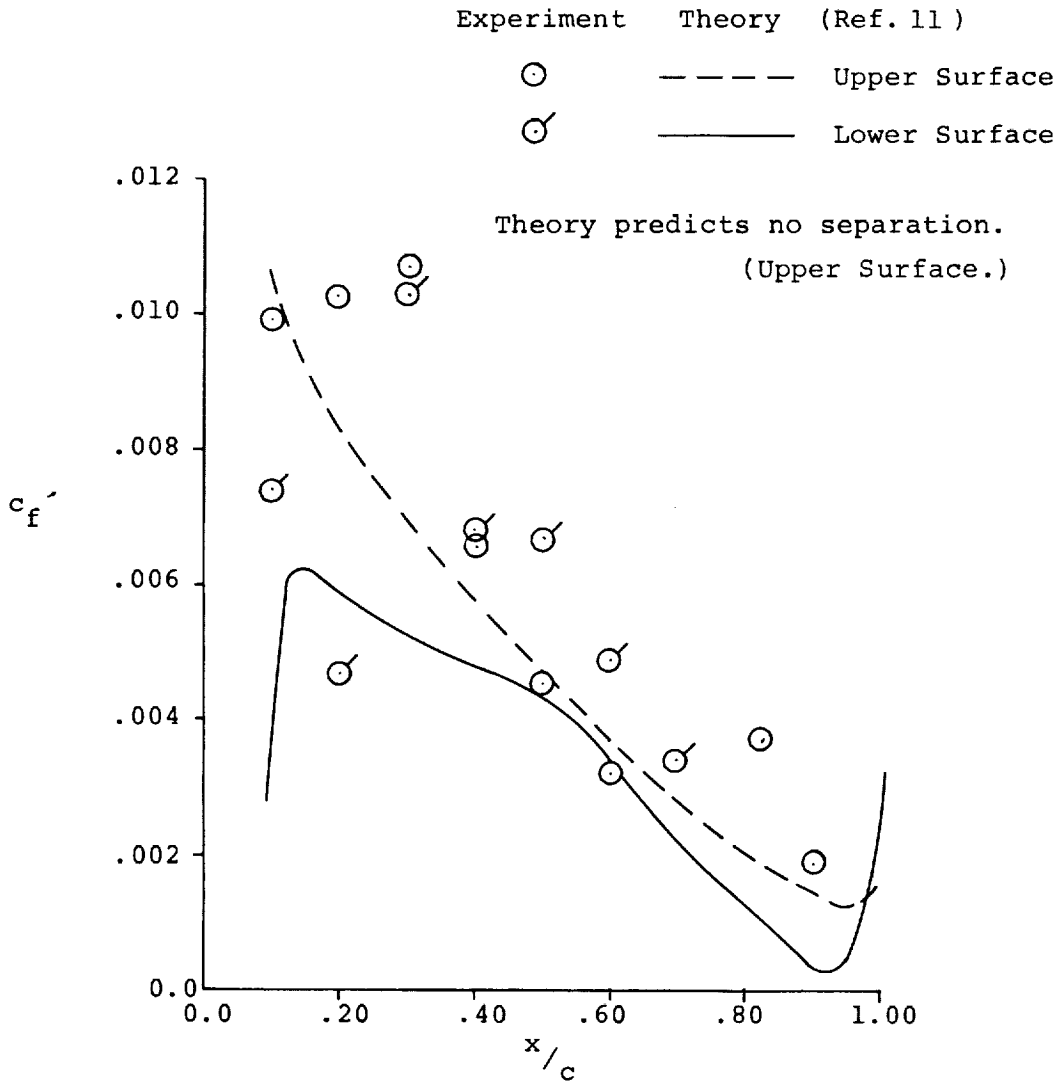
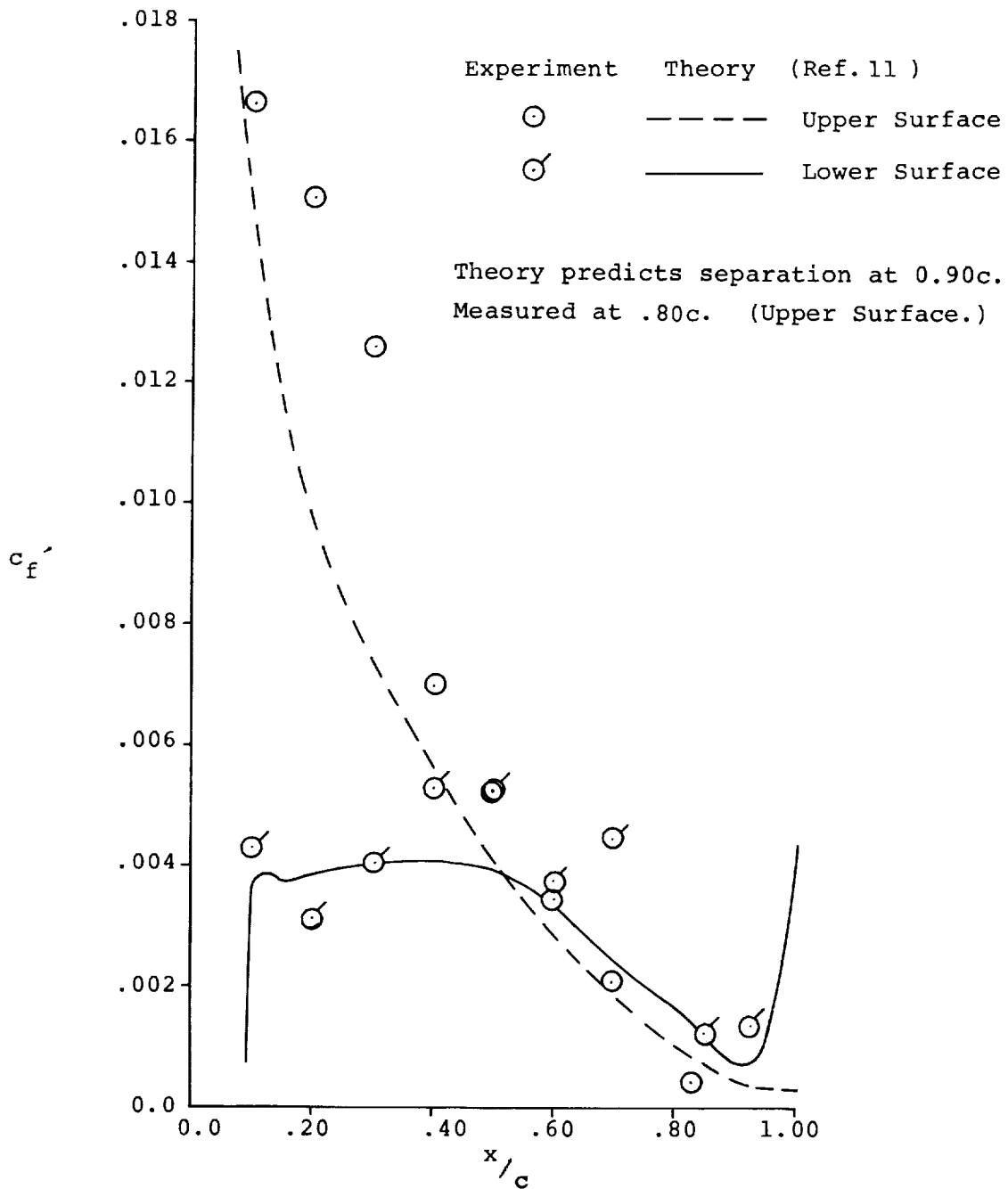


Figure 21C - Concluded.



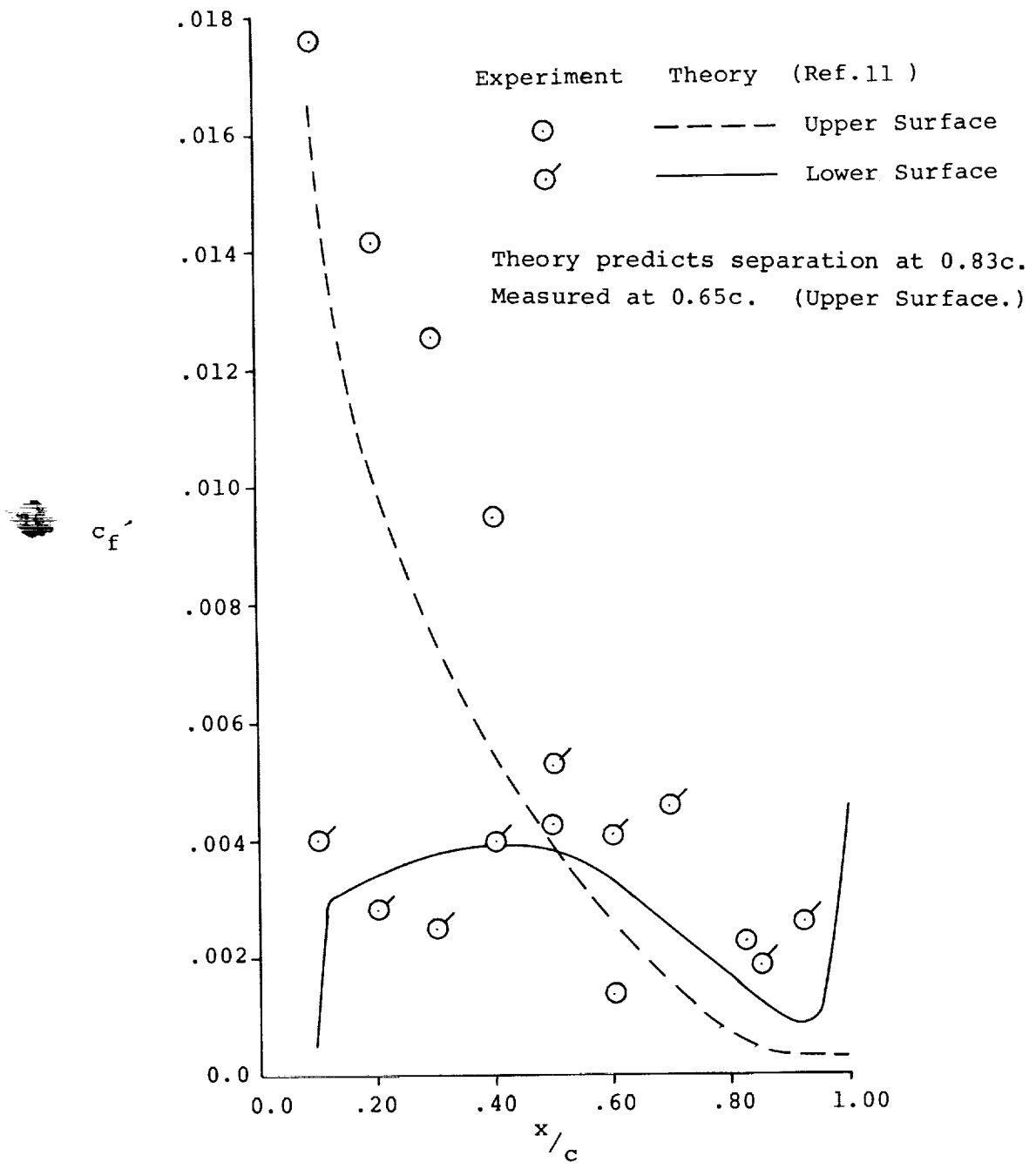
(1) $\alpha = 0.2^\circ$

Figure 22A- Comparison of Experimental and Theoretical Skin Friction Distributions, LS(1)-0421 Mod Airfoil.



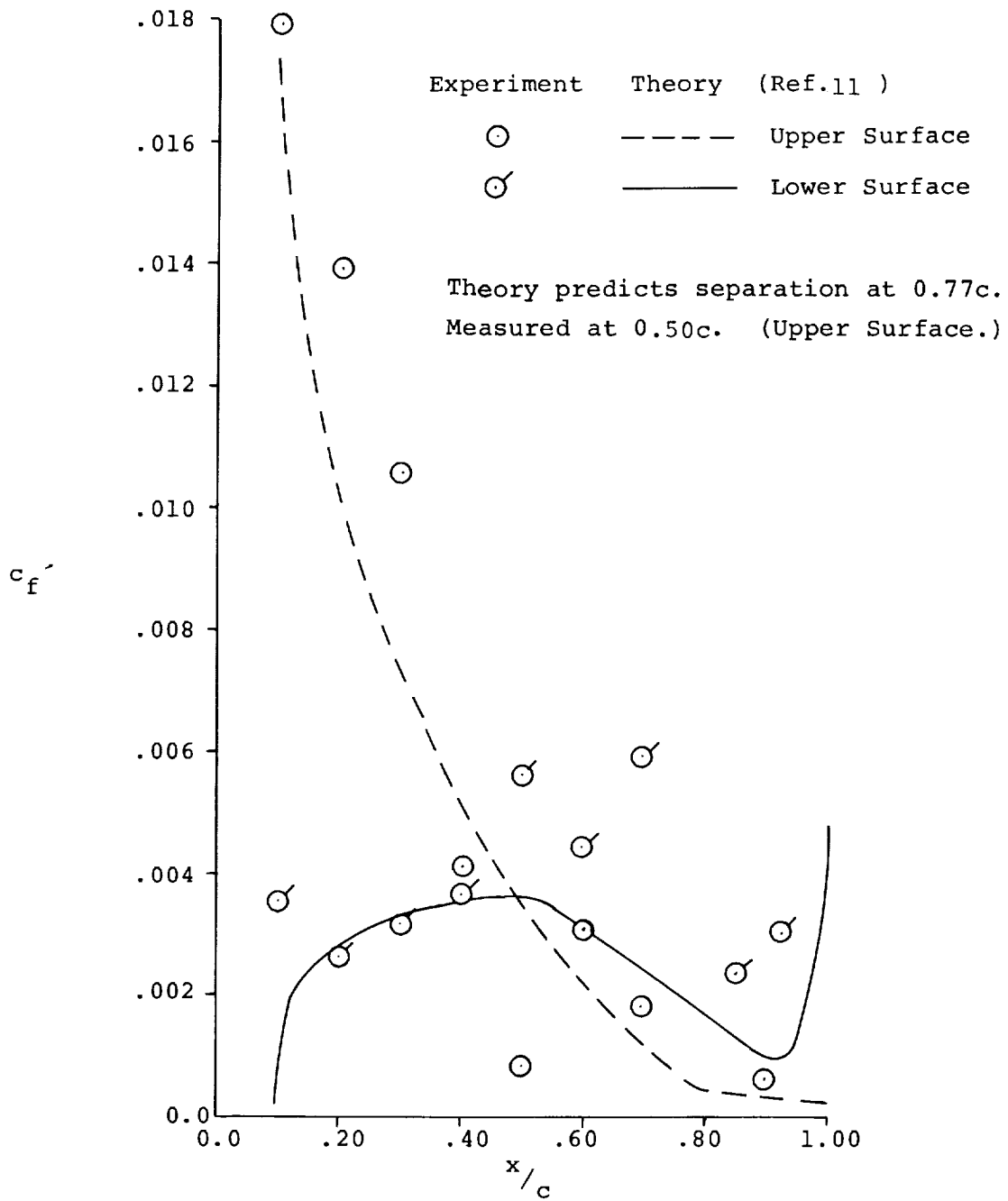
(2) $\alpha = 8.5^\circ$

Figure 22A- Continued.



(3) $\alpha = 10.6^\circ$

Figure 22A- Continued.



(4) $\alpha = 12.7^\circ$

Figure 22A- Concluded.

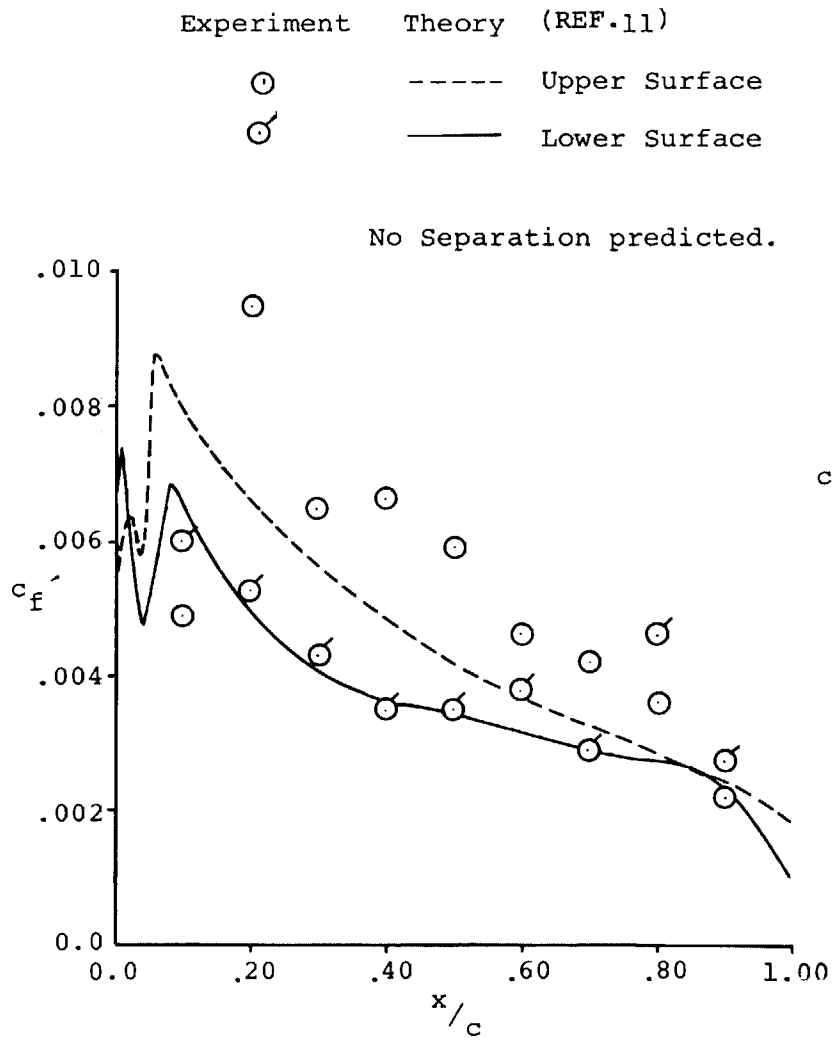
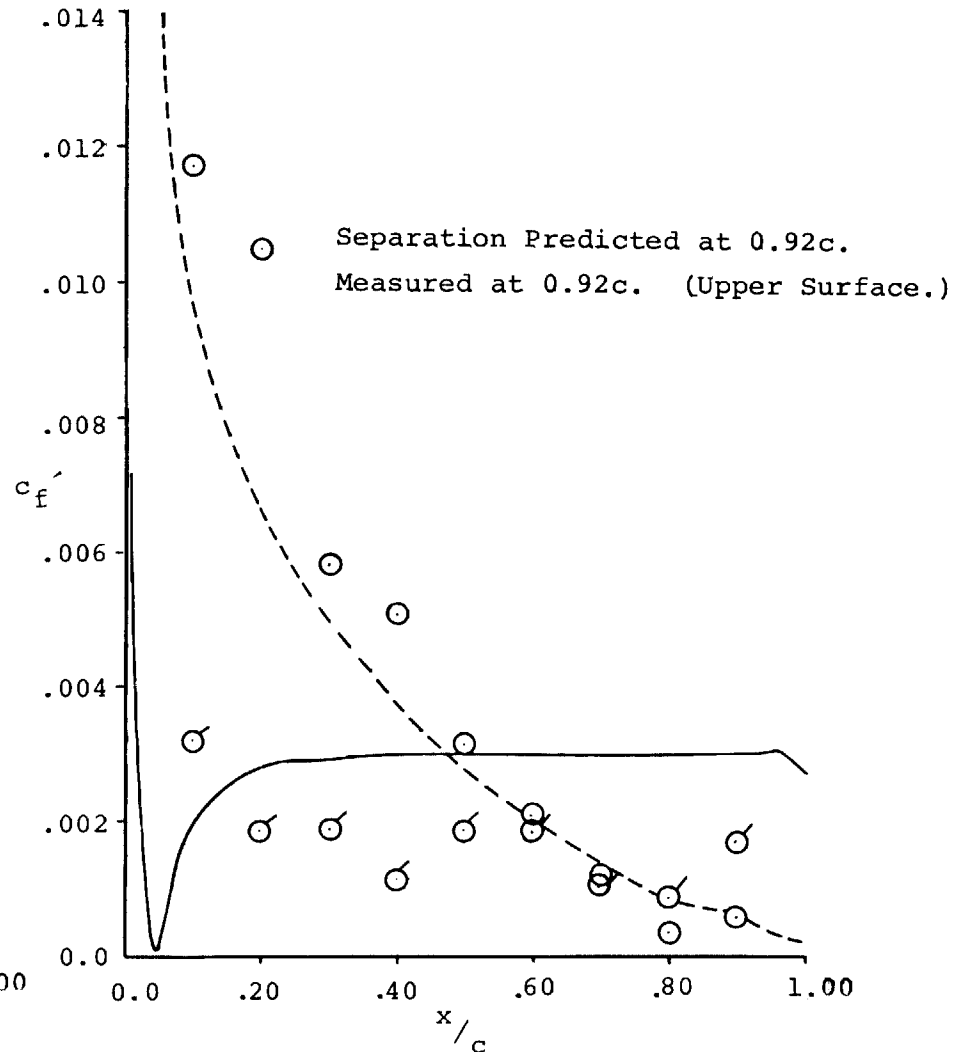
(1) $\alpha = .2^\circ$ (2) $\alpha = 12.4^\circ$

Figure 22B - Comparison of Experimental and Theoretical Skin Friction Distributions,
NACA 2412 Airfoil.

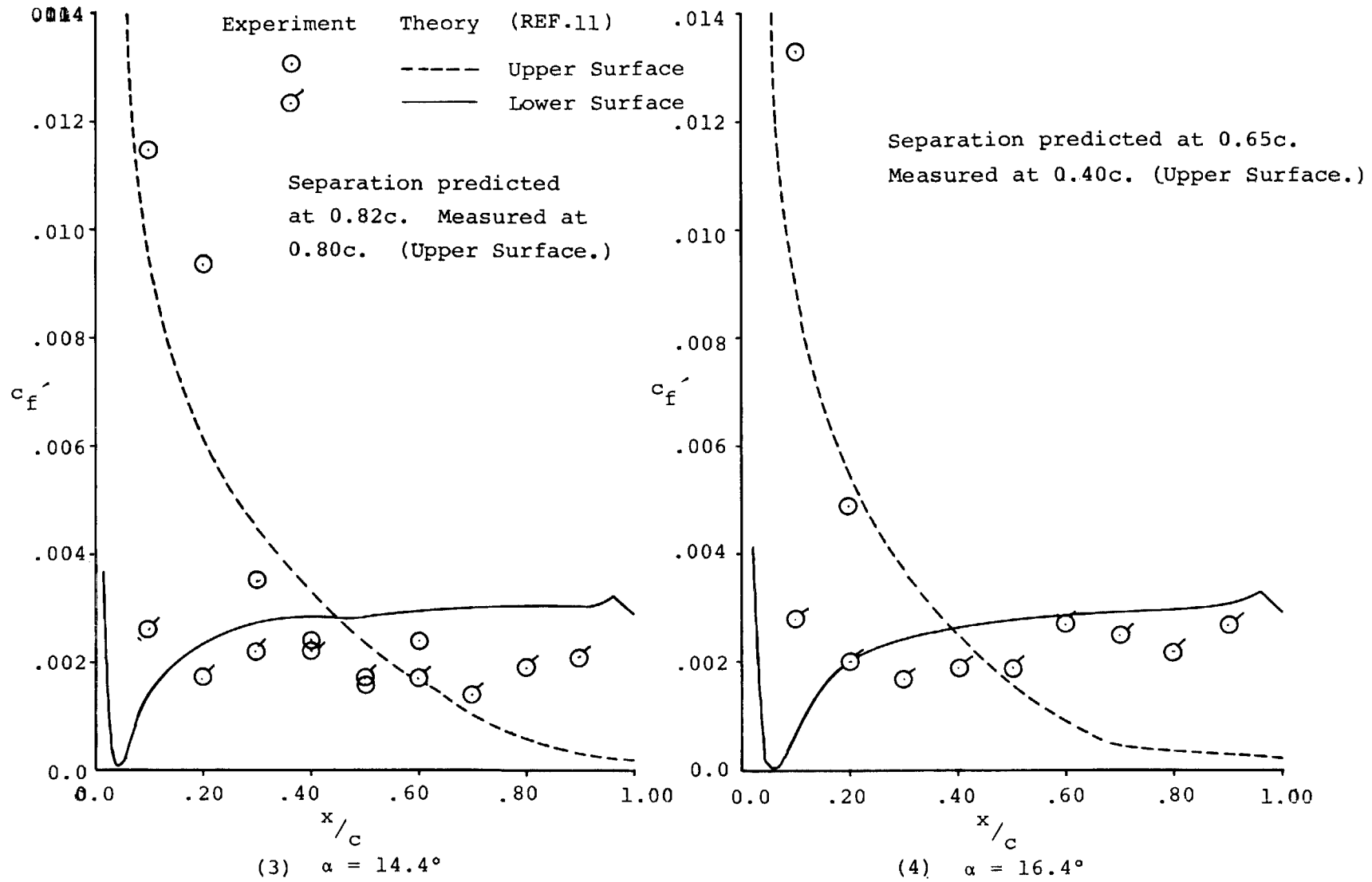


Figure 22B- Concluded.

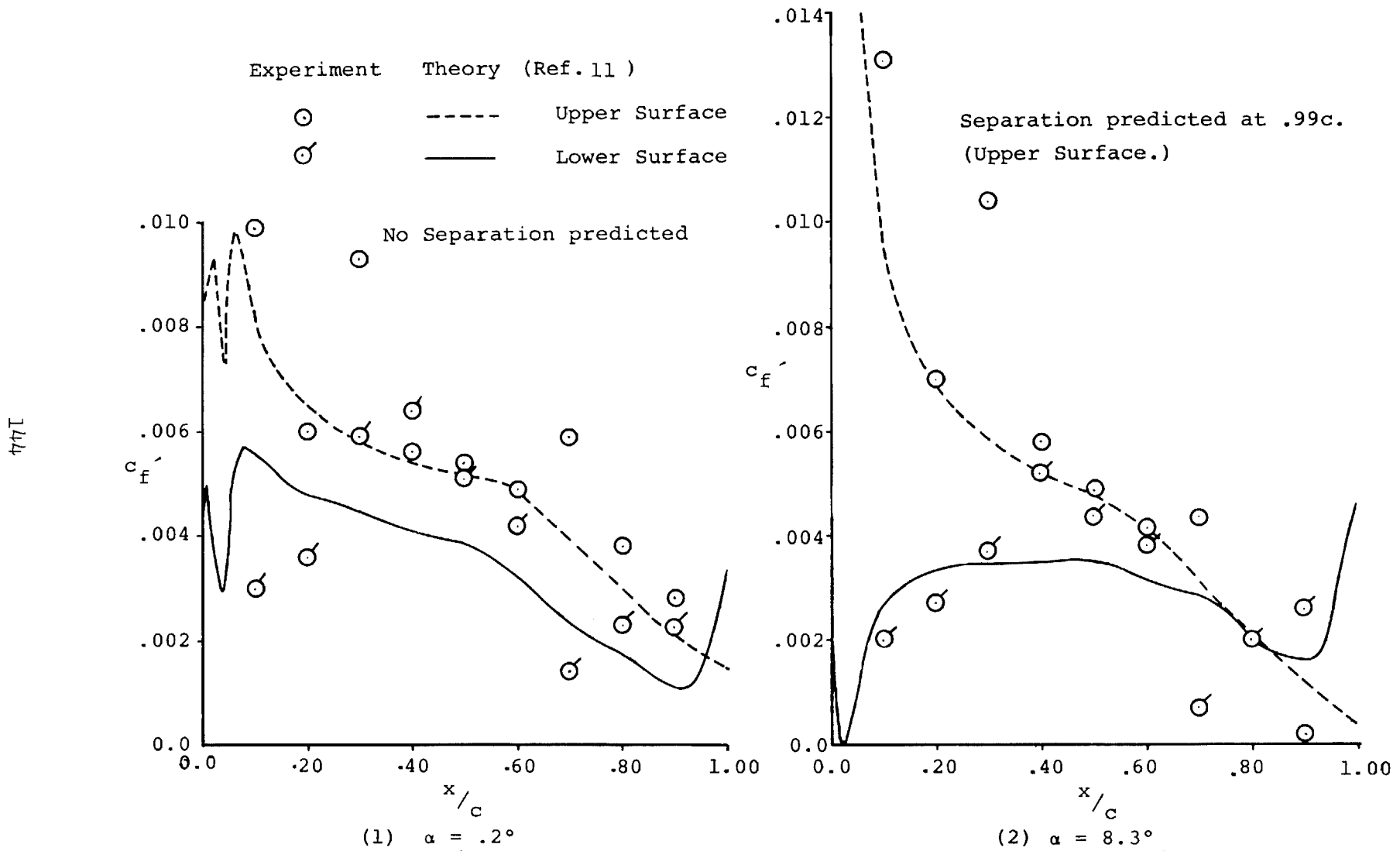


Figure 22C - Comparison of Experimental and Theoretical Skin Friction Distributions, GA(W)-2 Airfoil.

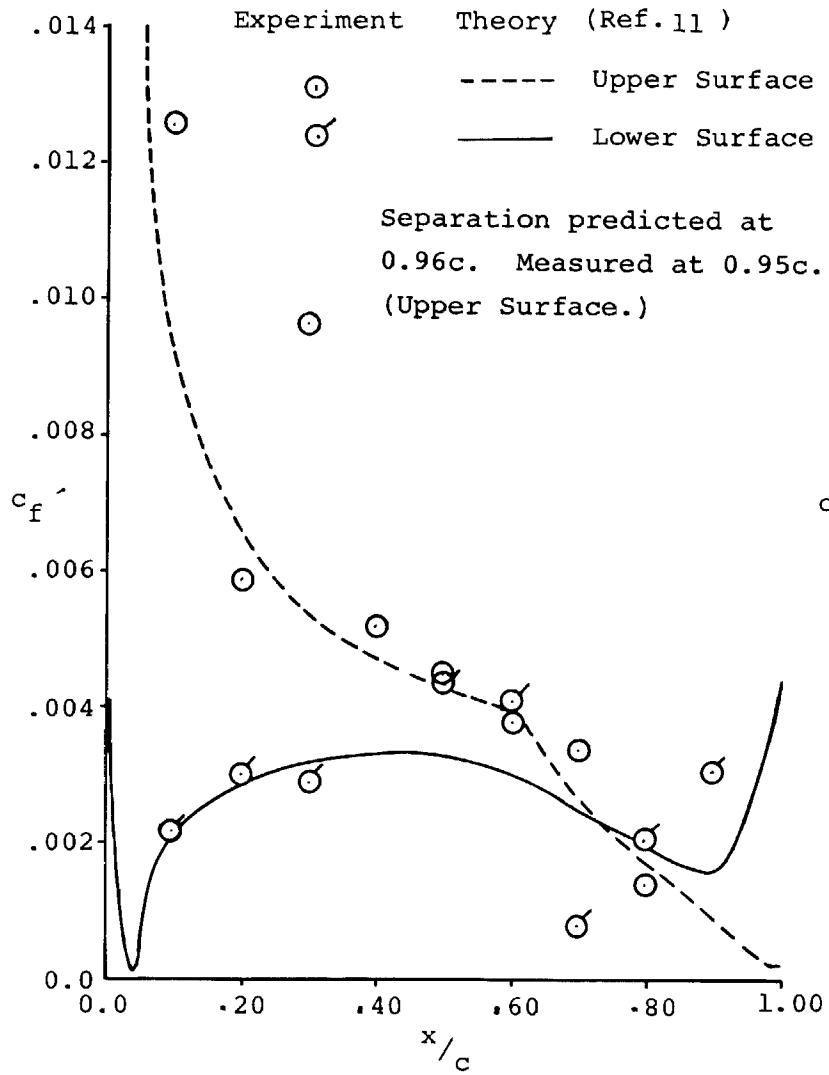
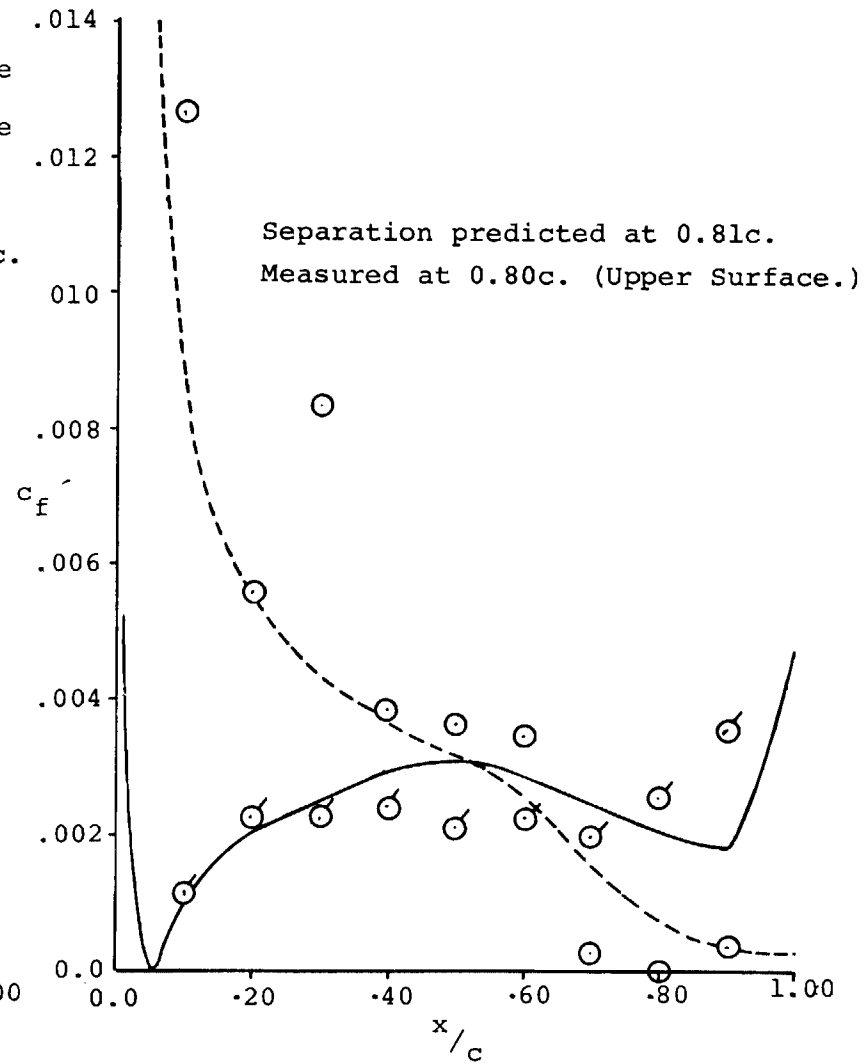
(3) $\alpha = 10.3^\circ$ (4) $\alpha = 14.4^\circ$

Figure 22C- Continued.

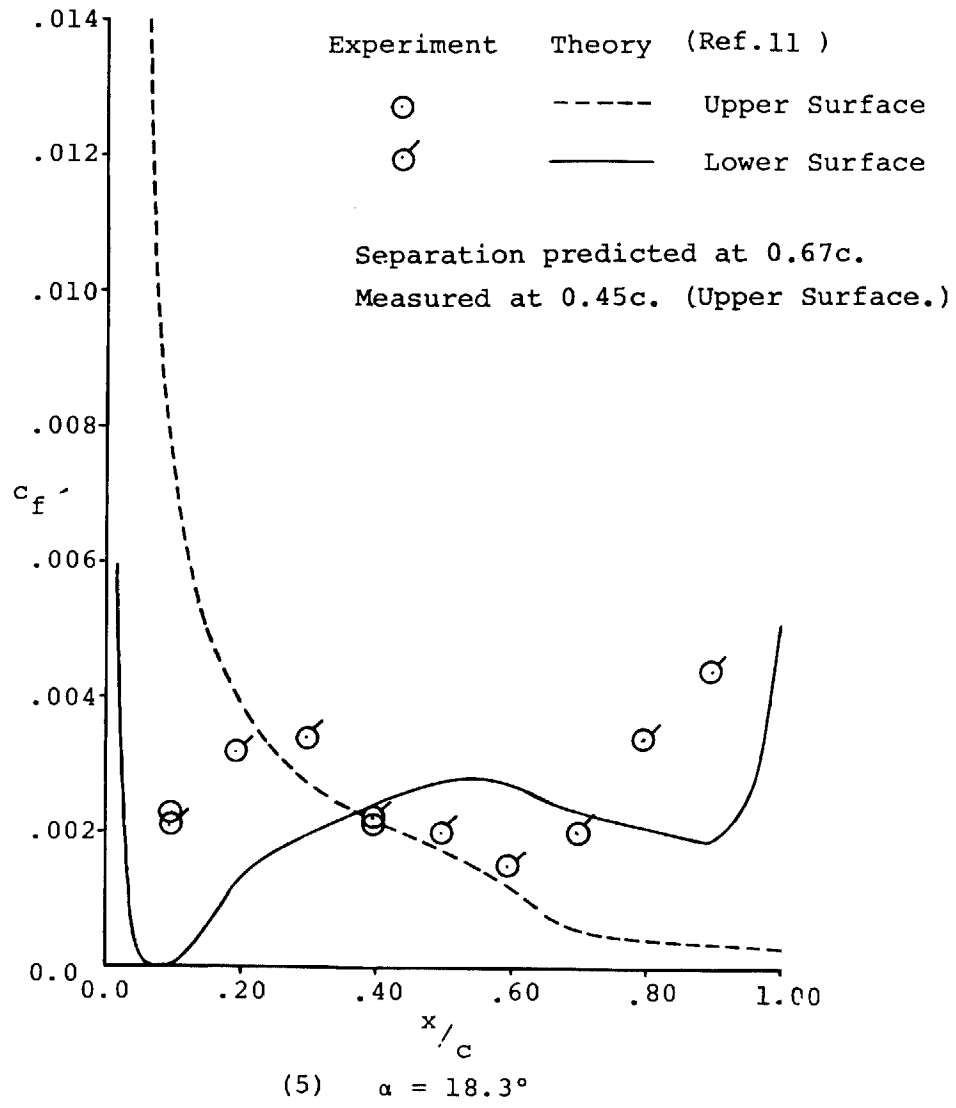


Figure 22C- Concluded.

Symbol	Airfoil
◇	GA(W)-1
△	GA(W)-2
□	NACA 2412
○	LS(1)-0421 Mod

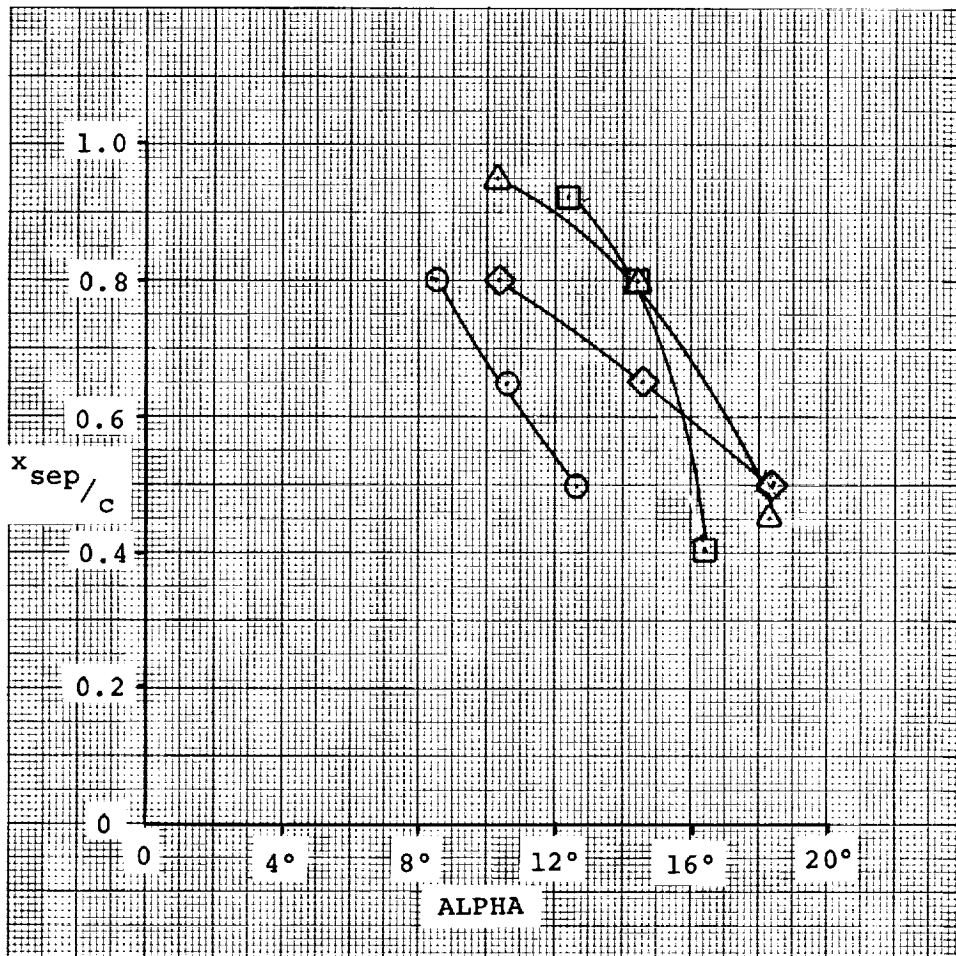
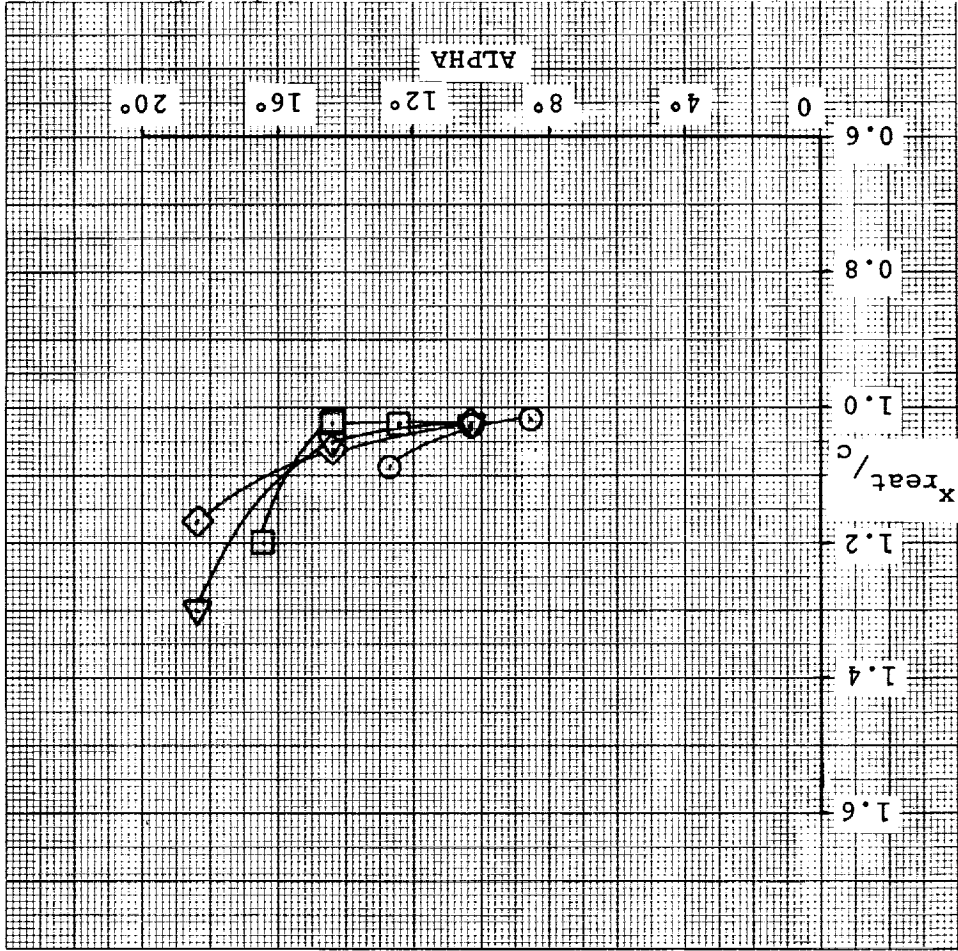


Figure 23 - Comparison of Flow Separation Points.

Figure 24 - Comparison of Flow Reattachment Points.



Symbol

○	IS (1) - 0421 MOD
□	NACA 2412
▽	GA (W) - 2
◇	GA (W) - 1
△	Airfoil

APPENDIX A

Probe Interference Effects on Static Pressure Measurements

During the course of the measurements of the flow properties over the NACA 2412 and GA(W)-2 airfoils, it was found that under certain conditions the probe and probe mechanism interfered with the static pressure distribution on the airfoil surface. These discrepancies appeared from comparisons of surface C_p measurements which had been recorded for a few airfoil stations with the probe mechanism in place, with pressure measurements made with the probe mechanism removed. Review of earlier test data showed that the discrepancy did not appear in tests conducted with the 17% thick GA(W)-1 airfoil (Ref. A-1).

Special runs were made with the GA(W)-2 airfoil to measure more complete upper surface pressure distributions with and without the probe mechanism in place. Results of these runs are shown in Figures A1 through A3. These results show that the probe system had a relatively small effect on surface C_p 's at 10.3° and 14.4° angle of attack. At 18.3° , on the other hand, a large change was observed. Tuft and oil dot studies revealed that without the probe in place, separation occurred at $0.40c$, while with the probe installed, no separation was present at this angle of attack. Apparently the probe mount installation created a pressure field which

reduced the airfoil adverse pressure gradient to the extent that separation point location for high angles of attack was strongly influenced. That this phenomenon was not observed during the GA(W)-1 tests is evidently a consequence of the less severe adverse pressure gradients associated with the 17% thick GA(W)-1 airfoil. This same reasoning also explains why the interference is significant only at the high angle of attack for the NACA 2412 and GA(W)-2 airfoils, since pressure gradients increase with angle of attack.

In order to reduce probe mount interference, a new test section ceiling was designed and installed. The new ceiling had a longitudinal slot and structural provisions for mounting the probe track and carriage outside the test section. The ceiling slot opening was fitted with foam seals to prevent leakage, and a new airfoil-shaped probe strut was designed and fabricated to replace the circular strut used in earlier tests. Figure A4 shows a sketch of the unmodified and modified probe mechanisms.

Figure A5 shows static pressure distributions at the 16.4° angle of attack condition for a series of probe mount configurations. These data show that with the modified hardware, some interference due to the probe is still present. The interference is greatly diminished, however, and is confined primarily to the region ahead of the separation point. The separation location was shifted less than $.05c$, based upon tuft and oil flow studies. Thus most of the interference encountered with the original set-up was eliminated by the probe mount system modifications.

Reference A-1. Seetharam, H.C., and Wentz, W.H., Jr.: Experimental Studies of Flow Separation and Stalling on a Two-Dimensional Airfoil at Low Speeds. NACA CR-2560, July 1975.

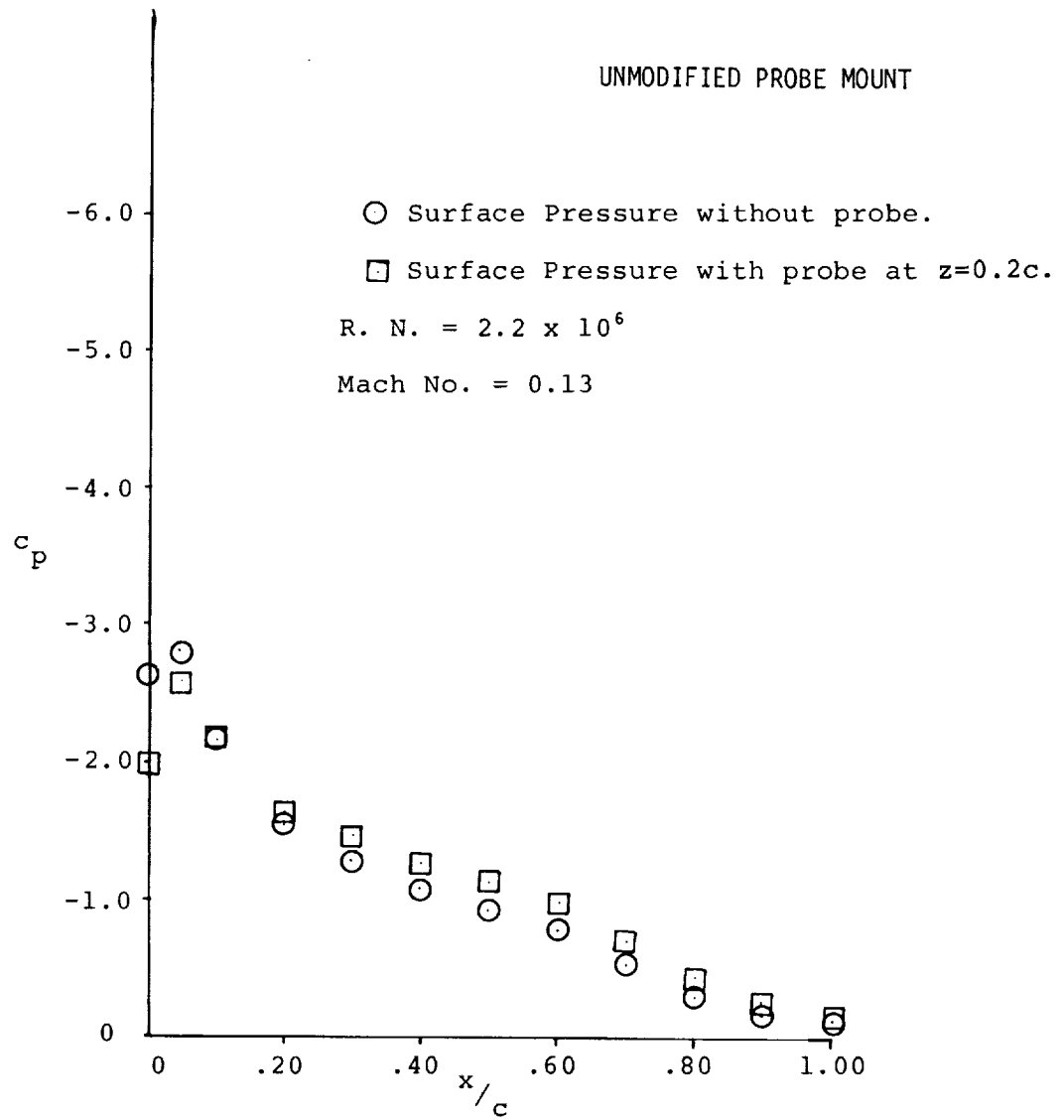


Figure A1 - Calibration for probe interference, GA(W)-2, $\alpha = 10.3^\circ$.

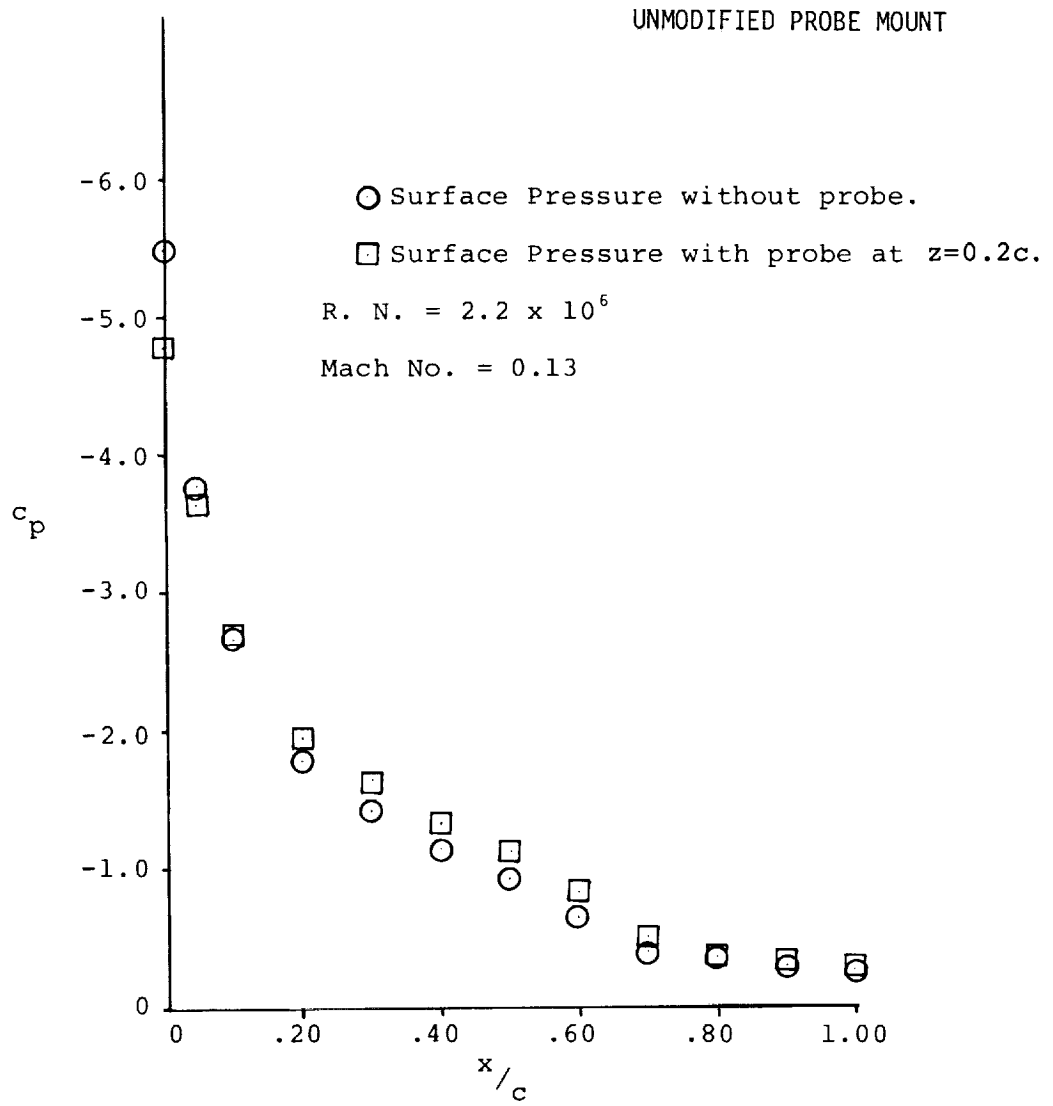


Figure A2 - Calibration for probe interference, GA(W)-2, $\alpha = 14.4^\circ$.

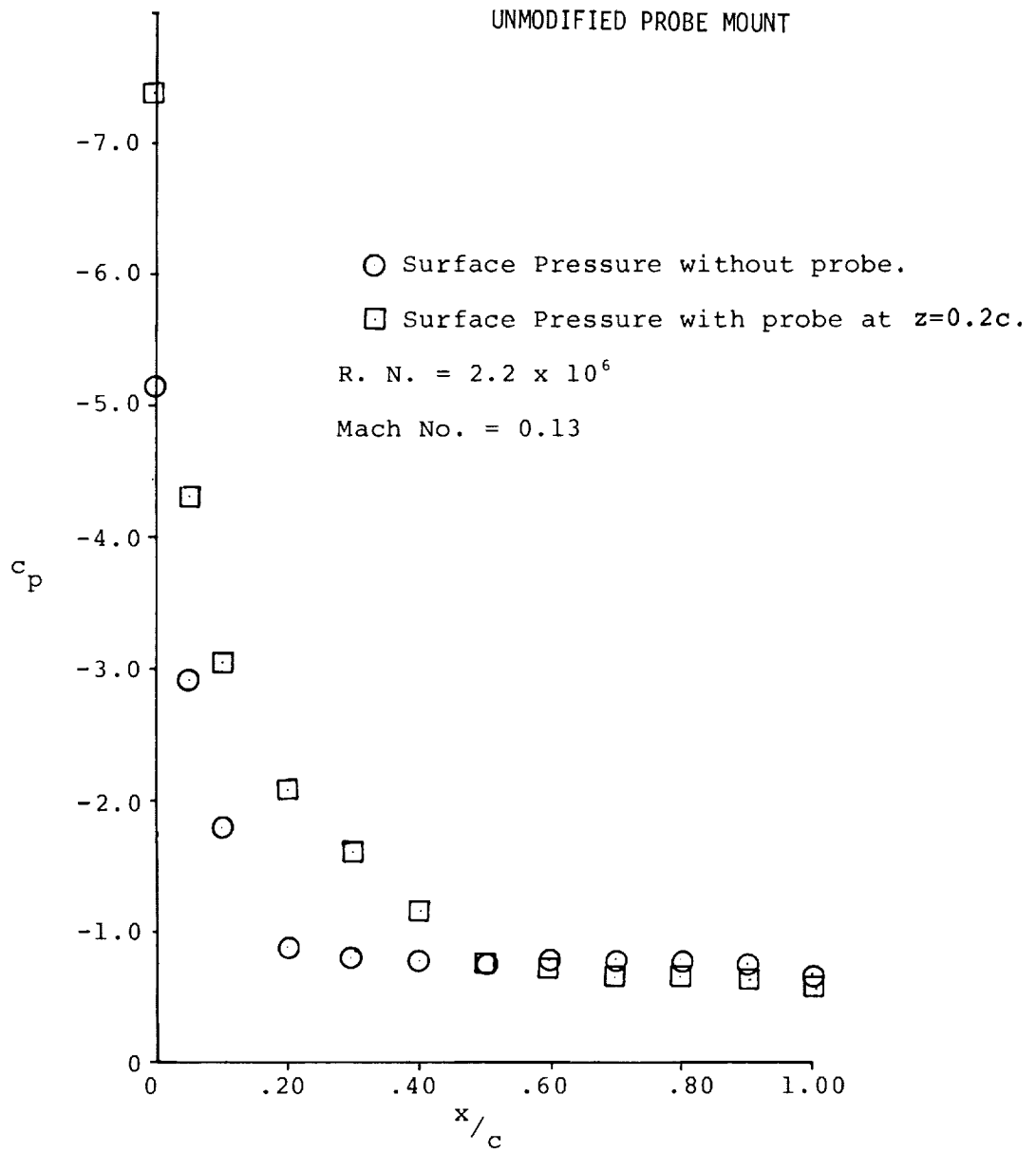
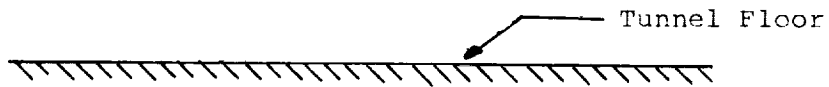
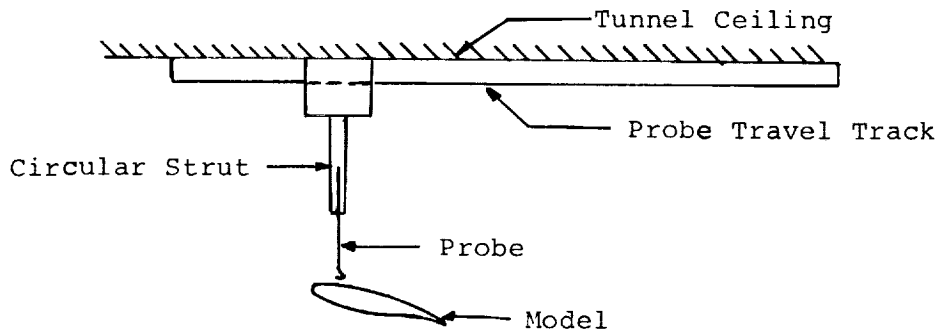
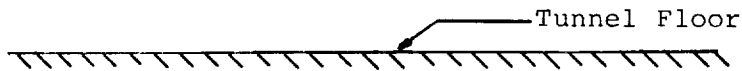
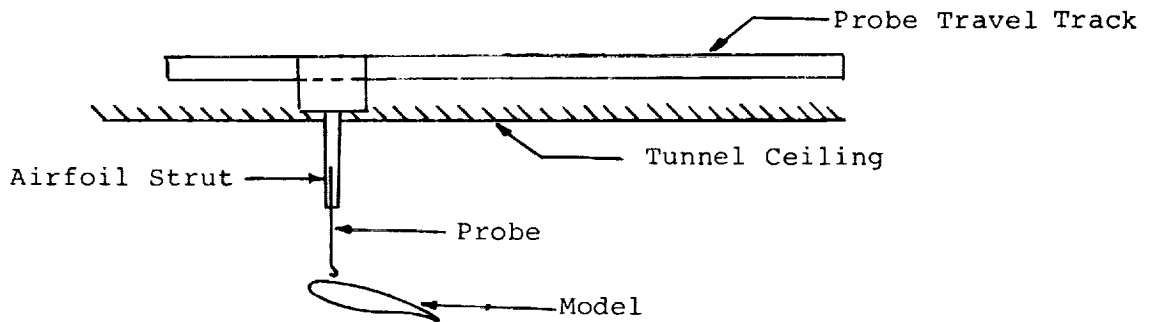


Figure A3 - Calibration for probe interference, GA(W)-2, $\alpha = 18.3^\circ$.



a) UNMODIFIED PROBE MOUNT



b) MODIFIED PROBE MOUNT

Figure A4 - Probe mount and tunnel modifications.

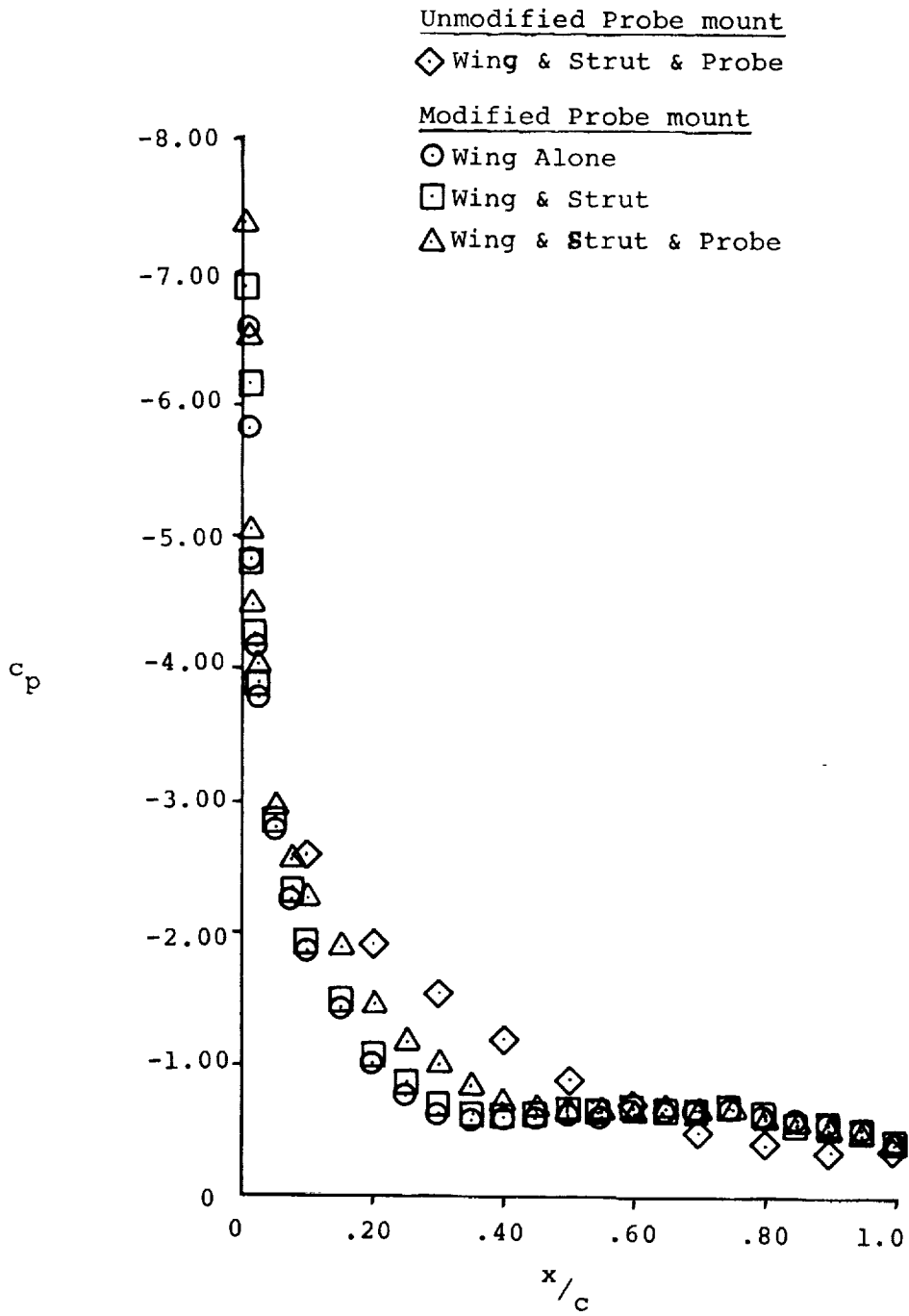


Figure A5 - Surface Static Pressure Interference, NACA 2412, $\alpha=16.4^\circ$.

APPENDIX B

Velocity Profiles as Measured by Various Instruments in Unsteady Reversed Flow Fields

In the course of the present investigation, various instrumentation has been developed and used to measure velocity profiles. The flow fields over the airfoil and in the wake are steady for certain angles of attack. For other larger angles of attack, regions of reversed flow accompanied by unsteady flow can occur over the aft portions of the airfoil and in the wake.

Initially a five-tube probe was used for measuring the velocity profiles. However this probe did not accurately sense the regions of reversed flow. Therefore, a four-tube probe was developed and used in the regions where reversed flow existed and regions near the surface of the body. Later the hot film became available and was used primarily to sense the unsteady portions of the flow field and to get the maximum excursions of the velocities. The hot film was also used to sense the regions of flow reversal. As explained in the text, if at any time the flow velocity at some point became zero the flow was deemed to have reversed. Near the end of the present research a split film anemometer was obtained. This allowed sensing of the velocity both in a positive and negative direction and therefore provided a clearer measurement of the reversed flow regions.

As mentioned in the text any pressure probe device such as the four- or five-tube probe cannot respond to rapid fluctuations of the flow field. These probes therefore measure some integrated average depending on the tube size, oscillation frequency, etc. Thus in the regions of unsteady flow some average velocity is measured by the four-tube or the five-tube probe,

whereas, with the split film actual velocity fluctuations are obtained. If a sufficient sample size can be recorded and processed, a true mean velocity can be determined.

Figure B1 shows a comparison of velocity measurements as obtained by the four-tube, five-tube and split film probes at various stations near the aft end of the airfoil. These data were obtained for the GA(W)-2 airfoil at an angle of attack of 18.3 degrees. For the split film data, the minimum and maximum values were recorded as read from the oscilloscope for $x/c = 0.70$ and $x/c = 1.00$. These data are shown as the shaded area indicating the maximum and minimum velocities. The dashed lines show the temporal mean of the output as read from the digital volt meter.

One can see from this figure that the four-tube and five-tube probe measurements show an average velocity somewhere between the maximum and minimum time fluctuating velocities. Thus, one must exercise caution in interpreting the data obtained with the various probes. The present comparison does reflect reasonably good agreement as to the flow reversal points measured by split film and pressure probes.

From this series of tests the advantages of using the split film are evident. High rate digital data acquisition and processing techniques are presently being developed to obtain statistical data associated with the velocity fluctuations such as the maximum and minimum velocities, the mean velocity, turbulence levels, standard deviations, etc. These techniques will be applied as standard testing methods at WSU as they are developed and incorporated in the data reduction computer programs.

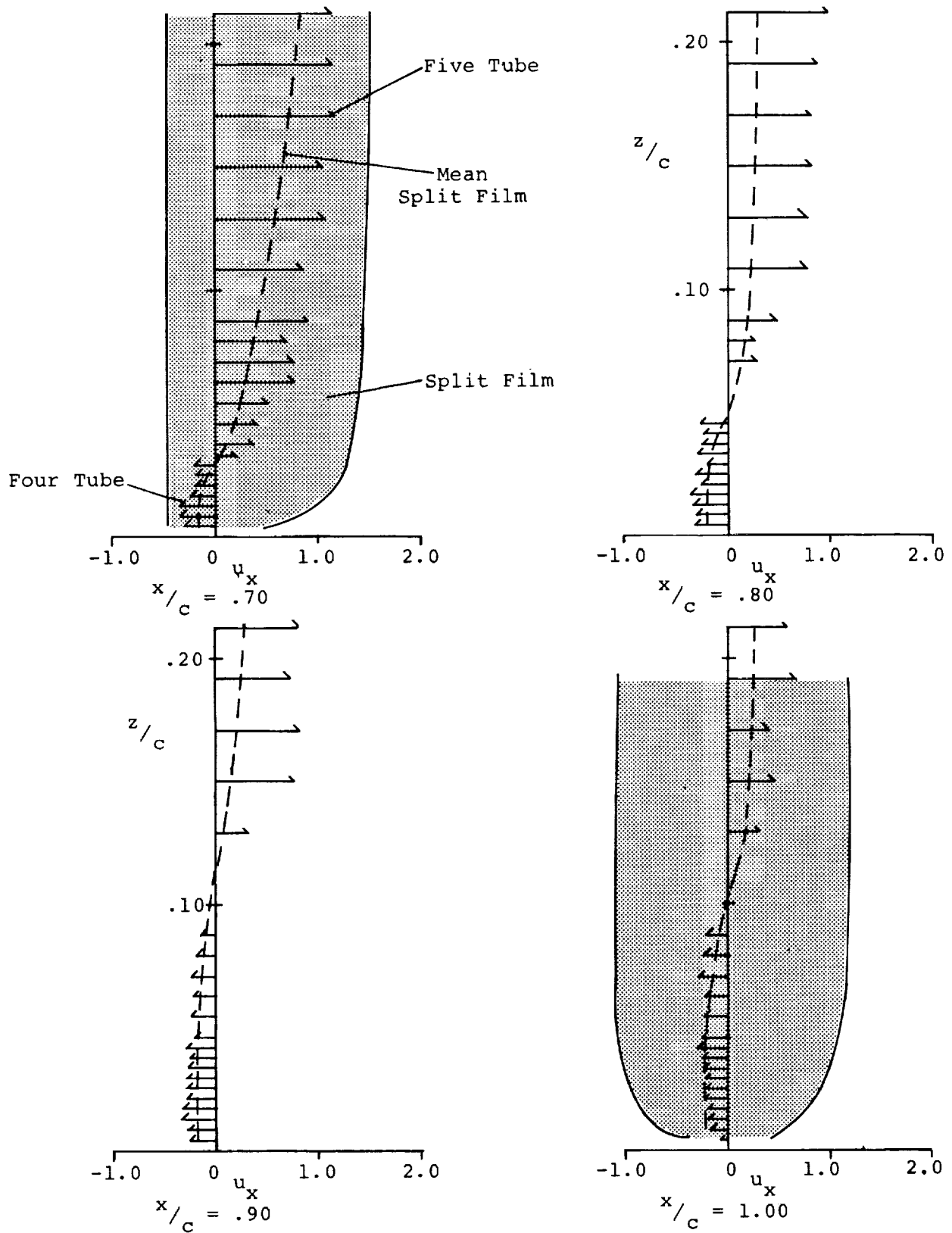
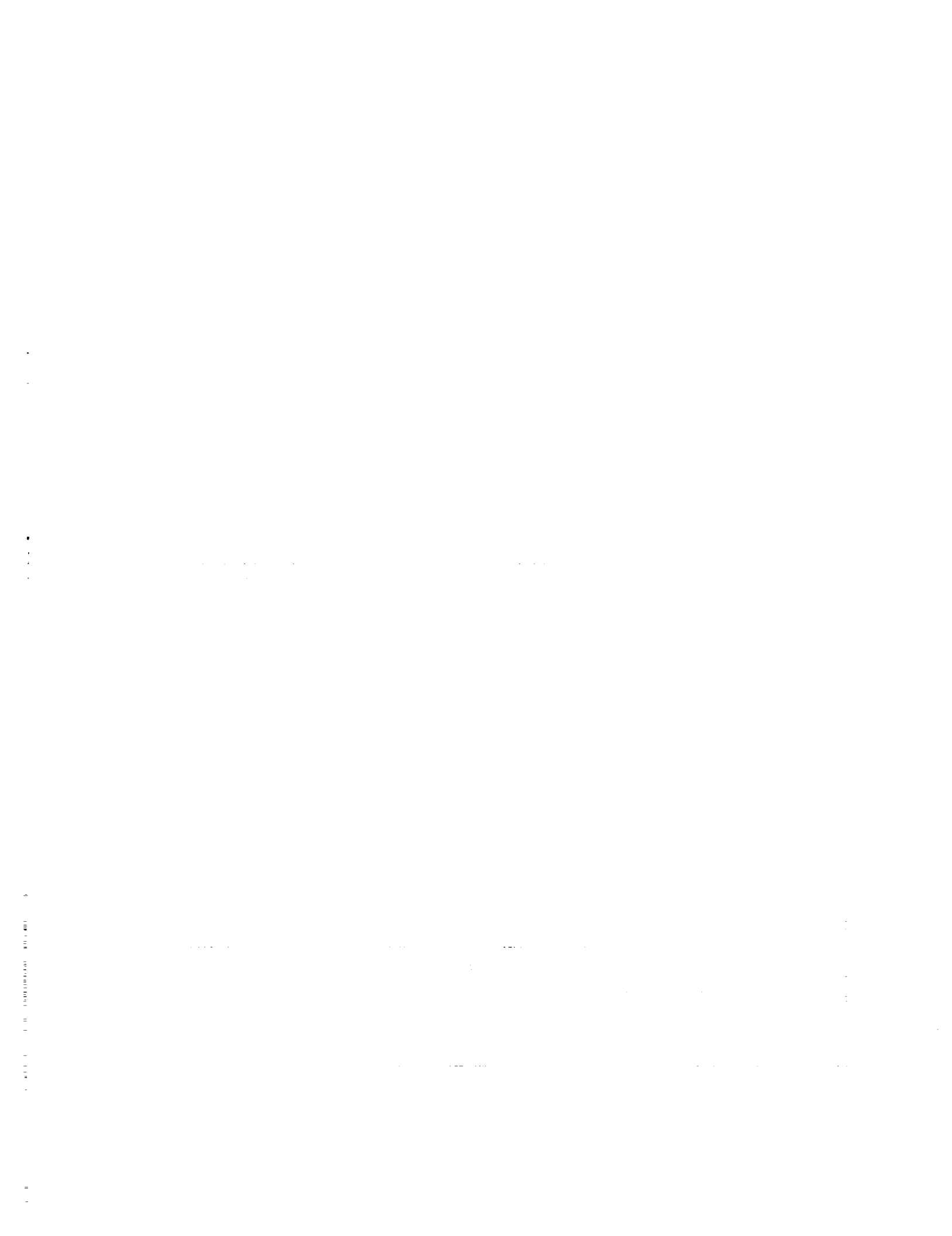


Figure B1 - Velocity profiles from various instruments in unsteady reverse flow. GA(W)-2 airfoil at $\alpha = 18.3^\circ$



1. Report No. NASA CR-3530		2. Government Accession No.		3. Recipient's Catalog No.	
4. Title and Subtitle EXPERIMENTAL STUDIES OF FLOW SEPARATION OF THREE AIRFOILS AT LOW SPEEDS				5. Report Date March 1982	
				6. Performing Organization Code	
7. Author(s) E. J. Rodgers; H. C. Seetharam; and W. H. Wentz, Jr.				8. Performing Organization Report No. AR 79-2	
9. Performing Organization Name and Address Wichita State University Wichita, Kansas				10. Work Unit No.	
				11. Contract or Grant No. NGR 17-003-021	
12. Sponsoring Agency Name and Address National Aeronautics and Space Administration Washington, DC 20546				13. Type of Report and Period Covered Contractor Report	
				14. Sponsoring Agency Code	
15. Supplementary Notes Langley Technical Monitor: Kevin W. Noonan Topical Report					
16. Abstract Wind tunnel tests have been conducted on the NASA LS(1)-0421 Mod, NACA 2412 and NASA GA(W)-2 airfoil sections at a Reynolds number of 2.2×10^6 and a Mach number of 0.13. Detailed measurements of flow fields associated with turbulent boundary layers of these airfoils have been obtained at pre-stall, near-stall, and post-stall angles of attack. Velocity and pressure survey results over the airfoil and in the associated wake are presented for fully attached flow conditions through the stalled flow condition. Extensive force, pressure, tuft survey, hot-film survey, local skin friction and boundary layer data are also included.					
17. Key Words (Suggested by Author(s)) General aviation airfoils Separated flow fields LS(1)-0421 Mod airfoil NACA 2412 airfoil GA(W)-2 airfoil			18. Distribution Statement FEDD Distribution Subject Category 02		
19. Security Classif. (of this report) Unclassified		20. Security Classif. (of this page) Unclassified		21. No. of Pages 162	22. Price A08

Available: NASA's Industrial Applications Centers